Kir7.1 expression and partial loss in the uterus, and therapeutic approaches for overcoming Kir7.1 disease mutants

By

Allison Kay Spillane

A dissertation submitted in partial fulfilment of

the requirements for the degree of

Doctor of Philosophy

(Endocrinology and Reproductive Physiology)

at the

UNIVERSITY OF WISCONSIN-MADISON

2025

Date of final oral examination: 07/16/2025

The dissertation is approved by the following members of the Final Oral Committee:

Bikash R. Pattnaik, Associate Professor, Pediatrics

Laura L. Hernandez, Professor, Animal and Dairy Sciences

Manish Patankar, Professor, Obstetrics and Gynecology

Krishanu Saha, Associate Professor, Biomedical Engineering

ABSTRACT

Adverse pregnancy outcomes (APO) and infertility are a global issue with unknown causes that lead to long-term health issues. **We aimed to investigate whether a genetic mutation in the ion channel Kir7.1, which is crucial for uterine quiescence, contributes to APOs and infertility.** Additionally, female patients with *KCNJ13* mutations, the gene encoding Kir7.1, are identified and suffer from vision issues. **Therefore, we also aimed to determine therapeutic targets to *KCNJ13* in the eye, that could be modified to treat the uterus.** We utilized genomic editing techniques to create and correct the R166X mutation to *KCNJ13* but were unable to insert the mutation successfully and only observed 10% correction once with a base editor (BE). Although the R166X mutation was challenging to correct using genomic editing techniques, anticodon-engineered tRNA (ACE-tRNA) was able to suppress the mutation, leading to the expression of full-length Kir7.1 protein on the membrane and partial recovery of channel function. We observed that both wild-type (WT) and mutant, R166X, protein express on the membrane; implicating that these subunits may be co-assembling to create a WT/R166X heterotetrameric channel and preventing full recovery. Further, we demonstrated the ability of a preclinical gene augmentation therapy, HUB-101, to deliver the WT *KCNJ13* gene to mouse retinal pigmented epithelial (RPE) cells in a dose-dependent manner. To further identify Kir7.1s role in the uterine myometrium, we used a novel camera system to monitor pregnancy and demonstrated a trend of longer labor times in heterozygous (HET) mice compared to WT; suggesting possible changes in myometrium function are due to a partial loss of Kir7.1. When investigating Kir7.1 expression throughout pregnancy, we confirmed that Kir7.1 is expressed in the mice myometrium only during mid-gestation. However, no Kir7.1 expression was observed in the non-human primate (NHP) myometrium during mid-gestation. Additionally, Kir7.1 was expressed in a non-pregnant (NP) state and throughout pregnancy in the luminal epithelium (LE), glandular epithelium (GEp), and vasculature of mice and NHP. Implicating that loss of Kir7.1 due to genetic mutations could play a role in various APOs. In summary, we further characterized Kir7.1 expression in the uterus and its potential role in APOs and infertility, observed trends in altered labor physiology following a partial loss of Kir7.1 using a novel camera system, and identified potential treatment options for *KCNJ13* mutations to restore the expression and function of Kir7.1.

TABLE OF CONTENTS

LIST OF FIGURES

CHAPTER 1

CHAPTER 2

CHAPTER 3

CHAPTER 4

CHAPTER 5

CHAPTER 6

Appendix I

GLOSSARY OF TERMS

AAV	associated adeno virus
ABE	adenosine base editor
ACE	anticodon-engineered
ACE-tRNA	anticodon-engineered tRNA
ACE-tRNA$^{Arg.UGA}$	arginine anticodon-engineered tRNA containing a UGA anticodon
AI	artificial intelligence
APO	adverse pregnancy outcome
BE	base editing
Ca^{2+}	calcium
CaCC	Ca^{2+}-activated Cl^- channel
Cav1.2	voltage-gated L-type Ca^{2+} channel
Cas9n	CRISPR-Cas9 nickase
Cas9n-RT	CRISPR-Cas9 nickase fused to an engineered reverse transcriptase
CBE	cytosine base editor
CF	cystic fibrosis
CFTR	cystic fibrosis transmembrane conductance regulator gene
Cl^-	chloride
C-terminal	carboxyl-terminal
CVD	cardiovascular disease
Cx43	connexin43
dsDNA	double-stranded DNA
D0	day 0 of gestation, first day of breeding
D2-18	days (2-18) of gestation
ENaC	Epithelial Na^+ channel
ER	endoplasmic reticulum
FDA	Food and Drug Administration
GDM	gestational diabetes mellitus
GD90	gestational day 90, mid-gestation in NHP
GE	gene editing

Geco1a	a Ca^{2+} visualizer
GEp	glandular epithelium
GFP	green fluorescent protein
GFP^{TGA}	sfGFP-N150TGA, a GFP containing a TGA stop codon
gRNA	guide RNA
glyburide	glibenclamide
HET	heterozygous
HDP	hypertensive disorders of pregnancy
HDR	homology-directed repair
HEK FRT R166X	R166X-*KCNJ13* gene inserted into HEK293T cells using FLP-FRT recombinase
HEK FRT WT	WT-*KCNJ13* gene inserted into HEK293T cells using FLP-FRT recombinase
HEK293T	HEK Flp-In 293 cells
h*KCNJ13*	human *KCNJ13* gene
HOMO	homozygous
HUtSMC	human uterine smooth muscle cells
H&E	Hematoxylin and eosin
IACUC	Institutional Animal Care and Use Committee
ICE	Inference of CRISPR Edits, a tool from Synthego
I_K	K^+ current
I_{Rb}/I_K	Rb^+ fold change
IR	infrared
IRT	infrared thermography
hiPSC	human induced pluripotent stem cells
hiPSC-RPE	human induced pluripotent stem cell retinal pigmented epithelium
K^+	potassium
K^{ATP}	ATP-sensitive K^+ channel
KCNJ2	gene that encodes the Kir2.1 channel
KCNJQ1	gene that encodes the Kv7.1 channel
KCNJ11	gene that encodes the inwardly rectifying Kir6.2 K^+ channel
KCNJ13	gene that encodes the inwardly rectifying Kir7.1 channel
Kir	inwardly rectifying K^+ channel

Kir6	subunits make up part of the K^{ATP} quaternary structure
KNa	Na^+-activated K^+ Slo2 channel
Kv7 and Kv11.1	voltage-dependent K^+ channels
LCA2	Leber's congenital amaurosis 2, in patients harboring *RPE65* mutations
LCA16	Leber's congenital amaurosis 16, in patients harboring *KCNJ13* mutations
LE	luminal epithelium
Lenti-Kir7.1	Lentivirus carrying the WT-*KCNJ13* gene
LNP	lipid nanoparticle
Luxterna	Voretigene Neparvovec
MC4R	melanocortin-4 receptor
m*Gapdh*	mouse *Gapdh* gene
m*Kcnj13*	mouse *Kcnj13* gene
mRPE	mouse RPE
Na^+	sodium
NALCN	Na^+ lead channel, nonselective
ngRNA	nicking guide RNA
NGS	next-generation sequencing
NHEJ	non-homologous end-joining
NHP	non-human primate
nick	single-stranded break
NMD	nonsense-mediated decay
NP	non-pregnant
NCT	near-cognate aminoacyl-transfer RNA
N-terminal	amino-terminal
NTC	native termination codon
ORF	open reading frame
OXT	oxytocin
OXTR	oxytocin receptor
PAM	protospacer adjacent motif
PCOS	polycystic ovarian syndrome
PE	prime editing

pegRNA	prime editing guide RNA
p*KCNJ13*	primate *KCNJ13* gene
PPROM	preterm premature rupture of membranes
PTC	premature termination codon
PVN	paraventricular nucleus
P4	progesterone
qPCR	quantitative PCR
Rb+	rubidium
RFP	red fluorescent protein
RNP	ribonucleoprotein
RPE	retinal pigmented epithelium
RPE65	gene that encodes the RPE-specific 65 protein
RT	reverse transcription/transcriptase
RUO	research use only
SGK1	serum- and glucocorticoid-inducible kinase
sgRNA	single guide RNA
SK	small-conductance Ca^{2+}-activated K^+ channel
SNV	single-nucleotide variant
ssODN	single-stranded oligodeoxynucleotides
SUR	sulphonylurea receptor
SVD	Snowflake Vitreoretinal Degeneration
TGH	total glycosylated hemoglobin
TRP	transient receptor potential channel
TRPM6	transient receptor potential melastatin 6
UT	untreated
VDCC	voltage-dependent Ca^{2+} channel
WHO	World Health Organization
WT	wild-type
XLRP	X-linked retinitis pigmentosa

ACKNOWLEDGMENTS

I first want to thank my mentor, Dr. Bikash Pattnaik, for providing me with the opportunity to pursue research. From first entering the lab as an undergraduate student to completing my PhD, you have helped me learn how to think more critically and scientifically about my research projects. Additionally, I appreciate that you never hesitated to take the time to explain topics I did not yet understand, which was vital in helping me grow as a young scientist.

I would also like to acknowledge my thesis committee members: Dr. Laura Hernandez, Dr. Manish Patankar, and Dr. Krishanu Saha. Additionally, my past committee member: Dr. Derek Boeldt. You were all critical in challenging me to consider variables within my thesis project that I had not thought about. Your constructive criticism and encouragement allowed me to improve my research project and continue pushing through the failures that I encountered along the way.

Thank you to the Endocrinology and Reproductive Physiology Graduate Program: Dr. Laura Hernandez, Bootsy Harden, Dr. Manish Patankar, Dr. Ian Bird, and Grace Jensen. I would especially like to thank Dr. Laura Hernandez and Bootsy Harden for your sincere support throughout the end of my PhD. Your encouragement and humbleness allowed me to feel supported through the hard times and helped form my sense of belonging in this field.

To the Pattnaik Lab members that I have had the pleasure of working with: Meha, Pawan, Katie, Enes, Yu, Sehrish, and Sanjai. Thank you for your support both in my research and personal lives. Your ability to simultaneously support and challenge my research has allowed me to be a better scientist. And your companionship throughout graduate school has allowed me to feel supported as we went through the successes and failures of research together. Additionally, to my undergraduate student mentees: Kaia Kapfer, Manya Mehra, and Clara Yu. Thank you for giving me the grace of growing as a mentor alongside you. Seeing the growth in your professional lives has given me a lot of joy.

To the family and friends that have supported me along this journey. I truly could not have done this without you being a village of support for me. First, to my husband, Tim. You have been the biggest encourager and supporter throughout this long process. Thank you for helping to keep me grounded and for making sure that I found life, joy, and adventure outside of graduate school. Being your wife has given me an irreplaceable sense of fulfillment and identity outside of being a graduate student. And thank you for blessing me with and helping to raise two beautiful children while I was pursuing this degree. To my children, Emmaleia and Kayden. Thank you for helping me find purpose and joy outside of graduate school. No matter how good or hard the day was, I got to end everyday with your love of life and amazement at the world. That was such a blessing. To my parents, in-laws, and siblings, I would never have been able to reach the end of this degree without your continued support and encouragement. You have played a key role in me reaching this part of my journey.

And lastly, but most importantly, I want to thank God. It is truly because of Him that I could complete this degree and have made it through all the seasons of life along the way; the good and the bad, both in my professional and personal life. All the glory is sincerely His.

Chapter 1: Background and Introduction

The problematic cases of unknown pregnancy related issues

Adverse pregnancy outcomes (APO) are a global issue that leads to lifelong health issues for mothers and offspring [1-3]. APOs affect 1 in 5 births in the United States, and include preterm labor, hypertensive disorders of pregnancy (HDP), gestational diabetes mellitus (GDM), high birth weight, and low birth weight [4, 5]. The causes of some of these issues are still unknown and, thus, require further investigation.

Preterm labor

Spontaneous preterm labor is defined as spontaneous labor before 37 weeks gestation [6, 7]. Globally, approximately 13.4 million births were premature in 2020 and health complications led to 900,000 deaths in children in 2019 [8]. In the United States, 10.41% of births were considered premature in 2023 [9]. Infants born prematurely, even those considered late preterm infants, are at a higher risk for developing long-term health issues compared to infants born at term [10-13]. The long-term risks that have been associated with premature birth include retinopathy of prematurity, cerebral palsy, and intellectual disabilities [13]. Progesterone (P4) withdrawal, activation of labor via oxytocin (OXT), and premature activation of the decidua are physiological causes of premature labor that have been theorized [13]. Premature activation of the decidua is thought to be caused by different pathogenic-associated causes that lead to spontaneous premature labor [6, 13]. However, the link between many of these causes is poorly understood and some causes of preterm labor remain unknown. Treatment options for preterm labor include bed rest and/or hydration for prevention, pharmacological agents aimed at delaying the onset of early contractions, and delivery in a hospital where the infant can be under constant medical care and observation [13]. There is no substantial evidence that bed rest or hydration prevents preterm labor. Administration of pharmacological agents poses health risks to both the infant and the mother. Additionally, treatments often only stop contractions and further delay labor by 24-48 hours with many not

preventing the risks to infants associated with preterm birth. Therefore, the identification of new treatments is necessary for preventing and treating preterm labor. Additionally, a retrospective study demonstrated that 78% of women with spontaneous preterm birth had no clinical risk factors, supporting the need for further investigation into the physiological causes of this diagnosis [14]. The further identification of unknown causes of preterm labor can lead to more successful treatment options for patients and improved health outcomes for both the mother and the infant.

Hypertensive disorder of pregnancy (HDP)

High blood pressure during pregnancy, HDP, can be differentiated into several categories, including chronic hypertension and preeclampsia [15, 16]. Chronic hypertension occurs when diagnosed with hypertension pre-pregnancy or before 20 weeks gestation. Preeclampsia is the most severe form of HDP, occurring in 2-8% of pregnancies and leading to about 46,000 maternal deaths and 500,000 fetal deaths every year [16, 17]. In the United States, the prevalence of HDP, including preeclampsia, increased from 13.3% in 2017 to 15.9% in 2019 [18]. There are many short-term health risks associated with hypertension in pregnancy, but mothers and infants also suffer from long-term health risks. For the mother, one highly investigated long-term health effect is increased rates of cardiovascular conditions [15, 16, 19]. Additionally, mothers who develop HDP are at a higher risk for developing end-stage renal disease [20]. For the infant, long-term health effects are often risks associated with preterm labor, fetal growth restriction, and low-birth weight [16, 21]. This is because the successful treatment of preeclampsia is limited and often results in medical induction of premature birth to prevent further adverse health outcomes and death. Recently, drug treatments such as statins, metformin, or oxidative stress targeting agents have emerged [22-25]. However, the most common treatment option is still medically induced labor. The lack of efficient treatments may be due to gaps in the physiological causes of hypertension during pregnancy. The progression of preeclampsia occurs when there is abnormal placentation in the first trimester and maternal vascular dysfunction in the second or third trimester [26]. However, the causes of abnormal placentation and maternal vascular dysfunction are not well understood, and several

theories have been proposed. Additionally, no pathophysiological factor has been identified in all investigated cases of preeclampsia, alluding to the possibility of several factors leading to disease onset and progression [16, 26]. Since preeclampsia is a leading global cause for maternal and neonatal mortality, and the most common treatment option is early induction of labor, further understanding of the physiological causes and, thus, effective treatment options are necessary.

Gestational diabetes mellitus (GDM)

GDM is recognized when a patient with no prior diagnosis of diabetes presents with glucose intolerance during pregnancy [16]. Between 2005 and 2015, range of GDM prevalence worldwide, in World Health Organization (WHO) defined regions, ranged from 5.8% of pregnancies in Europe to 12.9% in the Middle East and North Africa [27]. Studies ranging from 2005 to 2018 demonstrate that the prevalence increased to 6.1% in Europe and 15.2% in the Middle East and North Africa [28]. In the United States, the rate of GDM was 6.0% in 2016 and increased to 8.3% of births in 2021 [29]. This global increase in GDM diagnosis further supports the need for improved disease pathophysiology and treatment investigation. The long-term health risks in mothers who develop GDM include future development of type-2-diabetes (T2D), greater risk of GDM in subsequent pregnancies, and an increased risk of total mortality, including due to the development of cardiovascular disease (CVD) [30, 31]. For offspring, the long-term health effects associated with GDM include an increased risk of developing obesity and diabetes [31, 32]. While obesity and a family history of diabetes can increase the chance of GDM development in pregnancy, the physiological causes of GDM are still poorly understood [33, 34]. In most cases of GDM there is dysfunction in the beta-cells, leading to a reduction in insulin production [34, 35]. Therefore, glucose levels in the blood remain high and can lead to insulin resistance. However, in some cases of GDM beta-cell dysfunction is not the culprit and requires further investigation. The treatment options for GDM are scarce, relying on changes to lifestyle and drug treatments such as insulin, metformin, and glibenclamide (glyburide) [34, 36, 37]. Further investigation into the physiological causes of GDM can help guide the development of new and more effective treatment and prevention options.

High birth weight

Fetal macrosomia, or high birth weight, is classified by birth weights of 4000g (8lb, 13oz) or more, regardless of the gestational age; although no official and universal classification has been determined [38]. In 2017, the prevalence of infants born weighing >4000g was 7.8% in the United States and 9% globally. High weight infants are at an increased risk for childhood obesity, which can lead to other disorders, including diabetes, heart disease, and stroke [39-43]. There are no directly linked long-term risks to a mother who has a high weight infant. However, the mother is more likely to suffer from obesity and, therefore, is at the same risk for disease development as those listed for childhood obesity [38, 44]. While obesity in the mother is a significant risk factor associated with high birth weight, the pathophysiological cause appears to be more closely related to maternal hyperglycemia, which is high blood glucose [38, 44]. Since maternal glucose diffuses through the placenta and into the fetal blood flow, these infants are exposed to high glucose during pregnancy, leading to higher birth weights [38]. However, not all cases of high birth weight are caused by hyperglycemia; therefore, further investigation into the physiological causes of this disease is necessary for further treatment development. Currently, the only treatment, when the mother is not presenting with a second APO, is diet and weight interventions. Additionally, medical induction of labor is not often suggested, even with an increased risk of interventions and injuries, such as cesarean-section and shoulder dystocia [38, 45-47]. This is due to difficulty in assessing the true fetal weight with current ultrasound techniques. Improved identification of fetal macrosomia during gestation is necessary to enhance successful treatments and interventions. Additionally, an expanded understanding of the pathophysiological causes of high birth weight could lead to improvements in the prevention and outcomes for offspring.

Low birth weight

Low birth weight also leads to poor outcomes for infants. It is classified as an infant being born at <2500g (5lb 8oz) regardless of gestational age [48]. This can also include infants with fetal growth

restriction (FGR) or small for gestational age (SGA), which requires the infant to be born at <10th percentile based on gestational age. The incidence of low birth weight was 8.58% of births in the US for 2023 and 14.7% globally in 2000 [9, 49]. Long-term risks for infants include renal dysfunction leading to chronic kidney disease (CKD), hypertension, airway diseases, and neurodevelopmental outcomes [48, 50-52]. While not all cases of low birth weight are associated with maternal risk factors, many are linked to maternal body mass index and preeclampsia [53]. The physiological causes of low birth weight are not well understood. Current theories include abnormal fetal programming, abnormal placentation, placental dysfunction, and nutrient deficiency [48, 54]. Preventative treatments for low birth weight include nutritional interventions and preterm labor interventions discussed above; although these treatments are not always successful [55, 56]. Additionally, early developmental and nutritional interventions in infants born with low birth weight could help alleviate the long-term effects observed in these infants [57-59]. Further investigation into the pathophysiological causes of low birth weight can improve future pre-birth preventive measures and post-birth interventions, leading to better infant outcomes.

Infertility and impaired fecundity

In addition to APOs, another problem related to pregnancy is infertility and impaired fecundity. Infertility is defined as not becoming pregnant for at least a year [60]. Impaired fecundity is characterized as a woman having difficulty conceiving or carrying a pregnancy to term. Miscarriages is one way that a pregnancy does not make it to term, and as the number of prior miscarriages in a woman increases, fecundability decreases [61]. For women between the ages of 15-49, in the United States from 2015-2019, the incidence of infertility was 8.5% and the incidence of impaired fecundity was 13.4% [60]. Globally, infertility in women, aged 15-49, in 2021 was 3.7% and for men, aged 15-49, was 1.8% [62]. The rates of infertility increased in men and women aged 15-49 between 1990 to 2021, 0.49% and 0.68%, respectively. Although infertility and impaired fecundity do not directly put the physical health of the mother or offspring at risk, it increases the mental health risks of both men and women struggling to conceive [63]. Couples struggling with infertility had higher incidences of depression and anxiety,

compared to fertile couples. Therefore, demonstrating the impact infertility can have on a person's overall health. There are many known causes of infertility in men and women, including reproductive conditions and infection [64]. Generally, causes for women include irregular ovulation, obstructions to the fallopian tubes, uterine anomalies, genetic causes, and hormonal conditions [65, 66]. In men, functional issues with the testis or the ability to ejaculate, hormone conditions, and genetic causes are the general causes of infertility. Treatments and options for infertility often include alternative conception methods or adoption [64]. Despite the large number of factors leading to infertility, many cases of infertility are not known [67]. Therefore, it is necessary to continue understanding the physiological causes of infertility.

Overall, APOs and infertility affect a large population globally and have long-term health effects on mothers and offspring. There are still unknown causes of APOs and infertility, and a need for improved treatment to prolong pregnancy and improve health outcomes. Therefore, the pathophysiological causes of APOs and infertility require further investigation.

Genetic causes for pregnancy related issues

One potential physiological cause of APOs is genetic mutations and predispositions. The timing of birth has been correlated to both the maternal and fetal genetics [68]. Additionally, genetic sequencing on patients with preterm premature rupture of membranes (PPROM) has identified genetic mutations linked to inflammatory disorders such as inflammatory bowel disease and periodontal disease [69]. Suggesting that premature labor is, at least in part, caused by genetic factors related to immunology in the mother. Genetic mutations leading to HDP disorders, including preeclampsia, have been linked to genes necessary for the immune response [70, 71]. Mutations to genes involved in endothelial function and placental development have also been linked to HDP. Additionally, patients with a family history of hypertension have an increased risk of developing preeclampsia [72, 73]. Further emphasizing that HDPs can be caused by genetic predispositions. A family history of type 2 diabetes has been implicated in increasing the maternal risk of developing GDM [74]. Studies either investigated the link between GDM

and diabetes, with no separation between type 2 and type 1, or focused explicitly on the connection with type 2 diabetes. This is likely because those with pre-existing diabetes before pregnancy are not considered to have GDM, and those with a family history of type 1 diabetes are at a greater risk for being diagnosed with type 1 diabetes in adolescence [75]. Since the risk for type 1 diabetes is genetically linked, mothers with a genetic predisposition would likely have pre-existing diabetes before pregnancy. Still, the potential correlation between GDM and family histories of type 1 diabetes remains to be elicited. Additionally, several genetic mutations have been implicated in causing GDM, including those encoding proteins necessary for immunology, insulin regulation, glucose transport, and an ion channel gene [76, 77]. When considering high and low birth weight, infant weight is affected by both fetal and maternal genes [78, 79]. Genetic mutations to a glucokinase gene and a type 2 diabetes susceptibility gene have both been identified as increasing the birth weight of infants [80]. In contrast, genetic variants have also been implicated in the infant's low birth weight [81]. Additionally, infants born with low and high birth weights are at a higher risk of developing GDM, implicating a genetic predisposition and potential connection to gene mutations involved in birth weight and GDM [82, 83]. Interestingly, many genetic mutations associated with APOs appear to be involved in the immune processes or the ineffective breakdown of glucose. Therefore, providing insight into the types of genes that could be leading to unknown cases of APOs. When considering infertility, genetic disorders have been linked to male and female infertility. A few disorders that cause infertility in males are Klinefelter's syndrome, Y-chromosome microdeletion, and myotonic dystrophy, all of which lead to low or no sperm count [84-86]. Other genetic mutations in males have also been linked to infertility [87]. Polycystic ovarian syndrome (PCOS) is a disorder in females that is implicated in leading to infertility [88]. Although no monogenetic causes of PCOS have been identified, many genetic abnormalities have been linked to PCOS [88, 89]. Additionally, many genetic mutations have been implicated in causing infertility in females [90]. For both males and females, mutations to the cystic fibrosis transmembrane conductance regulator (*CFTR*) gene, which causes cystic fibrosis (CF), have been linked to infertility [91, 92]. In summary, many genetic mutations and genetic predispositions have been linked to APOs and infertility. The further identification of genetic

mutations that lead to APOs and infertility can improve patient outcomes by promoting the development of more specific treatment options.

Uterine structure and function:

The uterus consists of three main tissue layers. From the outermost layer to the innermost layer, they are the perimetrium, myometrium, and endometrium **(Fig. 1)** [93-96]. Additionally, the endometrium contains the luminal epithelium (LE), glandular epithelium (GEp) or uterine glands, and the stroma **(Fig. 1)** [95, 97]. The role of the perimetrium is unknown, although it is thought to provide structure to the uterus throughout pregnancy [94]. The myometrium is responsible for contraction during labor [98]. The endometrium layer is responsible for the implantation of the embryo [99]. Within the endometrium layer, the LE is necessary for successful implantation [100]. The GEp plays a role in implantation, placental development, placental growth, and support of the fetus during the first trimester [101-106]. Additionally, the stromal cells differentiate into secretory decidua, following embryo attachment to the LE [107]. The secretory decidua is vital for the healthy maintenance of pregnancy, including playing roles in immunology and nutrient supply [108]. The remainder of this thesis will focus on the myometrial layer and LE, GE, and vascular structures of the uterus.

Ion channel function and dysfunction in the uterus

Function

Ion channels are essential for the successful physiology of pregnancy and labor. Therefore, ion channel dysfunction could be a cause of unidentified APOs.

Uterine quiescence and contractility in the myometrium are controlled by calcium (Ca^{2+}), sodium (Na^{+}), potassium (K^{+}), and chloride (Cl^{-}) channels. During labor, the uterine myocyte cells become depolarized and open voltage-gated L-type Ca^{2+} (Cav1.2) channels [109, 110] **(Fig. 2)**. This leads to Ca^{2+}

flooding into the cell, which initiates a contraction. Na^+ leak channel, nonselective (NALCN) channels have also been demonstrated as contributing to uterine excitability [110]. Ca^{2+}-activated Cl^- channels (CaCCs) have been implicated in regulating uterine contractility. Studies have demonstrated that contractility increases when these channels are open and decreases when these channels are inhibited [111]. Additionally, these channels are expressed in 1/3 of the myocytes, thus demonstrating a possible role in acting as a pacemaker for uterine contractility. Connexin43 (Cx43) is responsible for forming gap junctions between neighboring myocytes and allowing synchronization of uterine contraction [112]. In contrast, many K^+ channels have been suggested in maintaining uterine quiescence, including K_{ATP} (Kir6), voltage-dependent Kv7 and Kv11.1 channels, inward rectifying Kir channels (Kir), large-conductance Ca^{2+}-activated K^+ (BK or $K_{Ca}1.1$) channels, small-conductance Ca^{2+}-activated K^+ (SK) channels, and Na^+-activated K^+ (KNa) Slo2 channels [110, 113]. These channels maintain resting membrane potential in myocytes, therefore, preventing the cells from depolarizing. Additionally, many of these K^+ channels have been shown to be highly expressed during early and mid-gestation, and their expression decreases near labor. Further supporting their role in maintaining uterine quiescence, and, therefore, a need to suppress them during labor.

Th expression of Na^+, Ca^{2+}, K^+, and Cl^- channels on the LE and GEp demonstrate their role in the normal physiology of these uterine structures. Epithelial Na^+ (ENaC) channels and *CFTR*, a cAMP-activated Cl^- channel, are expressed in epithelial cells of the LE [114]. These channels are suggested to be important for the maintenance of optimal levels of luminal secretions necessary for successful embryo implantation in the LE [114, 115]. Additionally, ENaC channels regulate the stromal decidualization process and gene expression in the LE and GEp [116]. Na+-dependent glucose transporters have also been identified on the LE and GEp and are necessary for effective glucose transport from the maternal side to the fetus [117]. Voltage-dependent Ca^{2+} (VDCC) channels and transient receptor potential (TRP) channels, other Ca^{2+} channels, are expressed in the epithelial cells of the endometrium. VDCC channels are also crucial for regulating decidualization and gene expression regulation. The function of the TRP

channel in decidualization is not fully elicited. Additionally, K+ channels are expressed in epithelial cells of the uterus, but their exact roles in implantation remain unclear.

For uterine vasculature, Ca^{2+}-activated K^+ channels, including the big K^+ or maxi-K (BK) channel, have been identified [118]. These channels have been implicated in regulating vascular tone and adaptation during pregnancy. Voltage-gated K^+ channels have also been identified in the uterine vasculature [119]. Depolarization of vascular smooth muscle cells opens these channels and allows K^+ to restrict contraction of the cells, thus limiting vasoconstriction. Additionally, ATP-sensitive K^+ channels (K_{ATP}), comprised of inwardly rectifying K^+ (Kir6.1 and Kir6.2) channel subunits, are expressed on uterine vasculature smooth muscle cells and play a role in vasodilation. L-type voltage-dependent Ca^{2+} (Cav1.2) channels are also expressed in the uterine vasculature and are responsible for vasoconstriction. Na^+ and Cl^- channels have not been studied explicitly in the uterine vasculature. However, the expression of channels such as CaCC and ENaC channels identified in the vasculature, outside of the uterus, suggests that these channels may be playing a role in uterine vasculature function [120, 121].

Dysfunction and their implications in APOs

Studies on ion channels have suggested roles of ion channel dysfunction in APOs. The role of K^+ channels in uterine quiescence indicates that dysfunctional K^+ channels could lead to contractility of the uterus during mid-gestation and cause preterm labor [110, 113]. One K^+ channel of particular interest is Kir7.1. McCloskey et al. (2014) demonstrated that this channel had increased expression in mouse uterus through day 15 (D15) of gestation, where expression peaked and decreased by D18 [113] **(Fig. 2)**. Additionally, Kir7.1 had lower expression in human uterus at term and in labor, compared to at term and not in labor. The reduced expression in this channel as the uterus moves into labor supports its role in preventing contractions during mid-pregnancy. This hypothesis was further supported by contractility studies demonstrating that over-expression of Kir7.1 in mouse uterus led to a decrease in contractions, and inhibition of Kir7.1 caused an increase in contractility. Another study confirmed these findings in the

mouse uterus and demonstrated that P4, a hormone that has been shown to activate Kir7.1 in the choroid plexus of the brain, further suppressed contractility through its activation of Kir7.1 [122, 123]. Other K^+ channels also show a reduction in K^+ channel expression during labor and increased contractility of uterine myometrium when chemically blocked [110]. While K^+ channel dysfunction has not been directly linked to preterm labor, expression and functional studies suggest that it could be an unknown cause of preterm labor.

Ion channel dysfunction has also been linked to GDM. Mutations in the *KCNJ11* gene, which encodes for the inwardly rectifying K^+ channel Kir6.2 subunits that form the K_{ATP} channel, have been shown to lead to GDM [124-126]. Mutations to transient receptor potential melastatin 6 (TRPM6), a magnesium channel, demonstrated an inability to respond to insulin [127]. Additionally, total glycosylated hemoglobin (TGH) was elevated in pregnant women with these mutations, thus demonstrating an increased risk of developing GDM. In two separate studies, human umbilical cords from GDM and non-GDM patients were assessed for changes in activation to BK or K_{ATP} channels [128, 129]. K_{ATP} current was reduced in the GDM group due to a decrease in K_{ATP} subunit expression in human umbilical arterial smooth muscle cells [129]. Additionally, reduced activity of BK channels in blood vessels from GDM patients was demonstrated, and it was suggested that this was due to a decrease in BK channel expression [128]. GDM has also been shown to cause other APOs, such as HDP, prematurity, and high birth weight in the offspring [128, 130, 131]. Therefore, improper expression and dysfunction of ion channels that led to GDM can increase the risk of developing other APOs, emphasizing the importance of identifying unknown causes of GDM. Studies demonstrating the role of ion channels in GDM suggest that there may be other cases of GDM caused by ion channel dysfunction that have not yet been identified.

Expression of an ion channel, Kv1.3, in the human umbilical vein from HDP patients, also called pregnancy induced hypertension (PIH), was decreased compared to GDM and normal pregnancies [132]. Demonstrating that reduced expression of Kv1.3 may cause HDP. Additionally, a specific blocker of Kv1.3 had a decreased effect in tissues from GDM and HDP patients. A decrease in sulphonylurea receptor (SUR)2B unit of K_{ATP} channels have been demonstrated in human umbilical arterial smooth muscle cells

from patients with varying severity of HDP [133]. The more severe the HDP, the more substantial the decrease in SUR2B was observed. In the case of preeclampsia, the most severe form of HDP, A wide range of K+, Na+, Ca2+, and Cl- channels have changes in expression in the placenta, compared to non-preeclampsia patients [134]. In most cases, a decrease in the expression of the channels was observed, suggesting that reduced expression and subsequent activity of ion channels may contribute to the development of preeclampsia.

As previously noted, mutations to the *CFTR* channel, which transports Cl^-, led to infertility in males and females [91, 92, 135]. An activator of ENaC channels, serum- and glucocorticoid-inducible kinase (SGK1), showed decreased expression in human endometrial stromal cells isolated from patients with recurring pregnancy loss [136]. Therefore, it is possible that decreased activation of ENaC channels by SGK1 could lead to increased infertility. Additionally, one study demonstrated that a patient presenting with infertility had reduced ENaC expression, further supporting that decreased ENaC channel activity is implicated in infertility [137]. Mutations to CatSper, a Ca2+ channel that allows for Ca2+ entry into sperm, have been demonstrated as leading to male infertility [138-141]. Knock-out models demonstrate that CatSper dysfunction causes the sperm to not develop hyperactivated motility [142, 143]. These cases of ion channel dysfunction causing infertility, suggest that unknown instances of infertility could be caused by unidentified ion channel dysfunction.

There are strong connections between ion channel dysfunction and dysregulated expression, and the development of APOs and infertility. Additionally, many channels have been shown to be essential for maintaining a normal, healthy pregnancy. Therefore, supporting a role for unidentified ion channel dysfunction and dysregulated expression of ion channels in causing other cases of currently unknown APOs and infertility.

Kir7.1: A potassium ion channel function and dysfunction

One ion channel that has been demonstrated in the maintenance of a normal pregnancy is Kir7.1. This channel prevents contractions during mid-gestation in mice and is suggested to play a similar role in humans, due to its reduction in expression in the human uterus as it moves into labor [113, 122].

Kir7.1, encoded by the *KCNJ13* gene, is an inwardly rectifying potassium channel [144-147]. Inwardly rectifying potassium channels are involved in cellular signaling in many different cell types [113, 148, 149]. They regulate membrane potential by allowing potassium ions to flow into cells. Specifically, Kir7.1 is expressed in the intestine, thyroid, proximal and distal tubules of the kidney, choroid plexus of the brain, paraventricular nucleus (PVN) of the hypothalamus, myometrium of the uterus, and retinal pigmented epithelial (RPE) cells of the retina [113, 122, 144-146, 148-151].

Mutations to *KCNJ13* have been linked to disease processes. In humans, *KCNJ13* mutations cause Leber's congenital amaurosis (LCA16; OMIM #614186) and Snowflake Vitreoretinal Degeneration (SVD; OMIM #193230) [147, 152-154]. These conditions lead to early-onset vision loss and blindness. The loss of vision is due to RPE cell dysfunction and subsequent degeneration [155]. Kir7.1 is necessary for maintaining ionic homeostasis within the subretinal space between the RPE cells and photoreceptors in the retina [156]. Disruption of this homeostasis, due to mutations in *KCNJ13*, leads to the dysregulation and degeneration of RPE cells. RPE cells are necessary for maintaining the health of the retina by transporting nutrients and removing waste through phagocytosis [155, 157]. Therefore, when the RPE cells are dysregulated and degraded, they lead to degradation of the rest of the retina. Loss of Kir7.1 function has also been implicated in obesity. In mice, deletion of *Kcnj13* on neurons expressing melanocortin-4 receptor (MC4R) led to late-onset obesity [151]. Previous studies observed that late-onset diabetes was induced in mice by deleting MC4R [158]. However, this new finding indicates that MC4R action depends on its ability to inhibit Kir7.1. MC4R inhibition of Kir7.1 allows for depolarization of PVN neurons in the hypothalamus [159]. The PVN regulates satiety and body weight [160, 161]. Therefore, these findings suggest that Kir7.1 dysfunction may play a role in obesity; however, studies in humans are needed to confirm that this finding is translatable to human physiology. In the mouse uterus, knocking

down and inhibiting Kir7.1 led to increased contractility [113]. Over-expressing Kir7.1 or activation with P4 resulted in decreased contractility [113, 122]. Additionally, blocking Kir7.1 in human uterine samples led to increased contractility. This study also noted a similar decrease in Kir7.1 expression in mice and humans as the uterus moves into labor. This suggests that Kir7.1 plays similar roles in mouse and human uterus, and, therefore, should be transferable between the two models. These changes in uterine contractility, resulting from altered Kir7.1 physiology and changes in the expression level of Kir7.1 throughout pregnancy, suggest that a loss of Kir7.1 physiology could play a role in unidentified cases of preterm labor. Investigation into the effects of altered Kir7.1 physiology can further elucidate if loss of Kir7.1 function is leading to unknown causes of APOs.

Kir7.1 has also been shown to interact with hormones that are essential for normal uterine physiology during pregnancy. The OXT hormone rises during parturition and stimulates contraction of the uterine myometrium to progress labor [162, 163]. In the RPE, the activation of oxytocin receptor (OXTR) inhibits Kir7.1 [164]. OXTR is a G-protein-coupled receptor that causes the hydrolysis of PIP2 and a subsequent increase in Ca^{2+} concentration within the RPE cells. Suggesting a similar physiological response of OXT on Kir7.1 function in the uterine myometrium during labor. P4's role in pregnancy includes assisting in the implantation and maintenance of a healthy pregnancy [165]. Levels of P4 are high at the start of pregnancy and fluctuate until the end of pregnancy, where they cease [166]. Studies have demonstrated that P4 activates Kir7.1 channels in the epithelium of the choroid plexus and the mouse myometrium [122, 123]. P4's ability to activate Kir7.1's expression suggests a similar influence on the uterine expression of Kir7.1. Therefore, P4 may be playing a key role in triggering this channel in the uterus and ensuring its ability to prevent contractions during mid-gestation [113].

The role of Kir7.1 in uterine contractility, along with its interaction with pregnancy hormones, highlights the importance of studying this channel's involvement in normal and diseased uterine function **(Fig. 2)**. Additionally, female patients with *KCNJ13* mutations have been identified, but have not reached reproductive age, thus further emphasizing the necessity of understanding how loss of Kir7.1 function affects pregnancy outcomes [167-170]. Female patients who are heterozygous (HET) for the mutation,

and therefore do not suffer from vision loss, have also been identified and have had successful pregnancies [152-154, 167, 168, 170]. Incidents of APOs, infertility, and impaired fecundity have not been investigated in HET females, so it is unknown how the loss of Kir7.1 in one allele affects pregnancy. Therefore, the role that Kir7.1 plays in a normal pregnancy, as well as the changes that total or partial loss of function in Kir7.1 has on pregnancy, requires further evaluation.

***KCNJ13* as a target for gene therapy:**

Most mutations in *KCNJ13* leading to LCA16 and SVD are point mutations, also called single-nucleotide variants (SNV) [171]. Therefore, they are characterized by the change of one nucleotide in the genetic sequence. As discussed, the phenotypes associated with these mutations in humans is dysfunction in the retina and subsequent vision loss [147, 152-156]. Additionally, the eye contains a blood-retina barrier and is immune privileged [172]. This has made the eye a target for drug delivery, as the blood-retina barrier inhibits most drugs from crossing into the circulatory system or having immune effects outside the eye. Therefore, *KCNJ13* mutations are a target for therapeutic development to prevent ocular disease development in patients presenting with LCA16 and SVD. Additionally, Kir7.1's role in uterine contractility could be a future target for therapies if patients harboring *KCNJ13* mutations display APOs due to loss of Kir7.1 function [113]. The target therapies discussed in this thesis will be gene augmentation therapy, genomic editing, readthrough therapy, and anticodon-engineered (ACE) tRNA (ACE-tRNA) therapy.

Gene therapies for genetic mutations: gene augmentation therapy

During gene augmentation therapy, a healthy copy of a gene is delivered to a cell containing the mutant gene [173] **(Fig. 3)**. Augmented, or increased, production of proteins from the exogenous healthy gene then leads to functional recovery in the cell.

Use of a viral vector is the most common delivery method for gene augmentation, although non-viral based deliveries are being explored [174]. In the viral delivery method, the viral capsid binds to receptors on the target cell membrane and is endocytosed into the cell **(Fig. 3)** [175]. Therefore, transduction efficiency can be improved by engineering viral capsids to target a particular cell type through adherence to specific cell membrane proteins [176]. The target gene is delivered to the nucleus, converted to double-stranded DNA (dsDNA), and held in an episome [177]. It then uses the cell's machinery to transcribe and translate the target gene into the target protein [178]. This transcription can then be specialized for specific cell types by choosing cell-specific promoter sequences, preventing non-target cell types from transcribing the healthy gene.

One limitation of gene augmentation is the necessity of mutations to be monogenic; therefore, caused by mutations to a single gene [179]. One reason for this is that the space inside the virus is limited [174]. To overcome this limitation, non-viral delivery methods are being explored. However, stringent government regulations on approved delivery methods, including types of viral vectors used in clinical trials, limit the current options. These regulations are due to concerns about safety, particularly in the case of viruses that can elicit an immune response [180]. Another potential limitation is that the target genes must be recessive. In a dominant mutation, the delivery of a healthy gene usually cannot overcome the dominant gene [181]. However, one study demonstrated that some dominant mutations can be targeted using gene augmentation, while other mutations in the same gene cannot [182].

Despite its limitations, gene augmentation has been a successful therapeutic for recessive, monogenic diseases [62]. A list of government-approved gene therapies, including gene augmentation therapy, can be found in a review by Shchaslyvyi et al. (2023) [183]. Of note, Luxturna (Voretigene Neparvovec) was the first gene augmentation approved by the US Food and Drug Administration (FDA) [183, 184]. Luxturna overcomes mutations to *RPE65*, which lead to LCA2 [185]. It demonstrated long-term treatment effects of at least 5 years, without any immune effects reported [186]. While there are currently no approved gene augmentation therapies targeting ion channels, studies have shown success in cell and animal models [187-191]. Our lab has previously demonstrated that a Lentivirus carrying a

wild-type (WT) *KCNJ13* gene (Lenti-Kir7.1) was able to restore function in human induced pluripotent stem cells (hiPSC) isolated from affected patients [187]. Additionally, a pre-clinical grade gene therapy targeting *KCNJ13* has been developed and is currently being tested for its safety and efficacy, showing preliminary success [192].

Gene therapies for genetic mutations: genomic editing

CRISPR genomic editing techniques, such as gene editing (GE), base editing (BE), and prime editing (PE), have demonstrated success in overcoming mutations and are discussed below. Special attention will be focused on the editing of ocular, uterine, and ion channel diseases.

Gene editing (GE)

In CRISPR-Cas9 GE, a double-stranded break is created near the mutation site and endogenous processes are recruited to the cut site **(Fig. 4A)** [193]. These processes are non-homologous end-joining (NHEJ) or homology-directed repair (HDR). They repair the DNA break by referencing a supplied donor template that contains the WT sequence; effectively changing the genomic DNA to the WT sequence.

GE successful editing requires the precise development of specific single guide RNA (sgRNA) and delivery methods, due to the specificity of the gene and the mutation site [194-196]. Therefore, the specificity of GE can be considered a limitation. Another limitation is off-target effects, such as undesired base changes [197]. Activation of the immune system is another limitation. Viruses are a standard delivery method, but they pose a risk of infection to the host and can reduce efficiency [193, 197]. Additionally, editing that utilizes HDR is limited to targeting dividing cells because the HDR process is dependent on homologous recombination [193].

Many studies have overcome these limitations to demonstrate successful editing [198-200]. Several clinical trials using GE approaches are ongoing [199]. While no clinical trials on ocular or uterine

disease have been investigated, preclinical studies using GE have successfully edited mutations that lead to vision conditions. GE to patient- hiPSCs harboring a RPGR mutation that leads to X-linked retinitis pigmentosa (XLRP), resulted in up to 13% editing [201]. LCA10, a disease characterized by vision loss due to mutations in the *CEP290* gene, demonstrated up to 60.8% editing in mouse models and up to 27.9% in non-human primates (NHP) [202]. GE approaches to *BEST1* mutations have demonstrated up to 24.9% of editing and functional recovery in patient-derived mutant hiPSC-RPE [182]. Additionally, one study evaluated the correction of a mutation to the *RPE65* gene in a mouse model and saw a notable but low editing efficiency of 1.6% [203]. Despite the low editing efficiency, improved function was observed. No studies have reported gene correction using GE for mutations in uterine cells.

Base editing (BE)

In contrast to GE, BE utilizes a CRISPR-Cas9 that is fused to a deaminase enzyme and creates a nick, or single-stranded break, in the target DNA **(Fig. 4B)** [193]. This enzyme can either target cytosine or adenosine and converts all cytosines within a five-base sequence to uracils or adenosines to inosines, respectively. Inosines are read by DNA repair machinery as guanine, allowing for targeting of all four bases. The introduction of a nick in the DNA strand recruits repair processes that use the altered base changes as the new template. Therefore, incorporating a WT base at the mutation site on the opposite strand of DNA. This leads to a more precise editing approach over GE and reduces the off-target edits that limit the GE technique.

Although BE has shown reduced off-target effects compared to GE, undesired edits can still occur [204]. For example, for a cytosine base editor (CBE), if there is more than one cytosine in the five-base window, all cytosines will be converted to uracils, leading to non-target edits to the DNA. The same limitation exists for adenosine base editors (ABE). Similarly to GE, BE requires a specific sgRNA and delivery design for each unique gene and mutation site [194-196]. Additionally, viral delivery is a common delivery method for both GE and BE; thus, activation of the immune system is a concern [193, 197]. The

BE will only edit a precise five-base sequence and requires a specific protospacer adjacent motif (PAM) site by the Cas9; therefore, limiting the mutations that can be targeted [204].

Several BE approaches have reached the clinical trial phase, although none of these are specific to ocular, uterine, or ion channel disease correction [205, 206]. Preclinical evaluation of BE to treat ocular and ion channel diseases has been investigated. Specifically, our lab investigated the use of a BE to overcome a mutation, W53X, to *KCNJ13* [169]. We demonstrated up to 53% of editing in stable-expressing mutant HEKFRT cells, 52.2% editing efficiency in fibroblasts derived from an LCA16-affected individual, 27.4% editing in hiPSC-RPE cells derived from an affected patient, and up to a 16.8% editing efficiency in mutant mice. Functional recovery was assessed for HEKFRT cells, hiPSC-RPE cells, and mutant mouse models, and all demonstrated functional recovery of Kir7.1. Additionally, we have reported up to 60% of editing when using a BE to correct an L144P mutation in *KCNJ13* [207]. Base editing in a mouse model presenting with an *RPE65* mutation resulted in up to 29% editing with functional recovery [208]. However, no base-editing has been reported in uterine conditions.

Prime editing (PE)

Prime editing (PE) is the most recent advancement in genomic editing. A prime editor is made up of four parts: a CRISPR-Cas9 nickase (Cas9n) that is fused to an engineered reverse transcriptase (RT), forming Cas9n-RT, a prime editing guide RNA (pegRNA), and a nicking guide RNA (ngRNA) **(Fig. 4C)** [193]. The pegRNA directs Cas9n-RT to the target gene location and uses the ngRNA to create a nick in the opposite strand. The pegRNA then hybridizes the non-target strand, and the DNA undergoes reverse transcription (RT), using the pegRNA as a template to correct the mutation. The template DNA sequence in the pegRNA contains the WT sequence, therefore, correcting the mutation.

PE is still limited by specific designs for each gene and mutation, as well as potential immune effects [193, 209]. Additionally, the specificity required when designing two guide RNAs (gRNA) for the PE approach requires additional precision compared to traditional GE and BE techniques [193]. PE has

shown minimal (<1%) off-target effects, overcoming this limitation, as demonstrated in GE and BE methods [210]. The reduction in limitations demonstrated in PE, compared to GE and BE, is promising. However, due to the novelty of PE, potential limitations of the technology are still being understood.

Several attempts to use PE as a genomic editor have demonstrated successful gene correction [210]. This includes one study on a mutation affecting the retina. A PE approach to editing an *RPE65* mutation in mice resulted in up to 7.4% editing, with an average of 6.4% [211]. Additionally, it was noted that the transfection efficiency was a limiting factor; therefore, increasing the average editing efficiencies up to 28% when only considering successfully transfected cells. Functional recovery was observed in mice. No attempts at PE have been reported for the correction of mutations affecting the uterus or ion channels.

Translational therapies for genetic mutations: Readthrough therapies

Translational therapies, also known as readthrough therapies, target the correction of premature termination codon (PTC) mutations, also referred to as nonsense mutations, at the translational level. In the presence of these readthrough agents, a near-cognate aminoacyl-tRNA (NCT) is read through at the site of the PTC, rather than initiating the termination of translation **(Fig. 5A)** [212]. Due to their mode of action, readthrough therapies do not have to be gene or mutation-specific; therefore, overcoming the specificity limitation of genome editing techniques.

One limitation of readthrough agents is that the incorporation of the NCT is randomized [212]. This could result in off-target amino acid insertions, missense phenotypes, and no functional recovery of the protein [213-215]. Readthrough agents are also limited to SNV PTCs because they target a single codon site without a way to target the specific mutation site directly [212]. These agents are termed “readthrough” because of their ability to insert a near-cognate amino acid to “read through” the PTC mutation and allow translation to continue. Additionally, aminoglycosides, a type of readthrough agent, have been demonstrated as being toxic to cells, due to binding to anionic phospholipids and accumulating

in lysosomes [216, 217]. Strategies to overcome this toxicity are being explored [212]. A concern with readthrough therapies is the potential for read through of native termination codons (NTC). However, studies have demonstrated that this does not occur [218]. This may be due to peptide sequences on the 3' tail of genes that could destabilize the translated protein, effectively forcing the end of translation. Studies identifying the mechanisms that allow NTCs to be unaffected by readthrough therapies require further investigation. Additionally, the immune effects of readthrough therapies have not been reported, unlike those of viral-based genomic editing approaches. This is likely due to using non-viral based delivery methods for readthrough therapies.

Approximately 100 studies on 40 diseases have been investigated for readthrough therapy suppression of PTCs [212, 219]. Readthrough therapies have demonstrated success in treating ocular and ion channel diseases caused by PTCs. Our lab studied the effect of several aminoglycosides including, gentamicin, RTC-14, NB-84, and G418, to overcome the W53X mutation of *KCNJ13* in patient-derived LCA16 hiPSC-RPE [220, 221]. While gentamicin, the most common aminoglycoside, was unable to suppress the mutation, RTC-14, NB-84, and G418 successfully read through the mutation and restored function. Gentamicin was also unable to overcome retinal degeneration or regain function in a rat model containing a recessive PTC to the rd12 gene [222]. In contrast, gentamicin successfully inhibited retinal degeneration and restored function in a rat model with a dominant PTC in S334ter. These studies demonstrate that readthrough therapy efficiency is gene-specific. Aminoglycosides and PTC124 both demonstrated readthrough and functional recovery of the p.R31X PTC in the *USH1C* gene in mouse models [223, 224]. If untreated, mutations to *USH1C* lead to blindness. Therefore, the success of a readthrough therapy providing functional recovery could prevent blindness in patients harboring these mutations. The use of readthrough therapies has not been investigated in uterine PTCs.

Translational therapies for genetic mutations: ACE-tRNA

ACE-tRNA therapies are also a form of readthrough therapy; however, factors such as their mode of action and target specificity make them distinct from other readthrough therapies. In this approach, a tRNA with the target amino acid is engineered at the anticodon site to contain a PTC capable of recognizing the stop codon **(Fig. 5B)** [225]. When translation of the PTC occurs, the ACE-tRNA recognizes the mutation, due to the engineered anticodon site, and inserts the correct amino acid. Therefore, translation continues, and the full-length WT protein is produced.

Similar to other readthrough drugs, ACE-tRNA therapy overcomes the specificity limitations and immune activation of viral-based genome editing, but is limited by treating SNV PTC mutations [225]. Additionally, ACE-tRNA overcomes limitations to readthrough therapies, including randomness and toxicity. The mechanism of ACE-tRNA therapy does not randomly incorporate a NCT, like readthrough therapies. Instead, it explicitly recognizes the mutant sequence and inserts a specific target amino acid. No toxicity has been reported in ACE-tRNA studies, as well as no evidence of suppressing NTCs [226]. Therefore, no limitations, aside from the types of mutations that can be targeted with ACE-tRNA, have been reported. However, since this is a novel therapeutic. Therefore, limitations and off-target effects require further investigation.

Due to its novelty, ACE-tRNA studies are limited. Successful suppression of PTCs in mutations causing CF, long-QT syndrome arrhythmia, and in the W53X mutant causing LCA16 by ACE-tRNA has been reported [221, 226-229]. In all cases, functional recovery was observed, and no off-target effects were reported. Therefore, ACE-tRNA could be a competitive alternative therapy to genomic editing techniques and other readthrough drugs. ACE-tRNA studies on PTCs causing uterine disease have not been investigated.

These studies strongly support the use of ACE-tRNA as a therapeutic approach to overcome PTC mutations with a minimal risk of off-target or immune effects. However, further investigation into the success and limitations of the novel therapy is required.

Thesis overview

The cases of unknown causes of APOs and infertility are concerning, due to the high incidence globally and the long-term health effects to the mother and fetus. Several genetic links to APOs or infertility have been identified, suggesting that other unknown cases could be due to genetic mutations. Additionally, ion channels have been implicated in some cases of APOs and infertility, requiring further investigation. One of these ion channels is Kir7.1, which is encoded by *KCNJ13*; a gene in which patients with disease-causing mutations have been identified and suffer vision loss. However, these patients have not yet reached reproductive maturity, and there is only one study on the role of Kir7.1 in the uterus. Therefore, the potential for *KCNJ13* mutations, and subsequent loss of Kir7.1 function in the uterus, to cause APOs and infertility in patients remains to be elicited. If loss of function in Kir7.1 is demonstrated to lead to APOs or infertility, it may suggest that other unknown cases are caused by genetic mutations. Additionally, it can support ion channel dysfunction as another possibility for unidentified causes, given the crucial role ion channels play in maintaining pregnancy.

The use of therapies to treat these mutations has been investigated to target restoration of retinal function. The current investigations have included the correction of W53X using gene augmentation, BE, readthrough agents, and ACE-tRNA therapy, and the correction of L144P using BE techniques. However, a study comparing the efficacy of genomic editing versus readthrough therapies on a *KCNJ13* mutation has not been reported. As Kir7.1 dysfunction in the uterus is further characterized, identifying therapies to treat patients harboring *KCNJ13* mutations is necessary to allow for modified therapies to target these mutations in the uterus.

The goals of this thesis are to: A) compare therapeutic approaches to overcome a *KCNJ13* mutation, R166X, B) to investigate the effect of a partial loss of Kir7.1 function in pregnancy and labor, and C) to further characterize Kir7.1's expression in the uterus throughout pregnancy to understand its role in pregnancy and potential role in APOs and infertility. To achieve objective A, I created R166X mutant stably expressing HEKFRT cells to investigate several genomic editing techniques (GE, BE, and PE). To compare these outcomes of genomic editing with a readthrough therapy, HEK293 cells

expressing the R166X mutant protein were used. Several ACE-tRNA readthrough agents were investigated for their ability to suppress the R166X mutation. Additionally, the efficacy of a clinical-grade gene augmentation therapy containing WT *KCNJ13* to target RPE cells was investigated. For aim B, C57BL/6J mice were used. WT mice were compared with previously engineered mice containing a HET W53X mutation. Video recordings of labor for each genotype were compared. To achieve goal C, uteri from non-pregnant (NP) and pregnant WT and HET mice were used to investigate Kir7.1 expression changes in the uterus. Collections from pregnant mice were taken at several time points to identify changes in Kir7.1 expression throughout mouse pregnancy. Additionally, the uterus from NP and mid-gestation non-human primates (NHP) was collected to determine if the expression of Kir7.1 in mice is translatable to humans.

Acknowledgements:

Schematic images were created with Biorender.com.

FIGURES AND TABLES

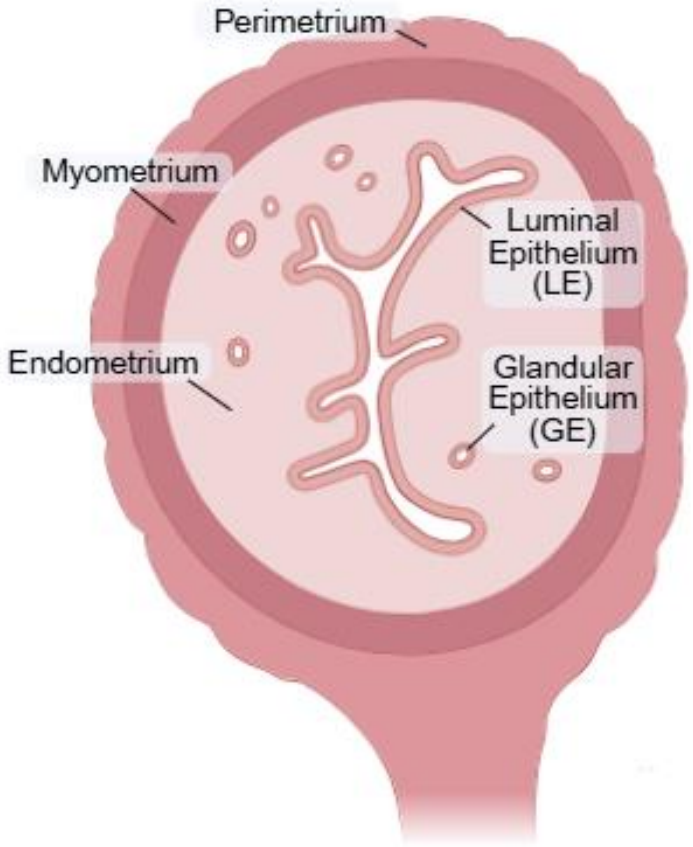

Figure 1: Uterine Structure. The three main layers of the uterus are the perimetrium (outermost), myometrium, and endometrium (innermost). The endometrium contains the LE and GEp.

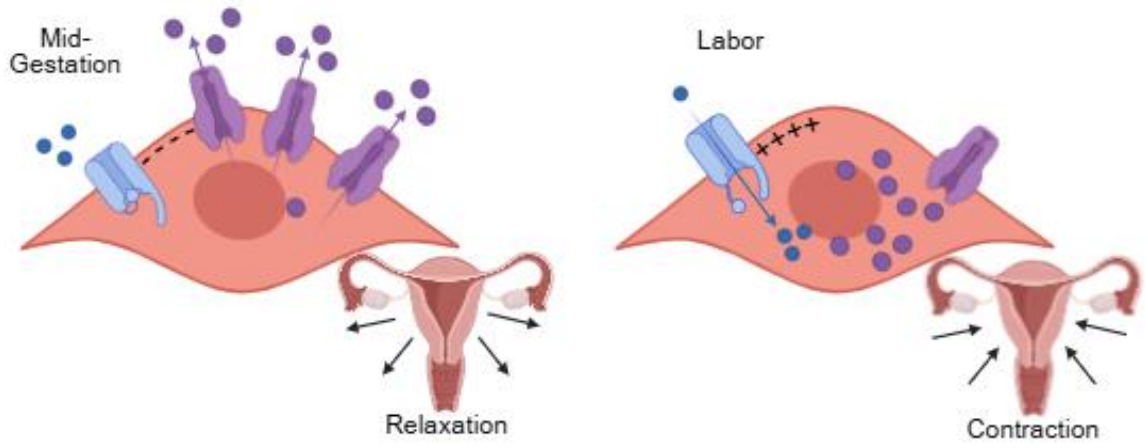

Figure 2: Current theorized mechanism of Kir7.1 expression and function in the uterine myometrium during pregnancy. (A) During mid-gestation, Kir7.1 (purple ion channel) expression is high, and it moves K+ (purple circle) out of the myocytes to maintain the cell's hyperpolarization (-). This hyperpolarization prevents voltage-gated Ca^{2+} channels (blue ion channel) from opening. Therefore, Ca^{2+} (blue circle) is prevented from entering the cell, thereby maintaining the myometrium in a state of relaxation (quiescence). **(B)** During labor, the expression of Kir7.1 is very low; therefore, K+ cannot move out of the cell fast enough to maintain the cell in a hyperpolarized state. The cell becomes depolarized (+) and voltage-gated Ca^{2+} channels open. Ca^{2+} floods into the cell and causes contraction of the myometrium.

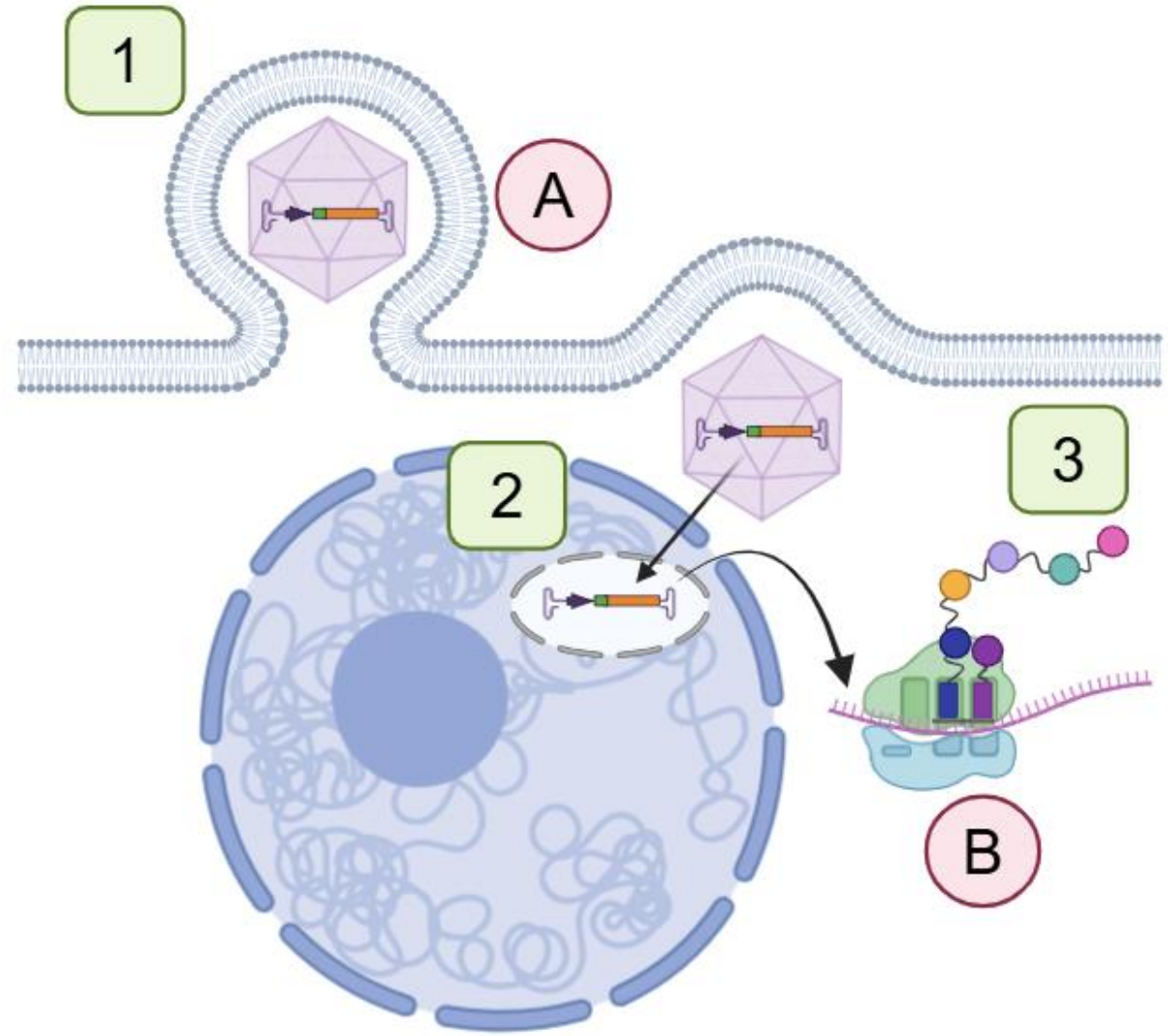

Figure 3: Viral delivery of gene augmentation therapy. (1) In gene augmentation therapy, a virus is commonly used for the delivery of a target gene. The virus is endocytosed by the cell. **(2)** The virus then delivers the target gene into the nucleus, where it is held in an episome. **(3)** The target gene is transcribed and translated into the WT functional protein. Additionally, two modifications can enhance delivery and expression in the correct cell type. These are A: Selection of different viral serotypes will have different chances of being endocytosed into a target cell type. B: Specific promotors can be selected that will only be transcribed in select cell types.

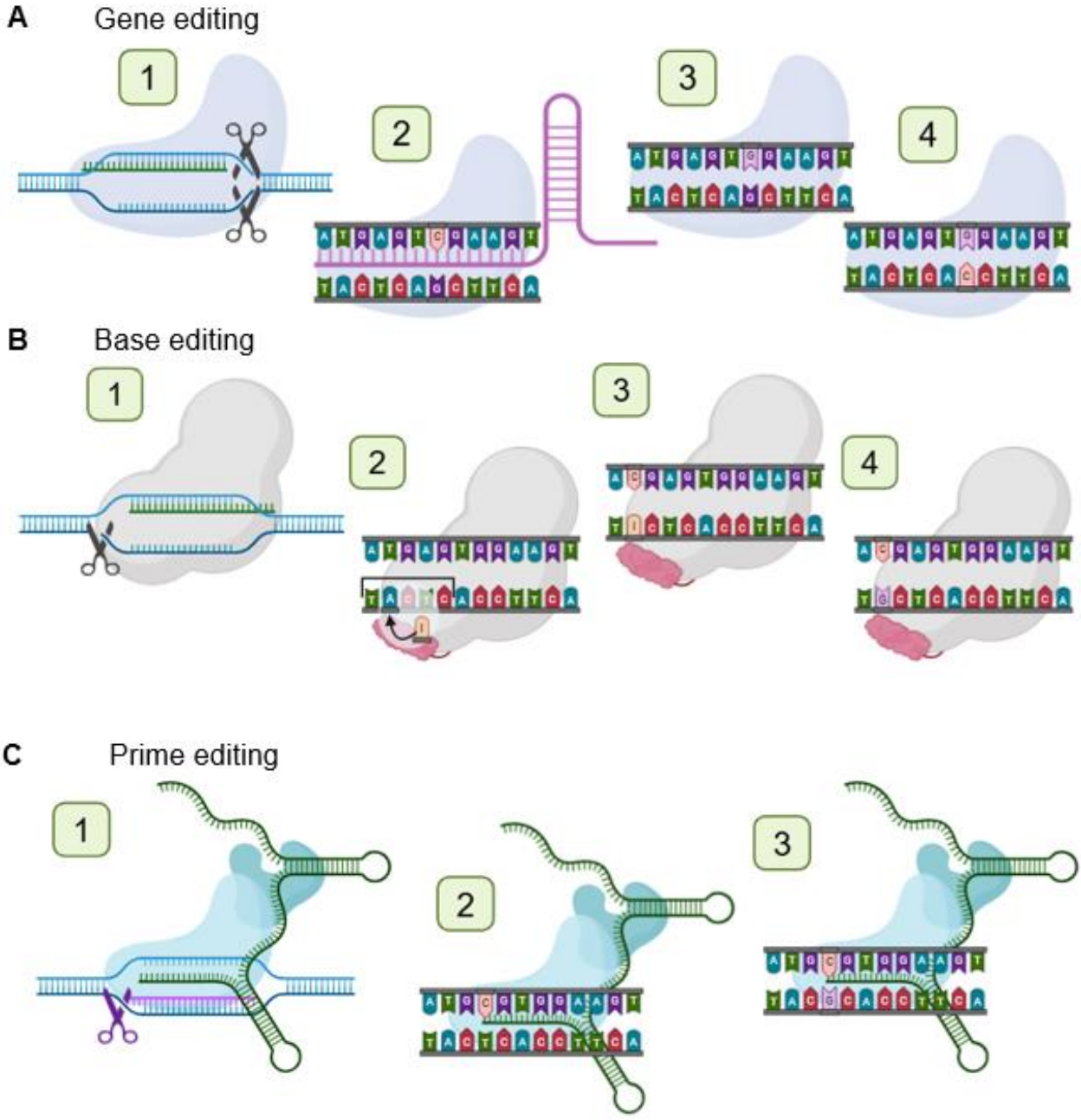
A
Gene editing
1
2
3
4
B
Base editing
1
2
3
4
C
Prime editing
1
2
3

Figure 4: Genomic editing techniques. (A) GE. (1) CRISPR-Cas9 is directed by a custom sgRNA (green) to the target site containing the mutation. Cas9 creates a cut (double-stranded break) in the DNA sequence, prompting the cellular machinery to fix the break. (2) A custom donor sequence (purple) containing the WT target sequence hybridizes to the target sequence. (3) The cellular machinery fixes the break by using the donor sequence as a template. Therefore, the correct nucleotide is inserted. (4) The opposite strand is corrected. **(B) BE.** (1) A custom sgRNA (green) directs CRISPR Cas9 to the target site containing the mutation and prompts the Cas9 to create a nick (single-stranded break) in the DNA sequence. (2) For base editing, the Cas9 is fused to a CBE or ABE. For the ABE, all adenosines on the target strand, within a 5-base window, will be converted to inosine. (3) Transcription machinery will read the inosine as guanine and convert the base on the opposite strand to cytosine. (4) Cellular machinery will then convert the inosine to guanine. **(C) PE.** (1) A Cas9n is fused to an RT (Cas9n-RT). A custom pegRNA (green) directs the Cas9n-RT to the target site, which contains the mutation. A gRNA (purple) is used by Cas9n-RT to create a nick (single-stranded break) in the opposite strand. (2) The pegRNA hybridizes to the opposite strand and the DNA undergoes RT by the Cas9n-RT. The pegRNA, which contains the WT sequence, is used as the template. This causes the mutant base to be converted to the WT base. (3) The mutant base on the target strand is then converted to the WT base.

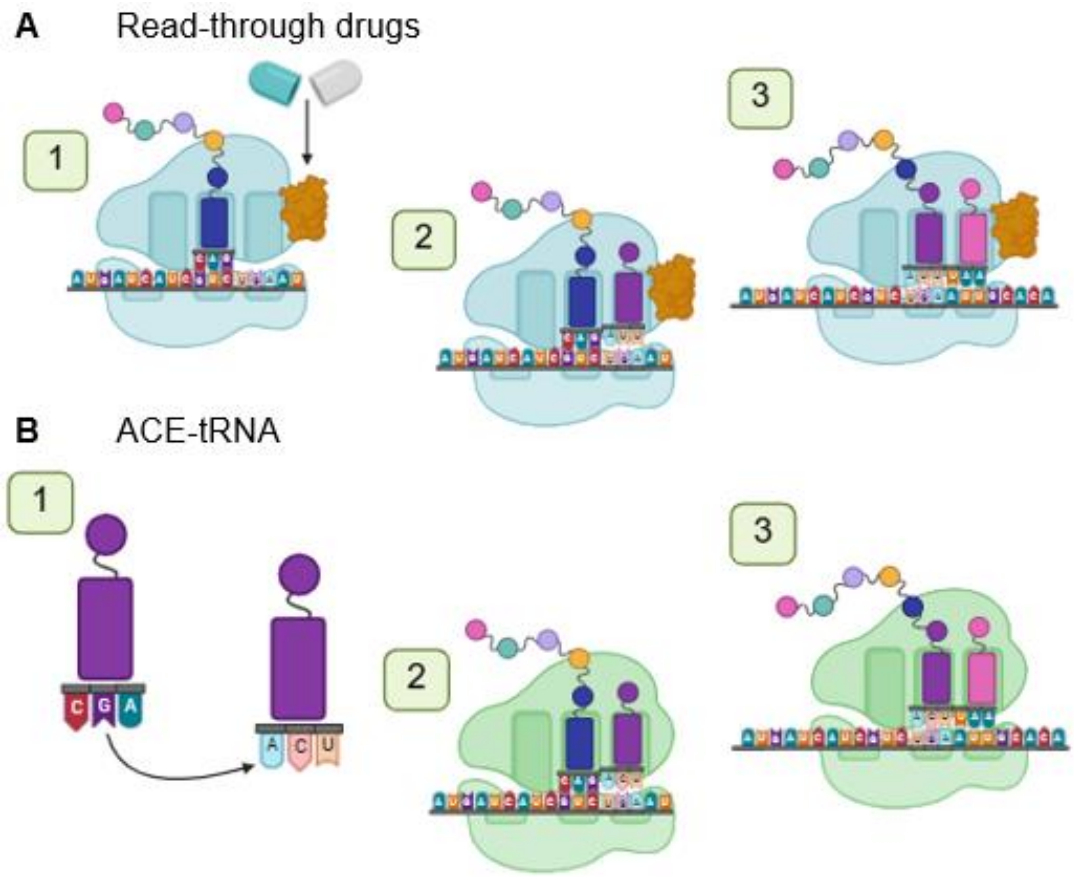

Figure 5: Readthrough therapeutic techniques for PTCs. (A) Readthrough drugs. (1) The readthrough drug binds to the ribosome during translation. (2) The drug causes the ribosome to skip over the PTC and instead insert a near-cognate amino acid. (3) A near-cognate amino acid is added to the protein sequence, and translation continues. **(B) ACE-tRNA therapy.** (1) A native tRNA containing the target amino acid is engineered to alter the anticodon sequence and recognize the PTC sequence at the anticodon site. (2) During translation, the ACE-tRNA recognizes the PTC. (3) The correct amino acid is added to the protein sequence and translation continues.

REFERENCES

1. Kramer, M.S., *The epidemiology of adverse pregnancy outcomes: an overview.* J Nutr, 2003. **133**(5 Suppl 2): p. 1592S-1596S.
2. *Adverse Birth Outcomes*, in *America's Children and the Environment*. 2013. p. 264-388.
3. Abadiga, M., et al., *Determinants of adverse birth outcomes among women delivered in public hospitals of Ethiopia, 2020.* Arch Public Health, 2022. **80**(1): p. 12.
4. Freaney, P.M., et al., *Temporal Trends in Adverse Pregnancy Outcomes in Birthing Individuals Aged 15 to 44 Years in the United States, 2007 to 2019.* J Am Heart Assoc, 2022. **11**(11): p. e025050.
5. Yee, L.M., E.C. Miller, and P. Greenland, *Mitigating the Long-term Health Risks of Adverse Pregnancy Outcomes.* JAMA, 2022. **327**(5): p. 421-422.
6. Romero, R., S.K. Dey, and S.J. Fisher, *Preterm labor: one syndrome, many causes.* Science, 2014. **345**(6198): p. 760-5.
7. Rundell, K. and B. Panchal, *Preterm Labor: Prevention and Management.* Am Fam Physician, 2017. **95**(6): p. 366-372.
8. *Preterm birth*. Newsroom 2023 [cited 2025; Available from: https://www.who.int/news-room/fact-sheets/detail/preterm-birth.
9. Osterman, M.J., et al., *Births: final data for 2021.* 2023.
10. Dong, Y. and J.L. Yu, *An overview of morbidity, mortality and long-term outcome of late preterm birth.* World J Pediatr, 2011. **7**(3): p. 199-204.
11. Khandre, V., J. Potdar, and A. Keerti, *Preterm Birth: An Overview.* Cureus, 2022. **14**(12): p. e33006.
12. Mwaniki, M.K., et al., *Long-term neurodevelopmental outcomes after intrauterine and neonatal insults: a systematic review.* Lancet, 2012. **379**(9814): p. 445-52.
13. Goldenberg, R.L., *The management of preterm labor.* Obstet Gynecol, 2002. **100**(5 Pt 1): p. 1020-37.

14. Ramachandran, A., et al., *Reframing spontaneous preterm birth as a preventable adverse outcome-A clinical audit of a preventative toolbox.* Acta Obstet Gynecol Scand, 2025. **104**(5): p. 906-912.

15. Agrawal, A. and N.K. Wenger, *Hypertension During Pregnancy.* Curr Hypertens Rep, 2020. **22**(9): p. 64.

16. Stephansson, O. and A. Sandstrom, *Can short- and long-term maternal and infant risks linked to hypertension and diabetes during pregnancy be reduced by therapy?* J Intern Med, 2024. **296**(3): p. 216-233.

17. *Pre-eclampsia*. 2025 [cited 2025; Available from: https://www.who.int/news-room/fact-sheets/detail/pre-eclampsia.

18. Ford, N.D., *Hypertensive disorders in pregnancy and mortality at delivery hospitalization—United States, 2017–2019.* MMWR. Morbidity and mortality weekly report, 2022. **71**.

19. Honigberg, M.C., et al., *Long-Term Cardiovascular Risk in Women With Hypertension During Pregnancy.* J Am Coll Cardiol, 2019. **74**(22): p. 2743-2754.

20. Wang, I.K., et al., *Association between hypertensive disorders during pregnancy and end-stage renal disease: a population-based study.* CMAJ, 2013. **185**(3): p. 207-13.

21. Paneth, N.S., *The problem of low birth weight.* Future Child, 1995. **5**(1): p. 19-34.

22. Gera, P., W.H. Frishman, and W.S. Aronow, *The Use of Statins During Pregnancy in Patients Diagnosed With Preeclampsia: A Systematic Review.* Cardiol Rev, 2025.

23. Afrose, D., S. Alfonso-Sanchez, and L. McClements, *Targeting oxidative stress in preeclampsia.* Hypertens Pregnancy, 2025. **44**(1): p. 2445556.

24. Afrose, D., et al., *Evaluating oxidative stress targeting treatments in in vitro models of placental stress relevant to preeclampsia.* Front Cell Dev Biol, 2025. **13**: p. 1539496.

25. Cluver, C.A., et al., *Use of metformin to prolong gestation in preterm pre-eclampsia: randomised, double blind, placebo controlled trial.* BMJ, 2021. **374**: p. n2103.

26. Rana, S., et al., *Preeclampsia: Pathophysiology, Challenges, and Perspectives.* Circ Res, 2019. **124**(7): p. 1094-1112.

27. Zhu, Y. and C. Zhang, *Prevalence of Gestational Diabetes and Risk of Progression to Type 2 Diabetes: a Global Perspective.* Curr Diab Rep, 2016. **16**(1): p. 7.

28. McIntyre, H.D., et al., *Gestational diabetes mellitus.* Nat Rev Dis Primers, 2019. **5**(1): p. 47.

29. Martin, J.A. and E.C.W. Gregory, *QuickStats: Percentage of Mothers with Gestational Diabetes, by Maternal Age — National Vital Statistics System, United States, 2016 and 2021*, in *MMWR Morb Mortal Wkly Rep*. 2023, CDC: cdc.gov.

30. Wang, Y.X., et al., *Association of Gestational Diabetes With Subsequent Long-Term Risk of Mortality.* JAMA Intern Med, 2023. **183**(11): p. 1204-1213.

31. Lowe, W.L., Jr., et al., *Association of Gestational Diabetes With Maternal Disorders of Glucose Metabolism and Childhood Adiposity.* JAMA, 2018. **320**(10): p. 1005-1016.

32. Dabelea, D., et al., *Intrauterine exposure to diabetes conveys risks for type 2 diabetes and obesity: a study of discordant sibships.* Diabetes, 2000. **49**(12): p. 2208-11.

33. Moosazadeh, M., et al., *Family history of diabetes and the risk of gestational diabetes mellitus in Iran: A systematic review and meta-analysis.* Diabetes Metab Syndr, 2017. **11 Suppl 1**: p. S99-S104.

34. Plows, J.F., et al., *The Pathophysiology of Gestational Diabetes Mellitus.* Int J Mol Sci, 2018. **19**(11).

35. Cerf, M.E., *Beta cell dysfunction and insulin resistance.* Front Endocrinol (Lausanne), 2013. **4**: p. 37.

36. Farrar, D., et al., *Treatments for gestational diabetes: a systematic review and meta-analysis.* BMJ Open, 2017. **7**(6): p. e015557.

37. Bodier, L., et al., *Efficacy and safety of pharmacological treatments for gestational diabetes: a systematic review comparing metformin with glibenclamide and insulin.* Diabetes Metab, 2025. **51**(2): p. 101622.

38. Akanmode, A.M. and H. Mahdy, *Macrosomia*, in *StatPearls*. 2025: Treasure Island (FL).

39. Ye, F., et al., *Full title: prevalence and risk factors of overweight in Beijing infants basing generalized estimating equation: a longitudinal study.* BMC Public Health, 2025. **25**(1): p. 543.

40. Nadeau, K.J., et al., *Childhood obesity and cardiovascular disease: links and prevention strategies.* Nat Rev Cardiol, 2011. **8**(9): p. 513-25.

41. Zou, X.L., et al., *Childhood Obesity and Risk of Stroke: A Mendelian Randomisation Analysis.* Front Genet, 2021. **12**: p. 727475.

42. Quezada-Gaibor, K., A. Gomis-Pomares, and L. Villanueva, *Adverse childhood experiences: A health risk in emerging adulthood.* J Health Psychol, 2024: p. 13591053241275592.

43. Reilly, J.J. and J. Kelly, *Long-term impact of overweight and obesity in childhood and adolescence on morbidity and premature mortality in adulthood: systematic review.* Int J Obes (Lond), 2011. **35**(7): p. 891-8.

44. Gaudet, L., et al., *Maternal obesity and occurrence of fetal macrosomia: a systematic review and meta-analysis.* Biomed Res Int, 2014. **2014**: p. 640291.

45. Najafian, M. and M. Cheraghi, *Occurrence of fetal macrosomia rate and its maternal and neonatal complications: a 5-year cohort study.* ISRN Obstet Gynecol, 2012. **2012**: p. 353791.

46. Combs, C.A., et al., *Sonographic EFW and macrosomia: is there an optimum formula to predict diabetic fetal macrosomia?* J Matern Fetal Med, 2000. **9**(1): p. 55-61.

47. Ewington, L.J., et al., *Accuracy of antenatal ultrasound in predicting large-for-gestational-age babies: population-based cohort study.* Am J Obstet Gynecol, 2025. **232**(2): p. 210 e1-210 e10.

48. Kim, H.Y., et al., *Short-term neonatal and long-term neurodevelopmental outcome of children born term low birth weight.* Sci Rep, 2024. **14**(1): p. 2274.

49. UNICEF. *Low birthweight*. Nutrition 2023 [cited 2025; Available from: https://data.unicef.org/topic/nutrition/low-birthweight/.

50. Reyes, L. and R. Manalich, *Long-term consequences of low birth weight.* Kidney Int Suppl, 2005(97): p. S107-11.

51. Grillo, M.A., G. Mariani, and J.R. Ferraris, *Prematurity and Low Birth Weight in Neonates as a Risk Factor for Obesity, Hypertension, and Chronic Kidney Disease in Pediatric and Adult Age.* Front Med (Lausanne), 2021. **8**: p. 769734.

52. Ikeda, K., et al., *Airway diseases in very low birth weight infants.* J Perinatol, 2025. **45**(1): p. 50-54.

53. Singh, G., R. Chouhan, and K. Sidhu, *Maternal Factors for Low Birth Weight Babies.* Med J Armed Forces India, 2009. **65**(1): p. 10-2.

54. Negrato, C.A. and M.B. Gomes, *Low birth weight: causes and consequences.* Diabetol Metab Syndr, 2013. **5**: p. 49.

55. Goldenberg, R.L. and J.F. Culhane, *Low birth weight in the United States.* Am J Clin Nutr, 2007. **85**(2): p. 584S-590S.

56. da Silva Lopes, K., et al., *Effects of nutrition interventions during pregnancy on low birth weight: an overview of systematic reviews.* BMJ Glob Health, 2017. **2**(3): p. e000389.

57. McCormick, M.C., et al., *Early intervention in low birth weight premature infants: results at 18 years of age for the Infant Health and Development Program.* Pediatrics, 2006. **117**(3): p. 771-80.

58. Donovan, R., et al., *Outcomes of early nutrition support in extremely low-birth-weight infants.* Nutr Clin Pract, 2006. **21**(4): p. 395-400.

59. Stephens, B.E., et al., *First-week protein and energy intakes are associated with 18-month developmental outcomes in extremely low birth weight infants.* Pediatrics, 2009. **123**(5): p. 1337-43.

60. Nugent, C.N. and A. Chandra, *Infertility and Impaired Fecundity in Women and Men in the United States, 2015-2019.* Natl Health Stat Report, 2024(202): p. 1-19.

61. Arge, L.A., et al., *The association between miscarriage and fecundability: the Norwegian Mother, Father and Child Cohort Study.* Human Reproduction, 2022. **37**(2): p. 322-332.

62. Liang, Y., et al., *Global, regional, and national prevalence and trends of infertility among individuals of reproductive age (15-49 years) from 1990 to 2021, with projections to 2040.* Hum Reprod, 2025. **40**(3): p. 529-544.

63. Doyle, M. and A. Carballedo, *Infertility and mental health.* Advances in psychiatric treatment, 2014. **20**: p. 297-303.

64. Anwar, S. and A. Anwar, *Infertility: A Review on Causes, Treatment and Management.* Women's Health & Gynecology, 2016. **2**(6).

65. *Infertility: Frequently Asked Questions*. Reproductive Health 2024 [cited 2025; Available from: https://www.cdc.gov/reproductive-health/infertility-faq/index.html.

66. Beke, A., *Genetic Causes of Female Infertility.* Exp Suppl, 2019. **111**: p. 367-383.

67. Isaksson, R. and A. Tiitinen, *Present concept of unexplained infertility.* Gynecol Endocrinol, 2004. **18**(5): p. 278-90.

68. York, T.P., et al., *The contribution of genetic and environmental factors to the duration of pregnancy.* Am J Obstet Gynecol, 2014. **210**(5): p. 398-405.

69. Strauss, J.F., 3rd, et al., *Spontaneous preterm birth: advances toward the discovery of genetic predisposition.* Am J Obstet Gynecol, 2018. **218**(3): p. 294-314 e2.

70. Tyrmi, J.S., et al., *Genetic Risk Factors Associated With Preeclampsia and Hypertensive Disorders of Pregnancy.* JAMA Cardiol, 2023. **8**(7): p. 674-683.

71. Williams, P.J. and F. Broughton Pipkin, *The genetics of pre-eclampsia and other hypertensive disorders of pregnancy.* Best Pract Res Clin Obstet Gynaecol, 2011. **25**(4): p. 405-17.

72. Ness, R.B., et al., *Family history of hypertension, heart disease, and stroke among women who develop hypertension in pregnancy.* Obstet Gynecol, 2003. **102**(6): p. 1366-71.

73. Bezerra, P.C., et al., *Family history of hypertension as an important risk factor for the development of severe preeclampsia.* Acta Obstet Gynecol Scand, 2010. **89**(5): p. 612-7.

74. Monod, C., et al., *Prevalence of gestational diabetes mellitus in women with a family history of type 2 diabetes in first- and second-degree relatives.* Acta Diabetol, 2023. **60**(3): p. 345-351.

75. Sipetic, S., et al., *Family history and risk of type 1 diabetes mellitus.* Acta Diabetol, 2002. **39**(3): p. 111-5.

76. Shaat, N. and L. Groop, *Genetics of gestational diabetes mellitus.* Curr Med Chem, 2007. **14**(5): p. 569-83.

77. Zhang, C., et al., *Genetic variants and the risk of gestational diabetes mellitus: a systematic review.* Hum Reprod Update, 2013. **19**(4): p. 376-90.

78. Magnus, P., *Causes of variation in birth weight: a study of offspring of twins.* Clin Genet, 1984. **25**(1): p. 15-24.

79. Magnus, P., *Further evidence for a significant effect of fetal genes on variation in birth weight.* Clin Genet, 1984. **26**(4): p. 289-96.

80. Hattersley, A.T., et al., *Mutations in the glucokinase gene of the fetus result in reduced birth weight.* Nat Genet, 1998. **19**(3): p. 268-70.

81. Freathy, R.M., et al., *Variants in ADCY5 and near CCNL1 are associated with fetal growth and birth weight.* Nat Genet, 2010. **42**(5): p. 430-5.

82. Seghieri, G., et al., *Relationship between gestational diabetes mellitus and low maternal birth weight.* Diabetes Care, 2002. **25**(10): p. 1761-5.

83. Savona-Ventura, C. and M. Chircop, *Birth weight influence on the subsequent development of gestational diabetes mellitus.* Acta Diabetol, 2003. **40**(2): p. 101-4.

84. Ramasamy, R., et al., *Successful fertility treatment for Klinefelter's syndrome.* J Urol, 2009. **182**(3): p. 1108-13.

85. Johnson, M., et al., *An analysis of the frequency of Y-chromosome microdeletions and the determination of a threshold sperm concentration for genetic testing in infertile men.* BJU Int, 2019. **123**(2): p. 367-372.

86. Hortas, M.L., et al., *Decreased sperm function of patients with myotonic muscular dystrophy.* Hum Reprod, 2000. **15**(2): p. 445-8.

87. Miyamoto, T., et al., *Human male infertility and its genetic causes.* Reprod Med Biol, 2017. **16**(2): p. 81-88.

88. Ajmal, N., S.Z. Khan, and R. Shaikh, *Polycystic ovary syndrome (PCOS) and genetic predisposition: A review article.* Eur J Obstet Gynecol Reprod Biol X, 2019. **3**: p. 100060.

89. Khan, M.J., A. Ullah, and S. Basit, *Genetic Basis of Polycystic Ovary Syndrome (PCOS): Current Perspectives.* Appl Clin Genet, 2019. **12**: p. 249-260.

90. Yatsenko, S.A. and A. Rajkovic, *Genetics of human female infertilitydagger.* Biol Reprod, 2019. **101**(3): p. 549-566.

91. Ahmad, A., A. Ahmed, and P. Patrizio, *Cystic fibrosis and fertility.* Curr Opin Obstet Gynecol, 2013. **25**(3): p. 167-72.

92. Chan, H.C., et al., *The cystic fibrosis transmembrane conductance regulator in reproductive health and disease.* J Physiol, 2009. **587**(Pt 10): p. 2187-95.

93. Gasner, A. and A.A. P, *Physiology, Uterus*, in *StatPearls*. 2025: Treasure Island (FL).

94. Fodera, D.M., et al., *Material properties of nonpregnant and pregnant human uterine layers.* J Mech Behav Biomed Mater, 2024. **151**: p. 106348.

95. Alchalabi, A.S.H., et al., *Histopathological changes associated with oxidative stress induced by electromagnetic waves in rats' ovarian and uterine tissues.* Asian Pacific Journal of Reproduction, 2016. **5**(4): p. 301-310.

96. Yang, Y., Q.Y. Zhu, and J.L. Liu, *Deciphering mouse uterine receptivity for embryo implantation at single-cell resolution.* Cell Prolif, 2021. **54**(11): p. e13128.

97. Cooke, P.S., et al., *Uterine glands: development, function and experimental model systems.* Mol Hum Reprod, 2013. **19**(9): p. 547-58.

98. Wray, S. and C. Prendergast, *The Myometrium: From Excitation to Contractions and Labour.* Adv Exp Med Biol, 2019. **1124**: p. 233-263.

99. Sehring, J., A. Beltsos, and R. Jeelani, *Human implantation: The complex interplay between endometrial receptivity, inflammation, and the microbiome.* Placenta, 2022. **117**: p. 179-186.

100. Enders, A.C. and S. Schlafke, *A Morphological Analysis of the Early Implantation Stages in the Rat.* American Journal of Anatomy, 1967. **120**: p. 185-226.

101. Hempstock, J., et al., *Endometrial glands as a source of nutrients, growth factors and cytokines during the first trimester of human pregnancy: a morphological and immunohistochemical study.* Reprod Biol Endocrinol, 2004. **2**: p. 58.

102. Burton, G.J., E. Jauniaux, and D.S. Charnock-Jones, *Human early placental development: potential roles of the endometrial glands.* Placenta, 2007. **28 Suppl A**: p. S64-9.

103. Spencer, T.E., *Biological roles of uterine glands in pregnancy.* Semin Reprod Med, 2014. **32**(5): p. 346-57.

104. Kelleher, A.M., et al., *Uterine glands coordinate on-time embryo implantation and impact endometrial decidualization for pregnancy success.* Nat Commun, 2018. **9**(1): p. 2435.

105. Kelleher, A.M., F.J. DeMayo, and T.E. Spencer, *Uterine Glands: Developmental Biology and Functional Roles in Pregnancy.* Endocr Rev, 2019. **40**(5): p. 1424-1445.

106. Burton, G.J., T. Cindrova-Davies, and M.Y. Turco, *Review: Histotrophic nutrition and the placental-endometrial dialogue during human early pregnancy.* Placenta, 2020. **102**: p. 21-26.

107. Hantak, A.M., I.C. Bagchi, and M.K. Bagchi, *Role of uterine stromal-epithelial crosstalk in embryo implantation.* Int J Dev Biol, 2014. **58**(2-4): p. 139-46.

108. Mori, M., et al., *The decidua-the maternal bed embracing the embryo-maintains the pregnancy.* Semin Immunopathol, 2016. **38**(6): p. 635-649.

109. Wray, S., et al., *Calcium signaling and uterine contractility.* J Soc Gynecol Investig, 2003. **10**(5): p. 252-64.

110. Wray, S. and S. Arrowsmith, *Uterine Excitability and Ion Channels and Their Changes with Gestation and Hormonal Environment.* Annu Rev Physiol, 2021. **83**: p. 331-357.

111. Jones, K., et al., *Electrophysiological characterization and functional importance of calcium-activated chloride channel in rat uterine myocytes.* Pflugers Arch, 2004. **448**(1): p. 36-43.

112. Kidder, G.M. and E. Winterhager, *Physiological roles of connexins in labour and lactation.* Reproduction, 2015. **150**(4): p. R129-R136.

113. McCloskey, C., et al., *The inwardly rectifying K+ channel KIR7.1 controls uterine excitability throughout pregnancy.* EMBO Mol Med, 2014. **6**(9): p. 1161-74.

114. Salleh, N., et al., *The hormonal control of uterine luminal fluid secretion and absorption.* Journal of Membrane Biology, 2005. **206**(1): p. 17-28.

115. Nobuzane, T., S. Tashiro, and Y. Kudo, *Morphologic effects of epithelial ion channels on the mouse uterus: differences between raloxifene analog (LY117018) and estradiol treatments.* Am J Obstet Gynecol, 2008. **199**(4): p. 363 e1-6.

116. Ruan, Y.C., H. Chen, and H.C. Chan, *Ion channels in the endometrium: regulation of endometrial receptivity and embryo implantation.* Hum Reprod Update, 2014. **20**(4): p. 517-29.

117. Gao, H., et al., *Select nutrients in the ovine uterine lumen. ii. glucose transporters in the uterus and peri-implantation conceptuses.* Biol Reprod, 2009. **80**(1): p. 94-104.

118. Hu, X.Q. and L. Zhang, *Ca(2+)-Activated K(+) Channels and the Regulation of the Uteroplacental Circulation.* Int J Mol Sci, 2023. **24**(2).

119. Bresnitz, W. and R.A. Lorca, *Potassium Channels in the Uterine Vasculature: Role in Healthy and Complicated Pregnancies.* Int J Mol Sci, 2022. **23**(16).

120. Wray, S., C. Prendergast, and S. Arrowsmith, *Calcium-Activated Chloride Channels in Myometrial and Vascular Smooth Muscle.* Front Physiol, 2021. **12**: p. 751008.

121. Kusche-Vihrog, K., et al., *The epithelial Na+ channel: a new player in the vasculature.* Curr Opin Nephrol Hypertens, 2014. **23**(2): p. 143-8.

122. Haoui, M., et al., *Kir7. 1 is the physiological target for hormones and steroids that regulate uteroplacental function.* Science Advances, 2025. **11**(10): p. eadr5086.

123. Bjorkgren, I., et al., *The epithelial potassium channel Kir7.1 is stimulated by progesterone.* J Gen Physiol, 2021. **153**(10).

124. Shaat, N., et al., *Association of the E23K polymorphism in the KCNJ11 gene with gestational diabetes mellitus.* Diabetologia, 2005. **48**(12): p. 2544-51.

125. Flanagan, S.E., et al., *Mutations in KCNJ11, which encodes Kir6.2, are a common cause of diabetes diagnosed in the first 6 months of life, with the phenotype determined by genotype.* Diabetologia, 2006. **49**(6): p. 1190-7.

126. Golshan-Tafti, M., et al., *Comprehensive data on the relationship between KCNJ11 polymorphisms and gestational diabetes mellitus predisposition: a meta-analysis.* J Diabetes Metab Disord, 2024. **23**(1): p. 475-486.

127. Nair, A.V., et al., *Loss of insulin-induced activation of TRPM6 magnesium channels results in impaired glucose tolerance during pregnancy.* Proc Natl Acad Sci U S A, 2012. **109**(28): p. 11324-9.

128. Li, H., et al., *Downregulation of large-conductance Ca(2+)-activated K(+) channels in human umbilical arterial smooth muscle cells in gestational diabetes mellitus.* Life Sci, 2022. **288**: p. 120169.

129. Li, H., et al., *Alterations of ATP-sensitive K(+) channels in human umbilical arterial smooth muscle during gestational diabetes mellitus.* Pflugers Arch, 2018. **470**(9): p. 1325-1333.

130. Hilden, K., et al., *Gestational diabetes and adiposity are independent risk factors for perinatal outcomes: a population based cohort study in Sweden.* Diabet Med, 2019. **36**(2): p. 151-157.

131. Alfadhli, E.M., *Maternal obesity influences Birth Weight more than gestational Diabetes author.* BMC Pregnancy Childbirth, 2021. **21**(1): p. 111.

132. Djokic, V., et al., *Pregnancy-induced hypertension decreases K(v)1.3 potassium channel expression and function in human umbilical vein smooth muscle.* Eur J Pharmacol, 2020. **882**: p. 173281.

133. Yin, B., et al., *Expression and influence of KATP in umbilical artery smooth muscle cells of patients with hypertensive disorders of pregnancy.* Sci Rep, 2024. **14**(1): p. 7517.

134. Moura, T.D.B., et al., *Preeclampsia and transport of ions and small molecules: A literature review.* Placenta, 2024. **156**: p. 77-91.

135. Reisin, I.L., et al., *The cystic fibrosis transmembrane conductance regulator is a dual ATP and chloride channel.* J Biol Chem, 1994. **269**(32): p. 20584-91.

136. Salker, M.S., et al., *Deregulation of the serum- and glucocorticoid-inducible kinase SGK1 in the endometrium causes reproductive failure.* Nat Med, 2011. **17**(11): p. 1509-13.

137. Boggula, V.R., et al., *Expression of the epithelial sodium channel (ENaC) in the endometrium - Implications for fertility in a patient with pseudohypoaldosteronism.* J Steroid Biochem Mol Biol, 2018. **183**: p. 137-141.

138. Avenarius, M.R., et al., *Human male infertility caused by mutations in the CATSPER1 channel protein.* Am J Hum Genet, 2009. **84**(4): p. 505-10.

139. Hildebrand, M.S., et al., *Genetic male infertility and mutation of CATSPER ion channels.* Eur J Hum Genet, 2010. **18**(11): p. 1178-84.

140. Smith, J.F., et al., *Disruption of the principal, progesterone-activated sperm Ca2+ channel in a CatSper2-deficient infertile patient.* Proc Natl Acad Sci U S A, 2013. **110**(17): p. 6823-8.

141. Luo, T., et al., *A novel copy number variation in CATSPER2 causes idiopathic male infertility with normal semen parameters.* Hum Reprod, 2019. **34**(3): p. 414-423.

142. Quill, T.A., et al., *Hyperactivated sperm motility driven by CatSper2 is required for fertilization.* Proc Natl Acad Sci U S A, 2003. **100**(25): p. 14869-74.

143. Qi, H., et al., *All four CatSper ion channel proteins are required for male fertility and sperm cell hyperactivated motility.* Proc Natl Acad Sci U S A, 2007. **104**(4): p. 1219-23.

144. Doring, F., et al., *The epithelial inward rectifier channel Kir7.1 displays unusual K+ permeation properties.* J Neurosci, 1998. **18**(21): p. 8625-36.

145. Krapivinsky, G., et al., *A novel inward rectifier K+ channel with unique pore properties.* Neuron, 1998. **20**(5): p. 995-1005.

146. Partiseti, M., et al., *Cloning and characterization of a novel human inwardly rectifying potassium channel predominantly expressed in small intestine.* FEBS Lett, 1998. **434**(1-2): p. 171-6.

147. Hejtmancik, J.F., et al., *Mutations in KCNJ13 cause autosomal-dominant snowflake vitreoretinal degeneration.* Am J Hum Genet, 2008. **82**(1): p. 174-80.

148. Hibino, H., et al., *Inwardly rectifying potassium channels: their structure, function, and physiological roles.* Physiol Rev, 2010. **90**(1): p. 291-366.

149. Beverley, K.M. and B.R. Pattnaik, *Inward rectifier potassium (Kir) channels in the retina: living our vision.* Am J Physiol Cell Physiol, 2022. **323**(3): p. C772-C782.

150. Nakamura, N., et al., *Inwardly rectifying K+ channel Kir7.1 is highly expressed in thyroid follicular cells, intestinal epithelial cells and choroid plexus epithelial cells: implication for a functional coupling with Na+,K+-ATPase.* Biochem J, 1999. **342 (Pt 2)**(Pt 2): p. 329-36.

151. Anderson, E.J.P., et al., *Late onset obesity in mice with targeted deletion of potassium inward rectifier Kir7.1 from cells expressing the melanocortin-4 receptor.* J Neuroendocrinol, 2019. **31**(1): p. e12670.

152. Pattnaik, B.R., et al., *A Novel KCNJ13 Nonsense Mutation and Loss of Kir7.1 Channel Function Causes Leber Congenital Amaurosis (LCA16).* Hum Mutat, 2015. **36**(7): p. 720-7.

153. Sergouniotis, P.I., et al., *Recessive mutations in KCNJ13, encoding an inwardly rectifying potassium channel subunit, cause leber congenital amaurosis.* Am J Hum Genet, 2011. **89**(1): p. 183-90.

154. Perez-Roustit, S., et al., *Leber Congenital Amaurosis with Large Retinal Pigment Clumps Caused by Compound Heterozygous Mutations in Kcnj13.* Retin Cases Brief Rep, 2017. **11**(3): p. 221-226.

155. Toms, M., et al., *Phagosomal and mitochondrial alterations in RPE may contribute to KCNJ13 retinopathy.* Sci Rep, 2019. **9**(1): p. 3793.

156. Kumar, M. and B.R. Pattnaik, *Focus on Kir7.1: physiology and channelopathy.* Channels (Austin), 2014. **8**(6): p. 488-95.

157. Strauss, O., *The retinal pigment epithelium in visual function.* Physiol Rev, 2005. **85**(3): p. 845-81.

158. Huszar, D., et al., *Targeted disruption of the melanocortin-4 receptor results in obesity in mice.* Cell, 1997. **88**(1): p. 131-41.

159. Ghamari-Langroudi, M., et al., *G-protein-independent coupling of MC4R to Kir7.1 in hypothalamic neurons.* Nature, 2015. **520**(7545): p. 94-8.

160. Kirchgessner, A.L. and A. Sclafani, *PVN-hindbrain pathway involved in the hypothalamic hyperphagia-obesity syndrome.* Physiol Behav, 1988. **42**(6): p. 517-28.

161. Li, M.M., et al., *The Paraventricular Hypothalamus Regulates Satiety and Prevents Obesity via Two Genetically Distinct Circuits.* Neuron, 2019. **102**(3): p. 653-667 e6.

162. Blanks, A.M. and S. Thornton, *The role of oxytocin in parturition.* BJOG, 2003. **110 Suppl 20**: p. 46-51.

163. Arrowsmith, S. and S. Wray, *Oxytocin: its mechanism of action and receptor signalling in the myometrium.* J Neuroendocrinol, 2014. **26**(6): p. 356-69.

164. York, N., et al., *Oxytocin (OXT)-stimulated inhibition of Kir7.1 activity is through PIP2-dependent Ca(2+) response of the oxytocin receptor in the retinal pigment epithelium in vitro.* Cell Signal, 2017. **37**: p. 93-102.

165. Di Renzo, G.C., et al., *Progesterone in normal and pathological pregnancy.* Horm Mol Biol Clin Investig, 2016. **27**(1): p. 35-48.

166. Johansson, E.D., *Plasma levels of progesterone in pregnancy measured by a rapid competitive protein binding technique.* Acta Endocrinol (Copenh), 1969. **61**(4): p. 607-17.

167. Toms, M., *Investigating the pathophysiology of KCNJ13 and USH2A retinopathies using zebrafish models*. 2018, UCL (University College London).

168. Toms, M., et al., *Missense variants in the conserved transmembrane M2 protein domain of KCNJ13 associated with retinovascular changes in humans and zebrafish.* Exp Eye Res, 2019. **189**: p. 107852.

169. Kabra, M., et al., *Nonviral base editing of KCNJ13 mutation preserves vision in a model of inherited retinal channelopathy.* The Journal of Clinical Investigation, 2023. **133**(19).

170. Khan, A.O., et al., *A distinct vitreo-retinal dystrophy with early-onset cataract from recessive KCNJ13 mutations.* Ophthalmic Genet, 2015. **36**(1): p. 79-84.

171. Hernandez, C.C., et al., *The unique structural characteristics of the Kir 7.1 inward rectifier potassium channel: a novel player in energy homeostasis control.* Am J Physiol Cell Physiol, 2023. **324**(3): p. C694-C706.

172. Katamay, R. and R.B. Nussenblatt, *Blood–retinal barrier, immune privilege, and autoimmunity.* Retina, 2012: p. 579.

173. Drag, S., F. Dotiwala, and A.K. Upadhyay, *Gene therapy for retinal degenerative diseases: progress, challenges, and future directions.* Investigative Ophthalmology & Visual Science, 2023. **64**(7): p. 39-39.

174. Toualbi, L., M. Toms, and M. Moosajee, *The Landscape of Non-Viral Gene Augmentation Strategies for Inherited Retinal Diseases.* Int J Mol Sci, 2021. **22**(5).

175. Kaminsky, P.M., et al., *Directing integrin-linked endocytosis of recombinant AAV enhances productive FAK-dependent transduction.* Mol Ther, 2012. **20**(5): p. 972-83.

176. Petrs-Silva, H., et al., *Novel properties of tyrosine-mutant AAV2 vectors in the mouse retina.* Mol Ther, 2011. **19**(2): p. 293-301.

177. Wang, J.-H., et al., *Adeno-associated virus as a delivery vector for gene therapy of human diseases.* Signal Transduction and Targeted Therapy, 2024. **9**(1): p. 78.

178. Heinz, S., et al., *The selection and function of cell type-specific enhancers.* Nat Rev Mol Cell Biol, 2015. **16**(3): p. 144-54.

179. Petrich, J., et al., *Gene Replacement Therapy: A Primer for the Health-system Pharmacist.* J Pharm Pract, 2020. **33**(6): p. 846-855.

180. Zhou, H.S., D.P. Liu, and C.C. Liang, *Challenges and strategies: the immune responses in gene therapy.* Med Res Rev, 2004. **24**(6): p. 748-61.

181. Nóbrega, C., L. Mendonça, and C.A. Matos, *Gene Therapy Strategies: Gene Augmentation*, in *A Handbook of Gene and Cell Therapy*. 2020, Springer International Publishing: Cham. p. 117-126.

182. Sinha, D., et al., *Human iPSC Modeling Reveals Mutation-Specific Responses to Gene Therapy in a Genotypically Diverse Dominant Maculopathy.* Am J Hum Genet, 2020. **107**(2): p. 278-292.

183. Shchaslyvyi, A.Y., et al., *Current State of Human Gene Therapy: Approved Products and Vectors.* Pharmaceuticals (Basel), 2023. **16**(10).

184. *FDA approves hereditary blindness gene therapy.* Nature Biotechnology, 2018. **36**(1): p. 6-6.

185. Shahryari, A., et al., *Development and Clinical Translation of Approved Gene Therapy Products for Genetic Disorders.* Front Genet, 2019. **10**: p. 868.

186. Darrow, J.J., *Luxturna: FDA documents reveal the value of a costly gene therapy.* Drug discovery today, 2019. **24**(4): p. 949-954.

187. Shahi, P.K., et al., *Gene Augmentation and Readthrough Rescue Channelopathy in an iPSC-RPE Model of Congenital Blindness.* Am J Hum Genet, 2019. **104**(2): p. 310-318.

188. Banin, E., et al., *Gene Augmentation Therapy Restores Retinal Function and Visual Behavior in a Sheep Model of CNGA3 Achromatopsia.* Mol Ther, 2015. **23**(9): p. 1423-33.

189. Gootwine, E., et al., *Gene Augmentation Therapy for a Missense Substitution in the cGMP-Binding Domain of Ovine CNGA3 Gene Restores Vision in Day-Blind Sheep.* Invest Ophthalmol Vis Sci, 2017. **58**(3): p. 1577-1584.

190. Petersen-Jones, S.M., et al., *Patients and animal models of CNGbeta1-deficient retinitis pigmentosa support gene augmentation approach.* J Clin Invest, 2018. **128**(1): p. 190-206.

191. Guziewicz, K.E., et al., *BEST1 gene therapy corrects a diffuse retina-wide microdetachment modulated by light exposure.* Proc Natl Acad Sci U S A, 2018. **115**(12): p. E2839-E2848.

192. Spillane, A., et al., *Preclinical Testing of HUB-101, a Potential Gene Therapy for LCA16.* Investigative Ophthalmology & Visual Science, 2021. **62**(8): p. 2601-2601.

193. Saber Sichani, A., et al., *A Review on Advanced CRISPR-Based Genome-Editing Tools: Base Editing and Prime Editing.* Mol Biotechnol, 2023. **65**(6): p. 849-860.

194. Dang, Y., et al., *Optimizing sgRNA structure to improve CRISPR-Cas9 knockout efficiency.* Genome Biol, 2015. **16**: p. 280.

195. Hasanzadeh, A., et al., *Smart Strategies for Precise Delivery of CRISPR/Cas9 in Genome Editing.* ACS Appl Bio Mater, 2022. **5**(2): p. 413-437.

196. Lino, C.A., et al., *Delivering CRISPR: a review of the challenges and approaches.* Drug Deliv, 2018. **25**(1): p. 1234-1257.

197. Li, Q., et al., *Applications of Genome Editing Technology in Animal Disease Modeling and Gene Therapy.* Comput Struct Biotechnol J, 2019. **17**: p. 689-698.

198. Pandey, V.K., et al., *Application of CRISPR/Cas9 genome editing in genetic disorders: a systematic review up to date.* J Genet Syndr Gene Ther, 2017. **8**(2): p. 1-10.

199. Kolanu, N.D., *CRISPR–Cas9 gene editing: curing genetic diseases by inherited epigenetic modifications.* Global Medical Genetics, 2024. **11**(01): p. 113-122.

200. Yun, Y. and Y. Ha, *CRISPR/Cas9-Mediated Gene Correction to Understand ALS.* Int J Mol Sci, 2020. **21**(11).

201. Bassuk, A.G., et al., *Precision Medicine: Genetic Repair of Retinitis Pigmentosa in Patient-Derived Stem Cells.* Sci Rep, 2016. **6**: p. 19969.

202. Maeder, M.L., et al., *Development of a gene-editing approach to restore vision loss in Leber congenital amaurosis type 10.* Nat Med, 2019. **25**(2): p. 229-233.

203. Jo, D.H., et al., *CRISPR-Cas9-mediated therapeutic editing of Rpe65 ameliorates the disease phenotypes in a mouse model of Leber congenital amaurosis.* Sci Adv, 2019. **5**(10): p. eaax1210.

204. Mishra, R., R.K. Joshi, and K. Zhao, *Base editing in crops: current advances, limitations and future implications.* Plant Biotechnol J, 2020. **18**(1): p. 20-31.

205. Ha, T.C., M. Morgan, and A. Schambach, *Base editing: a novel cure for severe combined immunodeficiency.* Signal Transduct Target Ther, 2023. **8**(1): p. 354.

206. Musunuru, K., et al., *Patient-specific in vivo gene editing to treat a rare genetic disease.* New England Journal of Medicine, 2025.

207. Kabra, M., et al., *CRISPR base editing as a potential therapeutic approach for Kir7. 1 channelopathy.* Investigative Ophthalmology & Visual Science, 2021. **62**(8): p. 1483-1483.

208. Suh, S., et al., *Publisher Correction: Restoration of visual function in adult mice with an inherited retinal disease via adenine base editing.* Nat Biomed Eng, 2020. **4**(11): p. 1119.

209. Hosseini, S.Y., et al., *Insights into Prime Editing Technology: A Deep Dive into Fundamentals, Potentials, and Challenges.* Hum Gene Ther, 2024. **35**(17-18): p. 649-668.

210. Zhao, Z., et al., *Prime editing: advances and therapeutic applications.* Trends Biotechnol, 2023. **41**(8): p. 1000-1012.

211. Jang, H., et al., *Application of prime editing to the correction of mutations and phenotypes in adult mice with liver and eye diseases.* Nat Biomed Eng, 2022. **6**(2): p. 181-194.

212. Keeling, K.M., et al., *Therapeutics based on stop codon readthrough.* Annu Rev Genomics Hum Genet, 2014. **15**: p. 371-94.

213. Roy, B., et al., *Ataluren stimulates ribosomal selection of near-cognate tRNAs to promote nonsense suppression.* Proc Natl Acad Sci U S A, 2016. **113**(44): p. 12508-12513.

214. Michorowska, S., *Ataluren-Promising Therapeutic Premature Termination Codon Readthrough Frontrunner.* Pharmaceuticals (Basel), 2021. **14**(8).

215. Spelier, S., et al., *Readthrough compounds for nonsense mutations: bridging the translational gap.* Trends Mol Med, 2023. **29**(4): p. 297-314.

216. Laurent, G., et al., *Mechanism of aminoglycoside-induced lysosomal phospholipidosis: in vitro and in vivo studies with gentamicin and amikacin.* Biochem Pharmacol, 1982. **31**(23): p. 3861-70.

217. Kaloyanides, G.J., *Drug-phospholipid interactions: role in aminoglycoside nephrotoxicity.* Ren Fail, 1992. **14**(3): p. 351-7.

218. Crawford, D.K., et al., *ELX-02 Generates Protein via Premature Stop Codon Readthrough without Inducing Native Stop Codon Readthrough Proteins.* J Pharmacol Exp Ther, 2020. **374**(2): p. 264-272.

219. Lee, H.L. and J.P. Dougherty, *Pharmaceutical therapies to recode nonsense mutations in inherited diseases.* Pharmacol Ther, 2012. **136**(2): p. 227-66.

220. Shahi, P.K., et al., *Readthrough of LCA16 nonsense mutation therapy using iPS-RPE cells.* Investigative Ophthalmology & Visual Science, 2016. **57**(12): p. 1103-1103.

221. Fulbright, S., et al., *Strategies for Readthrough of Premature Termination Codons to Restore Ion Channel Function.* Investigative Ophthalmology & Visual Science, 2023. **64**(8): p. 414-414.

222. Guerin, K., et al., *Systemic aminoglycoside treatment in rodent models of retinitis pigmentosa.* Exp Eye Res, 2008. **87**(3): p. 197-207.

223. Goldmann, T., et al., *Beneficial readthrough of a USH1C nonsense mutation by designed aminoglycoside NB30 in the retina.* Invest Ophthalmol Vis Sci, 2010. **51**(12): p. 6671-80.

224. Goldmann, T., et al., *PTC124-mediated translational readthrough of a nonsense mutation causing Usher syndrome type 1C.* Hum Gene Ther, 2011. **22**(5): p. 537-47.

225. Porter, J.J., C.S. Heil, and J.D. Lueck, *Therapeutic promise of engineered nonsense suppressor tRNAs.* Wiley Interdiscip Rev RNA, 2021. **12**(4): p. e1641.

226. Lueck, J.D., et al., *Engineered transfer RNAs for suppression of premature termination codons.* Nat Commun, 2019. **10**(1): p. 822.

227. Ko, W., et al., *Efficient suppression of endogenous CFTR nonsense mutations using anticodon-engineered transfer RNAs.* Mol Ther Nucleic Acids, 2022. **28**: p. 685-701.

228. Blomquist, V.G., et al., *Transfer RNA-mediated restoration of potassium current and electrical correction in premature termination long-QT syndrome hERG mutants.* Mol Ther Nucleic Acids, 2023. **34**: p. 102032.

229. Akyuz, E., P. Shahi, and B.R. Pattnaik, *Anticodon-Engineered transfer RNA as a novel therapy for nonsense mutation.* Investigative Ophthalmology & Visual Science, 2020. **61**(7): p. 4944-4944.

Chapter 2: Precision therapeutic tRNA rescue of nonsense mutation R166X in *KCNJ13* to restore K^+ channel function

Accepted for publication in The Journal of Precision Medicine: Health and Disease (Elsevier)

Allison Spillane[1,2], Enes Akyuz[1,2], Meha Kabra[1,2], Divya Sinha[2,3], Cheryl Soref[2,3], Lionel Gissot[4], Ahmad A.I. Saneh[4], Sanjai K. Pillala[1,2], Pawan K. Shahi[1,2], Krishanu Saha[5], David M. Gamm[2,3,6], Christopher A. Ahern[4], Bikash R. Pattnaik[1,2,6]

[1]University of Wisconsin-Madison, Department of Pediatrics, Wisconsin, USA.
[2]University of Wisconsin-Madison, McPherson Eye Research Institute, Wisconsin, USA.
[3]University of Wisconsin-Madison, Waisman Center, Wisconsin, USA.
[4]University of Iowa, Carver College of Medicine, Department of Molecular Physiology and Biophysics, Iowa, USA.
[5]University of Wisconsin-Madison, Department of Biomedical Engineering, Wisconsin, USA
[6]University of Wisconsin-Madison, Department of Ophthalmology and Visual Sciences, Wisconsin, USA

SUMMARY

The *KCNJ13* gene encodes the Kir7.1 protein, and mutations in this gene cause LCA and SVD, leading to early-onset vision loss. One such nonsense mutation, R166X, results in nystagmus, poor night vision, and visual impairment. We examined therapeutic options for the R166X nonsense point mutation. Unlike missense genetic mutations, which can be rectified by gene augmentation and genome editing, nonsense mutations provide an opportunity to test additional readthrough therapies. Attempts to produce hiPSCs with the R166X mutation (CGA to TGA) were unsuccessful. This may be due to challenges in chromatin structure and folding that hinder access to the targeted loci. Therefore, we constructed an open reading frame (ORF) stably integrated HEK293T line by inserting the WT or R166X-*KCNJ13* gene using the FLP-FRT recombinase technique. While genome editing strategies did not repair the R166X mutation efficiently in this cell line, an arginine ACE-tRNA (ACE-tRNA$^{Arg.UGA}$) restored K^+ channel expression and function. This study provides an example in precision medicine where translational readthrough strategies can rescue channel function at a mutation that is difficult to correct via genome editing.

INTRODUCTION

Genetic mutations cause human disease, with approximately 5,000 genes containing phenotypic mutations and over 510,000 reported mutation variants identified to date [1, 2]. Point mutations are classified into three categories: missense, frameshift, and nonsense mutations [3]. Missense mutations involve a single nucleotide change, with the possibility that it will lead to a change in the corresponding amino acid; though not all missense mutations result in protein dysfunction, for example, in cases where the amino acid properties do not change or are not intrinsically essential for function. In contrast, nonsense mutations introduce a PTC within a transcribed mRNA sequence, resulting in a truncated, nonfunctional protein and, consequently, disease phenotypes [3, 4]. Nonsense mutations account for approximately 11.5% of all inherited human diseases [5]. Cells use nonsense-mediated decay (NMD) as a cellular defense mechanism to combat issues with mutant mRNA; however, this cellular process does not overcome the dysfunction and disease resulting from PTCs [6, 7]. Instead, it reduces the amount of PTC mRNA available for translation. Among SNVs, arginine is the most commonly substituted amino acid, accounting for 20% of pathogenic and 13.9% of benign variants [8]. In terms of stop codons, a biochemical vulnerability in the CGA (encoding arginine) codon, where the deamination of cytosine to thymidine makes the CGA-to-TGA (designated Arg^{UGA}) is the most common *de novo* PTC [9]. Therefore, there is a greater need to study therapies that treat SNVs with arginine substitutions than other amino acid variants. We reasoned that using a PTC model caused by arginine substitution would allow for the unique ability to test therapies that treat missense and nonsense mutations **(Fig. 1)** [10, 11].

Several therapeutic approaches, including genome editing techniques and readthrough therapies, have been explored to treat PTCs and missense mutations. CRISPR-based genome-editing techniques, like conventional GE, BE, and PE, have shown promise in correcting mutations [12-14]. However, this approach requires reducing off-target effects and ensuring the effective delivery of CRISPR components to ensure the accuracy of genomic editing outcomes [20-23].

Compared to the translational readthrough drugs, such as aminoglycosides [24-28], that bind to anionic phospholipids and accumulate in lysosomes, leading to toxicity [29, 30], ACE-tRNA therapy is a

novel approach that can overcome the limitations of existing treatments due to PTCs [31]. During ribosomal translation of protein-encoding mRNA, tRNA anticodon pairing ensures the reliable production of functional proteins; however, no biological tRNA anticodons match nonsense codons, resulting in the premature termination of protein synthesis [32, 33]. To circumvent this problem in PTC mutations, ACE-tRNA can be designed by introducing a PTC anticodon into a WT amino acid-containing tRNA. ACE-tRNA base pairs are translated to incorporate a WT amino acid; thus, translation continues, resulting in a full-length WT protein product [34]. ACE-tRNAs do not affect the genome, avoiding the off-target concerns associated with genome editing techniques. Additionally, off-target effects, such as the suppression of NTCs, have not been observed with ACE-tRNA treatment [35]. Previous ACE-tRNA therapy studies have successfully suppressed PTCs in diseases such as CF and long-QT syndrome arrhythmia [35-37]. However, a comparison between ACE-tRNA and genomic therapy techniques for the same PTC has not yet been conducted.

Kir channels enable potassium ions to flow out of cells, playing a pivotal role in regulating the membrane potential, which is essential for cellular signaling across diverse cell types, from epithelial cells to neurons [38-40]. Apart from Kir5.1 and some Kir2.x, Kir3.x, and Kir4.x channels, Kir channels are homotetramers; meaning they have four separately translated identical subunits assembled to create a functional channel pore [41-43]. Each subunit comprises two transmembrane domains: an intracellular amino-terminal (N-terminal) domain and a carboxyl-terminal (C-terminal) domain [38]. Kir7.1, encoded by the *KCNJ13* gene, is expressed in many different tissues, including the intestine, thyroid, proximal and distal tubules of the kidney, choroid plexus of the brain, myometrium of the uterus, and RPE cells [38-41, 44, 45]. Mutations in the *KCNJ13* gene cause LCA16 and SVD, which lead to early-onset vision loss [46-49]. The c.496C>T (p.Arg166Ter or R166X) mutation in *the KCNJ13* gene introduces a PTC that results in a truncated protein, leading to visual impairments, including nystagmus and poor night vision in homozygous patients [47].

Our overall goal was to investigate the biological effects of the R166X mutation in the *KCNJ13* gene and assess its therapeutic implications. We hypothesized that creating and correcting the R166X mutation would be possible using several genomic editing techniques with varying efficiencies and that

treatment with ACE-tRNA$^{Arg.UGA}$ would suppress the R166X mutation, restoring membrane expression and function. Despite utilizing multiple genomic strategies, we were unable to insert or correct the R166X mutation. Our finding demonstrates the challenges of using CRISPR-Cas9 genome editing to create the R166X disease mutation in hiPSC cells. Due to the difficulty in accessing specific genomic structures, heterologous expression of the ORF in HEK293T cells was implemented to correct the R166X mutation. However, fixing the mutation also proved challenging when using various genome editing techniques. This study conclusively demonstrated that ACE-tRNA readthrough successfully overcomes the R166X mutation, resulting in the expression of WT-Kir7.1 protein on the membrane and the restoration of functional recovery in the channel, suggesting this approach as a viable therapeutic strategy for mutations resistant to traditional genome editing techniques.

RESULTS

Generating a R166X in vitro human disease model

We initially aimed to establish a stable cell line harboring the R166X mutation in *KCNJ13* for further disease characterization and therapeutic evaluation. hiPSCs are a valuable source of RPE cells for disease modeling and drug validation studies [53-56]. Without access to a patient-derived cell line, we attempted to employ CRISPR-Cas9 genome editing to introduce the R166X mutation into hiPSCs **(Supplementary Fig. S1A)**. The cells maintained their viability after treatment, indicating no toxic effects **(Supplementary Fig. S1B)**. The designs of the sgRNAs and single-stranded oligodeoxynucleotides (ssODNs) are shown in **Supplementary Fig. S1C**. Despite multiple efforts, we were unable to successfully introduce the R166X mutation using either sgRNA alone **(Supplementary Fig. S1D)**. Similarly, no editing was observed when the R166X mutation was introduced in WT fibroblasts **(Supplementary Fig. S2)**. The indel frequency, measured by the Inference of CRISPR Edits (ICE) online tool from Synthego [57], evaluates Cas9's DNA cleavage efficacy. Analysis of our results using ICE revealed 0% indels and 100% WT sequence readouts when using either sgRNA, thus demonstrating no insertion of the R166X mutation **(Supplementary Fig. S1E)**. Therefore, we concluded that generation of the R166X mutation in a hiPSC cell line was not achievable under our experimental conditions and

capabilities. Creating R166X mutation in hiPSCs may have been unsuccessful due to constraints in delivery, the limited biological activity of the editor, or the inaccessibility of the genomic structure at the mutation site.

To develop an alternative human preclinical system for the R166X disease mutation, we generated the mutation in a simplified ORF that stably expressed the R166X mutation in HEK293T cells (HEK FRT R166X) **(Fig. 2A and Supplementary Fig. S1A)**. We confirmed that our stable cell line contained the correct inserted nucleotide sequence (TGA) of the mutant R166X gene at codon 166 **(Fig. 2B)**. Additionally, WT Kir7.1-expressing cells (HEK FRT WT) were successfully generated for comparison, as indicated by their CGA sequence **(Supplementary Fig. S3)**.

Inefficient correction of the R166X mutation using genome editing

With the HEK FRT R166X cells, we investigated three different genome editing techniques: GE, BE, and PE **(Supplementary Fig. S1A)**. CRISPR-Cas9 GE works by creating a double-stranded break near the target site of the mutation and utilizing endogenous NHEJ or HDR to incorporate the correct sequence by referencing a donor or ssODN template containing the WT sequence [20]. Our ssODN sequence comprised a 33 nt 5' arm and a 32 nt 3' arm, consistent with previous studies demonstrating that arms ≥30 nt are ideal, and longer arm lengths lead to increased toxicity in the cells [58] **(Supplementary Fig. S1F)**. The sgRNA is shown in **Supplementary Fig. S1F**. GE approach yielded no detectable editing in this study **(Fig. 2C, blue diamonds)**.

In contrast to GE, BE utilizes a modified CRISPR-Cas9 fused to a deaminase enzyme that converts cytosine to uracil or adenosine to inosine on one strand at the target site containing the mutation, thereby creating a single-stranded break on the complementary strand of DNA [20]. The cell then repairs the break using the converted bases as a template, incorporating the WT base in the mutation site. To correct the R166X mutation, we targeted the reverse strand of the mutant sequence (ACT) to convert the mutant TGA sequence to the WT CGA sequence using an ABE. Identical gRNA

sequences were utilized for GE and BE approaches **(Supplementary Fig. S1F)**. We observed only 10% editing efficiency in a single sample using nucleofection of ribonucleoprotein (RNP)-delivered ABE8e BE **(Fig. 2C, green diamond)** [59]. However, this was not repeatable and had too low of an efficiency to perform functional testing.

PE incorporates Cas9n fused to an engineered RT (Cas9n-RT), a ngRNA, and a pegRNA containing the WT sequence [15]. The Cas9n-RT is guided by pegRNA and directed to create a nick in the opposite strand by the ngRNA. The pegRNA hybridizes to the non-target strand and serves as a template for RT to correct the mutant sequence to the WT sequence. Guide RNAs were designed using pegFinder [60], as described in the Methods section **(Supplementary Fig. S1G)**. Like other editing approaches, PE failed to produce detectable editing. **(Fig. 2C, orange diamonds)**.

Successful suppression of a PTC using ACE-tRNA$^{Arg.UGA}$ minicircles

Given the low efficiency of correcting the DNA via genome editing, we investigated the feasibility of PTCs readthrough at the translational level based on existing PTC-containing mRNA. We chose to test the ability of ACE-tRNA readthrough to avoid the undesirable outcomes associated with other readthrough drugs, such as aminoglycosides [26-30, 35]. We chose minicircles instead of plasmid-based delivery owing to their long-term expression [61-63]. As the length of ACE-tRNA is approximately 70 nucleotides, this combination makes it an attractive delivery system [61, 64, 65]. We evaluated six variations of ACE-tRNA (ACE-tRNA$^{Arg.UGA}$) minicircles based on (1) isocodon sequence, (2) structural differences, and (3) the number of repeated tRNA sequences within the minicircle **(Fig. 3A and 3C)**. Arginine ACE-tRNAs were selected based on validation in a previous study [35]. To test whether our minicircles could be delivered and had a biological readthrough, we used a previously validated green fluorescent protein (GFP) mutant that contained a TGA stop codon, sfGFP-N150TGA (GFP^{TGA}) [37]. Cells that contained successful delivery of both ACE-tRNA$^{Arg.UGA}$ and GFP^{TGA}, and where there was a biological readthrough of the TGA codon of the GFP protein by ACE-tRNA$^{Arg.UGA}$, expressed detectible GFP fluorescence **(Fig. 3B)**. All six minicircles had different levels of GFP^{TGA} suppression **(Fig. 3C)**.

Additionally, 3XCCT ACE-tRNA$^{Arg.UGA}$ minicircles had the highest percentage of cells showing GFP fluorescence, as determined by flow cytometry (42.5%) and confirmed by fluorescence microscopy (38%) **(Fig. 3C and Supplementary Fig. S4)**. Therefore, we continued to test the ability of 3XCCT ACE-tRNA$^{Arg.UGA}$ minicircles to suppress the R166X mutation.

3XCCT ACE-tRNA$^{Arg.UGA}$ suppression of R166X leads to full-length Kir7.1 protein expression

Next, we determined if 3XCCT ACE-tRNA$^{Arg.UGA}$ suppression of the R166X mutation led to full-length membrane-bound Kir7.1 [44, 66, 67]. The cells were treated with GFP-tagged R166X mutant plasmid and 3XCCT ACE-tRNA$^{Arg.UGA}$ minicircles in a 1:3 ratio, and immunocytochemistry was performed using a C-terminal Kir7.1-tagged antibody **(Fig. 4A)**. 3XCCT ACE-tRNA$^{Arg.UGA}$ successfully suppressed the R166X mutation and created a full-length Kir7.1 protein that appeared to, at least in part, be trafficked to the cell membrane **(Fig. 4B)**. This demonstrated that 3XCCT ACE-tRNA$^{Arg.UGA}$ successfully suppressed the R166X mutation, leading to the membrane trafficking of the full-length Kir7.1. When correlating the C-terminal Kir7.1 tagged antibody (red) with GFP-tagged R166X (green) or GFP-tagged WT Kir7.1 proteins (green), 3XCCT ACE-tRNA$^{Arg.UGA}$-treated cells showed colocalization as represented by Pearson's correlation **(Fig. 4C)**. Since Kir7.1 is a homotetrameric ion channel, this suggests that WT domains expressed following ACE-tRNA treatment could be assembled with R166X domains, resulting in a WT/R166X heterotetrameric channel that is trafficked to the membrane.

Functional rescue of the R166X mutation using 3XCCT ACE-tRNA$^{Arg.UGA}$

Next, we tested whether the full-length Kir7.1 protein translated after 3XCCT ACE-tRNA$^{Arg.UGA}$ suppression of R166X restored the functional activity of Kir7.1. As demonstrated above, Kir7.1 channels have a tetrameric structure following treatment with ACE-tRNA, which might contain both WT and mutant R166X subunits. Nevertheless, we reasoned that functional rescue was achievable following 3XCCT ACE-tRNA$^{Arg.UGA}$ suppression of R166X. Cells were co-transfected with the R166X plasmid and 3XCCT ACE-tRNA$^{Arg.UGA}$ minicircles **(Fig. 5A)**. R166X plasmid alone or WT Kir7.1 plasmid alone were used as

controls. Whole-cell currents for Kir7.1 showed increased currents in 3XCCT ACE-tRNA$^{Arg.UGA}$-treated cells compared to the cells expressing R166X alone, measured using +50mV to -150mV in 50mV steps, with a holding potential of 0mV over 600 ms **(Fig. 5B)**. Cells were then exposed to extracellular rubidium (Rb+), a charge carrier known to enhance the Kir7.1 channel current specifically, thus, allowing for further comparison between WT, mutant, and treated channels if the expression is low [68]. Rb+ treatment increased whole-cell currents of R166X + 3XCCT ACE-tRNA$^{Arg.UGA}$-and WT Kir7.1-expressing cells but not R166X alone **(Fig. 5B)**. The whole-cell current measured at -150 mV increased median -58.14 (IQR (-70.27)-(-36.85)) pA in R166X-expressing cells **(Fig. 5C, orange circles)** (n=6) to median -108.34 (IQR (-135.50)-(-65.00)) in 3XCCT ACE-tRNA$^{Arg.UGA}$-treated cells **(Fig. 5C, purple triangles)** (n=9) compared to median -375.37 (IQR (-517.88)-(-303.50)) pA in WT channel-expressing cells **(Fig. 5C, grey squares)** (n=7). The K+ current (I_K) at -150 mV (Fig. 5C) showed an increase (p=0.085) in the current from median -58.14 (IQR (-70.27)-(-36.85)) pA for R166X alone to median -108.34 (IQR (-135.50)-(-65.00)) pA for 3XCCT ACE-tRNA$^{Arg.UGA}$-treated treatment, compared to median -375.37 (IQR (-517.88)-(-303.50)) pA for WT **(Fig. 5D)**. Resting membrane potentials from whole-cell recordings demonstrated significantly increased hyperpolarization (p=0.0009) from -median -5.75 (IQR (-11.05)-(-4.05)) mV in R166X alone to median -40.89 (IQR (-57.47)-(-28.88)) mV in 3XCCT ACE-tRNA$^{Arg.UGA}$-treated cells, compared to median -60.60 (IQR (-61.75-(-59.40)) mV in WT-expressing cells **(Fig. 5E)**. Rb^+ currents increased from -median 68.51 (IQR (-84.76)-(-47.00)) pA in cells expressing R166X mutant protein **(Fig. 5F, orange circles)** to median -1200.26 (IQR (-1394.65)-(-799.87)) pA for 3XCCT ACE-tRNA$^{Arg.UGA}$-treated cells **(Fig. 5F, purple triangles)**, compared to median -3708.80 (IQR (-3943.48)-(-2492.52)) pA observed in WT channel expressing cells **(Fig. 5F, grey squares)**. Rb+ fold change:

$$I_{Rb}/I_K$$

at -150mV demonstrated an inward current fold change of 1.29±0.04, median 1.28 (IQR 1.20-1.40) in R166X alone cells, which was significantly improved (p=0.0001) to 12.38 ± 1.57, median 11.48 (IQR 9.78-11.96) in 3XCCT ACE-tRNA$^{Arg.UGA}$-treated cells and were comparable to a median of 6.56 (IQR 5.45-

11.30) in WT cells **(Fig. 5G)**. We demonstrated that 3XCCT ACE-tRNA$^{Arg.UGA}$ significantly suppressed the R166X mutation and successfully rescued the function of the Kir7.1 channel.

DISCUSSION

This study aimed to create an in vitro hiPSC model containing the single-nucleotide R166X mutation in *KCNJ13*, which would then be used to evaluate the molecular mechanism of RPE dysfunction associated with this mutation. Additionally, the study sought to investigate therapeutics that could overcome the mutation. We and others have successfully incorporated single-nucleotide mutations using CRISPR genome editing to develop diseased cell models from hiPSCs and fibroblasts [13, 54, 69-71]. We found that similar genome editing approaches to create R166X in hiPSCs or fibroblasts were challenging **(Supplementary Fig. S1 and Supplementary Fig. S2**). Based on previous BEST1 gene insertion in hiPSC cells, we excluded delivery as a limitation [69]. We posited that the complexities associated with targeting the *KCNJ13* gene chromatin structure accessibility within nucleosomes could be the prime reason for the difficulty in creating the R166X mutation [72, 73].

The ORFs of genes designated for recombinant protein expression studies in plasmids are characterized by the absence of higher-order chromatin folding structures [74]. Consequently, we proceeded with genome editing of our recombinant gene, expressing the stable R166X mutant cell line HEK FRT R166X (**Fig. 2B** and **Supplementary Fig. S3**). This strategy, which was applied to another PTC mutation in the *KCNJ13* (W53X) ORF located at an upstream position, resulted in the successful genome-edited rescue of channel function [13]. Neither GE nor PE-mediated editing of the R166X mutation was fruitful (**Fig. 2C**). Although one instance of 10% editing was noted following nucleofection of an RNP base editor (A8NG), this outcome could not be replicated in subsequent trials (**Fig. 2C**). Furthermore, the editing efficiency was suboptimal for conducting functional analysis. CRISPR-Cas9 GE techniques have demonstrated the capacity for gene correction and functional recovery of nonsense mutations both in vitro and in vivo [75-77]. Previous investigations employing ABE to rectify nonsense mutations have resulted in the correction of genes with therapeutic implications both in vitro and in vivo

[78, 79]. PE, a novel gene-editing technology, has also successfully corrected nonsense mutations and restored function both in vivo and in vitro [22, 80-82]. Since we employed analogous GE, ABE-BE, and PE techniques for the in vitro rectification of nonsense mutations, the biological activity of the genomic editors in our study is unlikely to be the cause of the challenges we encountered. We conclude that the R166X genomic loci present difficulties for targeted approaches, emphasizing that the efficacy of available genome editing approaches is site-dependent. Additionally, as we were not able to insert the R166X mutation into a primary cell line, our creation of a R166X stable cell line provides an alternative method for studying rare mutations in vitro. The reporting of rare mutations is increasing, and primary cell lines will not always be available to study the disease phenotypes and drug discovery [83, 84]. Therefore, employing a stable cell line, such as the one described in this study, can be used as an alternative method for therapeutic development.

The success of genome editing techniques depends on careful consideration of the design and delivery of sgRNAs [15-19]. The R166X loci exhibit substantial thymine (T) and adenine (A) base repeats, which may compromise the efficacy of sgRNA design (**Supplementary Fig. S4A**). sgRNAs are single-stranded nucleic acids that are recognized for their ability to form hairpin structures [85]. Consequently, the options for sgRNA design are limited to guides that incorporate repeating bases capable of establishing a hairpin structure; thus, they are deemed unsuitable for effectively editing loci **(Supplementary Fig. S4B, S4C, and S4D)** [86]. With ongoing advancements in CRISPR editing methodologies, which allow for the use of elongated gRNAs or those located at a significant distance from the mutation site, the potential for editing such mutation sites may become feasible.

We refocused our efforts towards a translation correction methodology to overcome the limitations imposed by genomic editing techniques. Translational readthrough approaches provide an alternative strategy for targeting monogenic mutations at the translational level, thereby eliminating the need for individualized treatment for each mutation type. Several agents for readthrough therapies have been tested, including aminoglycosides [24]. These readthrough drugs function by incorporating a NCT at the PTC site, instead of terminating translation [25]. Despite their promise for treating PTC-causing

diseases, they can lead to inconsistent off-target amino acid insertions with a missense phenotype [26-28]. Additionally, aminoglycosides can lead to toxicity through binding to anionic phospholipids and accumulating in lysosomes [29, 30]. Therefore, we chose to move forward with investigating the ability of ACE-tRNA to overcome the R166X PTC mutation.

During protein translation, mRNA codons engage in base pairing with tRNA anticodons, thereby facilitating the incorporation of a specific amino acids [87]. Pharmacological agents, such as aminoglycosides, have demonstrated a variable degree of translation readthrough in clinical trials [28, 88-92]. These pharmaceutical substances exert stress on the translation machinery and promote the incorporation of a near-cognate amino acid, frequently tryptophan, for UGA stop codons or glutamine for UAG and UAA [93-95]. Although small-molecule readthrough drugs are prospective candidates for addressing the R166X mutation, they may also lead to unintended amino acid substitutions and toxicity [26-30]. We evaluated the efficiency of six distinct ACE-tRNA$^{Arg.UGA}$ variants (2XACG, 3XACG, 2XTCT, 3XTCT, 2XCCT, and 3XCCT), which were incorporated into minicircles to counteract PTCs using a GFP plasmid (GFP^{TGA}) (**Fig. 3C**). All six ACE-tRNA$^{Arg.UGA}$ constructs effectively suppressed PTC and stimulated GFP expression. For therapeutic tRNA, it is crucial to account for the influence of varying isoacceptors and isodecoders on suppression efficiency. Isoacceptors are tRNAs that carry the identical amino acid yet differ in their anticodon sequences [96]. Additionally, tRNA isodecoders possess the same amino acid and anticodon, although their nucleotide sequences differ structurally. Previous studies have indicated that variations in tRNA isodecoders yield different suppression efficiencies for UAG stop codons [97]. This could be due to differences in the affinity of each isodecoder with the ribosome, as well as changes in the ribosomal conformation [98, 99]. In this study, arginine tRNAs with diverse isoacceptors were selected and engineered to maintain the same UGA anticodon. Furthermore, the structural sequence of tRNA varied, as illustrated in **Fig. 3C**. Consequently, our engineered tRNAs bore a closer resemblance to isodecoders, which feature the same anticodon with distinct structural components. This study demonstrated that isodecoders exhibited varying suppression efficiencies for the UGA stop codon, with the most pronounced therapeutic outcome observed with 3XCCT ACE-tRNA$^{Arg.UGA}$ (**Fig. 3C** and

Supplementary Fig. S5). Therefore, we selected the 3XCCT ACE-tRNA$^{Arg.UGA}$ to test suppression of the R166X mutation. We observed translational readthrough, resulting in the expression of the full-length Kir7.1 protein, at least partially, on the cell membrane (**Fig. 4B**).

Similarly, the translation readthrough of R166X by 3XCCT ACE-tRNA$^{Arg.UGA}$ resulted in functional channel rescue compared to the untreated (UT) mutant (**Fig. 5**). This rescue further demonstrated that R166X suppression by 3XCCT ACE-tRNA$^{Arg.UGA}$ resulted in at least partial expression of protein on the membrane observed in **Fig. 4B**. Since the functional rescue was shy of the WT channel current, we reason that this variation is likely attributable to channels containing different ratios of WT and truncated mutant domains. Suppression of the R166X gene by ACE-tRNA$^{Arg.UGA}$ treatment likely results in two distinct protein molecules; one is a full-length protein andhe other is the truncated protein, both of which can be localized to the membrane (**Fig. 4B**). Each of the four subunits of Kir7.1 is produced separately following ACE-tRNA treatment, which permits the potential assembly of WT and mutant domains in varying ratios within the same channel protein complex [41]. Heterogeneity among the channels likely hinders their function, culminating in our observed partial recovery **(Fig. 5)**. Live-cell imaging co-transfection experiments further demonstrate that WT and R166X proteins are co-localized and can be trafficked to the membrane, further supporting this hypothesis **(Supplementary Fig. S6)**. This phenomenon is evident in a missense mutation in the *KCNJ2* gene, which encodes Kir2.1 [100]. Furthermore, an increase in the WT-to-mutant protein ratio was correlated with an enhancement in channel function. We conclude that co-assembly of WT and mutant proteins within tetrameric channels, in various possible ratios, may precipitate a reduction in channel function. Additionally, some of these heterotetrameric WT/R166X channels could get caught in the ER or Golgi, potentially further contributing to partial recovery due to a decrease in membrane channel expression **(Fig. 4B and Fig. 5)**. To our knowledge, this constitutes the first report of a nonsense mutation that is translocated to the membrane, disrupting channel function. Despite observing partial rescue of Kir7.1 channel function using ACE-tRNA$^{Arg.UGA}$, the level of recovery of membrane potential and current remains promising, suggesting that future refinement of the treatment protocols for tetrameric channels may yield enhanced functional

rescue. Our findings, along with prior studies, suggest that ACE-tRNA represents a promising biological therapeutic molecule for treating diseases associated with PTCs, reaffirming previous observations of PTC suppression by ACE-tRNA in various diseases, including CF and long-QT syndrome [35-37].

In addition to their efficacy in suppressing PTCs, previous research has demonstrated that NTCs remain unaffected by ACE-tRNAs, suggesting minimal off-target effects during the translation process [35]. Although this phenomenon is not yet understood, some possible reasons include genes containing multiple NTCs that would not allow for the interference of the ACE-tRNA, biases for specific nucleotide sequences in NTCs compared to those typically observed in PTCs, or differences in ribosomal complex confirmation at PTC codons compared to NTC codons that would not allow for proper binding of an ACE-tRNA to the ribosome at the NTC site [101-103]. Consequently, ACE-tRNA therapies have the potential to mitigate off-target impacts commonly associated with genomic editing techniques and other readthrough agents. Furthermore, for monogenic disorders such as LCA16, wherein various mutations can influence disease phenotypes, ACE-tRNA therapies present a promising gene-agnostic strategy that can address multiple mutations, thereby benefiting a broader patient population affected by these PTCs, without necessitating individualized approaches typically required by genomic editing techniques.

CONCLUSION

In conclusion, our study showed that ACE-tRNA$^{Arg.UGA}$ minicircles exemplify a promising therapeutic approach for addressing PTC mutations in proteins that are challenging to target using genomic methodologies, including CRISPR-Cas9. Furthermore, our study demonstrated the need for further enhancement of therapeutic tRNA screening to improve its effectiveness and for employing creative delivery mechanisms, such as minicircles.

MATERIALS AND METHODS

Cell Culture

HEK293 cells (ATCC, CRL-3216), HEK Flp-In 293 (HEK293T) host cells (Thermo Fisher Scientific, R75007), and fibroblasts were cultured in complete Dulbecco's modified Eagle's high-glucose medium containing l-glutamine (DMEM, GIBCO, 11965-092) with 10% fetal bovine serum (FBS, HyClone™ Characterized Fetal Bovine Serum, Heat-inactivated, SH30396.03HI), 1% penicillin-streptomycin (Pen-Strep, GeminiBio, 400-109), and 1% antibiotic-antimycotic (Anti-Anti, Gibco, 15240062) at passages #5-25. The cells were maintained in an incubator at 37°C and 5% CO_2. The medium was changed every 2-3 days. Cells were split once they reached 80% confluence by washing with Dulbecco's Phosphate-buffered Saline (DPBS, GIBCO, 14190144) and gently dissociated using Accutase (Corning, 25-058-CI).

hiPSC cells were maintained in mTeSR Plus Medium (StemCell, 100-0276, kit). The medium was changed every other day, and the cells were maintained in an incubator at 37°C and 5% CO2. Once cells reached 60-80% confluency, they were detached using 0.5 mM EDTA in DPBS.

CRISPR-Cas9 Approach to creating R166X mutation in hiPSC

A previously published WT line [104] was used to edit the *KCNJ13* locus to introduce an R166X encoding mutation. The sgRNA sequences tested were identified using the CRISPOR design tool (Version 4.99) [105]. They were purchased from Synthego as a 1.5 nmol synthetic sgRNA with 2'-O-methyl 3' phosphorothioate modification at the first and last three nucleotides, as recommended. The ssODN sequence was ordered from Integrated DNA Technologies (IDT). The two sgRNAs and ssODNs tested for editing are described in **Supplementary Fig. S1C**. Before use, the stocks were reconstituted to 150 pmol/µL.

For editing, hiPSCs were cultured on Matrigel-coated plates in mTeSR Plus media (STEMCELL Technologies) until they reached ~80% confluence using standard hiPSC culture protocols. 24 h before

electroporation, the cells were treated with CloneR (STEMCELL Technologies), following the manufacturer's protocol. On the day of electroporation, 1 µL of reconstituted sgRNA was pooled with 4 µg Cas9 Nuclease protein (TrueCut Cas9 Protein V2, Thermo Fisher Scientific) and 5 µL of Neon Buffer R (Invitrogen) to promote Cas9-RNP complex formation. After 15 min, 1.0 µL of ssODN (reconstituted to 50 pmol/µL concentration, designed with homology overhangs of at least 35 bp) was added to the Cas9-RNP mix.

For the singularization of hiPSCs, the cells were incubated with a 1:1 mixture of 0.5 mM EDTA: Accutase for 3-4 min, lifted off the culture surface, resuspended in 1 mL PBS, counted, and ~400,000 cells were pelleted at 200xg for 3 min. Pelleted cells were resuspended in 35 µL Neon Buffer R and mixed with 8 µL of the pre-prepared Cas9-RNP complex with the repair ssODN. Cells were electroporated using a 10 µL NEON electroporation format with 1200V, 30 msec, and 1x pulse settings. Cells were pooled following four rounds of electroporation and plated in mTeSR Plus media with CloneR supplement at the manufacturer-recommended concentrations following a serial dilution to promote single-cell clonal growth. Following expansion for 10-14 days, clones were identified and selected using standard techniques.

Bulk gDNA was collected from dissociated cells using QuickExtract DNA Extraction Solution 1.0 (Epicenter) to confirm editing efficiency before clonal selection. Single-cell clones were manually selected and mechanically disaggregated into single cells. Genomic DNA was isolated from some cells using QuickExtract DNA Extraction Solution 1.0 (Epicenter). Genotyping primers were designed to flank the mutation site, allowing amplification of this region using Q5 polymerase-based PCR (NEB), and were ordered through IDT **(Supplementary Table S1C)**. The Forward primer, combined with one of the reverse primers, was used for amplification. PCR products were identified using agarose gel electrophoresis and purified using a Zymoclean Gel DNA Recovery Kit (Zymo Research). The clones were submitted to Quintara Biosciences for Sanger sequencing using the forward primer as the sequencing primer to identify clones with the appropriate genetic modification. ICE analysis was performed using the Synthego ICE analysis online tool [57].

CRISPR-Cas9 Approach to creating R166X mutation in WT fibroblast cells

Base editor mRNAs (BE4 and eVDCN) were a gift from Dr. David R. Liu. sgRNAs were designed using Benchling (https://www.benchling.com) to target the R166X location of the human *KCNJ13* (h*KCNJ13*) gene and ordered from Synthego. Fibroblasts were subcultured to 70% confluency for 24 h before treatment. The cells were then nucleofected using the Lonza 4D Nucleofector CM-130 program with GE mRNA (3µg), sgRNA 1 (50 pmol), and sgRNA 2 (50 pmol). Following electroporation, the cells were maintained in 6-well plates in cell medium, which was changed 24-48 h after treatment. Cells were collected for deep sequencing 5-7 days after treatment.

Creation of HEK FRT R166X and HEK FRT WT cell lines

GFP-tagged Kir7.1 (WT and R166X) was expressed in HEK Flp-ln 293 (HEK293T) host cells (Thermo Fisher Scientific, R75007) using a pFRT/lacZeo target site vector, as described by Kabra et al. (2023) **(Fig. 2A)** [13]. Cells were maintained in DMEM containing 10% FBS, 1% penicillin-streptomycin, and 2 mM l-glutamine with 100 µg/mL zeocin before co-transfection with the GFP-tagged h*KCNJ13* sequence (WT or R166X) containing the Flp-In expression vector (pcDNA5/FRT) and pOG44 recombinase expression plasmid. Cells were passaged to 25% confluency 48 h after co-transfection and maintained at 200 µg/mL hygromycin B for selection purposes. Clones resistant to hygromycin B were selected and maintained at 100 µg/mL hygromycin B. Following the expansion of each clone, the clones were analyzed using Sanger sequencing and immunocytochemistry. A list of the in-fusion cloning and Sanger sequencing primers used is provided in **Supplementary Table S2**.

CRISPR Cas9 GE

Cas9 mRNA was obtained from TriLink Biotechnology. sgRNAs were designed using Benchling (https://www.benchling.com) to target the R166X locus in h*KCNJ13*. sgRNA designs were validated using

CRISPR-RGEN [106] and PnB Designer [80] online tools. The sgRNAs and ssODNs tested are described in **Supplementary Fig. S1F**. Following validation, sgRNAs were ordered from Synthego Inc. (Menlo, CA). An ssODN sequence was designed to have a 33 nt 5' and 32 nt 3' arm complementary to the target strand. R166X stably expressing HEK293T cells were subcultured at 70% confluence for 24 h before treatment. Cells were then nucleofected using the Lonza 4D Nucleofector CM-130 program with GE mRNA (3 µg), sgRNA (100 pmol), and donor sequence (ssODN) (100 pmol). Nucleofection was performed using an RNP complex formed by incubating GE protein (3 µg) and sgRNA (100 pmol) for 10 min at room temperature. Following nucleofection, cells were maintained in 6-well plates and the medium (DMEM, 10% FBS, 1% Pen-strep, 1% Anti-anti, 100 µg/mL hygromycin B) was changed 24-48 h after treatment. Cells were collected for deep sequencing 5-7 days after treatment.

CRISPR Cas9 BE

For base editing, sgRNAs from gene editing (above) were used, as described in **Supplementary Fig. S1F**. ABE8e base editor mRNAs were obtained from TriLink BioTechnologies.

HEK293T R166X stable expressing cells, subcultured at 70% confluence 24 h before treatment, were collected for nucleofection using the Lonza 4D Nucleofector CM-130 program with ABE8e mRNA (spCas9-NG, 3 µg) [107] and sgRNA (100 pmol). Nucleofection was performed using the RNP complex formed after incubation with ABE8e protein (3 µg) and sgRNA (100 pmol) for 10 min at room temperature. Nucleofected cells were maintained as described above. Additionally, the cells were transfected with ABE8e mRNA (spCas9-NG, 3 µg) [49] and sgRNA (100 pmol) using Lipofectamine 2000 (Thermo Fisher Scientific, 11668–030). The medium was changed after 24-48 h and the cells were collected for deep sequencing 5-7 days post-treatment.

CRISPR Cas9 PE

Prime editing mRNA was synthesized as described by Doman et al. [81]. The custom design of the sgRNA was performed using (pegFinder) [60] and ordered using Synthego. sgRNA designs were validated using CRISPR-RGEN [106] and PnB Designer [80] online software. The sgRNA, ngRNA, and pegRNA are illustrated in **Supplementary Fig. S1G**. Following validation, sgRNAs were ordered from Synthego. R166X stably expressing HEK293T cells were subcultured at 70% confluence 24 h before treatment. Nucleofection was performed as described above, with the following treatment groups: PE mRNA Nucleofection1: PE2 mRNA (1 µg), R166X pegRNA (100 pmol), and R166X nicking sgRNA (60 pmol), or PE mRNA Nucelofection2: PE2mRNA (3 µg), R166X pegRNA (200 pmol), and R166X nicking sgRNA (100 pmol). Additionally, the cells were transfected with Lipofectamine 3000 (Thermo Fisher Scientific, L3000-001) with PE2 mRNA (3 µg), R166X pegRNA (200 pmol), and R166X nicking sgRNA (150 pmol). The cells were maintained and subjected to deep sequencing 5-7 days after post-treatment, as described below.

ACE-tRNA$^{Arg.UGA}$ Design

ACE-tRNA$^{Arg.UGA}$ minicircles were selected and validated according to the methods described by Lueck et al. [35]. Minicircles were custom-ordered from System Biosciences [(MN100B-2XArg and 3XArg ACG2-1, 109641) (MN100B-2XArg and 3XArg TCT3-2, 109094) (MN100B-2XArg and 3XArg CCT2-1, 109641)].

Suppression of PTC in GFP^{TGA} Plasmid Treated Cells by ACE-tRNA$^{Arg.UGA}$ minicircles

A GFP^{TGA} plasmid construct was created and validated according to the method described by Blomquist et al. [37]. HEK293 cells were co-transfected with the GFP^{TGA} plasmid (1 µg) and one variation of ACE-tRNA$^{Arg.UGA}$ minicircle (2XACG, 3XACG, 2XTCT, 3XTCT, 2XCCT, or 3XCCT) (1 µg) or dummy plasmid (1 µg) in a 1:1 ratio using PolyJet^{TM} (Signa Gen). Additionally, cells were treated with either the GFP^{WT} plasmid (1 µg) or minicircle DNA carrying GFP (MN601MC-1; System Biosciences) (1 µg), with a dummy

plasmid (1 µg) in a 1:1 ratio, as positive controls. Cells were maintained in cell culture medium [DMEM, 10% FBS, 1% Penstrep, 1% Anti-anti] for 48 h, and the medium was changed 24 h after transfection.

Suppression of R166X mutation by 3XCCT ACE-tRNA$^{Arg.UGA}$ minicircle

HEK293 cells were co-transfected with a GFP-tagged R166X plasmid (0.5 µg) and 3XCCT ACE-tRNA$^{Arg.UGA}$ minicircle (1.5 µg), or dummy plasmid (1.5 µg) at a 1:3 ratio using PolyJet^{TM} (SignaGen) in 6-well plates. Additionally, the cells were treated with a GFP-tagged WT-*KCNJ13* plasmid (0.5 µg) and a dummy plasmid (1.5 µg) in a 1:3 ratio as a positive control. Cells were maintained in cell culture medium [DMEM, 10% FBS, 1% Penstrep, 1% Anti-anti] for 48 h, changing the medium 24 h after transfection. Whole-cell patch-clamp and immunocytochemistry were performed 48 h after transfection.

Flow cytometry

48 h after transfection with GFP^{TGA} and ACE-tRNA$^{Arg.UGA}$ minicircle variant, cells were collected for flow cytometry. Cells were washed with PBS, incubated in Accutase for 3–5 min in a cell incubator to dissociate from the plate, and collected with flow medium [PBS, 0.1% BSA, 2 mM EDTA, and 10 mM HEPES]. Cells were spun at 100 RCF for 3 min and resuspended in flow media twice for washing purposes. The cells were filtered, and DAPI (0.8 µg/ml) was added. Flow cytometry was performed using a BD FACSAria^{TM} III Cell Sorter.

Immunocytochemistry

48 h after transfection with R166X plasmid and 3XCCT ACE-tRNA$^{Arg.UGA}$ minicircle, R166X plasmid, and dummy plasmid, or WT-Kir7.1 plasmid and dummy plasmid. The cells were plated on glass coverslips. 24 h after plating on glass coverslips, cells were fixed in 4% paraformaldehyde for 15 min at 4°C. The

coverslips were washed three times with PBS for 5 minutes each at 4°C. Cells were permeabilized in 0.5% Triton X-100 at 4°C for 5 min and blocked using 4% horse serum and 0.25% Triton X-100 for 1 h at 4°C. Overnight incubation in primary antibody solution was performed at 4°C to probe for full-length Kir7.1 using a Kir7.1 C-12 mouse monoclonal antibody (1:200) (sc-398810, Santa Cruz Biotechnology, Santa Cruz, CA). Cells were washed twice with PBS, for 5 min each at 4°C, before incubation with the secondary antibody, donkey anti-mouse AlexaFluor-594 (1:500) (AB_#, Invitrogen) at room temperature for 1 h. The coverslips were washed twice with PBS containing 0.05% Tween-20 at room temperature, followed by incubation with DAPI (1:500) at room temperature for 20 min. HEK293 UT cells were used as negative controls. The coverslips were mounted on microscope slides and imaged using a Nikon-C2 confocal microscope. Detection was performed using wavelengths of 488 nm for GFP, 568 nm for primary antibody-tagged Kir7.1, and 405 nm for DAPI. NIS Elements (Nikon, Melville, NY, USA) software was used for image analysis.

Co-transfection of WT and mutant Kir7.1

HEK293 cells were transfected using PolyJetTM (Signa Gen, SL100688) for co-transfection in a 1:1 ratio of the following plasmids: WT (1 µg) + R166X (1 µg), or WT (1 µg) + W53X (1 µg), or WT (1 µg) + dummy plasmid (1 µg), or R166X (1 µg) + dummy plasmid, or W53X (1 µg) + dummy plasmid. The R166X and W53X plasmids were each GFP tagged, and the WT plasmid was RFP tagged for fluorescent visualization. For 24 hours, cells were maintained in medium (DMEM, 10% FBS, 1% Penstrep, 1% Anti-anti). Cells were then split using DPBS and Accutase and plated on poly-d-lysine-coated 35mm imaging dishes (MATTEK, P35GC-1.0-14-C) with a diameter of 14 mm. Twenty-four hours after plating, the cells were used for imaging.

Live-cell Imaging

Z-stacks of co-transfected cell fluorescence were imaged using Andor iQ 3.6.5 software on a Nikon Eclipse Ti microscope, an iXon x3 897 EM-CCD camera, and the Andor Revolution XD spinning disk confocal microscopy system (Andor, Belfast, Northern Ireland) under a 60X objective. Cells were maintained in extracellular HEPES-buffered Ringer's solution (HR) (135 mM NaCl, 1 mM $MgCl_2$, 10 mM HEPES, 1.8 mM $CaCl_2$, 10 mM glucose, and 5 mM KCl; pH: 7.4; osmolarity: 300 mOsm) during imaging studies. Images were analyzed using ImageJ (Fiji, 1.54p) software, and Pearson's coefficient was calculated by comparing red and green fluorescence using the BIOP JaCoP Plugin in ImageJ.

Next-generation Sequencing

Off-target analysis using deep sequencing with next-generation sequencing (NGS) was performed on all genome-edited samples. The cells were washed with PBS and collected using Accutase. Genomic DNA (gDNA) (Zymo Research, D4069) was isolated, samples were quantified using Nanodrop 200 (Thermo Fisher Scientific), and RT was performed to generate complementary DNA (cDNA) (Thermo Fisher Scientific, 4368814). Sample off-target analysis was performed using *KCNJ13* Illumina-specific primers **(Supplementary Table S3)**. Sequencing of the indexed libraries was performed using an Illumina MiniSeq instrument. The results were analyzed using an R-GEN Cas-Analyzer [108]. NGS was performed using NovaSeq 6000 (Illumina).

Single-Cell Patch Clamp

Functional impact of 3XCCT ACE-$tRNA^{Arg.UGA}$ of the R166X mutation was investigated at the single-cell level using whole-cell patch-clamp recordings. Co-transfection with R166X and a dummy plasmid or a WT plasmid and a dummy plasmid was used as negative and positive controls, respectively. Extracellular HEPES-buffered Ringer's solution (HR) consisted of (in mM) 135 NaCl, 1 $MgCl_2$, 10 HEPES, 1.8 $CaCl_2$, 10 glucose, and 5 KCl. The pH was adjusted to 7.4 using NaOH, and the osmolality was confirmed to be

300 mOsm. The pipette solution (H1L) contained (in mM): 30 KCl, 83 K-gluconate, 5.5 EGTA-KOH, 0.5 $CaCl_2$, 4 $MgCl_2$, 10 HEPES, and 4 ATP. The pH was adjusted to 7.2 using KOH, and the osmolality was confirmed to be 280 mOsm. The Rb+ solution contained the same components as the HR solution, except that Na+ was replaced with 135 mM Rb+. The pH was adjusted to 7.4 using RbOH, and the osmolality was confirmed to be 300 mOsm. A ramp protocol, ranging from +50 to -150 mV, was used for the voltage-clamp recordings from a holding potential of 0 mV. Similarly, channel currents were recorded using a protocol that ranged from +50 to -150 mV in 50 mV increments from a 0 mV holding potential for over 300 milliseconds. The pipette resistances ranged from 3 to 5 MΩ, and the seals were maintained under GΩ conditions. Data acquisition was conducted using an Axopatch 200 B, Digidata 1550, and Clampex 11. Data were analyzed using Clampfit 11.2 (Molecular Devices, CA).

Statistical Analysis

A two-tailed Student's t-test was performed using Microsoft Excel for the statistical analysis. Differences were considered statistically significant at $p < 0.05$; the results are expressed as mean ±SEM.

Acknowledgements:

David R. Liu gifted our lab base editor mRNAs (BE4 and eVDCN).

Schematic images were created with Biorender.com.

UW Biotechnology Center Core Acknowledgement:

The author(s) utilized the University of Wisconsin–Madison Biotechnology Center's DNA Sequencing Facility (Research Resource Identifier – RRID:SCR_017759) for Sanger and next-generation sequencing.

UW Flow Cytometry Core Acknowledgements:

The authors utilized the University of Wisconsin Carbone Cancer Center (Support Grant P30 CA014520) for flow cytometry results.

Grant Acknowledgement

This study was supported by a grant (R24EY032434) from the National Institute of Health. Additionally, it was partially funded by a core grant from the National Institute of Child Health and Human Development (P50HD105353) to the Waisman Center, USA. The research was also supported by the University of Wisconsin– Partnership Education and Research Committee funds and the Harrington Discovery Institute's Gund-Harrington Scholar award (to KS) and unrestricted funding from Research to Prevent Blindness. We acknowledge the Retina Research Foundation's Kathryn and Latimer Murfee Chair (to KS), the M.D. Matthews Research Professorship and Daniel Albert Chair (to BRP), the Retina Research Foundation Emmett A. Humble Distinguished Directorship (to DMG), and the McPherson ERI Sandra Lemke Trout Chair in Eye Research (DMG).

FIGURES AND TABLES

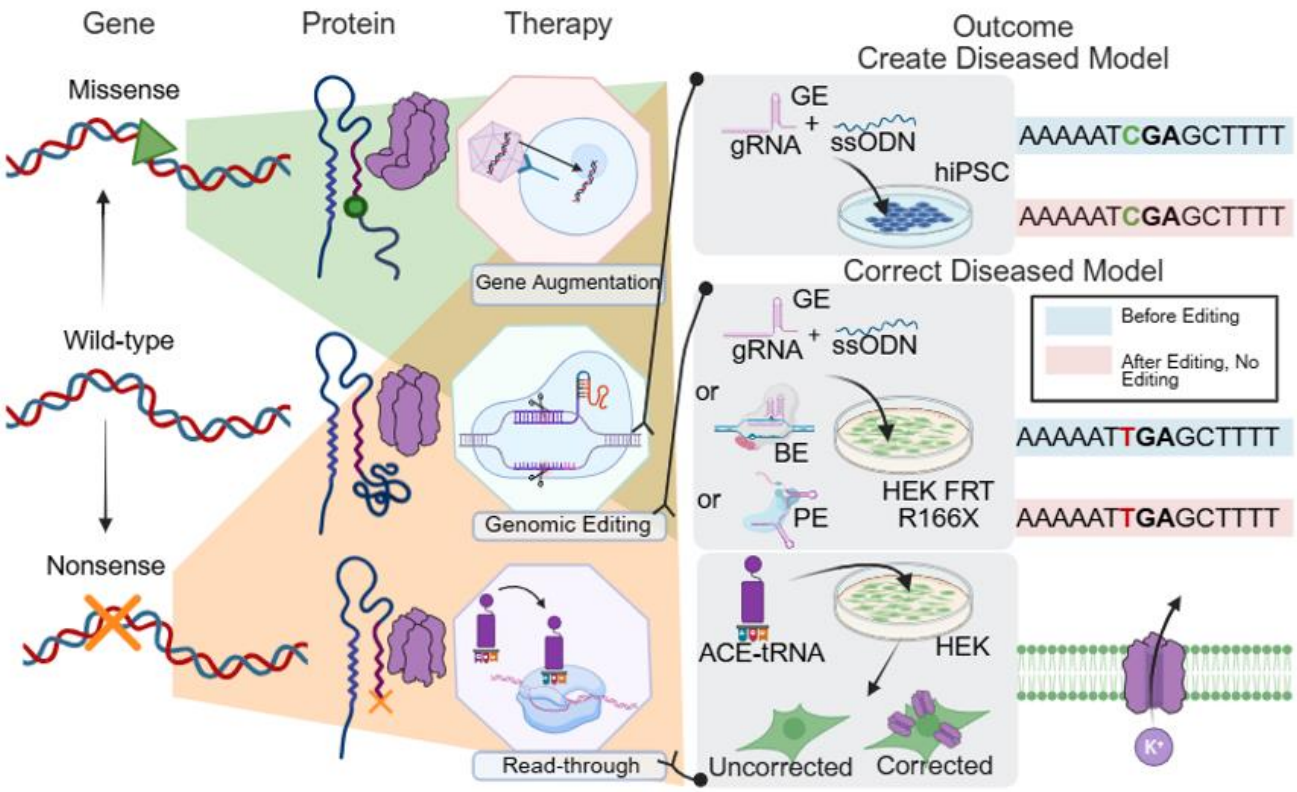

Summary Figure: Therapeutic options for nonsense mutations, which lead to a premature stop codon and non-functional, truncated protein product, include gene augmentation, genomic editing, and readthrough therapies. Options for missense mutations that can lead to a full-length product containing an incorrect amino acid at the mutation site, only include gene augmentation and genomic editing. Therefore, nonsense mutations as a model provide a broader opportunity to compare the success of therapeutics. In our study we were not able to successfully create a nonsense mutation, R166X, expressing a hiPSC cell line through genomic editing, GE techniques, thus there was no insertion of a nonsense mutation in our WT sequence. R166X expressing cells were also difficult to edit using genomic editing techniques, including GE, BE, and PE, leading to no correction of the mutant sequence. In contrast, treatment using an ACE-tRNA$^{Arg.UGA}$ on HEK cells containing an R166X ORF was able to suppress the mutation and lead to a functional WT protein product expressed on the membrane. The cell population after treatment

resulted in a mixed cell population with some cells containing corrected channels and others not. Therefore, we demonstrated that ACE-tRNA can be a therapeutic option for mutations that are challenging to target using genomic editing techniques.

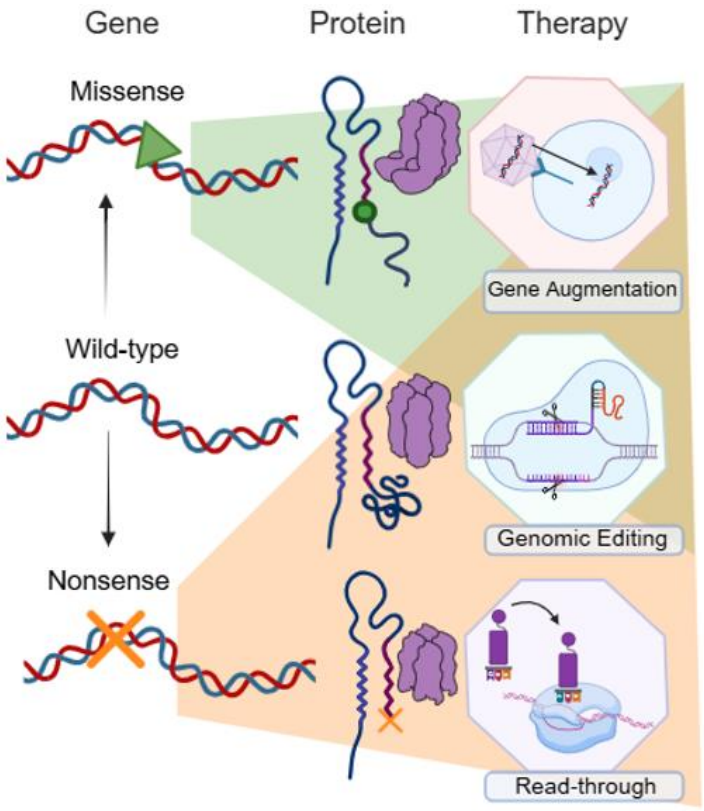

Figure 1: Therapeutic options for point mutations. Both gene augmentation and genome editing are therapeutic options for missense mutations. Nonsense mutation can be additionally treated via translational readthrough.

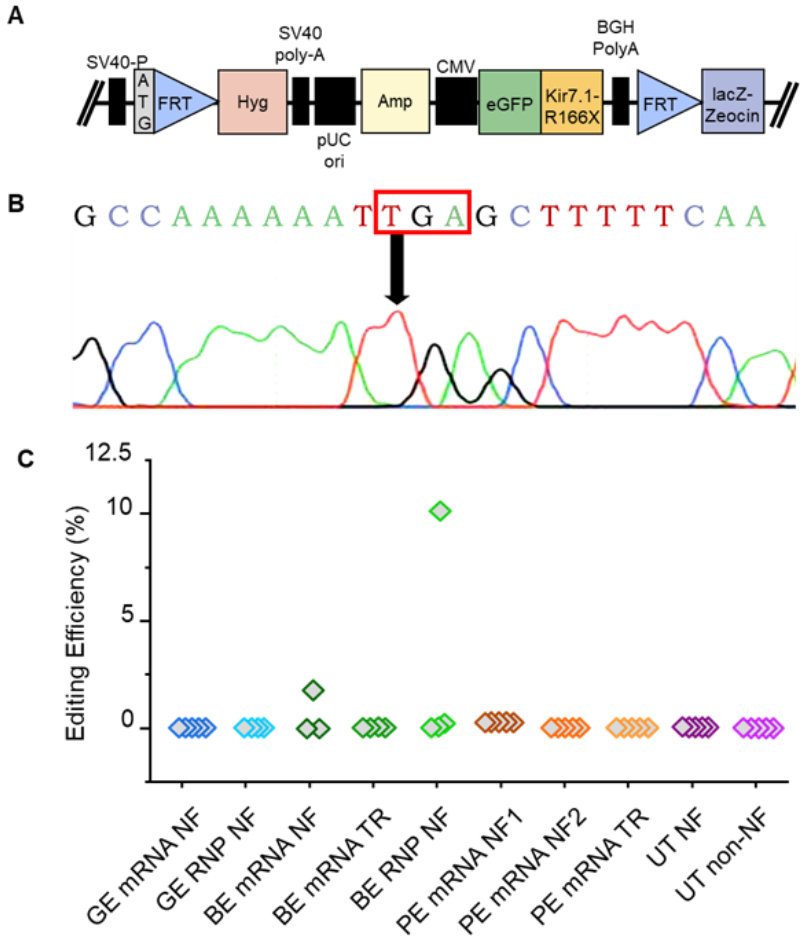

Figure 2: Genome editing of the *KCNJ13* R166X locus. (A) Illustration of the construct design used to generate HEK293 FRT cells with stable expression of the R166X mutation. **(B)** Sanger sequencing results of the HEK FRT R166X stable cell line, showing the mutant TGA codon (highlighted in red). **(C)** Percentage of editing outcomes across different genomic editing methods. GE - genome editing; BE - base editing; PE - prime editing; NF - nucleofection; TR - transfection; UT - untreated.

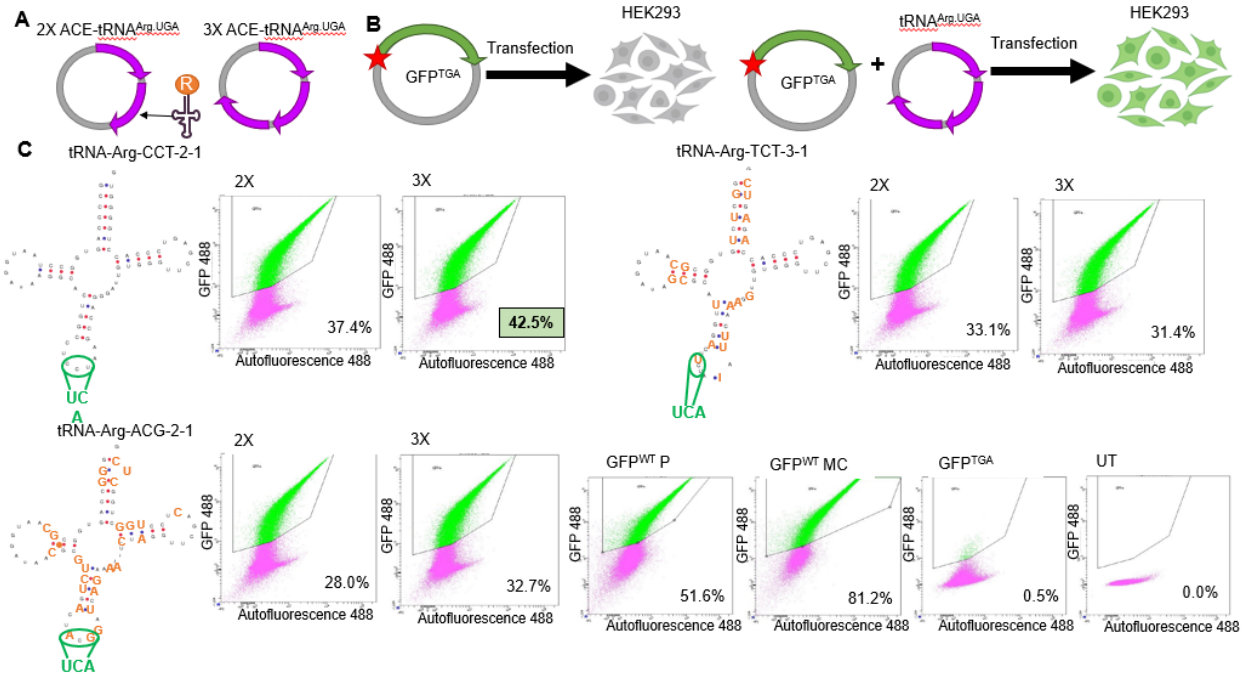

Figure 3: Strongest suppression of UGA premature codon by 3XCCT ACE-tRNA$^{Arg.UGA}$. (A) Minicircles contained either 2X or 3X copies of the ACE-tRNA. A single copy of the tRNA sequence is illustrated as a purple arrow. **(B)** Representation of UGA PTC suppression of GFP GFP^{TGA} plasmid co-transfected with an ACE-tRNA$^{Arg.UGA}$ minicircle in HEK293 cells. **(C)** Modified nucleotide sequence between CCT-2-1, TCT-3-1, and ACG-2-1 tRNA-Arg isodecoders. The base alterations are highlighted in orange. The insertion site of the mutant TGA change within the anticodon region is indicated in green. Flow cytometry plots of HEK293 cells co-transfected with a GFP^{TGA} plasmid and one of six ACE-tRNA$^{Arg.UGA}$ isodecoders, GFP^{TGA} alone, a WT GFP plasmid (GFP^{WT} P) alone, a WT GFP minicircle (GFP^{WT} MC), or untreated (UT). The proportion of GFP-positive cells indicates that 3XCCT ACE-tRNA$^{Arg.UGA}$ was the most effective.

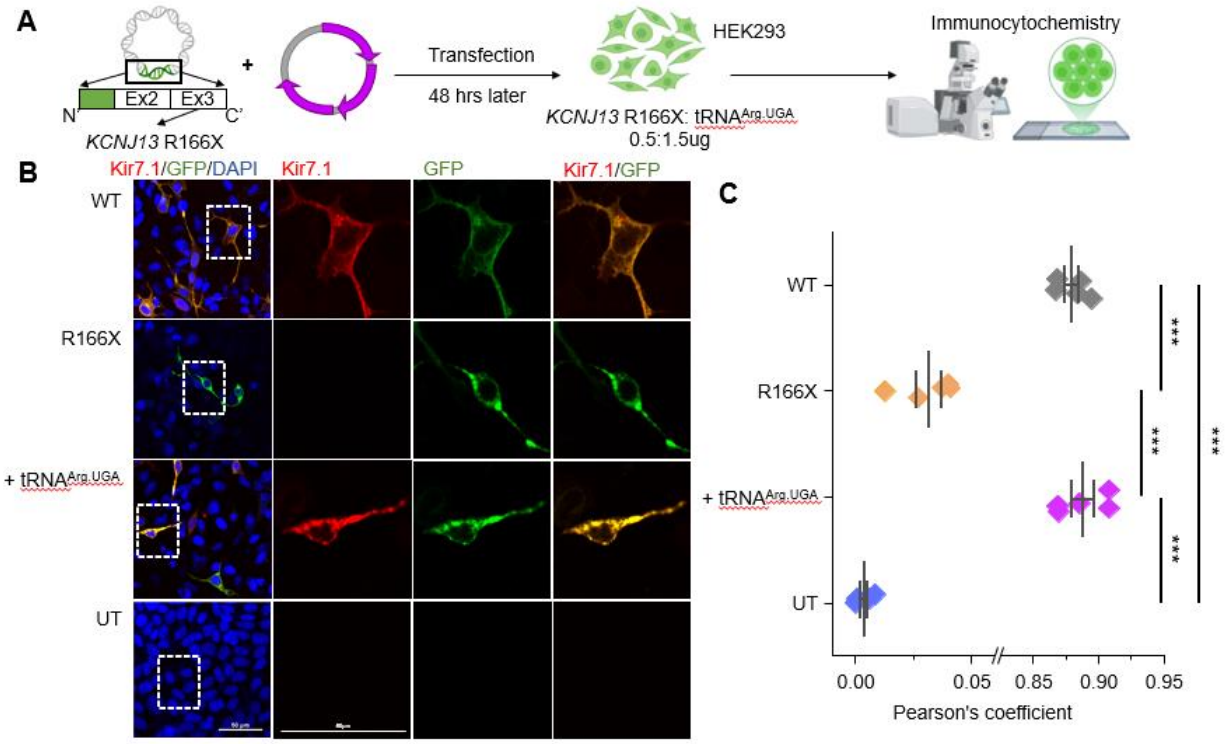

Figure 4: *KCNJ13* nonsense mutation R166X suppression leads to Kir7.1 protein expression. (A) Schematic of methods. The R166X mutation site is within exon 3 (Ex3) of the *KCNJ13* gene, as illustrated. Ex2: exon 2. **(B)** Immunocytochemistry (ICC) images of co-transfected HEK293 cells illustrate the expression of full-length C-terminal Kir7.1 protein (red) on the cell membrane in cells treated with R166X plasmid combined with 3XCCT ACE-tRNA$^{Arg.UGA}$ minicircle, or with *KCNJ13*-WT (WT) plasmid plus a control plasmid, in contrast to the absence of full-length Kir7.1 protein (red) expression in cells treated solely with R166X plasmid or UT. N-terminal GFP-tagged expression of WT or R166X protein is visualized in green. Scale bars measure 50 μm. **(C)** Pearson's correlation coefficients of ICC images. The entire set of images from the n = 5 technical repeats was analyzed using NIS-Elements AR software to determine the Pearson's correlation between the red and green channels. Statistical significance was assessed using a two-tailed Student's t-test, with ***P<0.001.

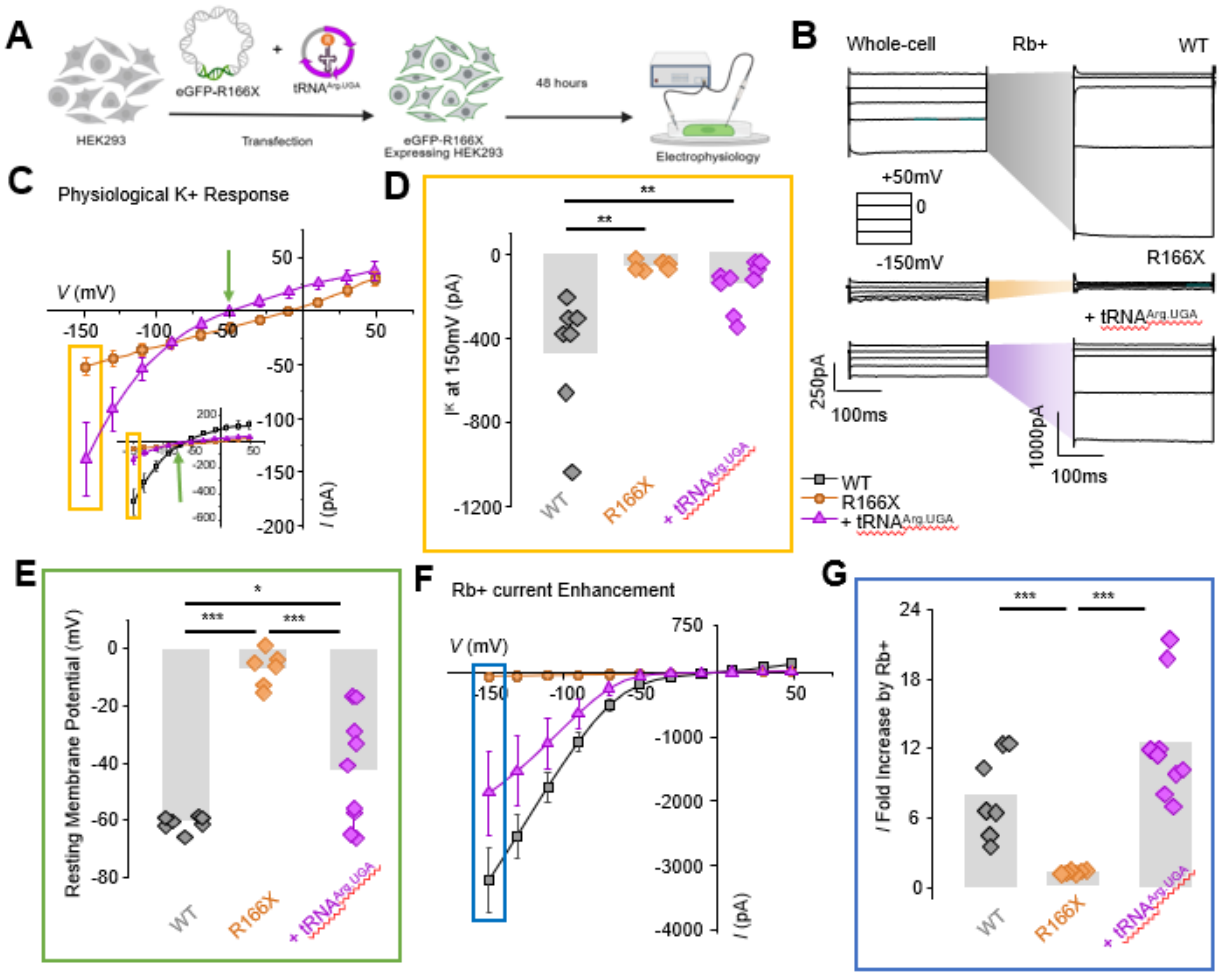

Figure 5: Rescue of Kir7.1 function following 3XCCT ACE-tRNA$^{Arg.UGA}$ minicircle treatment. (A) Schematic experimental design. **(B)** Current response to voltage steps +50 to -150 mV (inset) from a holding potential of 0 mV showing whole-cell or Rb+ ionic current steps in HEK293 cells expressing WT, R166X, or R166X+3XCCT ACE-tRNA$^{Arg.UGA}$. Scale bars are shown for the whole cell, measuring 250 pA vertically and 100 ms horizontally. Scale bars for Rb+ are 1000 pA vertically and 100 ms horizontally. **(C)** Current-voltage plot for K+ in HEK293 cells demonstrating rescued current in R166X+3XCCT ACE-tRNA$^{Arg.UGA}$ tRNA treated cells (purple triangles) compared to R166X alone (orange circles). Inset highlights WT (grey squares) compared to R166X+3XCCT ACE-tRNAArg.UGA tRNA (purple triangles) with expanded y-axis to demonstrate partial recovery following ACE-tRNA treatment. **(D)** Average K+ currents at -150 mV and **(E)** average resting membrane potentials shown for WT (grey quadrangles),

R166X (orange quadrangles), and R166X+3XCCT ACE-tRNA$^{Arg.UGA}$ (purple quadrangles) expressing cells. Data show average values ± SEM. Statistical significance measured by two-tailed Student's t-test and denoted as *$P<0.05$, **$P<0.01$, and ***$P<0.001$. n=9 for R166X+3XCCT ACE-tRNA$^{Arg.UGA}$, n=7 for WT, and n=6 for R166X. **(F)** Rb+ current in HEK293 cells demonstrating rescued current in R166X+3XCCT ACE-tRNA$^{Arg.UGA}$ tRNA treated (purple triangles). WT-treated cells are shown in grey squares, and R166X-treated cells are shown in orange circles. **(G)** Current (*I*) fold increase when treating cells with Rb+ is shown for WT (grey quadrangles), R166X (orange quadrangles), and R166X+3XCCT ACE-tRNA$^{Arg.UGA}$ (purple quadrangles) treated cells.

SUPPLEMENTARY FIGURES AND TABLES

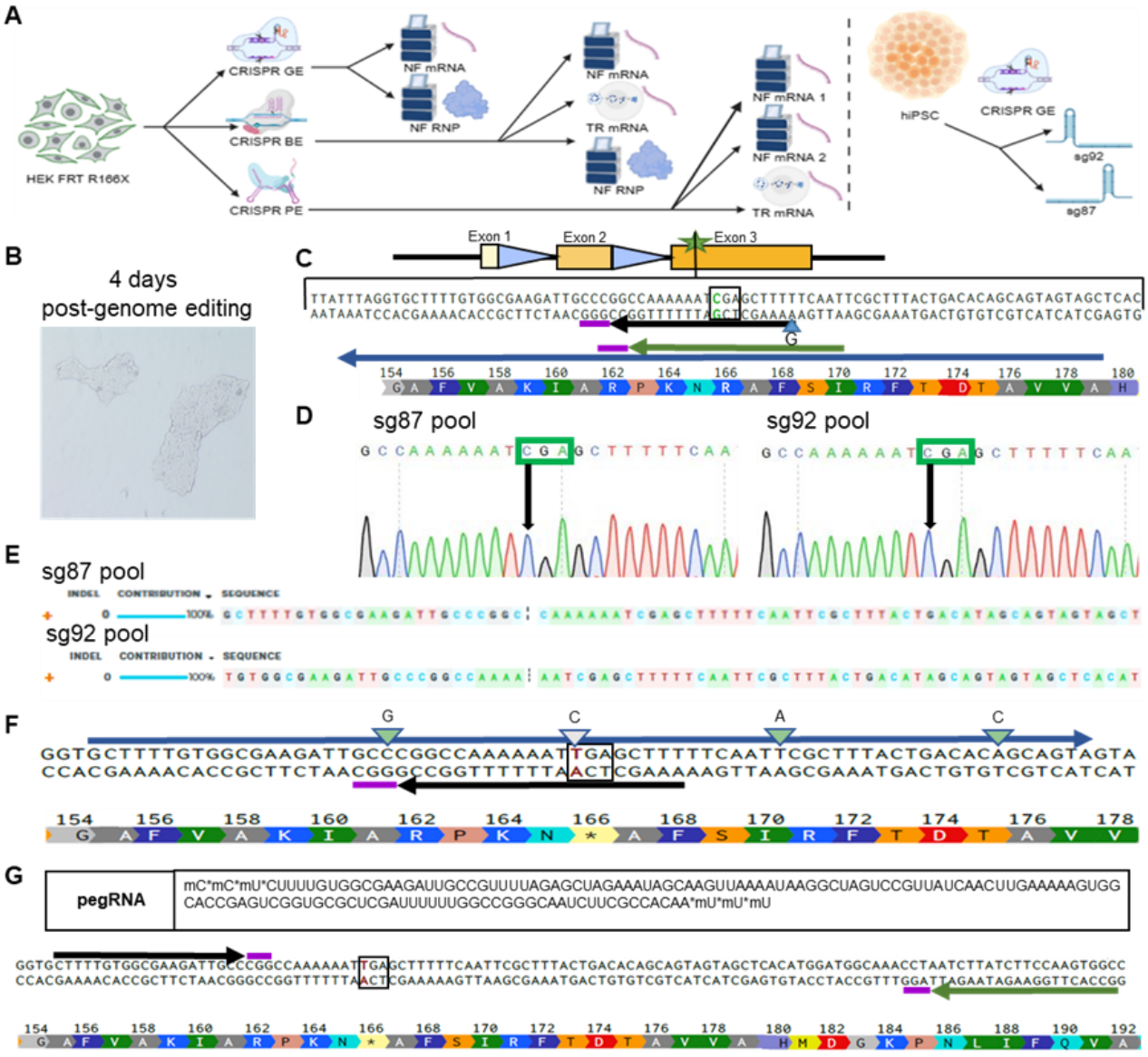

Supplementary Figure S1: Strategies for R166X locus genome editing. (A) Experimental design of genome editing techniques in HEK FRT R166X and hiPSC cells. **(B)** hiPSC cells appear healthy post-genome editing. **(C)** Schematic representation of CRISPR GE design. PAM sites are depicted in purple. A black arrow indicates guide RNA 87 (sg87). A green arrow indicates guide RNA 92 (sg92). A black box and green lettering emphasize the target site within the sequence. The ssODN sequence is depicted with

a blue arrow. **(D)** Sanger sequencing results of hiPSC-treated cells, using either guide RNA sg87 or sg92, demonstrating no editing following treatment, as evidenced by the presence of the WT CGA codon (highlighted in a green box). **(E)** Synthego ICE Analysis (https://ice.editco.bio/#/) results displaying the relative contribution of each sequence following editing with sg87 (top) and sg92 (bottom), indicating 0% insertions or deletions (indels) and 100% contribution of the WT sequence for either guide RNA. **(F)** Schematic representation of gene editing (GE) and base editing (BE) design. It should be noted that the ssODN was utilized solely for GE. The PAM site is shown in purple. A black arrow indicates the guide RNA. A black box and red lettering highlight the mutant site within the sequence. The ssODN sequence is shown with a blue arrow, with wobble bases denoted by green arrowheads and letter modifications. The ssODN sequence contains the WT (CGA) sequence, indicated by a grey arrowhead with a letter change from TGA to CGA. **(G)** Schematic illustration of prime editing (PE) design. The PAM site is depicted in purple. A black arrow represents the guide RNA. A black box and red letters indicate the mutant site in the sequence. A green arrow shows the prime editing nicking guide.

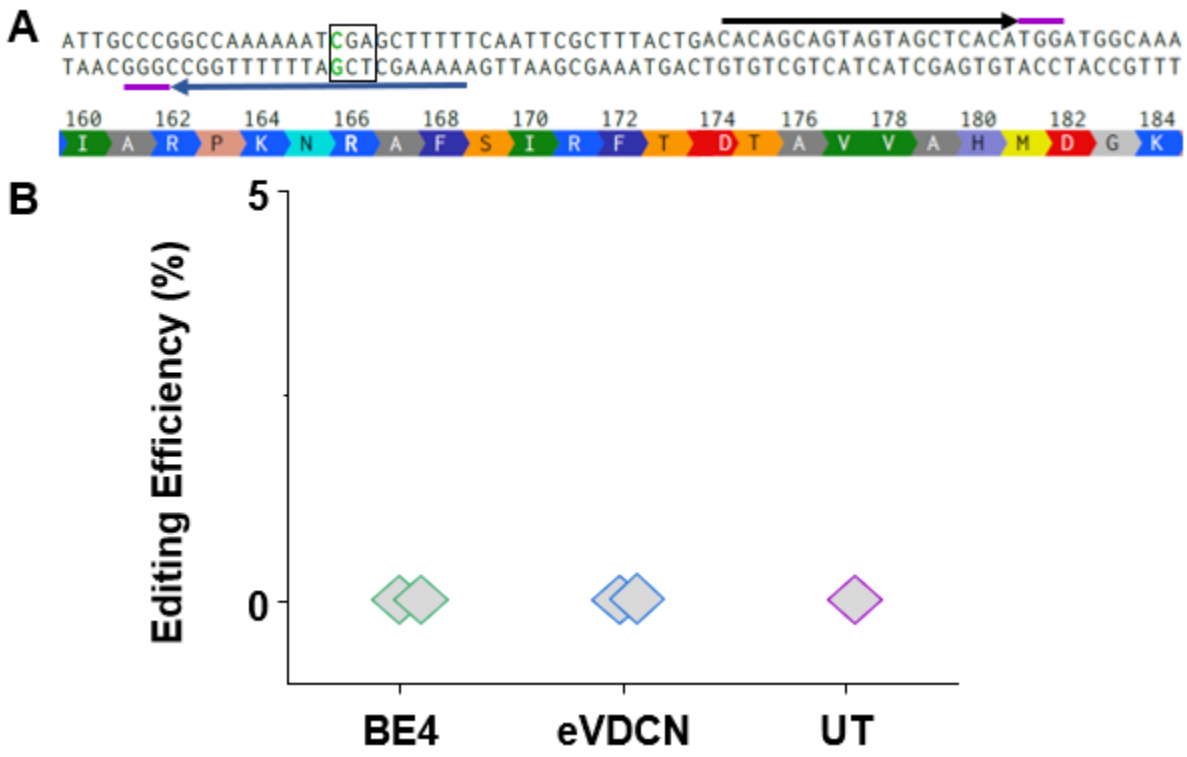

Supplementary Figure S2: Outcome of CRISPR editing on *KCNJ13* WT (WT) expressing patient-derived fibroblasts to create a R166X mutation. (A) Schematic representation of the BE design, with PAM sites indicated in purple. a black arrow marks sgRNA1, while a blue arrow denotes sgRNA2. The mutant site is emphasized with a black box and red letters within the sequence. **(B)** Illustrates the percentage of editing efficiencies for each treatment type, indicating the absence of editing activity with either base editor. Green and grey diamonds represent the BE4 base editor, whereas the eVDCN base editor is depicted with blue and grey diamonds. UT indicates untreated samples.

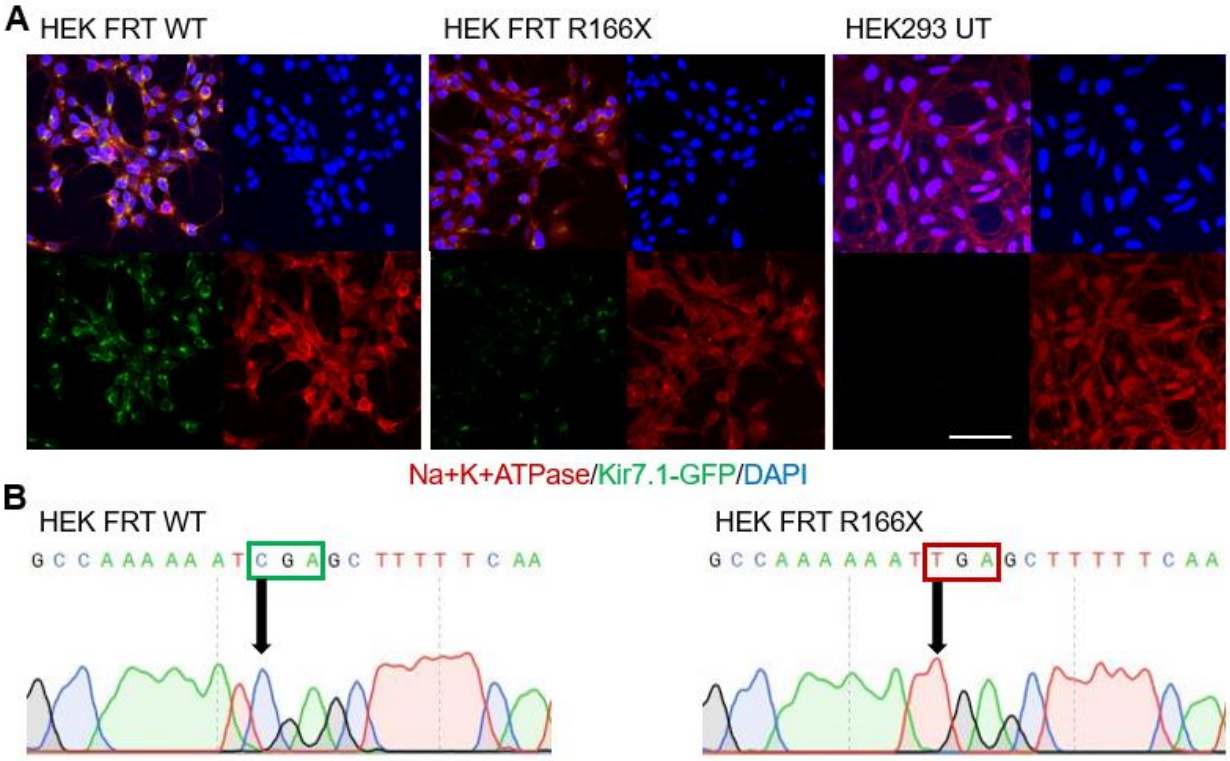

Supplementary Figure S3: Creation of stably expressing *KCNJ13* WT (WT) and R166X mutant cell lines. (A) A comparison was made between the established stable cell lines, HEK FRT R166X and HEK FRT WT, and HEK293 UT cells, utilizing immunocytochemistry (ICC). The Kir7.1 protein is tagged with GFP in the stable cell lines. Na+K+ATPase serves as a membrane marker. GFP expression is localized on the membrane in HEK FRT WT stable cells, on both the membrane and within the cytoplasm in HEK FRT R166X stable cells, and is absent in HEK293 UT cells. Scale bars represent 50 μm. **(B)** Sanger sequencing results confirm that the stable cell lines contain either WT (CGA) or R166X mutant (TGA) genomic DNA sequences. UT = untreated.

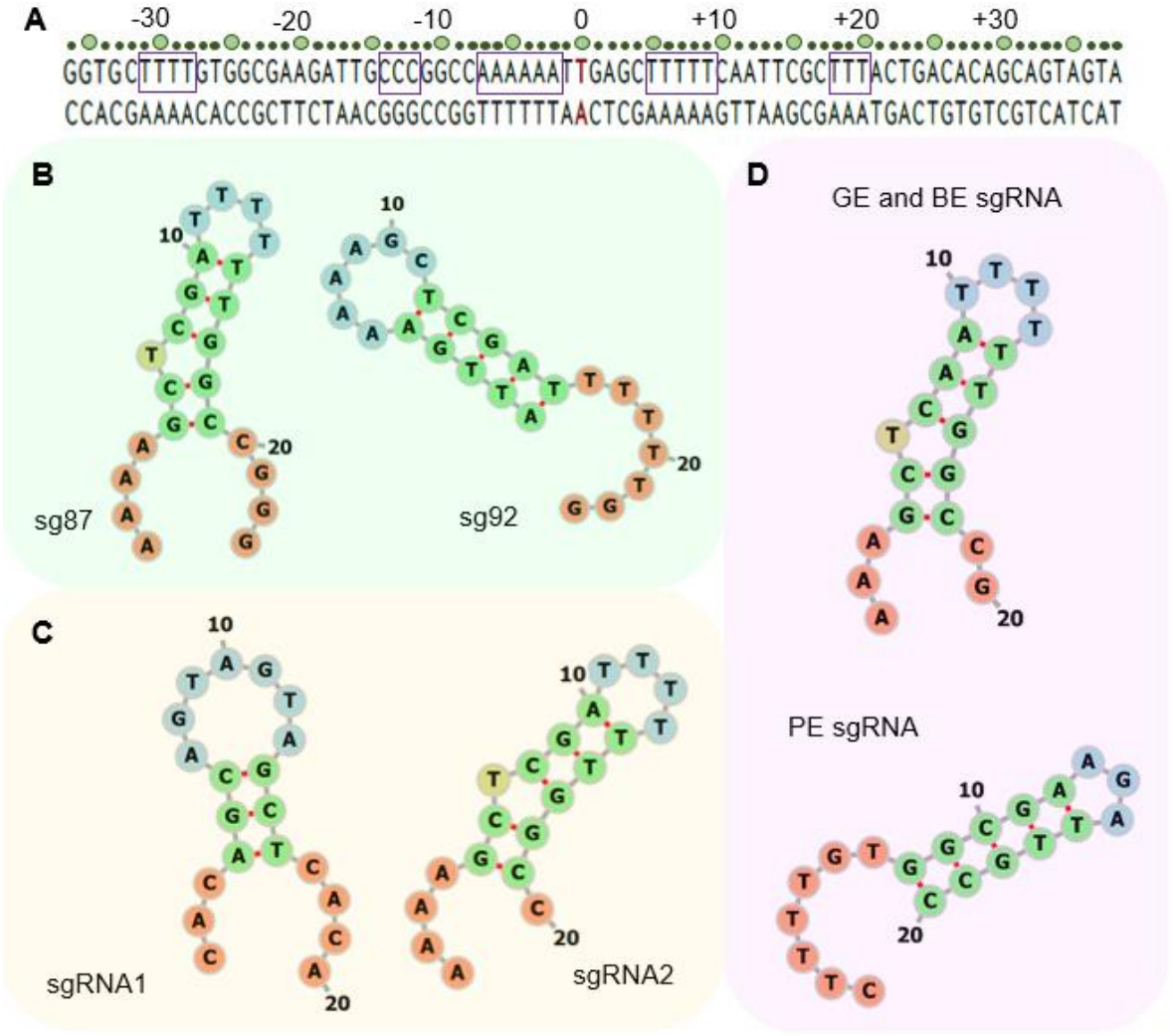

Supplementary Figure S4: Computational models of hairpin structures from gRNAs for genomic editing techniques. (A) The mutation site of R166X, with the mutant nucleotide base change highlighted in red, is detailed. Green circles indicate the number of bases from the mutated site. Base repeats of three or more are enclosed within purple boxes. These repeats are located at specific positions in the 3' to 5' target strand relative to the mutation site: thymine (T) repeats at positions +5 to +9, +18 to +20, and -28 to -31; adenosine (A) repeats at positions -2 to -7; and cytosine (C) repeats at positions -12 to -14. **(B)** Depicts a hairpin structure hypothesized to form in the sgRNAs employed in the CRISPR technique for introducing the R166X mutation into hiPSC cells. **(C)** Illustrates the potential hairpin structure formed by

the sgRNAs used for CRISPR editing to generate the R166X mutation in patient-derived WT fibroblast cells. (**D**) Shows the expected hairpin structure that may form in the sgRNAs utilized in CRISPR genomic editing techniques aimed at correcting the R166X mutation in cells with stable expression. All computational models of hairpin structures were generated using the Forna visualization tool (http://rna.tbi.univie.ac.at/forna/).

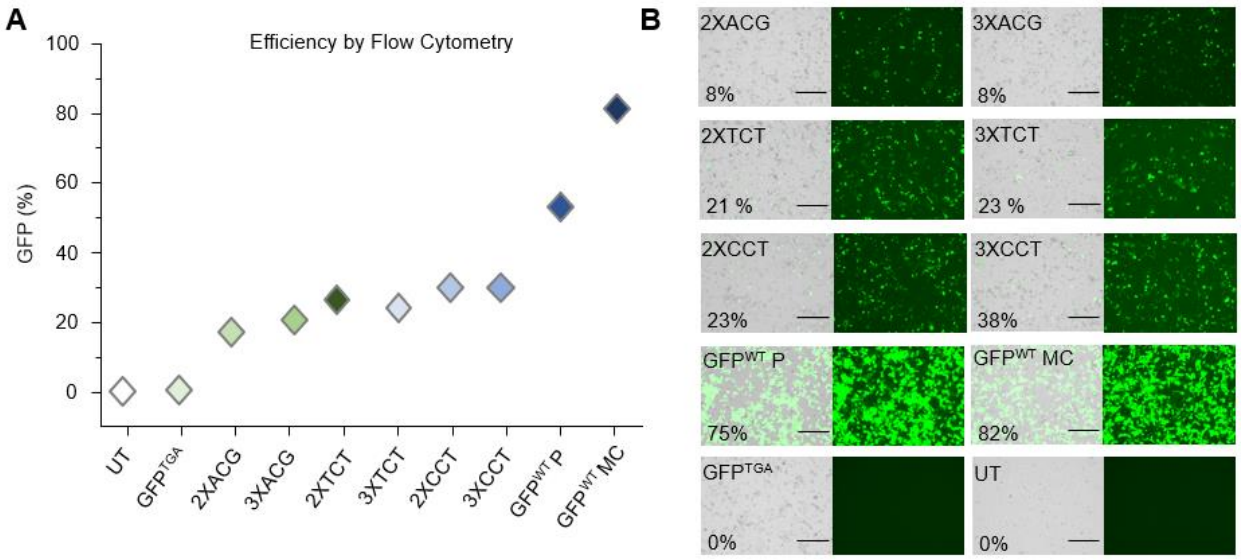

Supplementary Figure S5: Strongest suppression of UGA PTC using 3XCCT ACE-tRNA$^{Arg.UGA}$ minicircle formulation. (A) The graphical representation of the mean values derived from two flow cytometry experiments illustrates that the highest number of cells exhibiting fluorescence (Percent GFP) are those treated with the 2XCCT and 3XCCT formulations. We proceeded with the 3XCCT ACE-tRNAArg.UGA, as it contains an additional copy of the tRNA sequence, thereby increasing the availability of tRNA for suppression. **(B)** Fluorescent microscopy images display GFP fluorescence in HEK293 cells 48 hours post-co-transfection with a GFPTGA plasmid and one of six different formulations of ACE-tRNAArg.UGA, GFPTGA alone, or untreated. Scale bars = 300 µm. P = plasmid; MC = minicircle; UT = untreated.

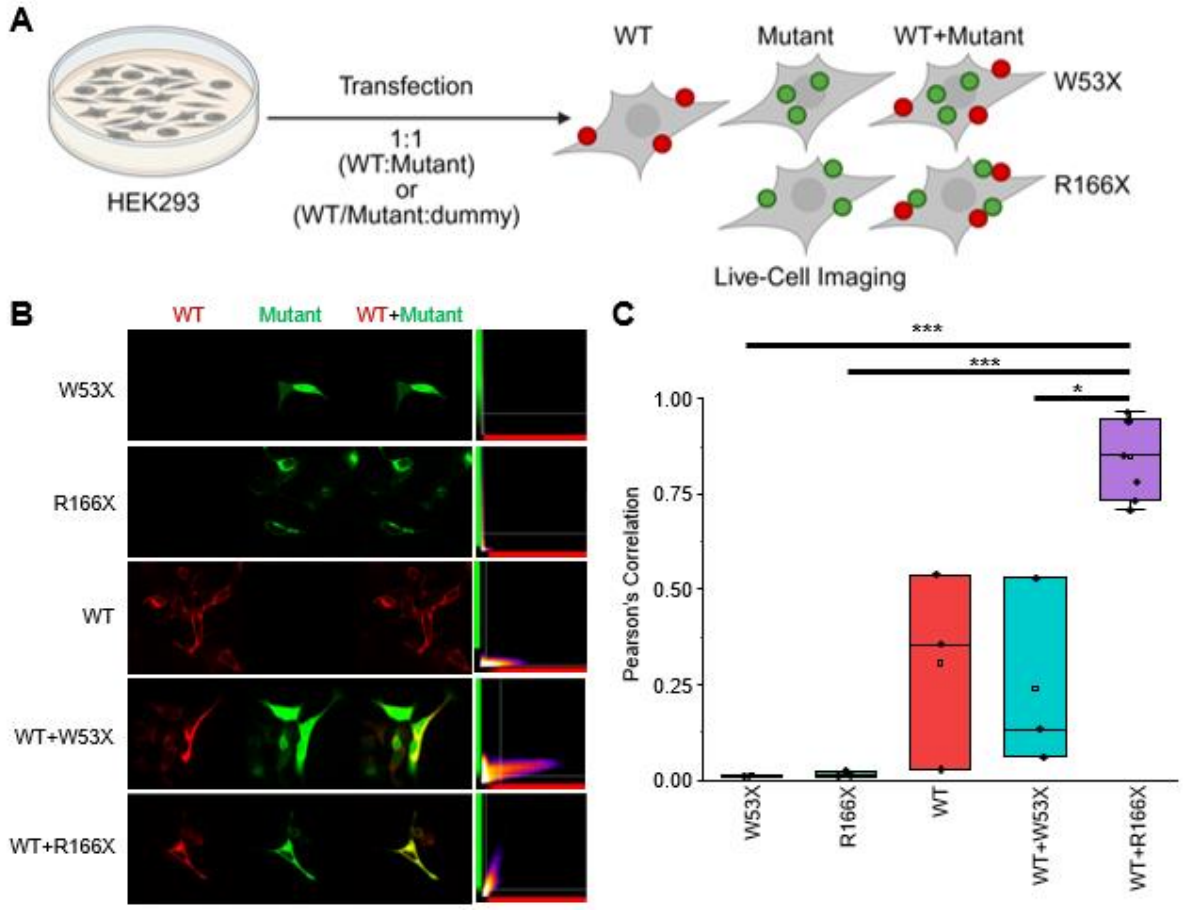

Supplementary Figure S6: Co-localization of R166X and WT protein in HEK293 cells. (A) Schematic of experimental design and expected results. HEK293 cells were transfected in a 1:1 ratio with either RFP-WT:GFP-Mutant or RFP-WT:dummy plasmid or GFP-Mutant:dummy plasmid. Expected results are that WT, R166X, and WT+R166X will be expressed on the membrane. Additionally, W53X will remain in the cytoplasm. Therefore, we expected that co-localization of WT (red) and mutant (green) would be high in WT+R166X and low in all other treatments. **(B)** Confocal Images of WT (red), mutant (green), and WT + mutant (yellow) cells. Pearson's correlation was performed using the BIOP JACoP plugin in Fiji analysis software by comparing the correlation between the red and green channels. Heat map from Pearson's correlation analysis is shown on the right. **(C)** Box and whisker plot of Pearson's correlation values using the BIOP JACoP plugin for cells treated with W53X alone (orange; n=2), R166X alone (green; n=3), WT alone (red; n=3), WT+W53X (teal; n=3), or WT+R166X (purple; n=7). Average values for each are as

follows: 0.012 for W53X, 0.016 for R166X, 0.308 for WT, 0.242 for WT+W53X, and 0.846 for WT+R166X. SEM values are: 0.001 for W53X, 0.004 for R166X, 0.149 for WT, 0.146 for WT+W53X, and 0.041 for WT+R166X. Statistical significance measured by two-tailed Student's t-test and denoted as *$P<0.05$, **$P<0.01$, and ***$P<0.001$. P-values for each sample compared to WT+R166X are: 8.533x10E-7 for W53X, 7.565x10E-7 for R166X, 0.0595 for WT, and 0.045 for WT+W53X. All other P-values between compared values were not significant.

Primer Name	5'-3' Sequence	GC%
FWD Primer	TCTGGCTGTAGCCAAGTTGC	50
RVS Primer 1	TGGAGCAGAGTAGCCAGAGG	60
RVS Primer 2	ATTCACCTTTGGAACCTCGG	50

Supplementary Table S1: Sanger sequencing primers for insertion of the R166X mutation in hiPSC. Primers used for detecting the insertion of the R166X mutation in hiPSC cells were custom-designed and obtained from Synthego (https://www.synthego.com). FWD: forward primer; RVS: reverse primer.

Primer Name	5’-3’ Sequence	GC %
In-fusion FWD	TCACTATAGGGAGACCCAAGCTGGCTAGCGTTTAAACTTA	50
In-fusion REV	AGTCGAGGCTGATCAGCGGGTTTAAACGGGCCCTCTAGAC	50
GFP FWD	CAAGTCCGGACTCAGATCTCGAGCTC	57
Kir7.1 RVS	TTATTCTGTCAGTCCTGTTT	72

Supplementary Table S2: In-fusion *KCNJ13* cloning in FLP-In expression vector and Sanger sequencing primers. The Gibson assembly primer design tool (https://tools.sgidna.com/gibson-assembly-primers.html) was employed for primer design. Primers were procured from IDT (https://www.idtdna.com). The annealing sequences for in-fusion primers are as follows: FWD: 5’-ATGGTGAGCAAGGGCGAGGA-3’; RVS: 5’-TTATTCTGTCAGTCCTGTTT-3’. The NCBI Primer-BLAST tool (https://www.ncbi.nlm.nih.gov/tools/primer-blast/) was used to design Sanger sequencing primers, specifically GFP FWD and Kir7.1 RVS. FWD denotes the forward primer; RVS signifies the reverse primer.

Primer Name	5'-3' Sequence	GC %
R166X NGS FWD	GTGCAATCGCCTTACTTGCC	55
R166X NGS RVS	TGCCATCCATGTGAGCTACT	50

Supplementary Table S3: Primers for amplifying h*KCNJ13* at the R166X location for off-target analysis. The NCBI Primer-BLAST tool (https://www.ncbi.nlm.nih.gov/tools/primer-blast/) was used for primer design. The primers were procured from IDT (https://www.idtdna.com) and included adaptor sequences suitable for the Illumina NGS platform. The adaptor sequence for the forward primer (FP) is: 5'-ACACTCTTTCCCTACACGACGCTCTTCCGATCT-3'. The adaptor sequence for the reverse primer (RP) is: 5'-GTGACTGGAGTTCAGACGTGTGCTCTTCCGATCT-3'. The abbreviations NGS, FWD, and RVS denote next-generation sequencing, forward primer, and reverse primer, respectively.

REFERENCES

1. *Online Mendelian Inheritance in Man, OMIM*. 2025 April 4, 2025 [cited 2025 April 7]; Available from: https://www.omim.org/statistics/geneMap.
2. Stenson, P.D., et al., *Human Gene Mutation Database (HGMD): 2003 update.* Hum Mutat, 2003. **21**(6): p. 577-81.
3. Maquat, L.E., *The power of point mutations.* Nat Genet, 2001. **27**(1): p. 5-6.
4. Cartegni, L., S.L. Chew, and A.R. Krainer, *Listening to silence and understanding nonsense: exonic mutations that affect splicing.* Nat Rev Genet, 2002. **3**(4): p. 285-98.
5. Mort, M., et al., *A meta-analysis of nonsense mutations causing human genetic disease.* Hum Mutat, 2008. **29**(8): p. 1037-47.
6. Frischmeyer, P.A. and H.C. Dietz, *Nonsense-mediated mRNA decay in health and disease.* Hum Mol Genet, 1999. **8**(10): p. 1893-900.
7. Kuzmiak, H.A. and L.E. Maquat, *Applying nonsense-mediated mRNA decay research to the clinic: progress and challenges.* Trends Mol Med, 2006. **12**(7): p. 306-16.
8. Schulze, K.V., N.A. Hanchard, and M.F. Wangler, *Biases in arginine codon usage correlate with genetic disease risk.* Genet Med, 2020. **22**(8): p. 1407-1412.
9. Lindahl, T., *Instability and decay of the primary structure of DNA.* Nature, 1993. **362**(6422): p. 709-15.
10. Chan, P.P. and T.M. Lowe, *GtRNAdb: a database of transfer RNA genes detected in genomic sequence.* Nucleic Acids Res, 2009. **37**(Database issue): p. D93-7.
11. Chan, P.P. and T.M. Lowe, *GtRNAdb 2.0: an expanded database of transfer RNA genes identified in complete and draft genomes.* Nucleic Acids Res, 2016. **44**(D1): p. D184-9.
12. Yun, Y. and Y. Ha, *CRISPR/Cas9-Mediated Gene Correction to Understand ALS.* Int J Mol Sci, 2020. **21**(11).
13. Kabra, M., et al., *Nonviral base editing of KCNJ13 mutation preserves vision in a model of inherited retinal channelopathy.* J Clin Invest, 2023.

14. Pandey, V.K., et al., *Application of CRISPR/Cas9 Genome Editing in Genetic Disorders: A Systematic Review Up to Date.* J Genet Syndr Gene Ther, 2017. **8**(2): p. 1000321.

15. Dang, Y., et al., *Optimizing sgRNA structure to improve CRISPR-Cas9 knockout efficiency.* Genome Biol, 2015. **16**: p. 280.

16. Hasanzadeh, A., et al., *Smart Strategies for Precise Delivery of CRISPR/Cas9 in Genome Editing.* ACS Appl Bio Mater, 2022. **5**(2): p. 413-437.

17. Lino, C.A., et al., *Delivering CRISPR: a review of the challenges and approaches.* Drug Deliv, 2018. **25**(1): p. 1234-1257.

18. Pandey, V.K., et al., *Application of CRISPR/Cas9 genome editing in genetic disorders: a systematic review up to date.* J Genet Syndr Gene Ther, 2017. **8**(2): p. 1-10.

19. Kolanu, N.D., *CRISPR–Cas9 gene editing: curing genetic diseases by inherited epigenetic modifications.* Global Medical Genetics, 2024. **11**(01): p. 113-122.

20. Saber Sichani, A., et al., *A Review on Advanced CRISPR-Based Genome-Editing Tools: Base Editing and Prime Editing.* Mol Biotechnol, 2023. **65**(6): p. 849-860.

21. Li, Q., et al., *Applications of Genome Editing Technology in Animal Disease Modeling and Gene Therapy.* Comput Struct Biotechnol J, 2019. **17**: p. 689-698.

22. Anzalone, A.V., et al., *Search-and-replace genome editing without double-strand breaks or donor DNA.* Nature, 2019. **576**(7785): p. 149-157.

23. Guo, C., et al., *Off-target effects in CRISPR/Cas9 gene editing.* Front Bioeng Biotechnol, 2023. **11**: p. 1143157.

24. Finkel, R.S., *Readthrough strategies for suppression of nonsense mutations in Duchenne/ Becker muscular dystrophy: aminoglycosides and ataluren (PTC124).* J Child Neurol, 2010. **25**(9): p. 1158-64.

25. Keeling, K.M., et al., *Therapeutics based on stop codon readthrough.* Annu Rev Genomics Hum Genet, 2014. **15**: p. 371-94.

26. Roy, B., et al., *Ataluren stimulates ribosomal selection of near-cognate tRNAs to promote nonsense suppression.* Proc Natl Acad Sci U S A, 2016. **113**(44): p. 12508-12513.

27. Michorowska, S., *Ataluren-Promising Therapeutic Premature Termination Codon Readthrough Frontrunner.* Pharmaceuticals (Basel), 2021. **14**(8).

28. Spelier, S., et al., *Readthrough compounds for nonsense mutations: bridging the translational gap.* Trends Mol Med, 2023. **29**(4): p. 297-314.

29. Laurent, G., et al., *Mechanism of aminoglycoside-induced lysosomal phospholipidosis: in vitro and in vivo studies with gentamicin and amikacin.* Biochem Pharmacol, 1982. **31**(23): p. 3861-70.

30. Kaloyanides, G.J., *Drug-phospholipid interactions: role in aminoglycoside nephrotoxicity.* Ren Fail, 1992. **14**(3): p. 351-7.

31. Coller, J. and Z. Ignatova, *tRNA therapeutics for genetic diseases.* Nat Rev Drug Discov, 2024. **23**(2): p. 108-125.

32. Ivanov, V., et al., *A mechanism for stop codon recognition by the ribosome: a bioinformatic approach.* RNA, 2001. **7**(12): p. 1683-92.

33. Rodin, A.S., E. Szathmary, and S.N. Rodin, *On origin of genetic code and tRNA before translation.* Biol Direct, 2011. **6**: p. 14.

34. Porter, J.J., C.S. Heil, and J.D. Lueck, *Therapeutic promise of engineered nonsense suppressor tRNAs.* Wiley Interdiscip Rev RNA, 2021. **12**(4): p. e1641.

35. Lueck, J.D., et al., *Engineered transfer RNAs for suppression of premature termination codons.* Nat Commun, 2019. **10**(1): p. 822.

36. Ko, W., et al., *Efficient suppression of endogenous CFTR nonsense mutations using anticodon-engineered transfer RNAs.* Mol Ther Nucleic Acids, 2022. **28**: p. 685-701.

37. Blomquist, V.G., et al., *Transfer RNA-mediated restoration of potassium current and electrical correction in premature termination long-QT syndrome hERG mutants.* Mol Ther Nucleic Acids, 2023. **34**: p. 102032.

38. Hibino, H., et al., *Inwardly rectifying potassium channels: their structure, function, and physiological roles.* Physiol Rev, 2010. **90**(1): p. 291-366.

39. McCloskey, C., et al., *The inwardly rectifying K+ channel KIR7.1 controls uterine excitability throughout pregnancy.* EMBO Mol Med, 2014. **6**(9): p. 1161-74.

40. Beverley, K.M. and B.R. Pattnaik, *Inward rectifier potassium (Kir) channels in the retina: living our vision.* Am J Physiol Cell Physiol, 2022. **323**(3): p. C772-C782.

41. Hernandez, C.C., et al., *The unique structural characteristics of the Kir 7.1 inward rectifier potassium channel: a novel player in energy homeostasis control.* Am J Physiol Cell Physiol, 2023. **324**(3): p. C694-C706.

42. Pessia, M., et al., *Subunit positional effects revealed by novel heteromeric inwardly rectifying K+ channels.* EMBO J, 1996. **15**(12): p. 2980-7.

43. Ishihara, K., T. Yamamoto, and Y. Kubo, *Heteromeric assembly of inward rectifier channel subunit Kir2.1 with Kir3.1 and with Kir3.4.* Biochem Biophys Res Commun, 2009. **380**(4): p. 832-7.

44. Nakamura, N., et al., *Inwardly rectifying K+ channel Kir7.1 is highly expressed in thyroid follicular cells, intestinal epithelial cells and choroid plexus epithelial cells: implication for a functional coupling with Na+,K+-ATPase.* Biochem J, 1999. **342 (Pt 2)**(Pt 2): p. 329-36.

45. Cornejo, I., et al., *Tissue Distribution of Kir7.1 Inwardly Rectifying K(+) Channel Probed in a Knock-in Mouse Expressing a Haemagglutinin-Tagged Protein.* Front Physiol, 2018. **9**: p. 428.

46. Pattnaik, B.R., et al., *A Novel KCNJ13 Nonsense Mutation and Loss of Kir7.1 Channel Function Causes Leber Congenital Amaurosis (LCA16).* Hum Mutat, 2015. **36**(7): p. 720-7.

47. Sergouniotis, P.I., et al., *Recessive mutations in KCNJ13, encoding an inwardly rectifying potassium channel subunit, cause leber congenital amaurosis.* Am J Hum Genet, 2011. **89**(1): p. 183-90.

48. Perez-Roustit, S., et al., *Leber Congenital Amaurosis with Large Retinal Pigment Clumps Caused by Compound Heterozygous Mutations in Kcnj13.* Retin Cases Brief Rep, 2017. **11**(3): p. 221-226.

49. Hejtmancik, J.F., et al., *Mutations in KCNJ13 cause autosomal-dominant snowflake vitreoretinal degeneration.* Am J Hum Genet, 2008. **82**(1): p. 174-80.

50. Anderson, E.J.P., et al., *Late onset obesity in mice with targeted deletion of potassium inward rectifier Kir7.1 from cells expressing the melanocortin-4 receptor.* J Neuroendocrinol, 2019. **31**(1): p. e12670.

51. Miraldi Utz, V., et al., *Gene therapy for RPE65-related retinal disease.* Ophthalmic Genet, 2018. **39**(6): p. 671-677.

52. Ford, J.L., et al., *Clinical Pharmacology Perspective on Development of Adeno-Associated Virus Vector-Based Retina Gene Therapy.* Clin Pharmacol Ther, 2024. **115**(6): p. 1212-1232.

53. Passier, R., V. Orlova, and C. Mummery, *Complex Tissue and Disease Modeling using hiPSCs.* Cell Stem Cell, 2016. **18**(3): p. 309-21.

54. Bassett, A.R., *Editing the genome of hiPSC with CRISPR/Cas9: disease models.* Mamm Genome, 2017. **28**(7-8): p. 348-364.

55. Okano, H. and S. Morimoto, *iPSC-based disease modeling and drug discovery in cardinal neurodegenerative disorders.* Cell Stem Cell, 2022. **29**(2): p. 189-208.

56. Rivetti di Val Cervo, P., et al., *hiPSCs for predictive modelling of neurodegenerative diseases: dreaming the possible.* Nat Rev Neurol, 2021. **17**(6): p. 381-392.

57. *Synthego Performance Analysis, ICE Analysis*. 2019; v3.0:[Available from: https://ice.editco.bio/#/.

58. Zhang, X., et al., *Homology-based repair induced by CRISPR-Cas nucleases in mammalian embryo genome editing.* Protein Cell, 2022. **13**(5): p. 316-335.

59. Lapinaite, A., et al., *DNA capture by a CRISPR-Cas9-guided adenine base editor.* Science, 2020. **369**(6503): p. 566-571.

60. Chow, R.D., et al., *A web tool for the design of prime-editing guide RNAs.* Nat Biomed Eng, 2021. **5**(2): p. 190-194.

61. Huang, M., et al., *Novel minicircle vector for gene therapy in murine myocardial infarction.* Circulation, 2009. **120**(11 Suppl): p. S230-7.

62. Jia, F., et al., *A nonviral minicircle vector for deriving human iPS cells.* Nat Methods, 2010. **7**(3): p. 197-9.

63. Florian, M., et al., *Gene engineered mesenchymal stem cells: greater transgene expression and efficacy with minicircle vs. plasmid DNA vectors in a mouse model of acute lung injury.* Stem Cell Res Ther, 2021. **12**(1): p. 184.

64. Chen, Z.Y., et al., *Minicircle DNA vectors devoid of bacterial DNA result in persistent and high-level transgene expression in vivo.* Mol Ther, 2003. **8**(3): p. 495-500.

65. Gracey Maniar, L.E., et al., *Minicircle DNA vectors achieve sustained expression reflected by active chromatin and transcriptional level.* Mol Ther, 2013. **21**(1): p. 131-8.

66. Kumar, M. and B.R. Pattnaik, *Focus on Kir7.1: physiology and channelopathy.* Channels (Austin), 2014. **8**(6): p. 488-95.

67. Derst, C., et al., *Cellular localization of the potassium channel Kir7.1 in guinea pig and human kidney.* Kidney Int, 2001. **59**(6): p. 2197-205.

68. Wright, P.D., et al., *A High-Throughput Electrophysiology Assay Identifies Inhibitors of the Inwardly Rectifying Potassium Channel Kir7.1.* J Biomol Screen, 2015. **20**(6): p. 739-47.

69. Steyer, B., et al., *Scarless Genome Editing of Human Pluripotent Stem Cells via Transient Puromycin Selection.* Stem Cell Reports, 2018. **10**(2): p. 642-654.

70. Cai, L., et al., *CRISPR-mediated genome editing and human diseases.* Genes Dis, 2016. **3**(4): p. 244-251.

71. Gerlach, M., et al., *Efficient Knock-in of a Point Mutation in Porcine Fibroblasts Using the CRISPR/Cas9-GMNN Fusion Gene.* Genes (Basel), 2018. **9**(6).

72. Schep, R., et al., *Chromatin context-dependent effects of epigenetic drugs on CRISPR-Cas9 editing.* Nucleic Acids Research, 2024. **52**(15): p. 8815-8832.

73. Goolab, S. and J. Scholefield, *Making gene editing accessible in resource limited environments: recommendations to guide a first-time user.* Frontiers in Genome Editing, 2024. **6**: p. 1464531.

74. Woodcock, C.L. and R.P. Ghosh, *Chromatin higher-order structure and dynamics.* Cold Spring Harbor perspectives in biology, 2010. **2**(5): p. a000596.

75. Valletta, S., et al., *ASXL1 mutation correction by CRISPR/Cas9 restores gene function in leukemia cells and increases survival in mouse xenografts.* Oncotarget, 2015. **6**(42): p. 44061-71.

76. Santos, L., et al., *Comparison of Cas9 and Cas12a CRISPR editing methods to correct the W1282X-CFTR mutation.* J Cyst Fibros, 2022. **21**(1): p. 181-187.

77. Afanasyeva, T.A.V., et al., *CRISPR-Cas9 correction of a nonsense mutation in LCA5 rescues lebercilin expression and localization in human retinal organoids.* Mol Ther Methods Clin Dev, 2023. **29**: p. 522-531.

78. Lee, C., et al., *CRISPR-Pass: Gene Rescue of Nonsense Mutations Using Adenine Base Editors.* Mol Ther, 2019. **27**(8): p. 1364-1371.

79. Jin, M., et al., *Correction of human nonsense mutation via adenine base editing for Duchenne muscular dystrophy treatment in mouse.* Mol Ther Nucleic Acids, 2024. **35**(2): p. 102165.

80. Siegner, S.M., et al., *PnB Designer: a web application to design prime and base editor guide RNAs for animals and plants.* BMC Bioinformatics, 2021. **22**(1): p. 101.

81. Doman, J.L., et al., *Designing and executing prime editing experiments in mammalian cells.* Nat Protoc, 2022. **17**(11): p. 2431-2468.

82. Liu, P., et al., *Improved prime editors enable pathogenic allele correction and cancer modelling in adult mice.* Nature communications, 2021. **12**(1): p. 2121.

83. Chung, C.C.Y., et al., *Rare disease emerging as a global public health priority.* Front Public Health, 2022. **10**: p. 1028545.

84. Gurkan, H. and N. Bilge Satkin, *The Importance of Genetic Diagnosis in Rare Diseases.* Balkan Med J, 2025. **42**(2): p. 92-93.

85. Bikard, D., et al., *Folded DNA in action: hairpin formation and biological functions in prokaryotes.* Microbiol Mol Biol Rev, 2010. **74**(4): p. 570-88.

86. Kerpedijiev, P., S. Hammer, and I. Hofacker, *Forna (force-directed RNA): Simple and effective online RNA secondary structure diagrams.* Bioinformatics, 2015. **31**(20): p. 3377-3379.

87. Rodin, A.S., E. Szathmáry, and S.N. Rodin, *On origin of genetic code and tRNA before translation.* Biology Direct, 2011. **6**: p. 1-24.

88. Haas, M., et al., *European Medicines Agency review of ataluren for the treatment of ambulant patients aged 5 years and older with Duchenne muscular dystrophy resulting from a nonsense mutation in the dystrophin gene.* Neuromuscular Disorders, 2015. **25**(1): p. 5-13.

89. Kerem, E., et al., *Ataluren for the treatment of nonsense-mutation cystic fibrosis: a randomised, double-blind, placebo-controlled phase 3 trial.* The Lancet Respiratory Medicine, 2014. **2**(7): p. 539-547.

90. Peabody Lever, J.E., et al., *Ataluren/ivacaftor combination therapy: Two N-of-1 trials in cystic fibrosis patients with nonsense mutations.* Pediatr Pulmonol, 2020. **55**(7): p. 1838-1842.

91. Woodley, D.T., et al., *Gentamicin induces functional type VII collagen in recessive dystrophic epidermolysis bullosa patients.* J Clin Invest, 2017. **127**(8): p. 3028-3038.

92. Leubitz, A., et al., *A randomized, double-blind, placebo-controlled, multiple dose escalation study to evaluate the safety and pharmacokinetics of ELX-02 in healthy subjects.* Clinical pharmacology in drug development, 2021. **10**(8): p. 859-869.

93. Harrell, L., U. Melcher, and J.F. Atkins, *Predominance of six different hexanucleotide recoding signals 3′ of readthrough stop codons.* Nucleic acids research, 2002. **30**(9): p. 2011-2017.

94. Brooks, D.A., V.J. Muller, and J.J. Hopwood, *Stop-codon readthrough for patients affected by a lysosomal storage disorder.* Trends in molecular medicine, 2006. **12**(8): p. 367-373.

95. Matalonga, L., et al., *Effect of readthrough treatment in fibroblasts of patients affected by lysosomal diseases caused by premature termination codons.* Neurotherapeutics, 2015. **12**(4): p. 874-886.

96. Schimmel, P., *The emerging complexity of the tRNA world: mammalian tRNAs beyond protein synthesis.* Nat Rev Mol Cell Biol, 2018. **19**(1): p. 45-58.

97. Geslain, R. and T. Pan, *Functional analysis of human tRNA isodecoders.* J Mol Biol, 2010. **396**(3): p. 821-31.

98. Ogle, J.M., et al., *Selection of tRNA by the ribosome requires a transition from an open to a closed form.* Cell, 2002. **111**(5): p. 721-32.

99. Lodmell, J.S., et al., *Conformational dynamics within the ribosome.* Translation Mechanisms. Kluwer Academic/Plenum Publishers, Georgetown, 2003: p. 264-279.

100. Ordog, B., et al., *Identification and functional characterisation of a novel KCNJ2 mutation, Val302del, causing Andersen-Tawil syndrome.* Can J Physiol Pharmacol, 2015. **93**(7): p. 569-75.

101. Major, L.L., et al., *Tandem termination signals: myth or reality?* FEBS Lett, 2002. **514**(1): p. 84-9.

102. Brown, C.M., et al., *The translational termination signal database.* Nucleic Acids Res, 1993. **21**(13): p. 3119-23.

103. Sachs, M.S., et al., *Toeprint analysis of the positioning of translation apparatus components at initiation and termination codons of fungal mRNAs.* Methods, 2002. **26**(2): p. 105-14.

104. Capowski, E.E., et al., *Reproducibility and staging of 3D human retinal organoids across multiple pluripotent stem cell lines.* Development, 2019. **146**(1).

105. Haeussler, M., et al., *Evaluation of off-target and on-target scoring algorithms and integration into the guide RNA selection tool CRISPOR.* Genome Biol, 2016. **17**(1): p. 148.

106. Hwang, G.H., et al., *Web-based design and analysis tools for CRISPR base editing.* BMC Bioinformatics, 2018. **19**(1): p. 542.

107. Richter, M.F., et al., *Author Correction: Phage-assisted evolution of an adenine base editor with improved Cas domain compatibility and activity.* Nat Biotechnol, 2020. **38**(7): p. 901.

108. Park, J., et al., *Cas-analyzer: an online tool for assessing genome editing results using NGS data.* Bioinformatics, 2017. **33**(2): p. 286-288.

Chapter 3: Co-localization of mutant R166X and WT-Kir7.1 protein on cell membranes

Allison Spillane[1,2], Pawan K. Shahi[1,2], Bikash R. Pattnaik[1,2,3]

[1]University of Wisconsin-Madison, Department of Pediatrics, Wisconsin, USA.
[2]University of Wisconsin-Madison, McPherson Eye Research Institute, Wisconsin, USA.
[3]University of Wisconsin-Madison, Department of Ophthalmology and Visual Sciences, Wisconsin, USA

SUMMARY

Mutations in the *KCN13* gene, which encodes the inwardly rectifying potassium channel Kir7.1, lead to loss of vision in human patients. Therefore, the optimization of therapies, such as ACE-tRNA, to treat mutations is necessary for the future development of clinical treatments. One mutation in *KCNJ13*, identified in patients, is R166X. In **Chapter 2,** we evaluated the efficacy of genomic editing and ACE-tRNA techniques in treating the R166X mutation. 3XCCT ACE-tRNA$^{Arg.\ UGA}$ treatment to R166X demonstrated successful expression of WT Kir7.1 on cell membranes and partial recovery of channel function. Interestingly, the mutant R166X protein was also expressed on the membranes of treated cells. Kir7.1 is a tetrameric channel; therefore, leading us to hypothesize that mutant and WT subunits could be co-assembling and hindering full functional recovery following 3XCCT ACE-tRNA$^{Arg.\ UGA}$ treatment. To further confirm this, we performed live-cell imaging on cells treated with GFP-tagged R166X and red fluorescent protein (RFP)-tagged WT plasmids. The W53X mutation to *KCNJ13* does not get trafficked to the membrane; therefore, GFP-tagged W53X and RFP-tagged WT-treated cells were used for comparison. Live-cell imaging results demonstrated co-expression of mutant R166X and WT protein on the cell membrane, which was not observed in W53X+WT-treated cells. Additionally, R166X+WT cells resulted in a high Pearson's coefficient value. In contrast, W53X+WT treatment resulted in a low Pearson's coefficient. These results suggest that the partial recovery observed following 3XCCT ACE-tRNA$^{Arg.\ UGA}$ treatment to R166X is due to the co-assembly of WT and R166X subunits to form a WT/R166X heterotetrameric Kir7.1 channel.

INTRODUCTION

Kir7.1 is an inwardly rectifying potassium channel encoded by the *KCNJ13* gene [1]. Mutations in the *KCNJ13* gene lead to LCA16 and SVD and are characterized by vision loss [2-5]. Eventual blindness occurs from the loss of RPE cell function due to Kir7.1 dysfunction [6]. The RPE cells are responsible for maintaining the health of the eye [7, 8]. Therefore, dysfunction and subsequent degradation of RPE cells, results in loss of the other retinal cells. The progression of this disease warrants the development of therapies that can overcome mutations, restore RPE function, and prevent further degradation of the retina.

One of these mutations is c.496C>T (p.Arg166Ter or R166X) [3]. This recessive mutation is characterized by a PTC, resulting in a truncated non-functional protein product. Several therapeutic options have been investigated for the treatment and suppression of PTCs. Genomic editing techniques such as GE, BE, and PE have demonstrated successful efficiency in correcting PTCs at the genomic level [9-11]. However, off-target editing effects and barriers to efficient delivery have prevented many genomic editing techniques from progressing to clinical trials [12-15]. Readthrough therapies target suppression of the mutation at the translational level and have demonstrated successful suppression of PTC mutations [16, 17]. However, translational readthrough therapy drugs result in inconsistent insertion of off-target amino acids, and some drugs have demonstrated toxicity [18-22]. Recently, another form of readthrough therapy, ACE-tRNA, was tested and found to be successful at suppressing PTCs [23-25]. The native tRNA, which contains the target amino acid, is engineered to recognize the PTC codon of the mutation and incorporate the correct amino acid [26]. Therefore, translation continues and results in the production of the correct full-length protein. This therapy targets PTC suppression at the translational level, and no off-target effects have been observed [23]. Demonstrating that future ACE-tRNA therapies should also suppress PTCs in different disease models, without resulting in off-target effects.

In **Chapter 2**, we wanted to compare the ability of genomic editing and ACE-tRNA to overcome the R166X mutation. We demonstrated that while genomic editing was not successful in overcoming the mutation, likely due to the presence of repeated base sequences at the mutation site, 3XCCT ACE-

$tRNA^{Arg.\ UGA}$ was able to suppress the mutation. 3XCCT ACE-$tRNA^{Arg.\ UGA}$ therapy resulted in the expression of WT protein on the membrane and partial recovery of channel function. Interestingly, we also observed that the R166X mutant protein is expressed on the membrane. This led us to hypothesize that the R166X and WT subunits may co-assemble on the membrane following treatment, thereby decreasing the effectiveness of the functional rescue.

Kir7.1 is a homotetrameric channel that does not co-assemble with other Kir channel subunits [27]. Therefore, the partial recovery demonstrated in **Chapter 2** may be due to co-assembling subunits of R166X and WT protein to create a mixed WT/R166X heterotetrameric protein. Variability in functional recovery could be due to varying levels of treatment to the cells or due to tetrameric channels consisting of various ratios of R166X to WT subunits.

We wanted to understand if R166X and WT subunits were co-assembling on the cell membrane. To test this, we performed live-cell imaging on cells treated with GFP-tagged R166X and RFP-tagged WT plasmids. Additionally, a study on the W53X mutation to *KCNJ13* demonstrated that the mutant protein gets stuck in the cytoplasm [28]. Therefore, cells were treated with GFP-tagged W53X and RFP-tagged WT plasmids for comparison. We hypothesized that we would observe R166X and WT subunits on the membrane and that analysis using Pearson's coefficient would demonstrate a high correlation between the two subunits. In contrast, a low Pearson's coefficient would be observed in W53X and WT channels due to W53X cytoplasmic and WT membrane expression.

RESULTS

R166X and WT-Kir7.1 protein display correlated membrane expression on HEK293 cells.

We wanted to elicit further if R166X and WT protein were co-expressing on the membrane and leading to partial recovery of Kir7.1 expression, following 3XCCT ACE-$tRNA^{Arg.\ UGA}$ treatment, as displayed in **Chapter 2**. HEK293 cells were co-transfected with a WT-Kir7.1 plasmid and a plasmid with a mutant form of Kir7.1 (W53X or R166X), at a 1:1 ratio **(Fig. 1A)**. *KCNJ13* mutations were GFP-tagged,

and WT-Kir7.1 was RFP tagged to allow for visualization. Expected results were that WT, R166X, and WT+R166X would be expressed on the membrane, as observed in **Fig. 4B of Chapter 2**. Therefore, a high correlation is expected between R166X and WT in WT+R166X samples. Additionally, previous studies have demonstrated that the W53X mutation to *KCNJ13* does not get trafficked to the membrane [28]. Therefore, W53X is expected to be expressed in the cytoplasm and show no correlation with WT in WT+W53X-treated cells. Live-cell images taken 48 hours after plasmid transduction resulted in R166X (green) and WT (red) expression on cell membranes **(Fig. 1B)**. Therefore, co-transfection with WT+R166X showed high correlation and yellow (red + green) fluorescence. In contrast, W53X (green) was expressed in the cytoplasm, and WT+W53X co-transfected cells showed low correlation and very little yellow fluorescence. Pearson's coefficient values confirm this observation when correlating red (RFP) and green (GFP) fluorescence in confocal images **(Fig. 1C)**. A statistically significant difference between WT+R166X and the following samples was observed: W53X (p=8.533XE-7), R166X (7.565x10E-7), WT (0.0595), and WT+W53X (0.045), further supporting the correlation between R166X protein and WT-Kir7.1 protein expressing on the membrane.

DISCUSSION

In **Chapter 2**, we observed both WT and mutant R166X expression on the membranes, following treatment with 3XCCT ACE-tRNA$^{Arg.\ UGA}$. Additionally, only a partial recovery of channel function was demonstrated. Therefore, we wanted to investigate further if WT and R166X subunits can co-assemble on cell membranes, to explain the partial recovery.

Live-cell imaging of R166X and WT-treated cells demonstrated co-localization of mutant and WT channels on the membrane **(Fig. 1B)**. This was confirmed using analysis of Pearson's coefficient **(Fig. 1C)**. A similar phenomenon has been reported in missense and deletion mutations that result in a loss of function. A missense mutation, F508del-*CFTR*, in the *CFTR* gene demonstrated channel trafficking to the membrane [29]. A Val302del missense mutation to the *KCNJ2* gene demonstrated mutant Kir2.1

expression on cell membranes [30]. Additionally, a mutation that results in the deletion of three bases, ΔF275 in the *KCNJQ1* gene, did not disrupt the trafficking of the mutant Kv7.1 protein to the membrane [31]. The phenomenon of mutant protein being trafficked to the membrane has been reported. However, to our knowledge, this is the first report of a nonsense mutation demonstrated to be trafficked to the membrane.

In contrast, W53X and WT treatment resulted in low membrane co-localization and a low Pearson's coefficient value **(Fig. 1B and C)**. Therefore, confirming our strong correlation results observed in the R166X+WT treatment. A previous study observed that the W53X mutation resulted in the protein getting stuck in the cytoplasm [28]. Our results confirm this characteristic of the W53X mutation.

These results support the expression results demonstrated in **Chapter 2**. Since Kir7.1 is a homotetrameric channel, these results further suggest that partial recovery of 3XCCT ACE-tRNA$^{Arg.\ UGA}$ treatment is a result of R166X and WT subunits co-assembling and creating a mixed WT/R166X heterotetrameric channel [27]. In a similar study, mutant missense Val302del-*KCNJ2* was co-transfected with WT protein and demonstrated reduced function, compared to WT, but not a total loss of function unless cells were treated with Val302-del-*KCNJ2* alone [30]. Additionally, this study demonstrated that an increase in ratios of WT to mutant protein resulted in a dose-dependent improvement to channel function. Therefore, demonstrating that in the case of a therapy such as 3XCCT ACE-tRNA$^{Arg.\ UGA}$ to the R166X mutation, optimization of treatment dose could improve functional recovery. By delivering a higher dose of the treatment, the cell should produce a higher ratio of WT protein. This optimization of drug dosage could improve the chances of homotetrameric WT channels assembling without mutant subunits. Additionally, studies have demonstrated that only a small percentage of cells containing native functional CFTR Cl^- channels is required to allow for normal function [32-34]. The necessary levels of functional Kir7.1 channels required for cellular function remain to be investigated but would aid in further optimization of ACE-tRNA dosage.

ACE-tRNA therapies have been investigated in nonsense mutations to the *CFTR* gene. Full function has been restored to these channels following treatment [23, 25]. The differences in ACE-tRNA

success in *CFTR* PTC mutations, compared to the R166X PTC mutation in *KCNJ13*, are likely due to the monomeric nature of the CFTR protein and the membrane trafficking of the WT/R166X heterotetrameric proteins that we have demonstrated in this study [35].

In summary, tetrameric proteins that contain membrane trafficking mutants, such as R166X, are likely more complex to target with ACE-tRNA therapy than monomeric proteins. Additionally, these mutants require more precise optimization of therapy dosage to restore full-channel function than monomeric protein mutations.

MATERIALS AND METHODS

Cell Culture

HEK293 cells (ATCC, CRL-3216) were maintained in complete medium containing: Dulbecco's modified Eagle's high-glucose medium with l-glutamine (DMEM, GIBCO, 11965-092), 10% fetal bovine serum (FBS, HyClone™ Characterized Fetal Bovine Serum, Heat-inactivated, SH30396.03HI), 1% penicillin-streptomycin (Pen-Strep, GeminiBio, 400-109), and 1% antibiotic-antimycotic (Anti-Anti, Gibco, 15240062). Cells were cultured at passages #5-25 in an incubator at 37°C and 5% CO_2. Cells were split at around 80% confluency using Dulbecco's Phosphate-buffered Saline (DPBS, GIBCO, 14190144) for washing and Accutase (Corning, 25-058-Cl) for dissociation. Media was changed every 2-3 days.

Co-transfection of WT and mutant Kir7.1

HEK293 cells were transfected using PolyJet™ (Signa Gen, SL100688) for co-transfection in a 1:1 ratio of the following plasmids: WT (1ug) + R166X (1ug), or WT (1ug) + W53X (1ug), or WT (1ug) + dummy plasmid (1ug), or R166X (1ug) + dummy plasmid, or W53X (1ug) + dummy plasmid. The R166X and W53X plasmids were each GFP tagged, and the WT plasmid was RFP tagged for fluorescent visualization. For 24 hours, cells were maintained in medium (DMEM, 10% FBS, 1% Penstrep, 1% Anti-

anti). Cells were then split using DPBS and Accutase and plated on 14mm glass diameter, poly-d-lysine-coated 35mm imaging dishes (MATTEK, P35GC-1.0-14-C). 24 hours after plating, cells were used for imaging.

Live-cell Imaging

Z-stacks of co-transfected cell fluorescence were imaged using Andor iQ 3.6.5 software on a Nikon Eclipse Ti microscope, an iXon x3 897 EM-CCD camera, and the Andor Revolution XD spinning disk confocal microscopy system (Andor, Belfast, Northern Ireland) under a 60X objective. Cells were maintained in extracellular HEPES-buffered Ringer's solution (HR) (135mM NaCl, 1mM $MgCl_2$, 10mM HEPES, 1.8mM $CaCl_2$, 10mM glucose, and 5mM KCl; pH: 7.4; osmolarity: 300mOsm) during imaging studies. Images were analyzed using ImageJ (Fiji, 1.54p) software and Pearson's coefficient was calculated by comparing red and green fluorescence using the BIOP JaCoP Plugin in ImageJ.

Statistical Analysis

A two-tailed Student's t-test was performed using Microsoft Excel for the statistical analysis. Differences were considered statistically significant at $p < 0.05$; the results are expressed as mean ±SEM.

Acknowledgements:

Schematic images were created with Biorender.com.

FIGURES AND TABLES

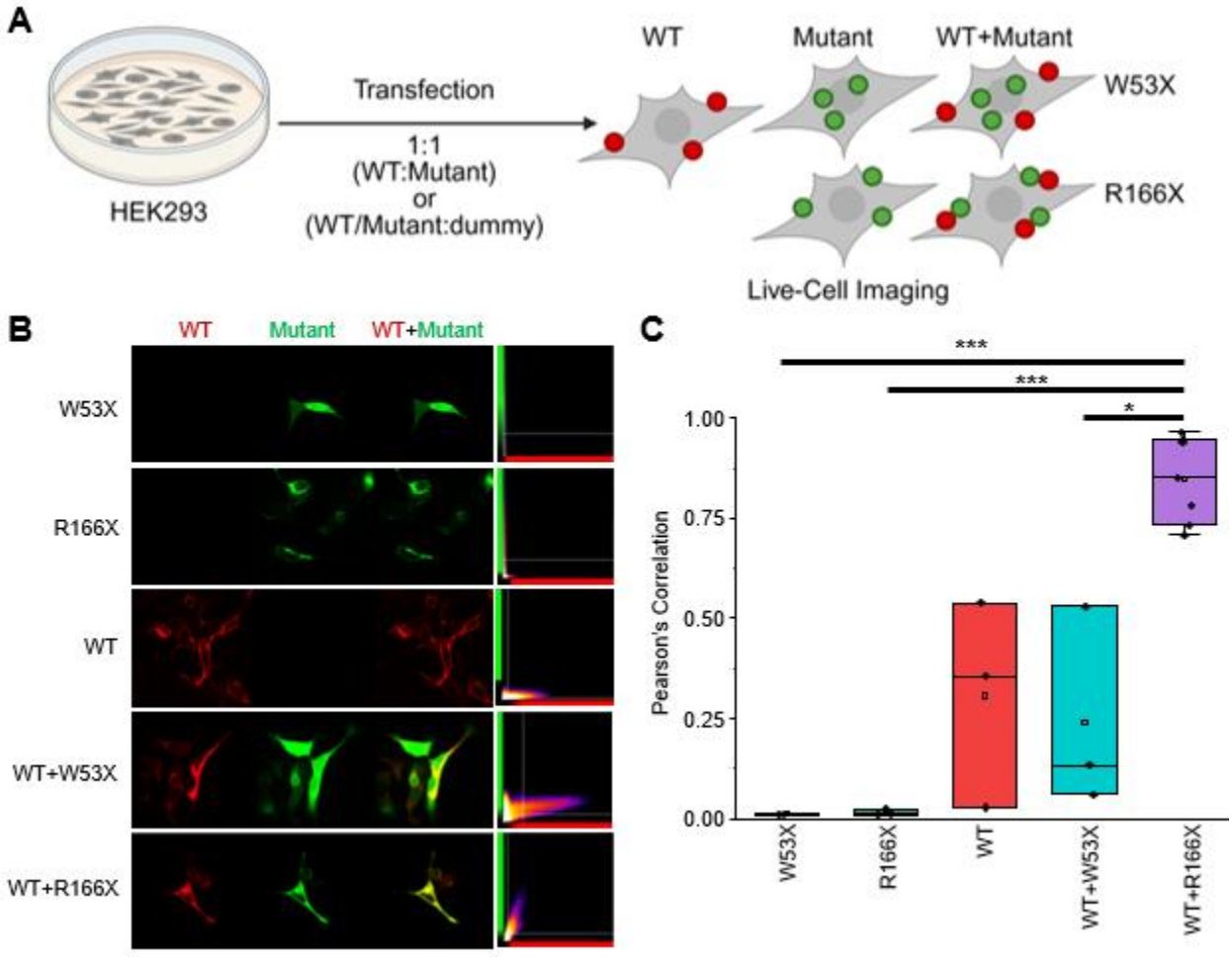

Figure 1: Correlation of R166X and WT protein on the membrane of HEK293 cells. (A) Schematic of experimental design and expected results. HEK293 cells were transfected in a 1:1 ratio with either RFP-WT:GFP-Mutant or RFP-WT:dummy plasmid or GFP-Mutant:dummy plasmid. Expected results are that WT, R166X, and WT+R166X will be expressed on the membrane. Additionally, W53X will remain in the cytoplasm. Therefore, we expected that co-localization of WT (red) and mutant (green) would be high in WT+R166X and low in all other treatments. **(B)** Confocal Images of WT (red), mutant (green), and WT + mutant (yellow) cells. Pearson's correlation was performed using the BIOP JACoP plugin in Fiji analysis software by comparing the correlation between the red and green channels. The heat map from Pearson's correlation analysis is shown on the right. **(C)** Box and whisker plot of Pearson's correlation values using the BIOP JACoP plugin for cells treated with W53X alone (orange; n=2), R166X alone (green; n=3), WT alone (red; n=3), WT+W53X (teal; n=3), or WT+R166X (purple; n=7). Average values for each are as follows: 0.012 for W53X, 0.016 for R166X, 0.308 for WT, 0.242 for WT+W53X, and 0.846 for WT+R166X. SEM values are: 0.001 for W53X, 0.004 for R166X, 0.149 for WT, 0.146 for WT+W53X, and 0.041 for WT+R166X. Statistical significance measured by two-tailed Student's t-test and denoted as *$P<0.05$, **$P<0.01$, and ***$P<0.001$. P-values for each sample compared to WT+R166X are: 8.533x10E-7 for W53X, 7.565x10E-7 for R166X, 0.0595 for WT, and 0.045 for WT+W53X. All other P-values between compared values were not significant.

REFERENCES

1. Hibino, H., et al., *Inwardly rectifying potassium channels: their structure, function, and physiological roles.* Physiol Rev, 2010. **90**(1): p. 291-366.
2. Pattnaik, B.R., et al., *A Novel KCNJ13 Nonsense Mutation and Loss of Kir7.1 Channel Function Causes Leber Congenital Amaurosis (LCA16).* Hum Mutat, 2015. **36**(7): p. 720-7.
3. Sergouniotis, P.I., et al., *Recessive mutations in KCNJ13, encoding an inwardly rectifying potassium channel subunit, cause leber congenital amaurosis.* Am J Hum Genet, 2011. **89**(1): p. 183-90.
4. Perez-Roustit, S., et al., *Leber Congenital Amaurosis with Large Retinal Pigment Clumps Caused by Compound Heterozygous Mutations in Kcnj13.* Retin Cases Brief Rep, 2017. **11**(3): p. 221-226.
5. Hejtmancik, J.F., et al., *Mutations in KCNJ13 cause autosomal-dominant snowflake vitreoretinal degeneration.* Am J Hum Genet, 2008. **82**(1): p. 174-80.
6. Kumar, M. and B.R. Pattnaik, *Focus on Kir7.1: physiology and channelopathy.* Channels (Austin), 2014. **8**(6): p. 488-95.
7. Toms, M., et al., *Phagosomal and mitochondrial alterations in RPE may contribute to KCNJ13 retinopathy.* Sci Rep, 2019. **9**(1): p. 3793.
8. Strauss, O., *The retinal pigment epithelium in visual function.* Physiol Rev, 2005. **85**(3): p. 845-81.
9. Yun, Y. and Y. Ha, *CRISPR/Cas9-Mediated Gene Correction to Understand ALS.* Int J Mol Sci, 2020. **21**(11).
10. Kabra, M., et al., *Nonviral base editing of KCNJ13 mutation preserves vision in a model of inherited retinal channelopathy.* J Clin Invest, 2023.
11. Pandey, V.K., et al., *Application of CRISPR/Cas9 Genome Editing in Genetic Disorders: A Systematic Review Up to Date.* J Genet Syndr Gene Ther, 2017. **8**(2): p. 1000321.
12. Saber Sichani, A., et al., *A Review on Advanced CRISPR-Based Genome-Editing Tools: Base Editing and Prime Editing.* Mol Biotechnol, 2023. **65**(6): p. 849-860.

13. Li, Q., et al., *Applications of Genome Editing Technology in Animal Disease Modeling and Gene Therapy.* Comput Struct Biotechnol J, 2019. **17**: p. 689-698.

14. Anzalone, A.V., et al., *Search-and-replace genome editing without double-strand breaks or donor DNA.* Nature, 2019. **576**(7785): p. 149-157.

15. Guo, C., et al., *Off-target effects in CRISPR/Cas9 gene editing.* Front Bioeng Biotechnol, 2023. **11**: p. 1143157.

16. Keeling, K.M., et al., *Therapeutics based on stop codon readthrough.* Annu Rev Genomics Hum Genet, 2014. **15**: p. 371-94.

17. Lee, H.L. and J.P. Dougherty, *Pharmaceutical therapies to recode nonsense mutations in inherited diseases.* Pharmacol Ther, 2012. **136**(2): p. 227-66.

18. Roy, B., et al., *Ataluren stimulates ribosomal selection of near-cognate tRNAs to promote nonsense suppression.* Proc Natl Acad Sci U S A, 2016. **113**(44): p. 12508-12513.

19. Michorowska, S., *Ataluren-Promising Therapeutic Premature Termination Codon Readthrough Frontrunner.* Pharmaceuticals (Basel), 2021. **14**(8).

20. Spelier, S., et al., *Readthrough compounds for nonsense mutations: bridging the translational gap.* Trends Mol Med, 2023. **29**(4): p. 297-314.

21. Laurent, G., et al., *Mechanism of aminoglycoside-induced lysosomal phospholipidosis: in vitro and in vivo studies with gentamicin and amikacin.* Biochem Pharmacol, 1982. **31**(23): p. 3861-70.

22. Kaloyanides, G.J., *Drug-phospholipid interactions: role in aminoglycoside nephrotoxicity.* Ren Fail, 1992. **14**(3): p. 351-7.

23. Lueck, J.D., et al., *Engineered transfer RNAs for suppression of premature termination codons.* Nat Commun, 2019. **10**(1): p. 822.

24. Ko, W., et al., *Efficient suppression of endogenous CFTR nonsense mutations using anticodon-engineered transfer RNAs.* Mol Ther Nucleic Acids, 2022. **28**: p. 685-701.

25. Blomquist, V.G., et al., *Transfer RNA-mediated restoration of potassium current and electrical correction in premature termination long-QT syndrome hERG mutants.* Mol Ther Nucleic Acids, 2023. **34**: p. 102032.

26. Porter, J.J., C.S. Heil, and J.D. Lueck, *Therapeutic promise of engineered nonsense suppressor tRNAs.* Wiley Interdiscip Rev RNA, 2021. **12**(4): p. e1641.

27. Hernandez, C.C., et al., *The unique structural characteristics of the Kir 7.1 inward rectifier potassium channel: a novel player in energy homeostasis control.* Am J Physiol Cell Physiol, 2023. **324**(3): p. C694-C706.

28. Kabra, M., et al., *Nonviral base editing of KCNJ13 mutation preserves vision in a model of inherited retinal channelopathy.* The Journal of Clinical Investigation, 2023. **133**(19).

29. Rogan, M.P., D.A. Stoltz, and D.B. Hornick, *Cystic fibrosis transmembrane conductance regulator intracellular processing, trafficking, and opportunities for mutation-specific treatment.* Chest, 2011. **139**(6): p. 1480-1490.

30. Ordog, B., et al., *Identification and functional characterisation of a novel KCNJ2 mutation, Val302del, causing Andersen-Tawil syndrome.* Can J Physiol Pharmacol, 2015. **93**(7): p. 569-75.

31. Aizawa, Y., et al., *A novel mutation in KCNQ1 associated with a potent dominant negative effect as the basis for the LQT1 form of the long QT syndrome.* J Cardiovasc Electrophysiol, 2007. **18**(9): p. 972-7.

32. Johnson, L.G., et al., *Efficiency of gene transfer for restoration of normal airway epithelial function in cystic fibrosis.* Nat Genet, 1992. **2**(1): p. 21-5.

33. Ramalho, A.S., et al., *Five percent of normal cystic fibrosis transmembrane conductance regulator mRNA ameliorates the severity of pulmonary disease in cystic fibrosis.* Am J Respir Cell Mol Biol, 2002. **27**(5): p. 619-27.

34. Farmen, S.L., et al., *Gene transfer of CFTR to airway epithelia: low levels of expression are sufficient to correct Cl- transport and overexpression can generate basolateral CFTR.* Am J Physiol Lung Cell Mol Physiol, 2005. **289**(6): p. L1123-30.

35. Chen, J.-H., et al., *CFTR is a monomer: biochemical and functional evidence.* The Journal of membrane biology, 2002. **188**(1): p. 55-71.

Chapter 4: Dose-dependent increase in Kir7.1 expression in mouse RPE cells following HUB-101 gene augmentation therapy

Allison Spillane[1,2], Pawan K. Shahi[1,2], Susan Macdonald[3], Sara M. Hall[3], Jeff Sabados[3], Bikash R. Pattnaik[1,2,4]

[1]University of Wisconsin-Madison, Department of Pediatrics, Wisconsin, USA.
[2]University of Wisconsin-Madison, McPherson Eye Research Institute, Wisconsin, USA.
[3] Hubble Therapeutics, Boston, Massachusetts, USA
[4]University of Wisconsin-Madison, Department of Ophthalmology and Visual Sciences, Wisconsin, USA

SUMMARY

Patients with *KCNJ13* mutations suffer from progressive vision loss. Therefore, therapies must reach the clinic and stop further disease progression. Gene augmentation therapy is a candidate that has demonstrated success in treating many disease-causing disorders. This includes an ocular clinical-grade gene augmentation therapy, Luxturna, that has demonstrated vision improvements for patients harboring *RPE65* mutations. These improvements have been observed even 5 years post-treatment. We have previously demonstrated success in delivering a gene augmentation therapy to patient-derived hiPSC-RPE. However, the therapy relied on a Lentivirus for delivery, which has not been approved by the US FDA for ocular gene augmentation therapy. Therefore, Hubble Therapeutics produced a clinical-grade gene therapy, HUB-101, that used an AAV viral capsid to deliver the human version of *KCNJ13* (h*KCNJ13*). We tested the ability of HUB-101 to transduce mouse RPE (mRPE) cells. A dose-dependent increase in h*KCNJ13* from HUB-101 treatment was observed. Additionally, no effect on endogenous mouse *Kcnj13* (m*Kcnj13*) expression was observed. Our results demonstrate that HUB-101 can efficiently deliver h*KCNJ13* to RPE cells. These results inform future pre-clinical *in vivo* studies aimed at confirming the efficacy and testing the safety of HUB-101 for eventual clinical approval.

INTRODUCTION

Mutations to *KCNJ13*, a gene encoding the inwardly rectifying potassium channel Kir7.1, lead to LCA16 and SVD [1-5]. These diseases are characterized by vision loss and eventual blindness due to loss of the RPE cells that maintain retinal health [6-8]. Therefore, the development of clinical-grade therapies to overcome these mutations and rescue vision in these patients is vital.

Gene augmentation is a therapy that has demonstrated successful treatment of genetic diseases. This is accomplished by delivering a healthy copy of the target gene to mutant cells, therefore, allowing for the transcription of the WT protein and functional recovery [9]. The most common method of delivery is using viral vectors [10]. The use of a viral capsid for gene delivery allows for the virus to be endocytosed by the cell and delivers the target gene to the nucleus, where it is held in an episome for translation [11-13]. Delivery and transcription of the target gene can be designed to target specific cell types through the selection of different viral serotypes and special promoters that can only be utilized by the transcription machinery of particular cell types [12, 14].

In **Chapter 2** we demonstrate that a *KCNJ13* PTC mutation that was challenging to correct using genomic editing techniques was partially rescued by using ACE-tRNA therapy. However, our lab has demonstrated that genomic editing of another PTC in the *KCNJ13* gene successfully edited the mutation and restored Kir7.1 channel function [15]. Therefore, for gene-specific therapies, such as genomic editing, efficacy is mutation-specific. One advantage to gene augmentation therapy is that it can overcome any mutation to a single gene, as demonstrated in human clinical trials [16]. Therefore, overcoming the need to specifically target each mutation with a new therapy, which is required in other types of genomic therapies [17-19]. Gene augmentation has been so successful in overcoming disease phenotypes that several therapies have been approved for clinical trials globally [20]. One of the most successful gene therapies has been Luxturna [20, 21]. This therapy was the first to be approved by the United States FDA and demonstrated improvement of vision in LCA2 patients harboring *RPE65* mutations [16, 21, 22]. Therapeutic effects were sustained even 5 years after treatment, and no immune effects were reported

[23]. Therefore, gene augmentation therapy holds promise in overcoming KCNJ13 mutations and restoring vision in patients with these mutations.

Our lab previously demonstrated the success of a research-grade gene augmentation therapy to deliver WT *KCNJ13* to mutant patient-derived hiPSC-RPE cells [24]. A Lentivirus was utilized for delivery of the WT gene, and functional studies demonstrated rescue of Kir7.1 channel function. However, Lentiviral delivery for ocular diseases is not approved by the US FDA. Therefore, the production and testing of a clinical-grade associated adeno virus (AAV) gene therapy was necessary to move towards clinical trial approval.

We wanted to test the ability of a clinical-grade gene therapy manufactured by Hubble Therapeutics (Boston, Massachusetts), HUB-101, to deliver WT human *KCNJ13* (h*KCNJ13*) to RPE cells. We chose to deliver HUB-101 to mouse RPE (mRPE) cells so that we could design primers that were able to differentiate between endogenous mouse *Kcnj13* (m*Kcnj13*) and the exogenous h*KCNJ13* transcript from our therapy. Therefore, allowing us to visualize dose effects of HUB-101.

One advantage of HUB-101 is that it uses an AAV5 viral capsid with a VMD2 promoter, thereby explicitly targeting RPE cells and reducing the possibility of delivery and expression of h*KCNJ13* to other retinal cells. AAV5 primarily targets RPE cells, with some transduction in photoreceptors [25]. Additionally, the VMD2 promoter is RPE specific, allowing for transcription of the target gene to only take place in the RPE cells of HUB-101 treated retinas [26, 27]. Another advantage to HUB-101 therapy to target mutations in the RPE cells is that the eye contains a blood-brain barrier and is immune privileged [28]. We are targeting a mutation that affects the RPE cells of the eye, which requires the therapy to be directly delivered to the eye. Therefore, this eliminates the chances of HUB-101 to reach other organs and have immune effects outside of the eye, in future animal studies and clinical trials.

RESULTS

Isolated mouse RPE cells mature in culture.

We wanted to determine if a clinical-grade gene therapy, HUB-101 (Hubble Therapeutics, Boston, MA), could transduce mRPE cells. The cells were isolated from C57BL6/J mice and placed into transwells to mature, according to a protocol outlined in Fernandez-Godino et al. (2016) **(Fig. 1A)** [29]. Cells were transduced with HUB-101 14+ days after plating in transwells and following visual identification of maturity markers. Quantitative PCR (qPCR) was performed 7 days post-transduction, using primers to differentiate the endogenous m*Kcnj13* and HUB-101-mediated exogenous h*KCNJ13* gene expression. Visual characteristics of maturity were observed in mRPE cells 7 days post-treatment and 14-days post-treatment **(Fig. 1B)**. These characteristics include the honeycomb shape and pigmentation outlined in Fernandez-Godino et al. (2016) [29].

HUB-101 successfully transduced mRPE cells in a dose-dependent manner.

The treatment of mature mRPE cells with HUB-101, demonstrated successful transduction of h*KCNJ13* transcript **(Fig. 1C)**. Additionally, transduction efficiency was dose-dependent with a titer of $1x10^8$ demonstrating the lowest h*KCNJ13* expression (5.968±2.107) and a titer of $1x10^{10}$ resulting in the highest h*KCNJ13* expression (308.625±94.544). Other averages and SEMs values were, as follows: 1.222±0.335 for h*KCNJ13* UT (hUT), 68.262±22.859 for h*KCNJ13* $1x10^9$ ($h10^9$), 0.722±0.138 for m*Kcnj13* UT (mUT), 1.510±0.677 for m*Kcnj13* $1x10^8$ ($m10^8$), 0.9556±0.347 for m*Kcnj13* 1x109 ($m10^9$), and 0.467±0.224 for m*Kcnj13* $1x10^{10}$ ($m10^{10}$). Statistically significant differences in h*KCNJ13* expression were observed as the dose increased as follows: p=0.018 between UT and $1x10^8$, and p=0.047 between $1x10^8$ to $1x10^9$. Additionally, a p-value of 0.067 was observed for h*KCNJ13* between $1x10^9$ and $1x10^{10}$. The expression of endogenous m*Kcnj13* transcript was investigated to demonstrate the specificity of the h*KCNJ13* primers and determine if HUB-101 treatment would lead to any changes in the endogenous transcript. No difference in m*Kcnj13* transcript was observed following treatment, demonstrating that

HUB-101 does not influence the endogenous transcript. A statistically significant difference of p=0.029 was observed at dose $1x10^{10}$ between m*Kcnj13* and h*KCNJ13*. Additionally, a difference of p=0.076 was observed at a dose of $1x10^{9}$ between m*Kcnj13* and h*KCNJ13*.

DISCUSSION

The progressive nature of the vision disorders caused by *KCNJ13* mutations requires the development of efficient therapies to rescue patients' vision [1-5]. We wanted to test the ability of a clinical-grade gene therapy, HUB-101, to deliver h*KCNJ13* to mRPE cells in a dose-dependent manner. We isolated mRPE cells from C57BL/6J mice and treated mature cells with various titers ($1x10^{8}$, $1X10^{9}$, and $1X10^{10}$) of HUB-101 carrying h*KCNJ13* **(Fig. 1A)**. Our cells were confirmed with visual maturity markers observed by day 7, and cells-maintained health and maturity by day 14 **(Fig. 1B)**. Although cells were visually mature by day 7, cells were treated 14+ days after plating, due to suggestions made in the protocol outlined by Fernandez-Godino et al. (2016) [29]. We did not observe a change in endogenous m*Kcnj13* expression following HUB-101 treatment **(Fig. 1C)**. This demonstrated the specificity of our primers and revealed that there were no off-target effects on the endogenous gene following treatment. A dose-dependent increase in h*KCNJ13* was demonstrated **(Fig. 1C)**. Statistically significant differences were observed in h*KCNJ13* expression between UT versus $1x10^{8}$ (p=0.018) and between $1x10^{8}$ versus $1x10^{9}$ (p=0.047). Additionally, a slight difference (p=0.067) was observed when comparing $1x10^{9}$ to $1x10^{10}$. This difference was not statistically significant due to variability in treated cells. Therefore, we demonstrated that our HUB-101 gene therapy efficiently delivered h*KCNJ13* to RPE cells.

The efficiency of our clinical-grade gene augmentation therapy to transduce mRPE cells, suggests that clinical trials in humans should result in h*KCNJ13* delivery to RPE cells. For clinical trials, in vivo studies must be performed to verify the efficacy of HUB-101 and validate that there is minimal immune response due to the treatment. We have demonstrated the successful delivery of h*KCNJ13* and subsequent vision improvement in mutant mice, following HUB-101 administration [30] (paper in

preparation). NHP studies will also be conducted to further demonstrate the efficacy and safety of HUB-101 before moving to the clinic.

One ocular gene therapy, Luxturna, has already demonstrated successful therapeutic effects, even 5 years post-treatment, with no reported immune effects [16, 22, 23]. This therapy utilized an AAV2 serotype with a chicken beta-actin promotor [16]. We decided to use an AAV5 serotype due to its higher specificity with RPE cells compared to photoreceptors [25]. Additionally, we selected a VMD2 promoter because studies have demonstrated its specificity to RPE cells [26, 27]. These modifications to enhance the ability of HUB-101 to explicitly target the RPE cells and our results demonstrating successful transduction of mRPE cells with HUB-101, coupled with the previous clinical success of an ocular AAV gene augmentation therapy, suggest that the ability of HUB-101 to deliver h*KCNJ13* to RPE cells in the clinic is promising.

Our results demonstrate that the clinical-grade gene augmentation therapy HUB-101 is efficient in delivering h*KCNJ13* to RPE cells in a dose-dependent manner. Validation of HUB-101 transduction of RPE cells can inform future studies into the *in vivo* investigation of this drug's safety and efficacy. HUB-101 is a promising therapy for overcoming mutations to *KCNJ13* that lead to progressive vision loss in mutation-harboring patients.

MATERIALS AND METHODS

Animal care

Animal protocols were approved by the University of Wisconsin School of Medicine and Public Health Institutional Animal Care and Use Committee (IACUC) (protocol #: M005434). C57BL/6J mice were housed in an animal facility at the University of Wisconsin-Madison in a temperature (25±5°C) and humidity (40-50%) controlled environment. Mice were kept under a 12-hour light/12-hour dark light cycle.

Mouse RPE cell collection and maturation

mRPE were collected according to a protocol from Fernandez-Godino et al. (2016) [29]. Cells were plated and maintained in transwells with cell medium containing Alpha-MEM (Lonza, BE02-002F) with 10% fetal bovine serum (FBS, HyCloneTM Characterized Fetal Bovine Serum, Heat-inactivated, SH30396.03HI), 1% penicillin-streptomycin (Pen-Strep, GeminiBio, 400-109), N1 medium supplement (Sigma, N6530), L-glutamine (GeminiBio, 400-106), Non-Essential amino acids (Irvine Scientific, 9304). Cells were held in a cell incubator at 37°C and 5% CO_2. Medium was changed every 2-3 days. Cells were allowed to mature for 14 days or longer before transduction. Cells were imaged on a Nikon Eclipse Ts2 microscope using NIS-Elements software to look for visual cell maturity markers.

HUB-101 transduction of mRPE

HUB-101 was synthesized and provided by Hubble Therapeutics (Massachusetts, USA). Mature mRPE cells were transduced with various titers ($1x10^8$, $1x10^9$, or $1x10^{10}$) of HUB-101. The cell medium was changed 3 days after transduction and every 2-3 days for 7 days. After 7 days post-transduction, cells were collected for RNA isolation (QIAGEN, 74134) and cDNA conversion (Applied Biosystems, 4368814). The cDNA was then used for qPCR.

Quantitative PCR

Specifically designed primers to differentiate between m*Kcnj13* and h*KCNJ13* for qPCR analysis were custom-ordered from IDT using mouse and human RNA transcripts from NCBI (https://www.ncbi.nlm.nih.gov/gene/) **(Table 1)**. Fold change was calculated as follows:

Fold Change = 2^(ΔΔCT)

qPCR of cDNA was performed using PowerUP SYBR Green Master Mix (ThermoFisher, A25741) on a QuantStudio 3 (Applied Biosystems) machine. Experiment setup and analysis was performed using QuantStudio (Applied Biosystems).

Statistical Analysis

A two-tailed Student's t-test was performed using Microsoft Excel for the statistical analysis. Differences were considered statistically significant at $p < 0.05$; the results are expressed as mean ±SEM.

Acknowledgements:

Schematic images were created using Biorender.com.

FIGURES AND TABLES

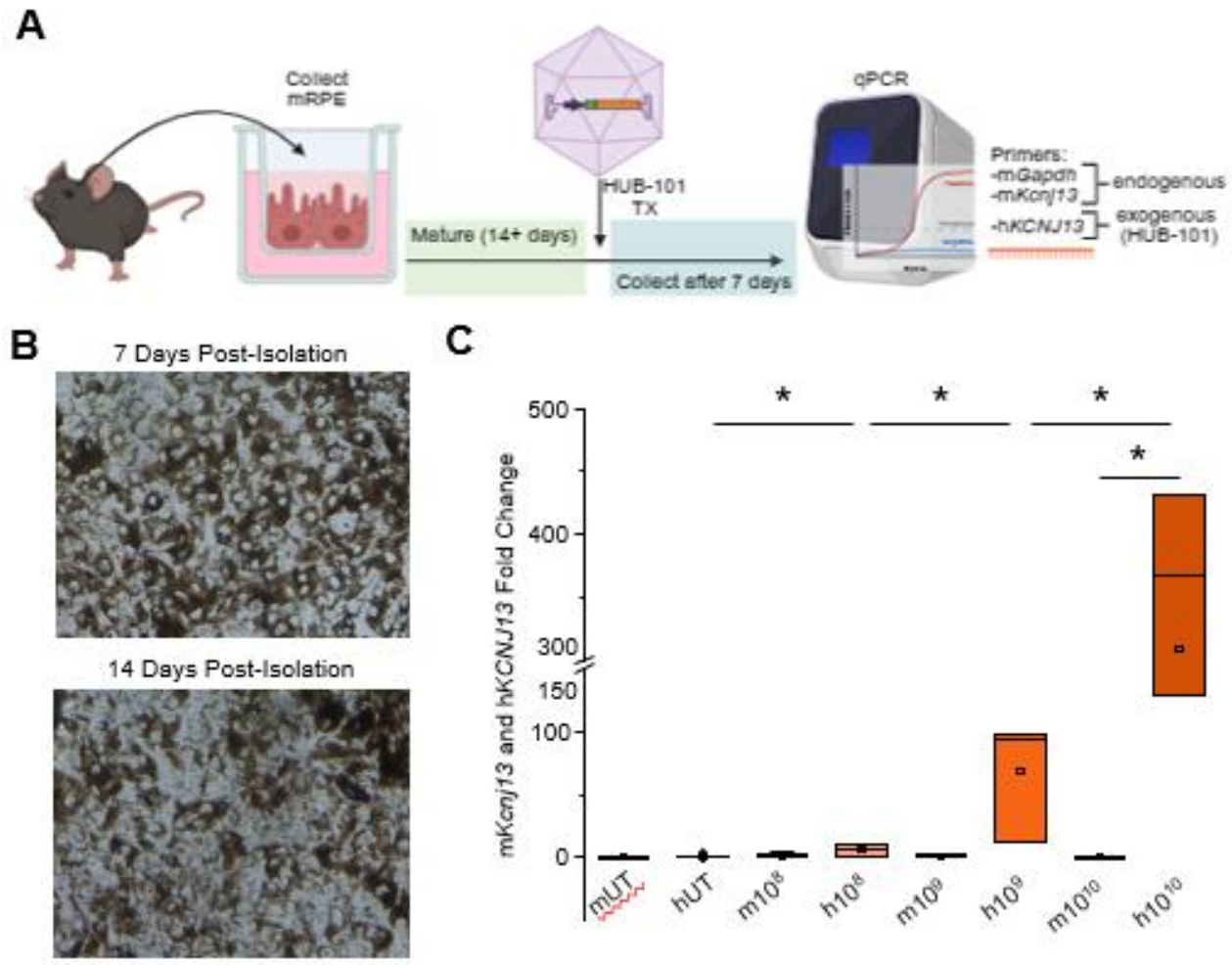

Figure 1: Dose-dependent increase of h*KCNJ13* transcript in mature mouse RPE cells treated with HUB-101. (A) Schematic of methodology. mRPE were collected and placed in transwell inserts to mature for 14 days or longer. Cells were then treated with HUB-101 via transduction and collected for qPCR analysis 7 days after treatment. Specifically designed primers were used for qPCR to detect endogenous m*Kcnj13* and exogenous h*KCNJ13* transcripts from HUB-101 transduction. Additionally, a mouse *Gapdh* (m*Gadph*) primer was designed for the detection of a housekeeping gene for analysis. **(B)** Images of mRPE cells 7 and 14 days after isolation, demonstrating mature RPE characteristics. **(C)** Box plot of qPCR fold change results. All samples were compared to the m*Gadph* housekeeping gene to determine fold change. m*Kcnj13* (m) fold change is depicted in blue and h*KCNJ13* (h) fold change is depicted in orange. Average values for fold changes from mRPE treated and UT samples are as follows: 0.722 for m*Kcnj13* UT (mUT, n=9), 1.222 for hUT, (n=9), 1.510 for $m10^8$ (n=4), 5.968 for $h10^8$ (n=4), 0.9556 for $m10^9$ (n=3), 68.262 for $h10^9$ (n=3), 0.467 for $m10^{10}$ (n=3), and 308.625 for $h10^{10}$ (n=3). SEM values are: 0.138 for mUT, 0.335 for hUT, 0.677 for $m10^8$, 2.107 for $h10^8$, 0.347 for $m10^9$, 22.859 for $h10^9$, 0.224 for $m10^{10}$, and 94.544 for $h10^{10}$. Statistical significance measured by two-tailed Student's t-test and denoted as *$P<0.05$, **$P<0.01$, and ***$P<0.001$. P-values were compared for all m*Kcnj13* transcripts between increasing treatment titers, with no significant p-values. P-values were compared for all h*KCNJ13* transcripts between increasing treatment titers, and the significant p-values were as follows: 0.018 for hUT versus $h10^8$, and 0.047 for $h10^8$ versus $h10^9$. A slightly insignificant p-value of 0.067 was observed for $h10^9$ versus $h10^{10}$. Additionally, p-values were compared between m*Kcnj13* and h*KCNJ13* transcripts for each sample, and a significant p-value of 0.029 was found between $m10^{10}$ and $h10^{10}$. A p-value of 0.076 was observed between $m10^9$ and $h10^9$.

Primer Name	**5’-3’ Sequence**
Mouse Gapdh FWD	CATTGCTCTCAATGACAACTTT
Mouse Gapdh RVS	GTGGTCCAGGGTTTCTTACT
Mouse *Kcnj13* FWD	GGGCCTTGTGTATCTCCGA
Mouse *Kcnj13* RVS	TGGGACGTCGTGGTCTATT
Human *KCNJ13* FWD	TAACCAGTGTCCGGGTCT
Human *KCNJ13* RVS	ACTTGATGGTGTAATGGAGTGATAG

Table 1: Primers for qPCR of HUB-101 treated mRPE cells. The NCBI Primer-BLAST tool (https://www.ncbi.nlm.nih.gov/tools/primer-blast/) was used for primer design. Primers were ordered from IDT (https://www.idtdna.com).

REFERENCES:

1. Hibino, H., et al., *Inwardly rectifying potassium channels: their structure, function, and physiological roles.* Physiol Rev, 2010. **90**(1): p. 291-366.
2. Pattnaik, B.R., et al., *A Novel KCNJ13 Nonsense Mutation and Loss of Kir7.1 Channel Function Causes Leber Congenital Amaurosis (LCA16).* Hum Mutat, 2015. **36**(7): p. 720-7.
3. Sergouniotis, P.I., et al., *Recessive mutations in KCNJ13, encoding an inwardly rectifying potassium channel subunit, cause Leber congenital amaurosis.* Am J Hum Genet, 2011. **89**(1): p. 183-90.
4. Perez-Roustit, S., et al., *Leber Congenital Amaurosis with Large Retinal Pigment Clumps Caused by Compound Heterozygous Mutations in Kcnj13.* Retin Cases Brief Rep, 2017. **11**(3): p. 221-226.
5. Hejtmancik, J.F., et al., *Mutations in KCNJ13 cause autosomal-dominant snowflake vitreoretinal degeneration.* Am J Hum Genet, 2008. **82**(1): p. 174-80.
6. Kumar, M., et al., *Application of CRISPR/Cas9-mediated gene editing for abiotic stress management in crop plants.* Front Plant Sci, 2023. **14**: p. 1157678.
7. Toms, M., et al., *Phagosomal and mitochondrial alterations in RPE may contribute to KCNJ13 retinopathy.* Sci Rep, 2019. **9**(1): p. 3793.
8. Strauss, O., *The retinal pigment epithelium in visual function.* Physiol Rev, 2005. **85**(3): p. 845-81.
9. Drag, S., F. Dotiwala, and A.K. Upadhyay, *Gene therapy for retinal degenerative diseases: progress, challenges, and future directions.* Investigative Ophthalmology & Visual Science, 2023. **64**(7): p. 39-39.
10. Toualbi, L., M. Toms, and M. Moosajee, *The Landscape of Non-Viral Gene Augmentation Strategies for Inherited Retinal Diseases.* Int J Mol Sci, 2021. **22**(5).
11. Kaminsky, P.M., et al., *Directing integrin-linked endocytosis of recombinant AAV enhances productive FAK-dependent transduction.* Mol Ther, 2012. **20**(5): p. 972-83.

12. Petrs-Silva, H., et al., *Novel properties of tyrosine-mutant AAV2 vectors in the mouse retina.* Mol Ther, 2011. **19**(2): p. 293-301.
13. Wang, J.-H., et al., *Adeno-associated virus as a delivery vector for gene therapy of human diseases.* Signal Transduction and Targeted Therapy, 2024. **9**(1): p. 78.
14. Heinz, S., et al., *The selection and function of cell type-specific enhancers.* Nat Rev Mol Cell Biol, 2015. **16**(3): p. 144-54.
15. Kabra, M., et al., *Nonviral base editing of KCNJ13 mutation preserves vision in a model of inherited retinal channelopathy.* The Journal of Clinical Investigation, 2023. **133**(19).
16. Maguire, A.M., et al., *Age-dependent effects of RPE65 gene therapy for Leber's congenital amaurosis: a phase 1 dose-escalation trial.* The Lancet, 2009. **374**(9701): p. 1597-1605.
17. Dang, Y., et al., *Optimizing sgRNA structure to improve CRISPR-Cas9 knockout efficiency.* Genome Biol, 2015. **16**: p. 280.
18. Hasanzadeh, A., et al., *Smart Strategies for Precise Delivery of CRISPR/Cas9 in Genome Editing.* ACS Appl Bio Mater, 2022. **5**(2): p. 413-437.
19. Lino, C.A., et al., *Delivering CRISPR: a review of the challenges and approaches.* Drug Deliv, 2018. **25**(1): p. 1234-1257.
20. Shchaslyvyi, A.Y., et al., *Current State of Human Gene Therapy: Approved Products and Vectors.* Pharmaceuticals (Basel), 2023. **16**(10).
21. *FDA approves hereditary blindness gene therapy.* Nature Biotechnology, 2018. **36**(1): p. 6-6.
22. Shahryari, A., et al., *Development and Clinical Translation of Approved Gene Therapy Products for Genetic Disorders.* Front Genet, 2019. **10**: p. 868.
23. Darrow, J.J., *Luxturna: FDA documents reveal the value of a costly gene therapy.* Drug discovery today, 2019. **24**(4): p. 949-954.
24. Shahi, P.K., et al., *Gene Augmentation and Readthrough Rescue Channelopathy in an iPSC-RPE Model of Congenital Blindness.* Am J Hum Genet, 2019. **104**(2): p. 310-318.
25. Auricchio, A., et al., *Exchange of surface proteins impacts on viral vector cellular specificity and transduction characteristics: the retina as a model.* Hum Mol Genet, 2001. **10**(26): p. 3075-81.

26. Marquardt, A., et al., *Mutations in a novel gene, VMD2, encoding a protein of unknown properties cause juvenile-onset vitelliform macular dystrophy (Best's disease).* Hum Mol Genet, 1998. **7**(9): p. 1517-25.

27. Petrukhin, K., et al., *Identification of the gene responsible for Best macular dystrophy.* Nat Genet, 1998. **19**(3): p. 241-7.

28. Katamay, R. and R.B. Nussenblatt, *Blood–retinal barrier, immune privilege, and autoimmunity.* Retina, 2012: p. 579.

29. Fernandez-Godino, R., D.L. Garland, and E.A. Pierce, *Isolation, culture and characterization of primary mouse RPE cells.* Nat Protoc, 2016. **11**(7): p. 1206-18.

30. Shahi, P.K., et al. *HUB101 Gene Therapy for Blindness Caused by Pediatric Lebers Congenital Amaurosis (LCA16)*. in *MOLECULAR THERAPY*. 2024. CELL PRESS 50 HAMPSHIRE ST, FLOOR 5, CAMBRIDGE, MA 02139 USA.

Chapter 5: A novel camera system as a tool for monitoring differences in mouse labor

Allison Spillane[1,2], Pawan K. Shahi[1,2], Zachary Wright[3], and Bikash R. Pattnaik[1,2,4]

[1]University of Wisconsin-Madison, Department of Pediatrics, Wisconsin, USA.
[2]University of Wisconsin-Madison, McPherson Eye Research Institute, Wisconsin, USA.
[3]SwiftSCIENCE, Philadelphia, Pennsylvania, USA.
[4]University of Wisconsin-Madison, Department of Ophthalmology and Visual Sciences, Wisconsin, USA

SUMMARY

Mice are a standard animal model used in reproductive research. The traditional monitoring of pregnancy and labor in mice relies on in-person visualization. These methods require more time and labor for researchers and the use of more invasive techniques. Additionally, since mice typically give birth at night and cannibalize sick or dead mouse pups, pregnancy factors such as time of labor, number of pups, and pup survival cannot be accurately identified using traditional methods. Several studies have demonstrated that the use of a camera system can more accurately determine the onset of labor in mice. However, these camera systems were not specifically designed for animal research or were not available for use in other labs. The investigation of several pregnancy and labor factors has not been reported in a single study using video recordings. Additionally, the use of a camera system to compare pregnancy and labor differences in genetically mutant mice, compared to WT mice, has not been reported. We demonstrated that the SwiftSCIENCE camera system, specifically designed for continuous monitoring of research animals, was successful in identifying multiple pregnancy factors. The number of pups born, pup survival, length of days between pregnancy, and labor times between mice harboring a HET mutation to *Kcnj13* were compared to WT mice. The integration of this camera system in rodent reproductive studies can provide a more accurate and specific understanding of pregnancy and labor, while decreasing the amount of animal handling and labor required of traditional monitoring.

INTRODUCTION

Rodents, including mice, are a standard animal model for the investigation of reproduction and are relatively translatable to human reproduction [1]. Additionally, a short gestational period makes mice a suitable model for pregnancy studies. Traditional identification of mouse labor and birth has relied on in-person visualization of mouse cages. The use of devices, such as transcervical intrauterine pressure catheters, has improved the ability to monitor labor in vivo [2]. Additionally, a few studies have utilized camera systems to determine the timing of labor. One study used a camera system to monitor the time of mouse delivery [3]. However, the details about the monitoring system used, including whether it is commercially available or for research use only (RUO), were not stated. Additionally, continuous pregnancy monitoring and assessment of other pregnancy and labor factors, such as pup number, were not described. Another study utilized a commercially available camera to monitor the length of gestation and to identify incidences of preterm labor in mice [4]. The analysis of other pregnancy or labor factors was not reported. A continuously monitoring camera system created explicitly for animal research use has not been used to compare several aspects of pregnancy and labor in mice.

Camera systems have progressed research in other areas of mouse model research. Several studies have used a video tracking and machine learning system for the analysis of mouse behavior [5-7]. Not only did these studies advance the understanding of mouse behavior, but they also reduced the amount of handling necessary for classic behavioral tests, thereby decreasing potential changes in mouse behavior caused by human handling. Video systems also reduced the amount of human labor required for traditional, non-video monitored methods. Infrared thermography (IRT) cameras have also been used to monitor the temperature of mice [8]. These camera studies have demonstrated the benefits of using a high-throughput, non-invasive method of monitoring mouse models. Therefore, we believe that using a camera system to monitor mouse pregnancy and labor can improve reproductive research studies.

Our lab was interested in studying how the loss of an ion channel, due to a PTC mutation, affected mouse pregnancy and labor. Mutations in *KCNJ13* lead to loss of function in Kir7.1, resulting in

blindness in human patients [9]. Additionally, chemical alteration of Kir7.1 activity and knock-out of Kir7.1 in the mouse uterus resulted in changes to uterine contractility [10]. Indicating that Kir7.1 is necessary for the prevention of contractions during mid-gestation. No other studies have investigated Kir7.1's role in pregnancy, demonstrating the necessity to further understand Kir7.1's function and dysfunction in pregnancy and labor.

Ideally, a homozygous *Kcnj13* mutant mouse model would be used to investigate Kir7.1 dysfunction in the uterus. However, previous attempts to create homozygous (HOMO) mouse models have observed that a HOMO phenotype is lethal in mice [11-13]. These studies reveal that functional Kir7.1 expression is necessary for lung development in mice, therefore leading to lethality shortly after birth when there is loss-of-function to this channel. A study investigating the effect of a HET mutation in *Kcnj13* in a mouse model, revealed that the HET mutation led to altered physiology in the kidney [13]. The effect of partial loss of Kir7.1 was not enough to cause hypertension, but was enough to cause alterations in the ability of the kidney to maintain electrolyte homeostasis. Therefore, we hypothesized that partial loss of Kir7.1, resulting from a HET mutation in a mouse model, would lead to physiological changes in the uterus that could be observed through changes in pregnancy and labor. Our lab has previously created a mouse model with a W53X HET mutation to *Kcnj13* [14]. Due to the success of camera monitoring in behavioral mouse studies, we aimed to use a novel camera system from SwiftSCIENCE that was created for animal research use to monitor pregnancy and labor differences between WT and HET mice.

PROTOCOL

Animal studies were approved and conducted in accordance with the University of Wisconsin-Madison Institutional Animal Care and Use Committee (IACUC) guidelines (protocol #: M005434). C57BL/6J WT and mice that were previously generated to be HET for the W53X mutation to *Kcnj13*, were

compared to WT mice [15]. Animals were housed in a temperature-controlled (25±5°C) animal facility at the University of Wisconsin-Madison. Additionally, mice were kept in a 12-hour light/12-hour dark cycle.

SwiftSCIENCE supplied all equipment used for the camera set-up.

Set-up of the camera system

1.) Two cameras from SwiftSCIENCE (USBFHD05MT-KL156IR) were attached to adjustable camera clamp mount ball heads (UTEBIT Mini Ball Head, Tripod Head with ¼" Hot Shoe, 360° Rotatable Ball Heads Camera Mount Adapter, Aluminum 20mm Ball head) **(Figure 1A)**. One camera was used to capture a view from the front side of the cage, and the other was positioned to capture a view from the rear side of the cage **(Figure 1B)**.

2.) Camera clamp mount ball heads were then attached to a desk clamp (UTEBIT Small C Clamps 2 inch with ¼" and 3/8" thread hole for desktop mount tables with aluminum support) **(Figure 1C)**. An extender camera desk mount was utilized in case the UTEBIT camera mount could not reach far enough to allow for cage visualization (JINSUI Camera desk mount webcam stand with 360° ball head, adjustable table light stand 14" to 33", tabletop C-clamp) **(Figure 1D)**.

3.) The clamps were then attached to the mouse rack system **(Figure 1E)**.

4.) Cameras were plugged into a data relay box supplied by SwiftSCIENCE that captured and transferred video footage over to the SwiftSCIENCE cloud server **(Figure 1F)**.

5.) The box has to be on the network either through Wi-Fi or a wired Ethernet port to allow for data transfer. Ethernet port connectivity is preferred for faster and more secure transfer without signal loss.

6.) An infrared (IR) light was fabricated using an 850nm LED light strip by SwiftSCIENCE. It was attached with zip-ties to the top of the mouse cage housing to allow for IR camera nighttime visualization **(Figure 1G)**. This was necessary for assessing the labor of mice due to labor typically taking place during the 12-hour dark cycle [9].

7.) A cage containing a breeding pair was housed within a rack that contained a camera for continuous monitoring **(Figure 1H)**. For our studies, the male and female mice were never separated; however, traditional separation of mice after 24-48 hours could be easily accomplished.

Downloading data from SwiftSCIENCE

Videos are recorded and stored continually on the SwiftSCIENCE cloud server and accessed through their website. This allowed for continuous monitoring of pregnancy. The website is secure with limited access to lab members with permission.

1.) "Video Viewer" within the SwiftSCIENCE website was selected and used to review collected data which have a date and time stamp. **(Figure 2A)**. The videos were analyzed for date and time of contractions and birth of the pups. The date and time of labor were noted for video downloads.
2.) "Download Videos By Date Range" was selected to search by date and time for data visualization and interpretation. **(Figure 2B)**.
3.) "Download" was selected, and videos were downloaded to the computer **(Figure 2C)**.
4.) Videos were visible in 30-second increments. The videos were opened, viewed, and analyzed using VLC Media Player (Version 3.0.20 Vetinari).
5.) Additionally, videos could be analyzed directly on the SwiftSCIENCE server. However, videos were typically stored on the server for a maximum of 3 months, so downloading necessary videos was suggested.

Data analysis for pregnancy and labor outcomes

Due to the continuous recording and storage of videos, several pregnancy and labor factors can be more accurately monitored. This includes the number of pups born, pup survival rates, interval

between pregnancies, and duration of labor. Pups are visible using the monitoring system, allowing for the accurate and straightforward identification of the number of pups born as well as their survival. Additionally, the length of labor can be assessed (described below). In our case, where breeding pairs were never separated, assessing the start and end of labor times provides for precise identification of the interval between pregnancies.

Length of labor was analyzed as follows:

1.) The first visible sign of the initiation of labor was contractions. During a contraction, the mouse arched her back down towards the floor of the cage and pushed her feet backwards, as visualized in **Figure 3A and B**.
2.) During the initiation of birth, the mouse would perform a pushing move. This was visualized by a large arching of the back up towards the top of the cage, followed by a downward motion to return to the pre-pushing positioning of the back **(Figure 3C and 3D)**.
3.) Following 1+ push, the pup exiting the birth canal is visible **(Figure 3C and 3D)**. Visualization of the pup exiting the birth canal is dependent on the position of the mouse.
4.) Once the pup is born, the mother will clean the pup and eat the placenta. This could be used as a secondary method of identification for pup birth, if visualization of the pup exiting the birth canal was not possible due to the mother's positioning during pushing.
5.) This process of contraction, pushing, birth of the new pup, cleaning of the pup, and eating the placenta is repeated until all pups have been born.

Statistical Analysis

A two-tailed Student’s t-test was performed using Microsoft Excel for the statistical analysis. Differences were considered statistically significant at $p < 0.05$; the results are expressed as mean ±SEM.

Acknowledgements:

Schematic images were created with Biorender.com.

REPRESENTATIVE RESULTS

Litter size, pup survival, and length between pregnancies monitored by a camera system

Differences between pregnancies were compared between WT and HET mice using the camera system. Comparison between litter sizes of WT (6.125 ± 0.701) and HET (6.600 ± 0.545) mice demonstrated no difference (p=0.601) **(Fig. 4A)**. Additionally, the length of time between pregnancy was investigated. No statistically significant differences (p=0.268) in length between pregnancies were observed in HET (30.050 ± 2.634) and WT (35.563 ± 4.182) mice **(Fig. 4B)**. There was a statistically significant difference (p=0.006) in pup survival between WT (29.618 ± 7.903) and HET (62.800 ± 7.380), with high variance **(Fig. 4C)**.

Length of labor monitored by the camera system

The length of labor was compared between WT and HET mice. A time-lapse of the birth of each pup through the labor of 4 WT (blue) and 4 HET (purple) mice are depicted in **Fig. 5A**. A comparison between the total time of labor, measured by first to last pup birth, demonstrated a trend towards longer length of labor in HETs (150.000 ± 26.481), compared to WT (86.000 ± 30.174) **(Fig. 5B)**. However, this trend was not statistically significant (p=0.217). Because labor time could be dependent on the number of pups birthed, time between each pup birth was compared between WT and HET mice **(Fig. 5C)**. A slight trend for longer times between HET pup births (20.690 ± 3.770), compared to WT pup births (18.105 ± 6.661), was observed. However, this difference was not statistically significant (p=0.724).

DISCUSSION

Previous studies using camera monitoring systems to assess pregnancy and labor differences have been used [3, 4]. However, the evaluation of multiple pregnancy and labor factors within one study was not assessed. Camera studies were also not used to compare genetically different mouse models, such as a HET and a WT model. Additionally, previous camera systems used in mouse pregnancy studies were not specifically designed for animal research use or made available for other research labs to use. We demonstrated that a continuously monitoring camera system from SwiftSCIENCE, specifically designed for animal research, was able to assess pregnancy and labor in mice. We used the camera system to continuously monitor HET and WT mice and determine the pregnancy and labor effects of partial loss of Kir7.1 function. Images of the camera setup and the process of downloading videos were illustrated in **Fig. 1 and 2**. Labor of mice was characterized by contractions **(Fig. 3A and B)**, pushing **(Fig. 3C and D)**, visualization of the pup exiting the birth canal **(Fig. 3C and D)**, cleaning of the pup, and consumption of the placenta.

We did not observe any differences between WT and HET mice in the number of pups born or the length of time between pregnancies **(Fig. 4A and B)**. A statistically significant ($p=0.006$) difference in pup survival was observed **(Fig. 4C)**. However, the reasons for this observation are unknown, and high variability warrants further investigation.

Total labor time and time between pup births demonstrated a non-statistically significant ($p=0.217$) trend towards longer labor times in HET mice, compared to WT mice **(Fig. 5B)**. This trend suggests that a partial loss of WT Kir7.1 in HET mice could be leading to altered myometrium physiology during labor. However, additional evaluation comparing partial loss of Kir7.1 mice to WT mice is necessary to further elucidate if these potential differences are present and to identify the pathophysiological differences leading to changes in labor.

One advantage of using this camera system is the ability to remotely and continuously monitor cages. This enables less invasive monitoring of pregnancy and labor, as well as more accurate

identification of the labor and birth stages. Additionally, this camera system allows for better accuracy in identifying the litter size and pup survival. Traditional monitoring methods of the number of pups born and pup survival rates are determined by in-person visualization of the cage. However, mice cannibalize pups that are stillborn or die shortly after birth [17]. Therefore, in-person visualization can be inaccurate if cages are not assessed soon after birth is complete. The versatility of this camera system also allows for modification of rack attachment equipment. Therefore, allowing for the versatility of different rack styles to use this camera system.

One limitation of the camera system used in this study was Wi-Fi disconnection issues. There was no available Ethernet port in our animal facility room; therefore, we relied on a Wi-Fi connection for the box to transfer videos to the SwiftSCIENCE website for analysis. When the Wi-Fi connection was lost, recordings were not saved, resulting in some lost data. Therefore, we suggest the use of a direct Ethernet connection to avoid this limitation. Another current limitation to this camera system is that pup identification is reliant on human assessment; therefore, it increases the time it takes to identify the time of labor and the number of pups. The use of artificial intelligence (AI) or machine learning can decrease the labor and time necessary to analyze videos. Previous studies have demonstrated a decrease in human labor times to assess videos by using machine learning with camera monitoring [5]. The future development of machine learning or AI, in conjunction with continuous camera monitoring, can help mitigate this limitation. Another limitation is that pups are difficult to identify under IR light due to their coloration **(Fig. 3C)**. However, movement of the pup was sufficient to detect its presence under IR light, and future improvements to this system can further aid in accurate identification. Mouse labor typically occurred during the 12-hour dark cycle; therefore, integrating IRT technology into this camera system could assist in identifying pups under IR light. IRT cameras have been successful in previous studies using cameras to monitor mouse behavior [8]. The IRT cameras used in the study were placed inside the animal cage. In the case of our camera system, the cameras are positioned outside of the cage. Therefore, thermal cameras would need to identify temperatures through the animal cages accurately.

CONCLUSION

In conclusion, we demonstrated that a novel camera system from SwiftSCIENCE, designed for animal monitoring in a research setting, was successfully able to monitor mouse pregnancy and labor continuously. The use of this system in future rodent reproductive studies could substantially improve the accuracy and understanding of pregnancy and labor within these animal models.

FIGURES AND TABLES

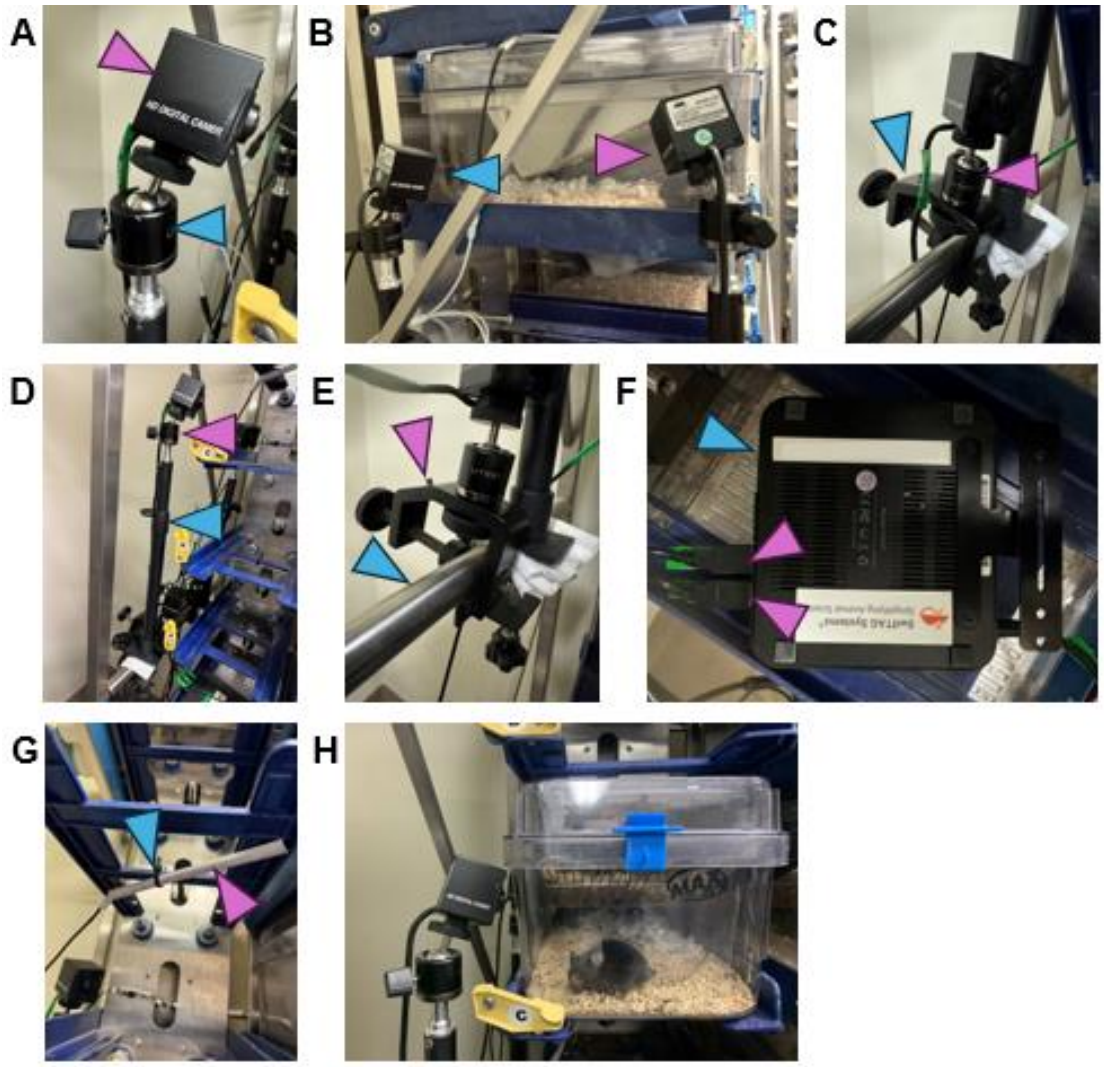

Figure 1: Camera setup illustrating rear and front camera, IR light, camera clamp for securing the camera to the cage rack, and box for collection of data and transfer to SwiftSCIENCE website for analysis. (A) The camera (indicated by the purple arrowhead) was attached to the ball head camera mount (blue arrowhead). **(B)** Each cage had a front camera (purple arrowhead) and a rear camera (blue arrowhead). **(C)** Ball head camera mount (purple arrowhead) was attached to desk clamp (blue arrowhead). **(D)** For cages that required extended reach, ball head camera mounts (purple arrowhead) were attached to extender camera desk mounts (blue arrowhead). **(E)** Desk clamps and desk mounts

(purple arrowhead) were attached to the mouse rack system (blue arrowhead). **(F)** Cameras (purple arrowheads) were plugged into the SwiftSCIENCE-supplied box (blue arrowhead). The box sent the videos over to the SwiftSCIENCE website for video analysis. **(G)** IR light (purple arrowhead) was attached to the mouse cage rack using a zip tie (blue arrowhead). **(H)** The breeding cage was positioned under the camera setup for video recording.

Figure 2: Schematic illustrating how to download videos from SwiftSCIENCE website for analysis. **(A)** On the SwiftSCIENCE website, “Video Viewer” (purple arrowhead) was selected to monitor videos captured by the cameras and uploaded by the SwiftSCIENCE box. **(B)** To download videos, “Download Videos By Date Range” (purple arrowhead) was selected. **(C)** The target date (orange box) and time ranges (green boxes) during labor were determined, and the “Download” (purple arrowhead) option was selected to download videos to the computer for analysis. Time ranges are in hour: minute: second (h:m:s).

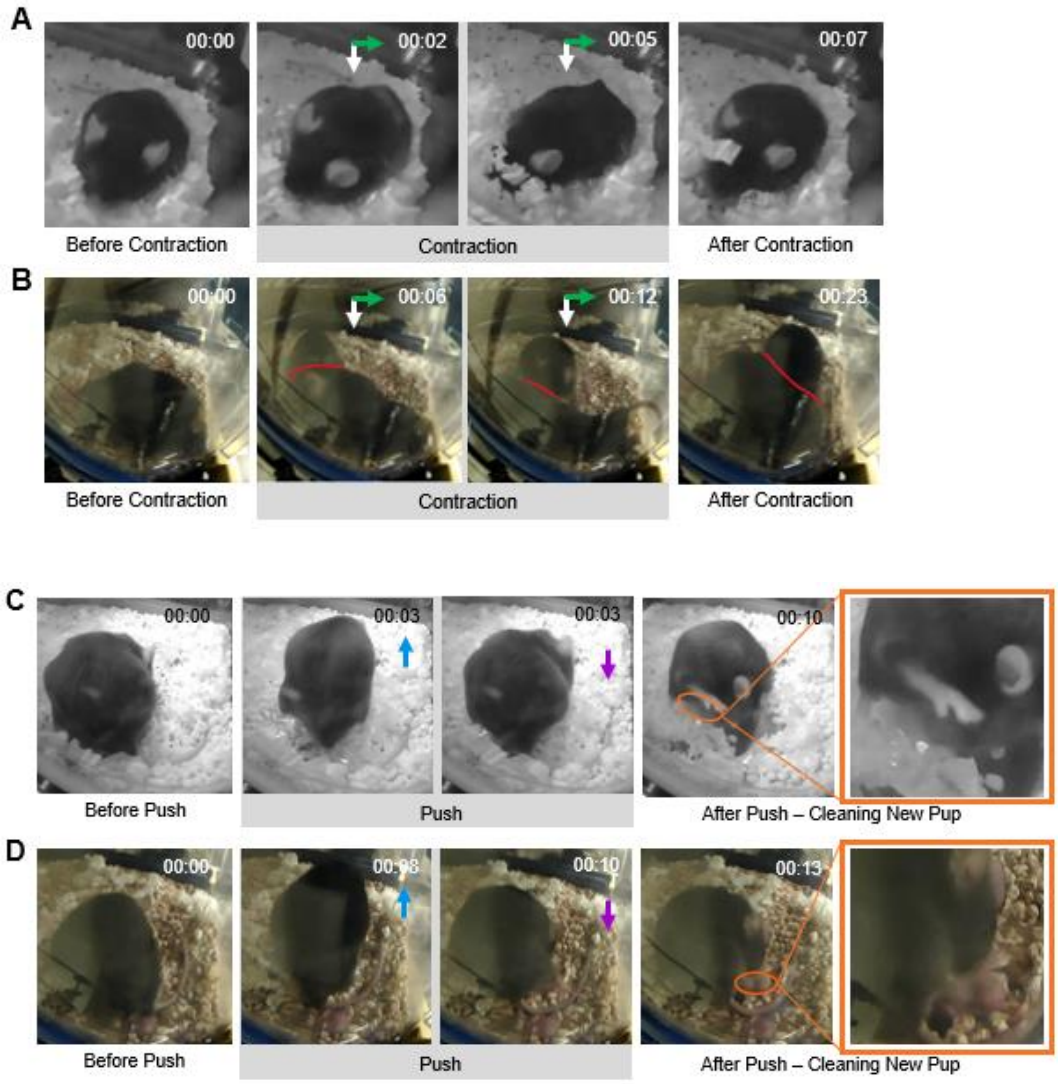

Figure 3: Methodology of video analysis for mouse labor and birth. (A) Contractions under the IR camera demonstrated that the back is arched down (white arrow) and the feet pushed backwards (green arrow). Time before contraction, starting at 00:00 (m:s) illustrated the length of the contraction. **(B)** Images under room light demonstrated a contraction. The red line denoted the separation of the female body (bottom) from the male body (top) in the image. **(C)** Pushing a pup out under IR light. The back arched up (blue arrow), then back down (purple arrow) during one push. Once the pup was wholly or partially pushed out, the female cleaned the new pups (orange circle and box). Time in m:s, beginning at 00:00, depicts the length of one push. **(D)** Images demonstrated pushing under the room light.

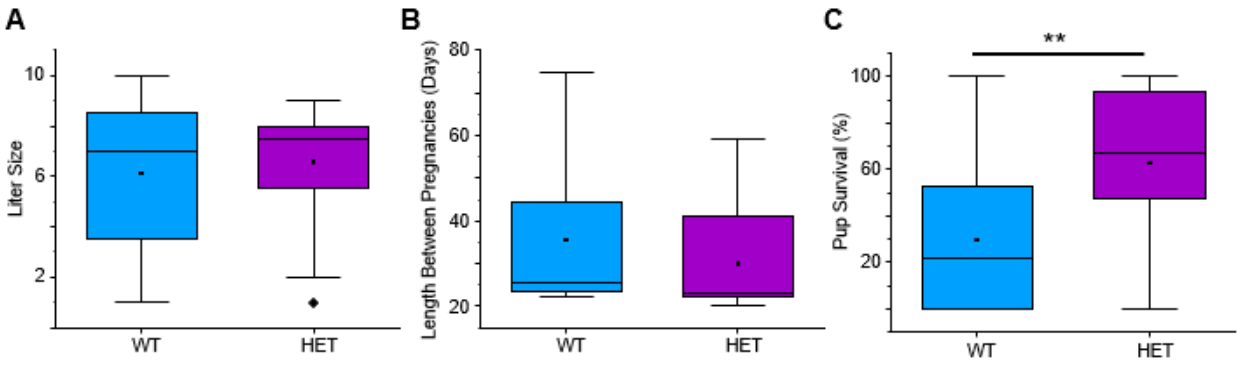

Figure 4: Comparison of pregnancy-related differences between WT and HET mice as analyzed on the camera system. (A) Litter size across pregnancies for WT (blue, n=23) vs HET (purple, n=20). Average litter size for each was: 6.125 for WT and 6.6 for HET. SEM was 0.701 for WT and 0.545 for HET. **(B)** Comparison of WT (blue, n=23) vs HET (purple, n=20) for length between pregnancies. Average values were as follows: 35.563 for WT and 30.050 for HET. SEM values for WT was 4.182 and for HET was 2.634. No statistically significant difference between WT and HET was observed. **(C)** Percentage of pups that survived for WT (blue, n=23) compared to HET (purple, n=20). The average pup survival rate for WT was 29.618%, and for HET, it was 62.800%. The SEM for WT was 7.903, and for HET was 7.380. A two-tailed Student's t-test demonstrated that the difference between WT and HET was significant (p=0.006).

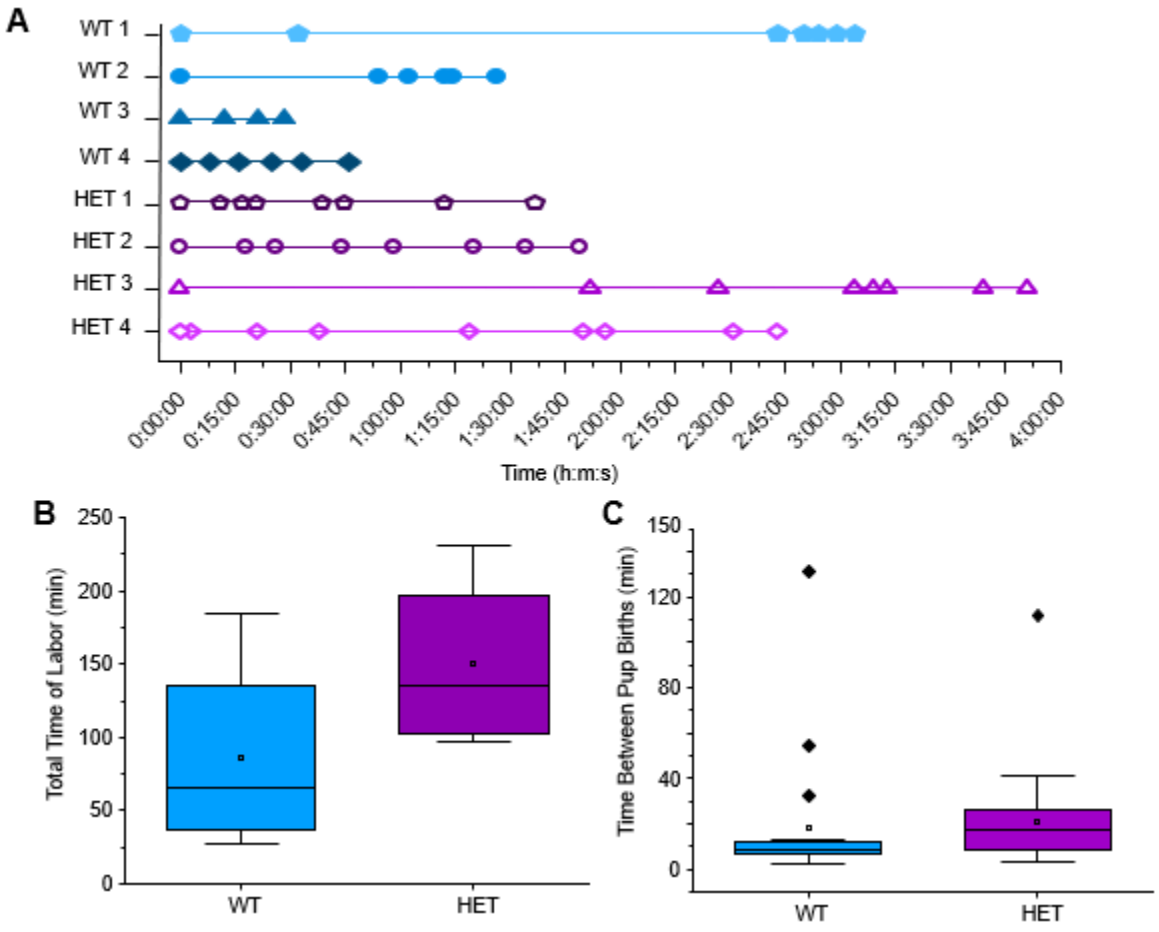

Figure 5: Labor differences between WT and HET mice as analyzed on the camera system. (A) Time-lapse indicating time of each pup birth for WT (blue, n=4) vs HET (purple, n=4). Time on the x-axis is shown as hours:minutes:seconds (h:m:s). **(B)** Total time of labor between WT and HET. A trend of HET having a longer total labor length was observed, but this difference was not statistically significant. The average time was 86 for WT and 150 for HET. SEM values were 30.174 for WT and 26.481 for HET. **(C)** Box plot representing the time between the birth of each pup across 4 pregnancies for each genotype, described in the time-lapse: WT (blue, n=19) vs HET (purple, n=29). The average for WT was 18.105, and for HET, it was 20.690. SEM values were as follows: 6.661 for WT and 3.770 for HET. The difference between WT and HET was not statistically significant.

REFERENCES

1. Elvis-Offiah, U.B., et al., *Our Clear-Cut Improvement to the Impact of Mouse and Rat Models in the Research Involving Female Reproduction*, in *Animal Models and Experimental Research in Medicine*. 2022, IntechOpen.
2. Robuck, M.F., et al., *Monitoring uterine contractility in mice using a transcervical intrauterine pressure catheter.* Reproduction, 2018. **155**(5): p. 447-456.
3. Rinaldi, S.F., et al., *Decidual neutrophil infiltration is not required for preterm birth in a mouse model of infection-induced preterm labor.* J Immunol, 2014. **192**(5): p. 2315-25.
4. Garcia-Flores, V., et al., *A single-cell atlas of murine reproductive tissues during preterm labor.* Cell reports, 2023. **42**(1).
5. Hong, W., et al., *Automated measurement of mouse social behaviors using depth sensing, video tracking, and machine learning.* Proc Natl Acad Sci U S A, 2015. **112**(38): p. E5351-60.
6. Spink, A.J., et al., *The EthoVision video tracking system--a tool for behavioral phenotyping of transgenic mice.* Physiol Behav, 2001. **73**(5): p. 731-44.
7. Noldus, L.P., A.J. Spink, and R.A. Tegelenbosch, *EthoVision: a versatile video tracking system for automation of behavioral experiments.* Behav Res Methods Instrum Comput, 2001. **33**(3): p. 398-414.
8. Mufford, J.T., et al., *The development of a non-invasive behavioral model of thermal heat stress in laboratory mice (Mus musculus).* J Neurosci Methods, 2016. **268**: p. 189-95.
9. Pattnaik, B.R., et al., *A Novel KCNJ13 Nonsense Mutation and Loss of Kir7.1 Channel Function Causes Leber Congenital Amaurosis (LCA16).* Hum Mutat, 2015. **36**(7): p. 720-7.
10. McCloskey, C., et al., *The inwardly rectifying K+ channel KIR7.1 controls uterine excitability throughout pregnancy.* EMBO Mol Med, 2014. **6**(9): p. 1161-74.
11. Villanueva, S., et al., *Cleft Palate, Moderate Lung Developmental Retardation and Early Postnatal Lethality in Mice Deficient in the Kir7.1 Inwardly Rectifying K+ Channel.* PLoS One, 2015. **10**(9): p. e0139284.

12. Anderson, E.J.P., et al., *Late onset obesity in mice with targeted deletion of potassium inward rectifier Kir7.1 from cells expressing the melanocortin-4 receptor.* J Neuroendocrinol, 2019. **31**(1): p. e12670.

13. Zietara, A., et al., *K(ir)7.1 knockdown and inhibition alter renal electrolyte handling but not the development of hypertension in Dahl salt-sensitive rats.* Am J Physiol Renal Physiol, 2023. **325**(2): p. F177-F187.

14. Kabra, M., et al., *Nonviral base editing of KCNJ13 mutation preserves vision in a model of inherited retinal channelopathy.* The Journal of Clinical Investigation, 2023. **133**(19).

15. Kabra, M., et al., *Nonviral base editing of KCNJ13 mutation preserves vision in a model of inherited retinal channelopathy.* J Clin Invest, 2023.

16. Burkholder, T., et al., *Health Evaluation of Experimental Laboratory Mice.* Curr Protoc Mouse Biol, 2012. **2**: p. 145-165.

17. Filipovich, Y., et al., *Maternal and fetal roles in bacterially induced preterm labor in the mouse.* Am J Obstet Gynecol, 2016. **214**(3): p. 386 e1-9.

Chapter 6: Novel expression of Kir7.1 in uterine structures in mice and non-human primates

Allison Spillane[1,2], Kaia Kapfer[1,2], Pawan K. Shahi[1,2], Bikash R. Pattnaik[1,2,3]

[1]University of Wisconsin-Madison, Department of Pediatrics, Wisconsin, USA.
[2]University of Wisconsin-Madison, McPherson Eye Research Institute, Wisconsin, USA.
[3]University of Wisconsin-Madison, Department of Ophthalmology and Visual Sciences, Wisconsin, USA

SUMMARY

APOs and infertility are a global issue that leads to long-term health problems in the mother and offspring. Therefore, cases of unknown causes of APOs are alarming and require further investigation into possible pathophysiological causes. Ion channel dysfunction and genetic mutations could be causes of unknown cases. One ion channel that has been implicated in the prevention of contractions during mid-gestation is Kir7.1. Additionally, patients harboring mutations to *KCNJ13*, which encodes Kir7.1, have been identified but have not reached reproductive age. If this channel is vital for preventing contractions, the loss of Kir7.1 could lead to preterm labor. We wanted to further investigate the expression of Kir7.1 in the uterus during pregnancy, using a mouse model. Additionally, uterine samples from NHP were used to ensure results in mice were translatable to human patients. Kir7.1 was expressed in the mouse uterus on D15, but not on D13, D18, or in a NP state; supporting previous literature. However, mid-gestation uterus from NHP on GD90 revealed no Kir7.1 expression. Only one NHP GD90 sample was obtained; therefore, this observation requires further investigation. Kir7.1 was also expressed in the LE of mice and NHP. Additionally, a novel finding of Kir7.1 expression across animal models in the GEp glands and vasculature was observed. This expression was present throughout pregnancy and in the NP state. Quantification of whole uterine samples revealed similar trends to those previously reported in mouse myometrium. The presence of Kir7.1 throughout the myometrium and endometrium tissues suggests that Kir7.1 plays a role in various pregnancy processes. Therefore, loss of Kir7.1, such as through a genetic mutation, could result in many different APOs or infertility. Further research into the role of Kir7.1 in the function and

dysfunction of these tissues is essential to determine if the loss of Kir7.1 could be a cause of unknown cases of APOs or infertility.

INTRODUCTION

APOs are a global issue and have been demonstrated as affecting 1 in every 5 births in the United States [1-5]. APOs lead to adverse outcomes for the mother and offspring, including long-term health issues. These outcomes include preterm labor, HDP, GDM, high birth weight, and low birth weight. Additionally, infertility and impaired fecundity prove to be another global pregnancy-related issue [6, 7]. Although long-term physical health issues are not associated with infertility and impaired fecundity, it increases mental health risks for the men and women facing these challenges [8]. The prevalence of each of these APOs and infertility-related problems is outlined in **Chapter 1**. Although some causes are known, many cases of unknown origin remain. Therefore, it is vital that further understanding into the pathophysiological causes of these APOs and infertility is investigated to improve short- and long-term health outcomes of mothers and their offspring.

One potential cause of these unknown cases is genetic mutations and predispositions. Genetic links between preterm birth [9], HDP [10, 11], gestational diabetes [12-17], high birth weight [18], low birth weight [16, 17], and infertility [19-26] have been identified. These findings demonstrate that other genetic mutations and predispositions could explain some of the unknown cases of APOs and infertility.

Ion channels are necessary for the initiation and maintenance of pregnancy, as well as for labor and birth. Uterine quiescence and contractility are controlled by Ca^{2+}, Na^{+}, K^{+}, and Cl^{-} channels [27-30]. Therefore, dysfunction of the uterine myometrium due to loss of ion channel function could lead to preterm labor. The LE and GEp, or uterine glands, within the uterine epithelial layer express Ca^{2+}, Na^{+}, K^{+}, and Cl^{-} channels [31-34]. The LE and GEp are critical for implantation, placental development, placental growth, and support of the fetus for the first trimester [35-41]. Therefore, ion channel dysfunction in these tissues could lead to issues with infertility or impaired fecundity. Additionally, low

birth weight or high birth weight could result if proper placental development and support of the fetus are not achieved. For the uterine vasculature, Ca^{2+} and K^+ channels have demonstrated essential roles in blood supply physiology [42-45]. The necessary role that ion channels play in pregnancy could explain some of the unknown causes of APOs and infertility and warrant further investigation.

One K^+ channel that has been identified in the uterus, which we were particularly interested in, was Kir7.1. One study has reported that Kir7.1 is expressed in mouse and human myometrium, demonstrating a decrease in expression as the uterus moves into labor [30]. Additionally, blocking the channel led to an increase in the contractility of mouse myometrium tissue, and overexpression of Kir7.1 demonstrated a decrease in contractility. This suggests a vital role of Kir7.1 in maintaining uterine quiescence in mid-gestation, and, therefore, in preventing preterm labor. Another study confirmed these results in mice and demonstrated that treatment with P4 led to an increase in Kir7.1 activity and a subsequent decrease in contractility [46]. P4 is circulated during early and mid-gestation and has been demonstrated to activate Kir7.1 in the choroid plexus of the brain [47, 48]. Therefore, Kir7.1 activity and P4 activation of Kir7.1 in mid-gestation help to maintain a state of uterine quiescence. However, follow-up studies are necessary to confirm if loss of Kir7.1 function is enough to cause preterm labor.

Female patients with mutations to *KCNJ13*, the gene encoding Kir7.1, have been identified [49-52]. However, these patients have not reached reproductive age. Due to the lack of investigation into the role of Kir7.1 in the uterus and the identification of human patients with loss-of-function Kir7.1 mutations, we wanted to further investigate the expression of Kir7.1 in the uterus. Mice are a standard model for investigating reproduction and pregnancy, and studies have demonstrated that these findings are predominantly translatable to human physiology [53]. Additionally, the gestational cycles in mice are fast, typically ranging from 18 to 21 days, thus allowing for an efficient model of pregnancy [54]. In comparison, on average, human gestation is 268 days and NHP is 165 to 168 days [55-57]. Therefore, we chose to use a mouse model to compare differences in Kir7.1 expression throughout pregnancy, between WT and mice that were HET for a mutation to the *Kcnj13* gene [51]. We aimed to use a HOMO mutant mouse model; however, complete loss of Kir7.1 leads to lung development issues and subsequent death in

mouse pups [58-60]. Therefore, we utilized HET mutant mice to identify changes to the partial loss of Kir7.1. NHP uterine tissue was used as a control to demonstrate if our mouse study would be translatable to humans.

RESULTS

HET mice weigh more than WT mice.

We wanted to collect the mouse uterus to identify changes in Kir7.1 expression throughout pregnancy and to investigate any differences in expression between WT and HET mice. Female mice were bred with males for 48 hours, before separation **(Fig. 1A)**. Female weights were measured between D7-D11 to determine gestational age. Previous studies have demonstrated that a weight gain of 1.4g occurs between D7.5 and D10.5:

D10.5-D7.5

Therefore, allowing for the identification of gestational age [61]. Pregnant mouse uteri were collected on D13, D15, and D18; as these time points have been identified as having varying levels of Kir7.1 in the uterus myometrium [30]. The NP mouse uterus was also collected to examine Kir7.1 expression prior to pregnancy. Additionally, NP and pregnant NHP uterus was collected to compare with the mouse uterus and understand if mouse studies would be translatable to human pregnancy. WT mice that did not become pregnant maintained a steady weight throughout the measured time periods of weight measurements **(Figure 1B, left graph)**. Averages and SEMs are, as follows: 21.400 ± 3.337 for D0, 22.200 ± 3.464 for D7, 22.300 ± 3.477 for D8, 22.200 ± 3.473 for D9, 22.300 ± 3.473 for D10, and 22.400 ± 3.507 for D11. For WT mice that became pregnant, a trend of increasing weight gain was observed with a significant difference between D0 and D11 of p=0.015 **(Fig. 1B, right graph)**. Average and SEM values for WT pregnant mice were: 21.9 ± 33.900 for D0, 23.100 ± 3.579 for D7, 23.700 ± 3.658 for D8, 23.700 ± 3.667 for D9, 24.300 ± 3.728 for D10, and 25.600 ± 3.958 for D11. For HET mice that were NP, steady weights were observed throughout the measurement days **(Fig. 1C, left graph)**. The average and SEM

values were: 25.100 ± 4.053 for D0, 24.908 ± 4.017 for D7, 25.000 ± 4.038 for D8, 25.100 ± 4.049 for D9, 25.100 ± 4.039 for D10, and 25.100 ± 4.062 for D11. HET mice that were pregnant demonstrated a slight increase in weight throughout the measured days of gestation **(Fig. 1C, right graph)**. Average and SEM values were as follows: 27.500 ± 3.826 for D0, 28.800 ± 3.991 for D7, 29.300 ± 4.054 for D8, 29.500 ± 4.079 for D9, 30.300 ± 4.180 for D10, and 31.600 ± 4.364 for D11. Although a trend towards increasing weight was observed, no statistically significant differences in weight were found between days. Comparisons between WT and HET mice's average weights over gestational days were compared **(Fig. 1D)**. When comparing the weight of WT versus HET for NP mice between each gestational day, a statistically significant increase in weight for HET mice was observed for all days except for D11. For D11, there was a slightly insignificant increase of p=0.052 **(Fig. 1D, top graph)**. Additionally, a statistically significant increase in HET mouse weight compared to WT at each time point in pregnant mice was observed **(Fig. 1D, bottom graph)**. Demonstrating that HET mice maintained a consistently heavier weight than WT mice. To determine the gestational age of mice, weight differences between D7 to D10, calculated as:

D10-D7

or D8 to D11, calculated as:

D11-D8

were compared; similar to a previously published study [61]. Two days were compared because mice were bred for a total of 48 hours. Trends between WT and HET mice suggested that HET mice gained slightly more weight during gestation than WT **(Fig. 1E)**. Averages and SEMS were: 1.028 ± 0.176 for WT D10-D7, 1.470 ± 0.353 for HET D10-7, 1.919 ± 0.372 for WT D11-D8, and 2.333 ± 0.735 for HET D11-D8.

Kir7.1 is expressed in the D15 mouse myometrium but is not expressed in NHP during mid-gestation.

Uteri collected pre-pregnancy and throughout pregnancy were collected from mice and NHP and analyzed for myometrial structure and Kir7.1 function. Only one HET mouse uterus on D18 was obtained due to breeding issues and pregnancy loss. Additionally, this mouse had experienced a miscarriage; therefore, the uterus was likely regressing towards a NP state. Myometrial structures appear visually similar between WT and HET mice. **(Fig. 2A)**. The general trends observed for both WT and HET mice were an increase in spacing between muscle fibers in the myometrium from NP and D13, and from D13 and D15. This appears to be slightly more distinct in HET mice as the myometrium appears to have more spacing between muscle fibers on D13 and D15, compared to WT. However, further confirmation of these potential differences between genotypes is necessary to draw strong conclusions. Additionally, the myometrium visually appears to have a decrease in spacing between muscle fibers from D15 to D18. This was more pronounced in HET mice, compared to WT, likely due to the miscarriage that led to regression towards a NP state. NHP uteri for NP and GD90, which is mid-gestation for NHP, were compared for myometrium structure **(Fig. 2A)**. Uterine myometrium appeared to have some increase in spacing between muscle fibers; however, this was not as pronounced as in the mice. Additionally, myometrium tissue had a reduction in the number of nuclei, signifying that cells may be larger in size during mid-gestation, due to the mononucleated nature of smooth muscle cells [62]. Kir7.1 expression was not observed in mouse or NHP myometrium for NP animals **(Fig. 2B)**. Additionally, no expression is observed on D13 or D18 for both WT and HET mice. Kir7.1 was expressed on D15 for both WT and HET mice. Expression in WT mice appeared to be more pronounced than was observed in HET mice. When comparing WT and HET mice at all other gestational time-points, no visual differences were identified. Surprisingly, no expression of Kir7.1 was observed in NHP myometrium during mid-gestation.

Kir7.1 is expressed in the LE of the mouse and NHP uterus throughout pregnancy.

Throughout the pregnancy of both mouse and NHP, an increase in size, surface area, and number of luminal projections in the LE was observed during pregnancy **(Fig. 3A)**. These changes were identified as early as D13 in the mouse uterus and GD90 in the NHP uterus; however, early time points of pregnancy were not investigated in each animal model. No observable differences in LE structure were observed in WT versus HET mice apart from D18; and on D18, HET LE had a reduction in size, surface area, and number of luminal projections, which was not observed in WT. This difference in the HET LE was likely attributed to the miscarriage. Kir7.1 expression in the LE of both mouse and NHP uterus was identified **(Fig. 3B)**. Kir7.1 expression can be observed on the apical side of the luminal epithelial cells in pre-pregnancy and throughout pregnancy. There are no visible differences between WT and HET mice for LE expression.

GEp contains Kir7.1 expression throughout pregnancy in the mouse and NHP.

Staining of GEp during pregnancy in NHP and mouse uterus demonstrated a reduction in the number of GEp glands between a NP and pregnant state, respectively, in WT mice **(Fig. 4A)**. However, this reduction in GEp gland number between NP and D13 was less prominent in HET mice, compared to WT. Additionally, an increase in the number of GEp glands between D15 and D18 was observed in HET mice, but not in WT mice. This observation was most likely due to a regression of the uterus towards a NP state due to the miscarriage in the HET mouse. When comparing the size of GEp glands, no differences were observed in NP state or on D13 between WT and HET mice. However, GEp glands appear larger in HET, compared to WT, on D15. Additionally, a decrease in GEp gland size was observed between a NP state and D13 in WT and HET mice, with no change throughout pregnancy in WT mice. However, in HET mice, an increase in GEp size was observed between D13 and D15, with a reduction in the size between D15 and D18. Comparison between WT mouse and NHP GEp demonstrated that glands were larger in NHP. Additionally, there was a reduction in the size and number of GEp from a NP state to GD90 in NHP. Analysis of Kir7.1 expression in the uterus throughout pregnancy demonstrates that Kir7.1 is expressed in the apical side of GEp cells throughout pregnancy and pre-pregnancy in

mouse and NHP **(Fig. 4B)**. There are no visible differences in Kir7.1 expression between WT and HET mice or NHP and mouse GEp throughout pregnancy.

Kir7.1 is expressed in vasculature of uterus of mouse and NHP throughout pregnancy and pre-pregnancy.

Throughout pregnancy, the vasculature of both mice and NHP contains arteries, veins, and spinal arteries **(Fig. 5A)**. Spinal arteries are larger in NHP, compared to mice. Therefore, it is more difficult to differentiate between arteries and spinal arteries in mice. Additionally, the size and number of veins and arteries appeared to increase between NP and pregnant samples in all animal models. A novel finding of Kir7.1 expression in vasculature muscle cells of the uterus of mouse and NHP was observed **(Fig. 5B)**. This expression was observed throughout pregnancy, and no differences were observed between WT and HET mice or NHP versus mouse uterine vasculature. However, Kir7.1 expression in a NP state appeared to have very little expression compared to the pregnant uterus. This was observed in both mouse and NHP samples.

Differences in whole uterine Kir7.1 expression are observed in mouse and NHP throughout pregnancy.

For mouse and NHP uteri used in IHC analysis, half of the uterus was processed for qPCR analysis, and whole-uterus expression differences in Kir7.1 (m*Kcnj13*) were observed. Differences in m*Kcnj13* expression were observed in WT mice throughout pregnancy **(Fig. 6A)**. The average and SEM values are as follows: 2.694 ± 0.699 for NP, 7.884 ± 2.166 for D13, 8.276 ± 4.576 for D15, and 1.212 ± 0.069 for D18. A slight increase in expression from NP to D13 ($p=0.238$), and from D13 to D15 ($p=0.938$) was identified. A non-significant ($p=0.058$) decrease in expression was observed between D15 and D18. Additionally, a statistically significant difference in NP versus D18 ($p=0.004$) and D13 versus D18 ($p=0.003$) was noted. For HET mice, the same trends were observed but were less pronounced, and no

significant differences between any time-points were identified **(Fig. 6B)**. Average and SEM for HET mice were: 5.241 ± 1.359 for NP, 5.437 ± 1.508 for D13, 5.408 ± 2.217 for D15, and 2.500 ± 0.227 for D18. A comparison of the m*Kcnj13* expression fold change was made between WT and HET mice for each gestational day **(Fig. 6C)**. Although not statistically significant, a trend of higher expression in WT during D13 (p=0.450) and D15 (p=0.715), compared to HET, was observed. Additionally, HET mice demonstrated a non-significant (p=0.353) higher pre-pregnancy expression level compared to WT. A statistically significant increase (p=0.00003) in expression was observed in HET on D18, compared to WT. Kir7.1 expression changes in NHP (p*KCNJ13*) NP (1.035 ± 0.178), and GD90 (3.329 ± 0.740) were compared using human *KCNJ13* (h*KCNJ13*) primers **(Fig. 6D)**. A statistically significant increase (p=0.003) in Kir7.1 expression in the whole uterus was observed in GD90, compared to the NP uterus.

DISCUSSION

The previous identification of Kir7.1 in uterine myometrium quiescence was a novel finding and suggested that Kir7.1 dysfunction may play a role in preterm labor [30]. Human patients with mutations to *KCNJ13*, the gene encoding Kir7.1, have been identified and have not reached reproductive age [49-52]. Therefore, the expression, function, and dysfunction of Kir7.1 throughout pregnancy must be further investigated. We aimed to study changes in Kir7.1 expression between a WT mouse and a mouse that was HET for a *Kcnj13* mutation [51]. Additionally, the NHP uterus was used to determine if mouse uterine findings were translatable to humans.

The gestational dates of mouse tissue collection (D13, D15, and D18) were modeled after time points of high and low Kir7.1 expression in mice, as demonstrated in McCloskey et al. (2014) [30]. WT female mice were bred with WT males, and HET females were bred with WT or HET males, for 48 hours before separation **(Fig. 1A)**. Gestational weights were determined by weighing the mouse on days D7-D11 and identifying a 1.4g+ increase in weight between D7-D10 [61]. A trend for increasing weights between D0-D11 was observed in both WT and HET **(Fig. 1B, right and 1C, right)**. In contrast, weights

for both WT and HET remained stable between D0-D11 in NP mice **(Fig. 1B, left, and 1C, left)**. When average weights of pregnant and NP mice were compared between WT and HET mice, we observed that HET mice had a significantly higher weight than WT mice **(Fig. 1D)**. Previous research has implicated Kir7.1 dysfunction leading to obesity [59]. These results further suggest that even the partial loss of Kir7.1 could lead to an increase in weight. Additionally, weights for D10-D7 or D11-D8 for pregnant mice were compared to understand weight gain trends **(Fig. 1E)**. We compared two time points, as our mice are bred for 48 hours, so the time of conception could have occurred at any point within that period. HET mice had slightly higher levels of weight gain for both time periods, compared to WT. Although this finding was not statistically significant due to variability, it further supports the notion that partial loss of Kir7.1 function may be implicated in higher levels of weight gain.

NP and pregnant mouse uteri were stained to assess structural differences throughout pregnancy. Additionally, NHP NP and mid-gestation uterine samples were compared. Notable changes in the uterine myometrium of the mouse and the NHP uterus were observed. For mice, the muscle fibers had progressively more space between fibers from the NP state to D13 and from D13 to D15 **(Fig. 2A).** The myometrial tissue appeared to have decreased spacing between muscle fibers between D15 and D18, with a more pronounced effect observed in HET vs. WT mice. This was likely due to the HET mouse experiencing a miscarriage before tissue collection on D18. Since HET breeding became difficult and several pregnancy losses occurred in HET mice, no other D18 HET samples were collected for comparison. For NHP, there was also an increase in the spacing between muscle fibers of the myometrium between the NP state and mid-gestation (GD90), however, it was not as pronounced as in the mouse myometrium. To our knowledge, this is the first histological demonstration of this change in spacing between muscle fibers of the muscle cells throughout pregnancy. An increase in muscle fiber spacing within the myometrium during mid-gestation may be beneficial to prevent the synthesis of muscle contraction, and therefore, keep the myometrium in a quiescent state. A previous study illustrated that cell adhesion molecules were reduced in a non-laboring human uterus, compared to a laboring uterus [63]. A decrease in cell adhesion molecules between myometrial cells could allow for an increase in spacing

between muscle fibers. Additionally, a reduction in the number of nuclei observed in the mononucleated smooth muscle cells decreased in NHP between the NP state and GD90 [62]. This is due to hypertrophy, an increase in the size of the myocytes, during pregnancy [64]. This hypertrophy allows for support of the growing fetus, and the reduction of hypertrophy in late gestation is involved in triggering a stretch response to initiate labor [64, 65].

When assessing Kir7.1 expression in the myometrium, no expression was observed in mice for NP, D13, or D18 samples **(Fig. 2B)**. However, Kir7.1 expression was observed in the mouse uterus on D15. These results confirm previous findings and further suggest the role of Kir7.1 in preventing contractions during mid-gestation in mice [30, 46]. Further confirmation of this role could imply that total loss of Kir7.1 function could lead to preterm labor if the channel is necessary for preventing contractions during mid-gestation. No visual differences in uterine myometrial Kir7.1 expression were observed between WT and HET mice, suggesting that there may be no changes to myometrial physiology with a partial loss of Kir7.1. In NHP samples, no Kir7.1 expression was observed in NP samples. Surprisingly, no Kir7.1 expression was observed in NHP samples on GD90. A typical NHP pregnancy lasts for 134-184 days; therefore, GD90 falls right in the middle of gestation [66]. This suggests that Kir7.1 expression may be delayed later in gestation, even though its role in the uterus is throughout to be necessary to prevent contractions during mid-gestation. Additionally, NHP studies are often translatable to humans, suggesting that the same lack of mid-gestational Kir7.1 expression may also be present in humans. This study was limited to one NHP GD90 sample. Therefore, follow-up studies are required before drawing conclusions about Kir7.1 expression in the uterine myometrium during mid-gestation in NHP.

An increase in size, surface area, and number of luminal projections in the LE was observed in mice and NHP between NP and pregnant animals **(Fig. 3A)**. In the literature, an initial proliferation of the LE in the pre-implantation phase with a reduction by D4 in mice has been demonstrated [67]. To our knowledge, no studies have characterized changes in mouse LE past D4, and no studies have reported structural changes in the NHP LE. In humans, other structural changes to the LE during early pregnancy (D18) have been investigated; but changes in mid-gestation, late-gestation, or concerning the surface

area have not been reported [68]. Additionally, changes in the number of luminal projections within the LE have not been explicitly addressed in the literature. Therefore, the physiological benefits of an increase in the size, surface area, and number of projections in mid- and late-gestation are not known. There were no notable differences in LE structure between gestational days in WT and HET mice, or between mice and NHP samples. However, in D18 HET mice, a decrease was observed in the size, surface area, and number of luminal projections within the LE compared to D15. As noted, this uterus was collected from a miscarried uterus that was likely regressing towards a NP state.

Identification of Kir7.1 on the apical membrane of LE cells was observed in all samples **(Fig. 3B)**. A previous study demonstrated Kir7.1 expression in the LE of mice on D15.5 [46]. We illustrated that this expression is present throughout pregnancy and in a NP state in both mice and NHP. One of the ways in which the LE assists in implantation is by controlling fluid excretion and uptake within the lumen [69]. Kir channels have been identified as playing a role in maintaining fluid homeostasis within epithelial cells in the kidney [70]. In our study, the identification of Kir7.1 in the LE of the uterus suggests that it may be playing a role in fluid maintenance. The LE's vital role in implantation suggests that Kir7.1 dysfunction could lead to infertility or impaired fecundity [35]. The similarity in Kir7.1 expression between mice and NHP suggests that these findings could be translatable to humans. Additionally, no visible difference in Kir7.1 expression was observed between WT and HET mice. Suggesting that a HET mutation may have no effect on changes in fertility that may be observed in the case of a total loss of Kir7.1. Further studies on the role of Kir7.1 in LE function and dysfunction are required to understand if Kir7.1 plays a role in the unknown causes of infertility.

A reduction in the presence and size of GEp glands during pregnancy, compared to NP animals, was observed in WT mice and NHP **(Fig. 4A)**. However, in HET mice, a less pronounced decrease in the number of GEp glands was observed between the NP and D13 uteri. Additionally, an increase in the size of the GEp glands between D13 and D15 was observed in HET mice, but not in WT mice. The GEp are essential for implantation, placental development and growth, and support of the fetus for the first trimester of pregnancy [36-41]. Therefore, a reduction in the number and size of these glands closer to

mid- and late-gestation is not surprising. Studies have demonstrated that hyperplasia and hypertrophy of the GEp occurs in early gestation in ruminants [71]. Additionally, the formation of new GEp and proliferation of the GEp occurs postnatally in ruminants [72]. Proliferation of GEp is observed in early pregnancy of human uterine samples [68, 72]. In pigs, the GEp also undergoes genesis in the postnatal stage [72]. Additionally, GEp identification and secretion still occurs after mid-pregnancy in pigs. The comparison between changes of the uterine glands in mice and NHP has not previously been compared throughout mid- and late gestation, as we have done in this study. Therefore, the physiological roles that the GEp plays in mid- and late gestation are yet to be elucidated.

A novel finding in this study was the identification of Kir7.1 expression on the apical process of uterine glands in the GEp **(Fig. 4B)**. The GEp is vital for fluid exchange for implantation, placental growth and development, and support of the fetus throughout early pregnancy [36-41]. Additionally, the demonstration of the important roles that Kir channels play in maintaining fluid homeostasis in the kidneys suggests that Kir7.1 could play a role in this maintenance in the GEp of the uterus [70]. This finding suggests that Kir7.1 may play a role in the unknown causes of infertility, low birth weight, or high birth weight, due to its functional role in the GEp. However, further investigation is necessary to confirm this. No differences in Kir7.1 expression in the GEp were observed between any animal models, suggesting that these results could be translatable to humans. This also suggests that the partial loss of Kir7.1 may have no effect on the GEp. However, changes in HET size and number of GEp glands, compared to WT, implies that partial loss of Kir7.1 could play a role in these differences. Further studies identifying the job that Kir7.1 plays in GEp function would help elicit this structural difference observed in mice with a partial loss of Kir7.1.

The vasculature of the uterus throughout pregnancy was also assessed. No visual differences between animal models were observed in the vasculature, aside from larger spinal arteries in NHP **(Fig. 5A)**. Additionally, the only visible differences noted in vasculature throughout pregnancy were that the size and number of veins and arteries appeared to increase. This could have occurred due to the growth of the uterus and the increase in blood flow to the uterus during pregnancy [73].

Kir7.1 expression was identified on the smooth muscle cells of the veins, arteries, and spinal arteries of mice and NHP; a novel finding **(Fig. 5B)**. This expression increased between a NP state and a pregnant state. No differences were observed between WT or HET mice, or between mice and NHP samples. The vasculature is involved in blood pressure maintenance, therefore, implying that Kir7.1 could play a role in HDP [74]. Kir2.1 channels play vital roles in the vasodilation of vascular smooth muscle cells [75, 76]. Therefore, Kir7.1 channels on the uterine vasculature are likely involved in vasodilation of these smooth muscle cells. Additionally, Kir7.1's role in preventing contractility of the myometrium smooth muscle cells suggests that it may be playing a similar role by preventing contractility of vasculature smooth muscle cells. If loss of Kir7.1 disrupts proper vasodilation, this could lead to pregnancy complications and warrants further investigation.

The identification of Kir7.1 in several tissues of the uterus suggests that the channel may be necessary for various functions of pregnancy and, thus, implicated in many APOs **(Fig. 7)**. Additionally, medications that affect Kir7.1 expression and function could lead to the development of APOs. Anti-depressants block Kir4.1 channels, suggesting these drugs could have similar effects on Kir7.1 and lead to changes in normal uterine function and subsequent development of APOs [77, 78]. The broad expression of Kir7.1 throughout the uterus throughout pregnancy, and the necessary function of these tissues to maintain normal uterine function, demonstrate the need for further studies on the role of Kir7.1 in pregnancy.

The expression differences of whole mouse and NHP uteri was quantified. A trend of increasing expression from NP to D13 and from D13 to D15 was observed in WT and HET mice **(Fig. 6A and B)**. A trend in decreasing expression between D15 and D18 was also observed in both. Although this trend was observed, there were no significant differences observed, except in WT mice between NP to D18 and D13 to D18 **(Fig. 6A)**. When comparing WT to HET mice for each gestational day, a trend of higher expression of Kir7.1 in HET samples in NP and on D18 was observed **(Fig. 6C)**. In contrast, WT appeared to have higher expression on D13 and D15. Additionally, a significant difference was observed between D18 in WT and HET mice. The changes in HET between gestational days were less pronounced

than in WT, suggesting that Kir7.1 expression in WT mice may be more controlled than in mutant HET mice. Additionally, expression differences in the NHP whole uterus between NP and GD90 demonstrated a statistically significant increase in Kir7.1 expression during mid-gestation **(Fig. 6D)**. Thus, demonstrating that Kir7.1 expression is increased during mid-gestation throughout the whole uterus. Amounts of cDNA used for qPCR studies were equal across all samples, demonstrating that these results are not due to differences in experimental sample sizes analyzed. Future studies separating the myometrium, perimetrium, and endometrium could give a more holistic view of tissue-specific Kir7.1 expression changes.

One limitation of this study was that only one pregnant NHP sample could be obtained. Therefore, firm conclusions about NHP GD90 data cannot be made. Another limitation was that HET mice struggled with breeding. No significant differences in breeding were observed in early generations. However, in later generations of HET breeding, very few mice became pregnant or successfully raised litters. Therefore, only 1 uterine sample from HET was collected for D15 and 1 for D18. Additionally, the sample from D18 came from a uterus that had suffered a miscarriage; so the histology and Kir7.1 expression appeared to be regressing towards a NP state. While the reasons for these observations are not known, it is possible that a partial loss of Kir7.1 contributed to this decrease in breeding, successful pregnancies, or the ability to keep pups alive. Due to our identification of Kir7.1 in the LE and GEp, it is possible that a partial loss of Kir7.1 could lead to increases in infertility or support of the fetus as the female mouse ages **(Fig. 3B and 4B)**. Additionally, we identified Kir7.1 in the vasculature, suggesting that changes in blood perfusion or blood pressure could have an effect on fertility and support of the pregnancy **(Fig. 5B)**.

Despite these limitations, we were able to report that Kir7.1 is expressed on the LE, GEp, and vasculature in an NP state and throughout pregnancy. These changes were like those in NHP, supporting the notion that mouse findings could be translatable to humans. Additionally, we observed Kir7.1 expression in the uterine myometrium on D15, but not on D13, D18, or in the NP mouse uterus, supporting previous findings. Surprisingly, no expression of Kir7.1 was observed in NHP in mid-

pregnancy, warranting further investigation. These results demonstrate that, aside from Kir7.1's role in the myometrium, Kir7.1 is also playing a role in the function of the LE, GE, and vasculature of the uterus. Therefore, total loss of Kir7.1 could be a cause of unknown APOs or infertility, if its role is necessary for proper function in these tissues. If Kir7.1 dysfunction is identified as a cause of APOs, this would indicate a genetic cause. Therefore, emphasizing the need for further investigation into ion channel dysfunction and genetic mutations that could be leading to the unknown cases of APOs and infertility.

MATERIALS AND METHODS

Animal care

Animal protocols using C57BL/6J mice were approved by the University of Wisconsin School of Medicine and Public Health Institutional Animal Care and Use Committee (IACUC) (protocol #: M005434). Mice were kept in a temperature (25±5°C) and humidity (40-50%) controlled environment in an animal facility at the University of Wisconsin-Madison. Animals were kept under a 12-hour light/12-hour dark light cycle.

Collection of mouse uterine tissue

4-16-month-old mice were bred for 48 hours before separation. Female mice were weighed at the onset of breeding and on days D7-D11 following breeding for observation of a 1.4g increase in weight between D7-D10, which signifies the timing of gestational age; as described in Domingues et al. (2022) [61]. Mice were euthanized using isoflurane (Isospire^{TM}, Dechra) and cervical dislocation on D13, D15, or D18, and the uterus was collected. Additionally, the uterus of NP mice was collected. The uterus was cut in half for use in RNA isolation (QIAGEN, 74134) and histology. RNA samples were converted to cDNA using the Applied Biosystems kit (4368814) and then used for qPCR analysis.

Non-human primate uterine tissue collection

All NHP uterine tissue was obtained from the Wisconsin National Primate Research Center (WNPRC, Wisconsin, USA). A section of uterine tissue was sent for histology, and another section was used for RNA isolation (QIAGEN, 74134). qPCR was performed on RNA isolated samples (QIAGEN, 74134) following cDNA conversion (Applied Biosystems, 4368814).

Histology and immunohistochemistry

Slides containing the histology of uterine tissue samples were prepared by the Translational Research Initiatives in Pathology (TRIP) core at the University of Wisconsin-Madison. Hematoxylin and eosin (H&E) stains were prepared by the TRIP lab and imaged using a Nikon Eclipse TE300 confocal microscope at a 20X objective with a Nikon Digital Sight DS-U3 camera. Images were captured and analyzed on NIS-Elements D 5.42.02 software. Unstained slides were prepared for immunohistochemical (IHC) analysis.

For IHC, slides were soaked twice in CitriSolv (Decon Laboratories, 1601) for 5 minutes. The slides were dipped in the following solutions 10 times each: 100% EtOH, 95% EtOH, 70% EtOH. They then soaked in water for 5 minutes. Slides were microwaved for 20 minutes in Citrate Buffer (0.01M Citric Acid Anhydrous (Fisher Scientific, A940-500), and 0.1% Tween-20 (Acros, AC233362500); pH 6.5) and allowed to cool for 20 minutes. Then, the slides were soaked and washed in deionized water for 5 minutes. A PAP pen (Biotum, 23024) was used to outline tissue sections, and blocking was performed with 0.25% diluted normal horse serum (Vector, S-2000) containing 0.1% Triton X-100 (Sigma, T-9284) for 20 minutes. Slides were incubated overnight with a Kir7.1 C-12 mouse monoclonal antibody (1:200) (sc-398810, Santa Cruz Biotechnology, Santa Cruz, CA) and ACTA2 rabbit polyclonal (SMA) (1:200) (Proteintech, 14395-I-A) or alpha-ENaC polyclonal (1:200) (Invitrogen, PA1-920A) primary antibody. All primary antibodies were diluted in Dulbecco's Phosphate-buffered Saline (DPBS, GIBCO, 14190144) containing 0.3% Triton X-100 (PBS + 0.3% TritonX-100). Slides were washed three times with PBS + 0.3% TritonX-100 for 5 minutes each wash. Secondary antibodies Alexa Fluor^{TM} 488 donkey anti-mouse

IgG (Invitrogen, A21202) (1:200) and Alexa Fluor™ donkey anti-rabbit IgG (A21207) (1:200), diluted in PBS + 0.3% TritonX-100, were applied to slides and incubated for 2 hours. Washing with PBS and 0.3% Triton X-100 was performed twice for 5 minutes each. DAPI (Biolegend, 422801) (1:200) diluted in PBS + 0.3% TritonX-100 was added to the slide and incubated for 10 minutes. Slides were washed once with PBS with 0.3% Triton X-100. Premium microscope slides (Fisher Scientific, 125441) were fixed onto slides using mounting medium (ibidi, 50001). IHC slides were then imaged for fluorescence on a confocal microscope (Nikon Eclipse Ti) and Nikon C2 camera at a 20X objective. Images were captured and analyzed using NIS-Elements AR 5.30.05.

Quantitative PCR

Primers were designed to specifically differentiate between m*Kcnj13* and h*KCNJ13* for qPCR analysis, and were custom ordered from IDT using mouse and human RNA transcripts from NCBI (https://www.ncbi.nlm.nih.gov/gene/) **(Table 1)**. Fold change was calculated as follows:

$$Fold\ change = 2^{(\Delta\Delta CT)}$$

cDNA was used for qPCR using PowerUP SYBR green master mix (ThermoFisher, A25741) on a QuantStudio (Applied Biosystems) machine. The setup and analysis of the experiment were performed using QuantStudio (Applied Biosystems).

Statistical Analysis

A two-tailed Student's t-test was performed using Microsoft Excel for the statistical analysis. Differences were considered statistically significant at $p < 0.05$; the results are expressed as mean ±SEM.

Acknowledgements:

Schematic images were created with Biorender.com.

FIGURES AND TABLES

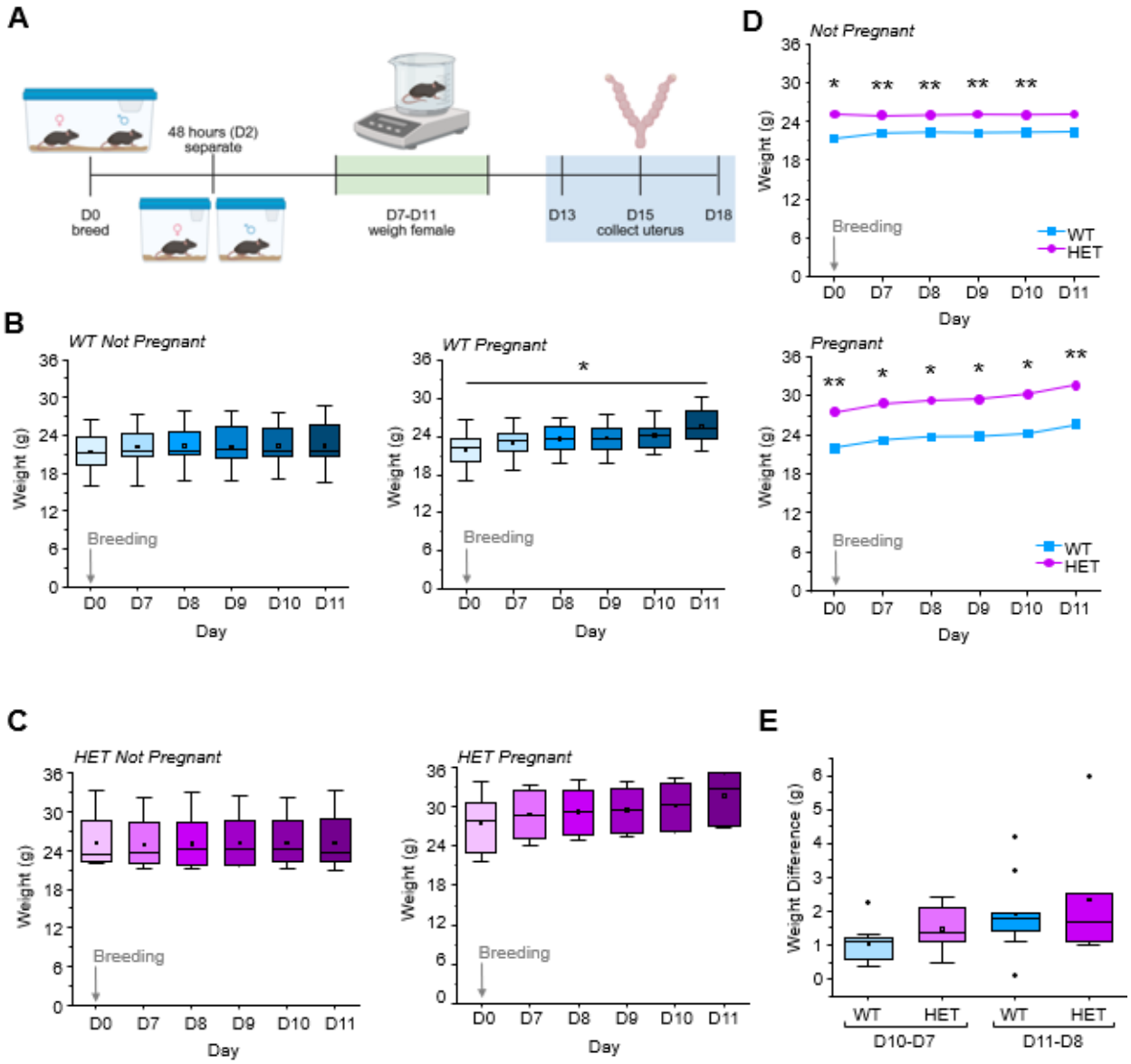

Figure 1: HET mice weigh more than WT mice (A) Schematic of experimental methods. Breeding pairs began breeding on D0 and were separated 48 hours later (D2). Female mice were weighed daily, starting on D7 and ending on D11, to determine gestational age. Uterus collected at time points D13, D15, or D18. D0= 0 days from breeding/onset of breeding, D7=7 days from breeding, D8=8 days from breeding; day 9 (D9)=8 days from breeding, day 10 (D10)=10 days from breeding, D11=11 days from breeding. **(B)** Weight (g) of WT female mice since onset of breeding (D0, grey arrow). The left graph depicts mice that did not become pregnant. Averages for WT not pregnant mice were: D0=21.4, D7=22.2., D8=22.3, D9=22.2, D10=22.3, and D11=22.4. SEMs were as follows: D0=3.337, D7=3.464, D8=3.477, D9=3.473, D10=3.473, and D11=3.507. There were no observed statistically significant differences in weights between days. The right graph depicts mice that became pregnant. Average values for WT pregnant mice were D0=21.9, D7=23.1, D8=23.7, D9=23.7, D10=24.2, and D11=25.6. And SEM for WT pregnant mice was D0=3.390, D7=3.579, D8=3.658, D9=3.667, D10=3.728, and D11=3.958. A statistically significant difference (p=0.015) was observed between D0 and D11 in WT pregnant mice. **(C)** HET female mice weight (g) since onset of breeding (D0, grey arrow). Mice that did not become pregnant depicted by left graph. Average values for HET not pregnant were as follows: D0=25.1, D7=24.908, D8=25.0, D9=25.1, D10=25.1, and D11=25.1, and SEM values were: D0=4.053, D7=4.017, D8=4.038, D9=4.049, D10=4.039, and D11=4.062. No statistically significant differences in weights between gestational days were observed. Mice that did become pregnant depicted by right graph. Averages for HET pregnant mice were D0=27.5, D7=28.8, D8=29.3, D9=29.5, D10=30.3, and D11=31.6. SEM values were: D0=3.826, D7=3.991, D8=4.054, D9=4.079, D10=4.180, and D11=4.364. There were no statistically significant differences in weights observed between days. **(D)** Comparison of average WT (blue squares) vs HET (purple circles) female weights (g), in Figure 1C and 1D, from the onset of breeding (D0). Top graph depicts mice that did not become pregnant. Bottom graph depicts mice that did become pregnant. Statistical significance measured by two-tailed Student's t-test and denoted as *$P<0.05$, **$P<0.01$, and ***$P<0.001$. All values were significant between WT and HET at each time point, except for NP at D11. For NP, p-values comparing WT and HET at each time-point were: 0.006 for D0, 0.040 for D7, 0.038 for D8, 0.031 for D9, 0.028 for D10, 0.052 for D11. For pregnant, p-values comparing WT and HET for each

time-point were: 0.014 for D0, 0.009 for D7, 0.007 for D8, 0.004 for D9, 0.002 for D10, and 0.004 for D11. **(E)** Weight difference between D10 to D7 (D10-D7) and D11 to D18 (D11-D8) between WT and HET to determine gestational age. Average values for D10-D7 were 1.028 for WT and 1.47 for HET, and SEM values were 0.176 for WT and 0.353 for HET. Average values for D11-D8 were 1.919 for WT and 2.333 for HET; with SEM values of 0.372 for WT and 0.735 for HET. No statistical significance was measured by a two-tailed Student's t-test for WT versus HET between each time range. Sample size used for all data analysis was WT not pregnant=15, HET not pregnant=12, WT pregnant=9, and HET pregnant=6.

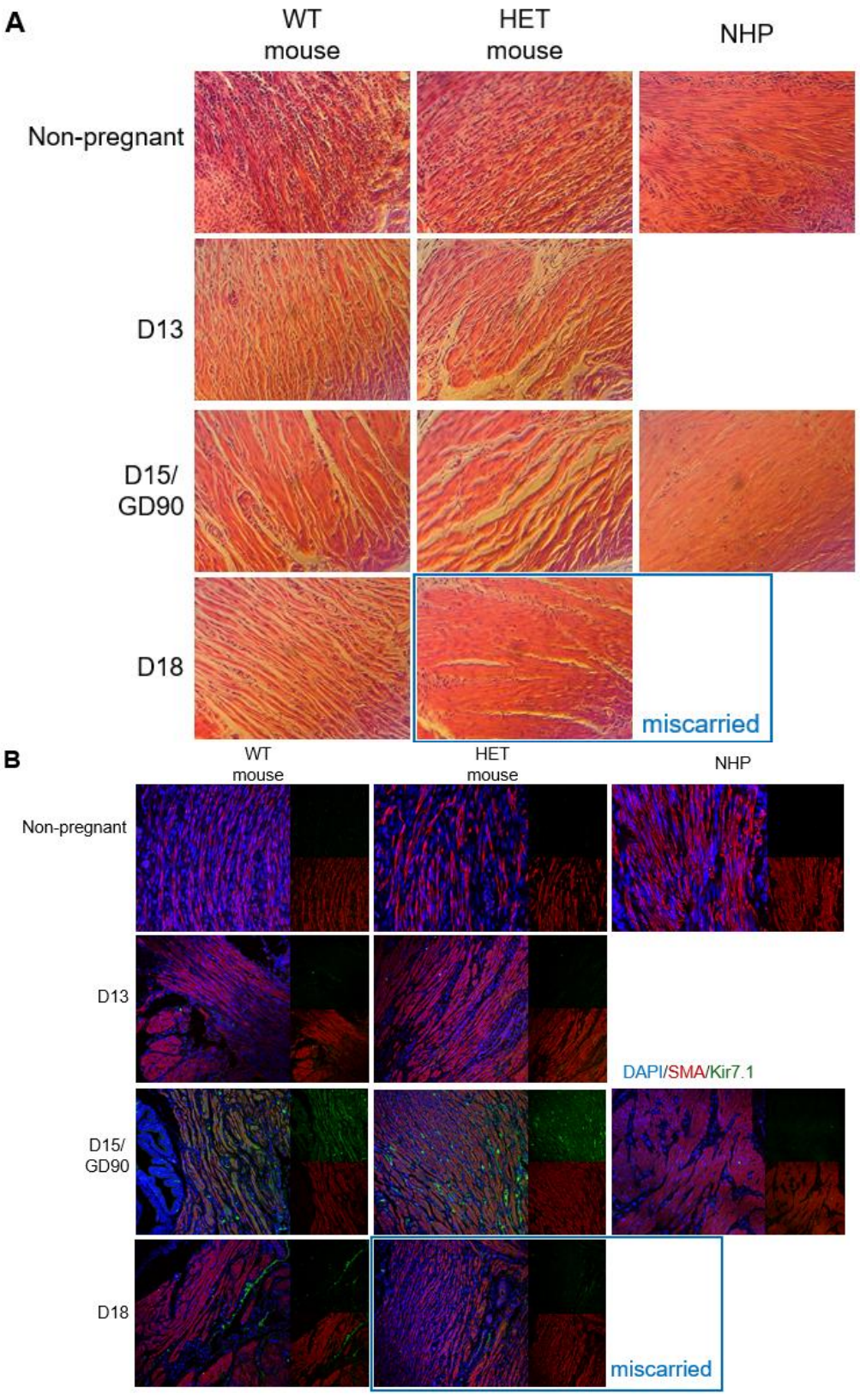
A
WT mouse
HET mouse
NHP
Non-pregnant
D13
D15/ GD90
D18
miscarried
B
WT mouse
HET mouse
NHP
Non-pregnant
D13
DAPI/SMA/Kir7.1
D15/ GD90
D18
miscarried

Figure 2: Myometrial histological changes in mouse and NHP, and expression of Kir7.1 in mid-gestation for WT and HET mice throughout pregnancy. (A) Hematoxylin and eosin (H&E) staining of the myometrium comparing WT mouse, HET mouse, and NHP throughout pregnancy. **(B)** Visual changes in Kir7.1 expression in the myometrium throughout pregnancy in WT mouse, HET mouse, and NHP. Fluorescent images demonstrating DAPI (blue), SMA (red), and Kir7.1 (green). D13=mouse gestational day 13, D15=mouse gestational day 15 and equivalent to mid-gestation, GD90=NHP gestational day 90 and equivalent to mid-gestation, D18=mouse gestational day 18.

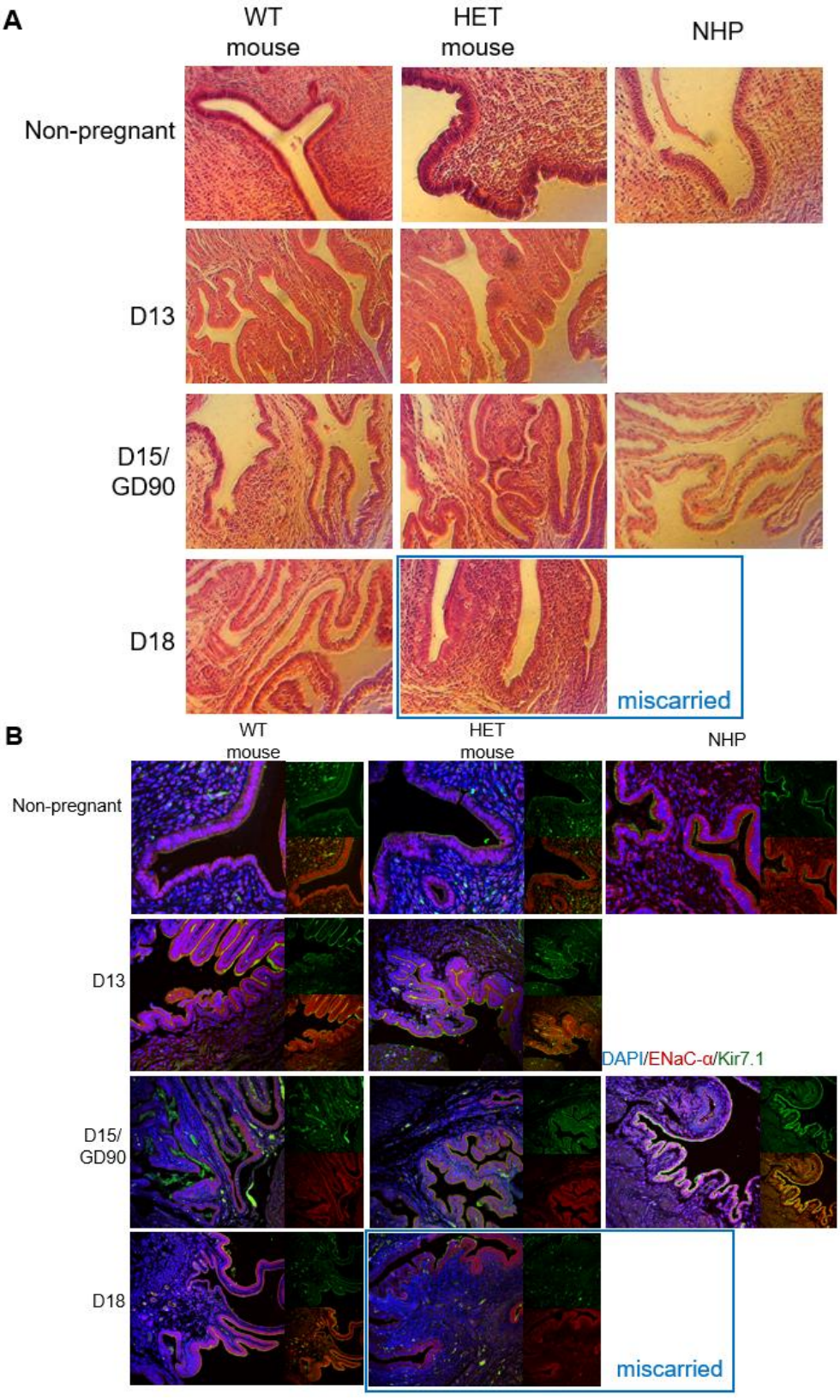
A
WT mouse
HET mouse
NHP
Non-pregnant
D13
D15/ GD90
D18
miscarried
B
WT mouse
HET mouse
NHP
Non-pregnant
D13
DAPI/ENaC-α/Kir7.1
D15/ GD90
D18
miscarried

Figure 3: Histology changes and expression of Kir7.1 in LE of mice and NHP throughout pregnancy. (A) Histological changes to the LE of WT mouse, HET mouse, and NHP throughout pregnancy. **(B)** IHC images demonstrating Kir7.1 expression changes in the LE throughout pregnancy in WT mouse, HET mouse, and NHP. Fluorescent images demonstrating DAPI (blue), ENaC-α (red), and Kir7.1 (green). D13=mouse gestational day 13, D15=mouse gestational day 15 and equivalent to mid-gestation, GD90=NHP gestational day 90 and equivalent to mid-gestation, D18=mouse gestational day 18.

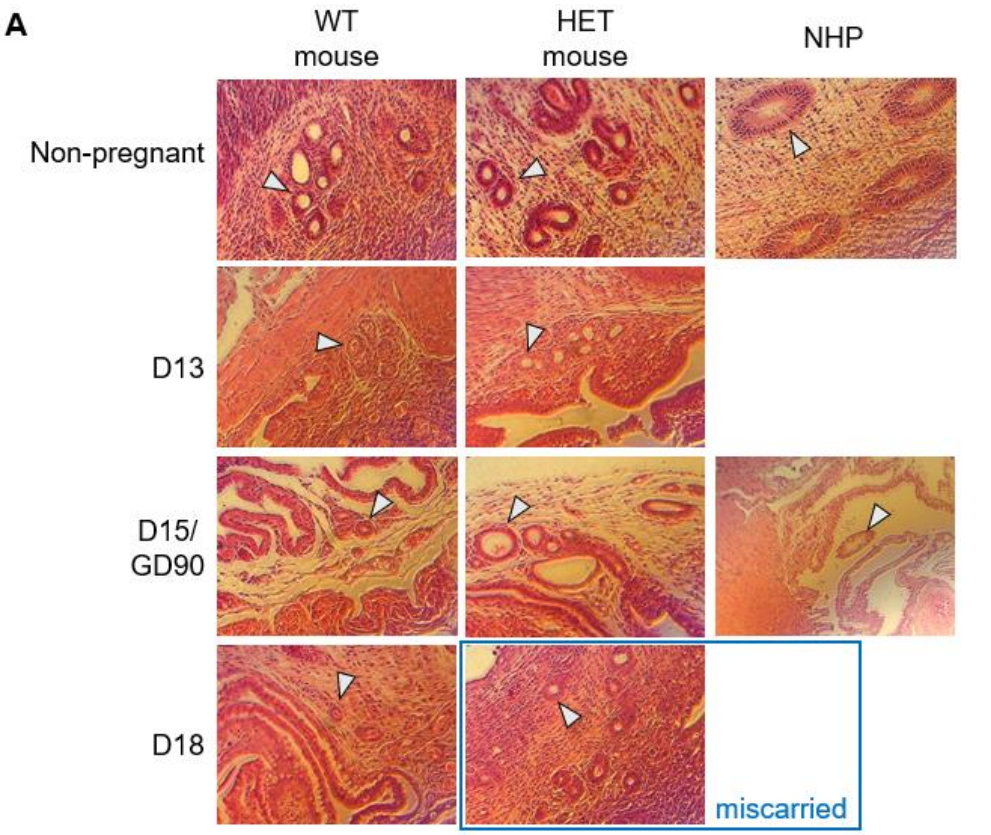
A
WT mouse
HET mouse
NHP
Non-pregnant
D13
D15/ GD90
D18
miscarried

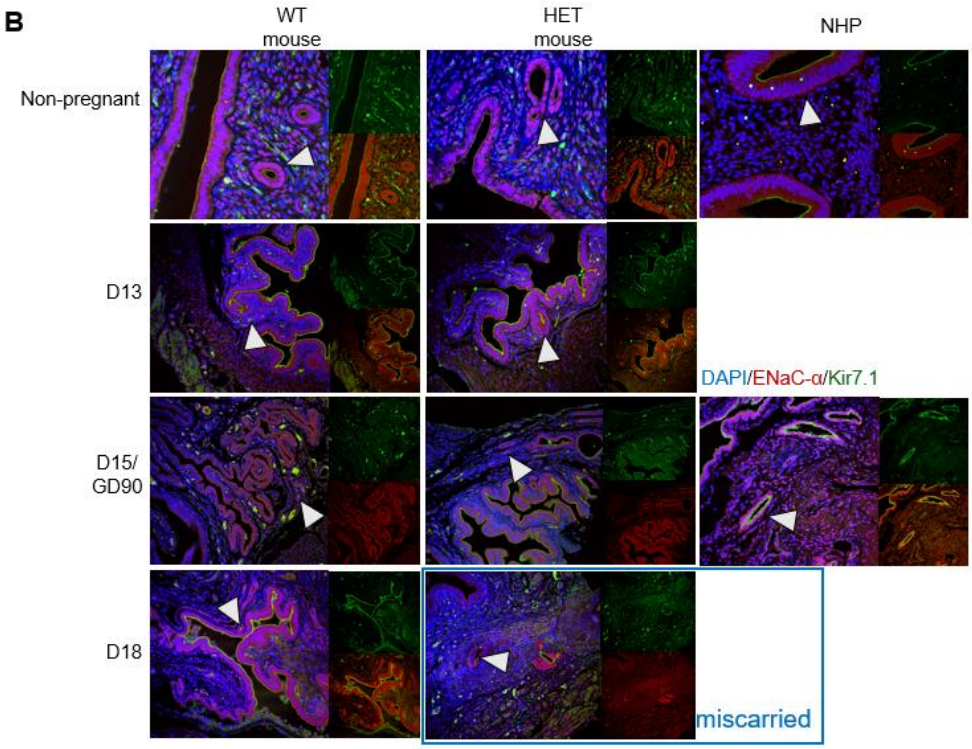
B
WT mouse
HET mouse
NHP
Non-pregnant
D13
D15/ GD90
D18
DAPI/ENaC-α/Kir7.1
miscarried

Figure 4: Changes in GEp histology and presence of Kir7.1 of mice and NHP throughout pregnancy. (A) H&E staining of the GEp comparing WT mouse, HET mouse, and NHP throughout pregnancy. GEp denoted by white arrowhead. **(B)** Expression changes of Kir7.1 expression changes in GEp throughout pregnancy of WT mouse, HET mouse, and NHP. Fluorescent images demonstrating DAPI (blue), ENaC-α (red), and Kir7.1 (green). GEp denoted by white arrowhead. D13=mouse gestational day 13, D15=mouse gestational day 15 and equivalent to mid-gestation, GD90=NHP gestational day 90 and equivalent to mid-gestation, D18=mouse gestational day 18.

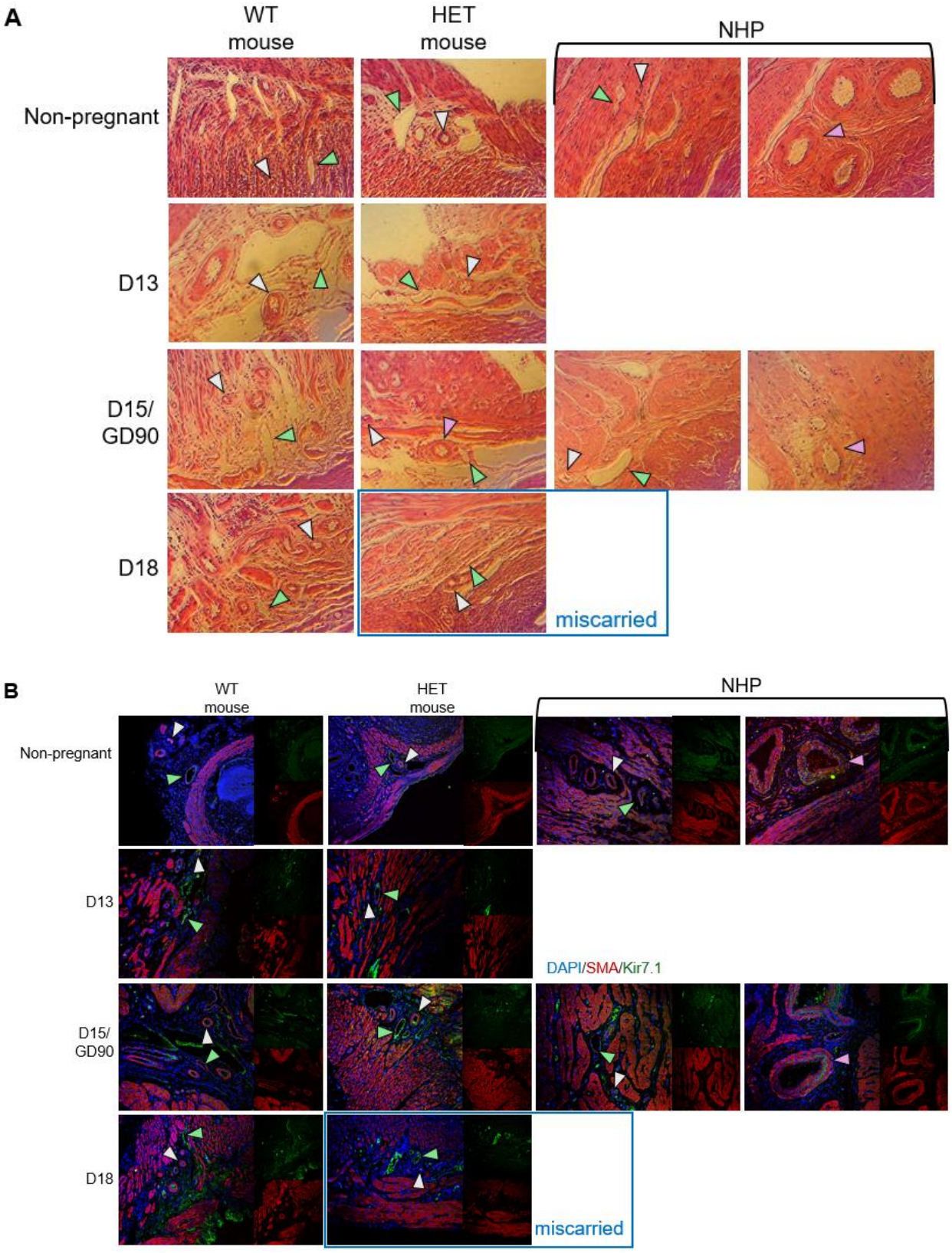
A
WT mouse
HET mouse
NHP
Non-pregnant
D13
D15/ GD90
D18
miscarried
B
WT mouse
HET mouse
NHP
Non-pregnant
D13
D15/ GD90
D18
DAPI/SMA/Kir7.1
miscarried

Figure 5: Changes in vasculature histology and Kir7.1 expression throughout pregnancy. (A) Changes in vasculature histology throughout pregnancy between WT mouse, HET mouse, and NHP throughout pregnancy. Vasculature denoted by: artery=white arrow, vein=green arrow, spinal artery=purple arrow. **(B)** IHC images demonstrating Kir7.1 expression changes in the myometrium throughout pregnancy in WT mouse, HET mouse, and NHP. Fluorescent images demonstrating DAPI (blue), SMA (red), and Kir7.1 (green). Vasculature denoted by: artery=white arrow, vein=green arrow, spinal artery=purple arrow. D13=mouse gestational day 13, D15=mouse gestational day 15 and equivalent to mid-gestation, GD90=NHP gestational day 90 and equivalent to mid-gestation, D18=mouse gestational day 18.

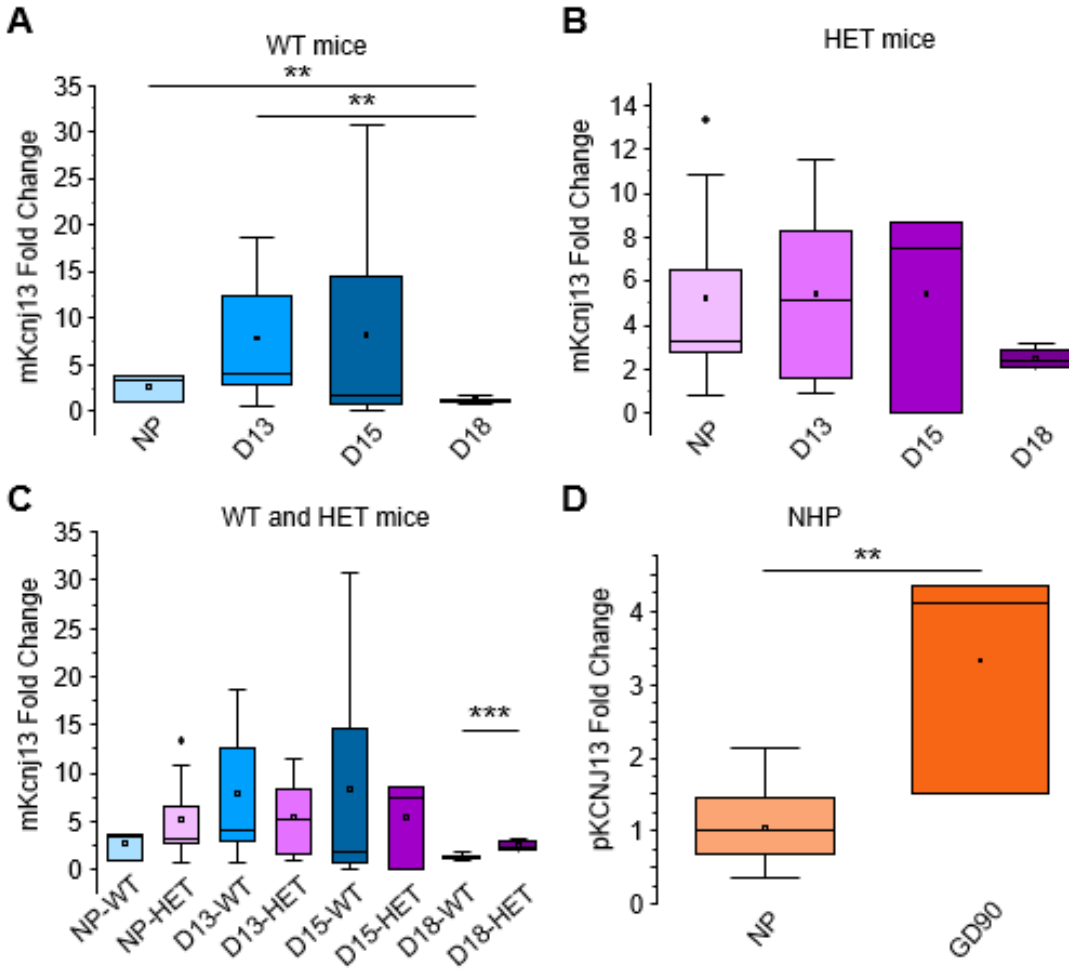

Figure 6: Kir7.1 expression throughout pregnancy in WT mice, HET mice, and NHP. (A) m*Kcnj13* expression fold change throughout pregnancy in WT mice. Average values are 2.694 for NP, 7.884 for D13, 8.276 for D15, and 1.212 for D18. SEM values are as follows: 0.699 for NP, 2.166 for D13, 4.576 for D15, and 0.069 for D18. Statistically significant differences in expression were observed between NP versus D18 (p=0.004) and D13 versus D18 (p=0.003). **(B)** HET mouse fold change in expression of m*Kcnj13* transcript throughout pregnancy. Averages are as follows: 5.241 for NP, 5.437 for D13, 5.408 for D15, and 2.500 for D18. For SEM, values are 1.359 for NP, 1.508 for D13, 2.217 for D15, and 0.227 for D18. No statistical significance is observed between days. **(C)** Comparison of m*Kcnj13* fold changes between WT (blue) and HET (purple) throughout pregnancy. Statistical significance was calculated between WT and HET for each time point. A statistically significant value was observed between WT and

HET for D18 (p=0.00003). **(D)** Box plot depicting a statistically significant difference (p=0.003) in fold change expression differences in p*KCNJ13* between NP and GD90, in NHP. Averages were 1.035 for NP and 3.329 for GD90. SEM values were as follows: 0.178 for NP and 0.740 for GD90. NP=non-pregnant, D13=mouse gestational day 13, D15=mouse gestational day 15, GD90=gestational day 90. A two-tailed Student's t-test calculated statistical analysis, and p-values were denoted as *$P<0.05$, **$P<0.01$, and ***$P<0.001$.

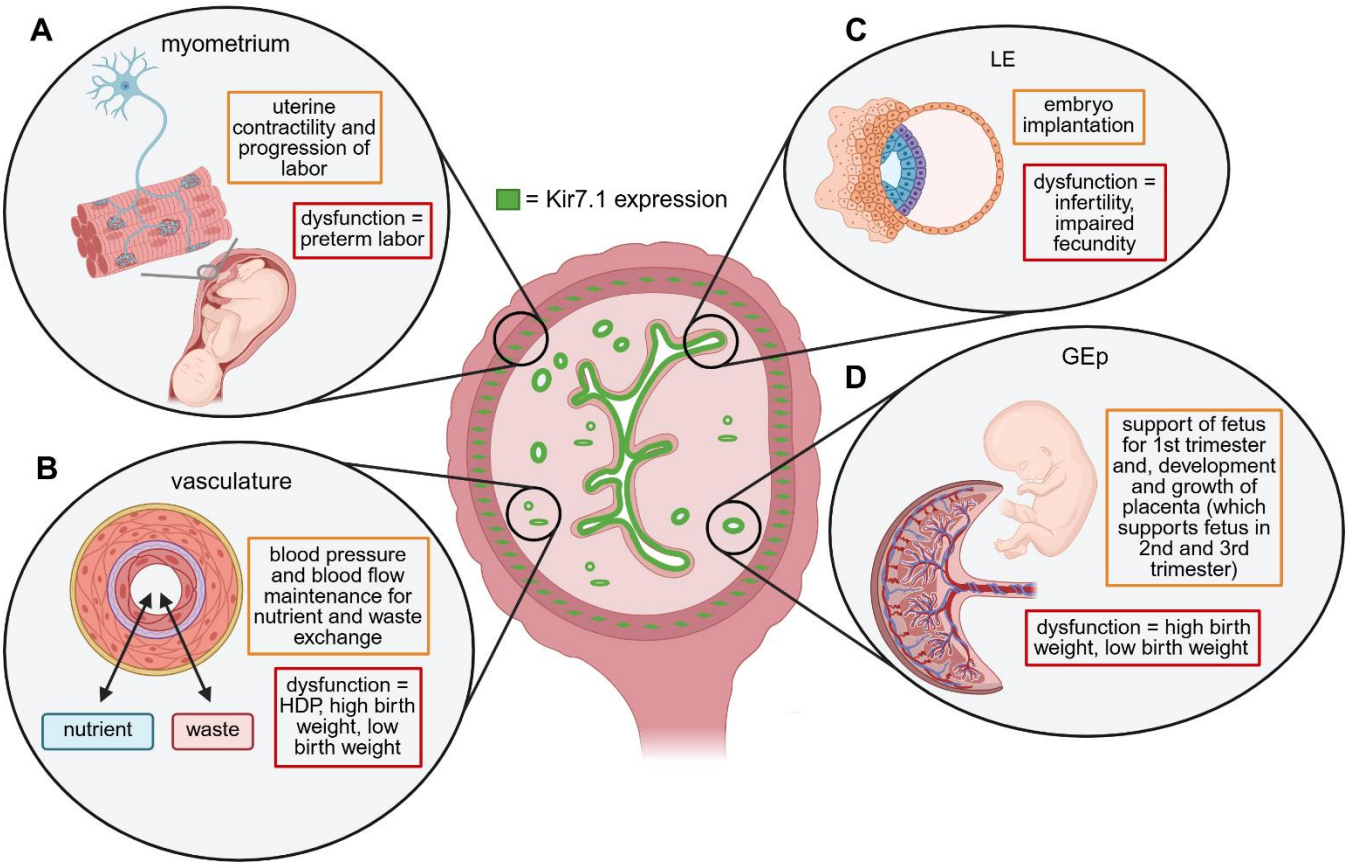

Figure 7: Potential role of Kir7.1 in normal uterine function and APOs. (A) We confirmed that Kir7.1 (green) was expressed in mouse uterine myometrium on D15, but not on D13, D18, or in a NP state. Additionally, no expression of Kir7.1 was observed in NHP myometrial tissue in a NP state or on GD90. Previous studies demonstrated the same results in mice, as well as expression of Kir7.1 in human uterine myometrium. The role of the myometrium is to control uterine contractility and progress labor at the end of gestation (as shown in the orange box). Previous studies have demonstrated that Kir7.1 prevents contractility, suggesting that dysfunctional Kir7.1 may lead to preterm labor (red box). **(B)** Kir7.1 (green) was expressed continuously in the vasculature of mice and NHP. This expression was more pronounced in a pregnant state compared to a NP state. During pregnancy, the vasculature maintains blood pressure and blood flow to control nutrient and waste exchange between the mother and fetus (orange box). If Kir7.1 is vital for the normal function of this tissue, dysfunction of Kir7.1 could lead to HDP, high birth

weight, or low birth weight (red box). **(C)** The continuous expression of Kir7.1 (green) throughout pregnancy was demonstrated in mice and NHP, as illustrated by the continual expression of Kir7.1 (green) in the LE. The LE is necessary for implantation (orange box), thus, implicating dysfunctional Kir7.1 in playing a role in infertility or impaired fecundity (red box). **(D)** Kir7.1 (green) was also observed throughout pregnancy and in a NP state in the GEp of the uterus from mice and NHP. The role of the GEp in pregnancy is to support the fetus during the 1st trimester, as well as support and assist in the development of the placenta, which supports the fetus during the 2nd and 3rd trimester (orange box). If Kir7.1 is necessary for these roles, dysfunction in this channel may lead to improper nutrient transfer to the fetus and cause high birth weight or low birth weight (red box). Additionally, the placenta may not develop properly, which can further lead to high or low birth weight (red box).

Primer Name	**5’-3’ Sequence**
Mouse Gapdh FWD	CATTGCTCTCAATGACAACTTT
Mouse Gapdh RVS	GTGGTCCAGGGTTTCTTACT
Mouse *Kcnj13* FWD	GGGCCTTGTGTATCTCCGA
Mouse *Kcnj13* RVS	TGGGACGTCGTGGTCTATT
Human *KCNJ13* FWD	TAACCAGTGTCCGGGTCT
Human *KCNJ13* RVS	ACTTGATGGTGTAATGGAGTGATAG

Table 1: Primers for qPCR. The NCBI Primer-BLAST tool (https://www.ncbi.nlm.nih.gov/tools/primer-blast/) was used for primer design. Primers were ordered from IDT (https://www.idtdna.com).

REFERENCES

1. Kramer, M.S., *The epidemiology of adverse pregnancy outcomes: an overview.* J Nutr, 2003. **133**(5 Suppl 2): p. 1592S-1596S.
2. *Adverse Birth Outcomes*, in *America's Children and the Environment*. 2013. p. 264-388.
3. Abadiga, M., et al., *Determinants of adverse birth outcomes among women delivered in public hospitals of Ethiopia, 2020.* Arch Public Health, 2022. **80**(1): p. 12.
4. Freaney, P.M., et al., *Temporal Trends in Adverse Pregnancy Outcomes in Birthing Individuals Aged 15 to 44 Years in the United States, 2007 to 2019.* J Am Heart Assoc, 2022. **11**(11): p. e025050.
5. Yee, L.M., E.C. Miller, and P. Greenland, *Mitigating the Long-term Health Risks of Adverse Pregnancy Outcomes.* JAMA, 2022. **327**(5): p. 421-422.
6. Nugent, C.N. and A. Chandra, *Infertility and Impaired Fecundity in Women and Men in the United States, 2015-2019.* Natl Health Stat Report, 2024(202): p. 1-19.
7. Liang, Y., et al., *Global, regional, and national prevalence and trends of infertility among individuals of reproductive age (15-49 years) from 1990 to 2021, with projections to 2040.* Hum Reprod, 2025. **40**(3): p. 529-544.
8. Doyle, M. and A. Carballedo, *Infertility and mental health.* Advances in psychiatric treatment, 2014. **20**: p. 297-303.
9. Strauss, J.F., 3rd, et al., *Spontaneous preterm birth: advances toward the discovery of genetic predisposition.* Am J Obstet Gynecol, 2018. **218**(3): p. 294-314 e2.
10. Tyrmi, J.S., et al., *Genetic Risk Factors Associated With Preeclampsia and Hypertensive Disorders of Pregnancy.* JAMA Cardiol, 2023. **8**(7): p. 674-683.
11. Williams, P.J. and F. Broughton Pipkin, *The genetics of pre-eclampsia and other hypertensive disorders of pregnancy.* Best Pract Res Clin Obstet Gynaecol, 2011. **25**(4): p. 405-17.
12. Monod, C., et al., *Prevalence of gestational diabetes mellitus in women with a family history of type 2 diabetes in first- and second-degree relatives.* Acta Diabetol, 2023. **60**(3): p. 345-351.

13. Sipetic, S., et al., *Family history and risk of type 1 diabetes mellitus.* Acta Diabetol, 2002. **39**(3): p. 111-5.

14. Shaat, N. and L. Groop, *Genetics of gestational diabetes mellitus.* Curr Med Chem, 2007. **14**(5): p. 569-83.

15. Zhang, C., et al., *Genetic variants and the risk of gestational diabetes mellitus: a systematic review.* Hum Reprod Update, 2013. **19**(4): p. 376-90.

16. Seghieri, G., et al., *Relationship between gestational diabetes mellitus and low maternal birth weight.* Diabetes Care, 2002. **25**(10): p. 1761-5.

17. Savona-Ventura, C. and M. Chircop, *Birth weight influence on the subsequent development of gestational diabetes mellitus.* Acta Diabetol, 2003. **40**(2): p. 101-4.

18. Hattersley, A.T., et al., *Mutations in the glucokinase gene of the fetus result in reduced birth weight.* Nat Genet, 1998. **19**(3): p. 268-70.

19. Ramasamy, R., et al., *Successful fertility treatment for Klinefelter's syndrome.* J Urol, 2009. **182**(3): p. 1108-13.

20. Johnson, M., et al., *An analysis of the frequency of Y-chromosome microdeletions and the determination of a threshold sperm concentration for genetic testing in infertile men.* BJU Int, 2019. **123**(2): p. 367-372.

21. Hortas, M.L., et al., *Decreased sperm function of patients with myotonic muscular dystrophy.* Hum Reprod, 2000. **15**(2): p. 445-8.

22. Ajmal, N., S.Z. Khan, and R. Shaikh, *Polycystic ovary syndrome (PCOS) and genetic predisposition: A review article.* Eur J Obstet Gynecol Reprod Biol X, 2019. **3**: p. 100060.

23. Khan, M.J., A. Ullah, and S. Basit, *Genetic Basis of Polycystic Ovary Syndrome (PCOS): Current Perspectives.* Appl Clin Genet, 2019. **12**: p. 249-260.

24. Yatsenko, S.A. and A. Rajkovic, *Genetics of human female infertilitydagger.* Biol Reprod, 2019. **101**(3): p. 549-566.

25. Ahmad, A., A. Ahmed, and P. Patrizio, *Cystic fibrosis and fertility.* Curr Opin Obstet Gynecol, 2013. **25**(3): p. 167-72.

26. Chan, H.C., et al., *The cystic fibrosis transmembrane conductance regulator in reproductive health and disease.* J Physiol, 2009. **587**(Pt 10): p. 2187-95.

27. Wray, S., et al., *Calcium signaling and uterine contractility.* J Soc Gynecol Investig, 2003. **10**(5): p. 252-64.

28. Wray, S., C. Prendergast, and S. Arrowsmith, *Calcium-Activated Chloride Channels in Myometrial and Vascular Smooth Muscle.* Front Physiol, 2021. **12**: p. 751008.

29. Jones, K., et al., *Electrophysiological characterization and functional importance of calcium-activated chloride channel in rat uterine myocytes.* Pflugers Arch, 2004. **448**(1): p. 36-43.

30. McCloskey, C., et al., *The inwardly rectifying K+ channel KIR7.1 controls uterine excitability throughout pregnancy.* EMBO Mol Med, 2014. **6**(9): p. 1161-74.

31. Salleh, N., et al., *The hormonal control of uterine luminal fluid secretion and absorption.* Journal of Membrane Biology, 2005. **206**(1): p. 17-28.

32. Nobuzane, T., S. Tashiro, and Y. Kudo, *Morphologic effects of epithelial ion channels on the mouse uterus: differences between raloxifene analog (LY117018) and estradiol treatments.* Am J Obstet Gynecol, 2008. **199**(4): p. 363 e1-6.

33. Ruan, Y.C., H. Chen, and H.C. Chan, *Ion channels in the endometrium: regulation of endometrial receptivity and embryo implantation.* Hum Reprod Update, 2014. **20**(4): p. 517-29.

34. Gao, H., et al., *Select nutrients in the ovine uterine lumen. ii. glucose transporters in the uterus and peri-implantation conceptuses.* Biol Reprod, 2009. **80**(1): p. 94-104.

35. Enders, A.C. and S. Schlafke, *A Morphological Analysis of the Early Implantation Stages in the Rat.* American Journal of Anatomy, 1967. **120**: p. 185-226.

36. Hempstock, J., et al., *Endometrial glands as a source of nutrients, growth factors and cytokines during the first trimester of human pregnancy: a morphological and immunohistochemical study.* Reprod Biol Endocrinol, 2004. **2**: p. 58.

37. Burton, G.J., E. Jauniaux, and D.S. Charnock-Jones, *Human early placental development: potential roles of the endometrial glands.* Placenta, 2007. **28 Suppl A**: p. S64-9.

38. Spencer, T.E., *Biological roles of uterine glands in pregnancy.* Semin Reprod Med, 2014. **32**(5): p. 346-57.

39. Kelleher, A.M., F.J. DeMayo, and T.E. Spencer, *Uterine Glands: Developmental Biology and Functional Roles in Pregnancy.* Endocr Rev, 2019. **40**(5): p. 1424-1445.

40. Kelleher, A.M., et al., *Uterine glands coordinate on-time embryo implantation and impact endometrial decidualization for pregnancy success.* Nat Commun, 2018. **9**(1): p. 2435.

41. Burton, G.J., T. Cindrova-Davies, and M.Y. Turco, *Review: Histotrophic nutrition and the placental-endometrial dialogue during human early pregnancy.* Placenta, 2020. **102**: p. 21-26.

42. Hu, X.Q. and L. Zhang, *Ca(2+)-Activated K(+) Channels and the Regulation of the Uteroplacental Circulation.* Int J Mol Sci, 2023. **24**(2).

43. Bresnitz, W. and R.A. Lorca, *Potassium Channels in the Uterine Vasculature: Role in Healthy and Complicated Pregnancies.* Int J Mol Sci, 2022. **23**(16).

44. Wray, S. and S. Arrowsmith, *Uterine Excitability and Ion Channels and Their Changes with Gestation and Hormonal Environment.* Annu Rev Physiol, 2021. **83**: p. 331-357.

45. Kusche-Vihrog, K., et al., *The epithelial Na+ channel: a new player in the vasculature.* Curr Opin Nephrol Hypertens, 2014. **23**(2): p. 143-8.

46. Haoui, M., et al., *Kir7. 1 is the physiological target for hormones and steroids that regulate uteroplacental function.* Science Advances, 2025. **11**(10): p. eadr5086.

47. Johansson, E.D., *Plasma levels of progesterone in pregnancy measured by a rapid competitive protein binding technique.* Acta Endocrinol (Copenh), 1969. **61**(4): p. 607-17.

48. Bjorkgren, I., et al., *The epithelial potassium channel Kir7.1 is stimulated by progesterone.* J Gen Physiol, 2021. **153**(10).

49. Toms, M., *Investigating the pathophysiology of KCNJ13 and USH2A retinopathies using zebrafish models*. 2018, UCL (University College London).

50. Toms, M., et al., *Missense variants in the conserved transmembrane M2 protein domain of KCNJ13 associated with retinovascular changes in humans and zebrafish.* Exp Eye Res, 2019. **189**: p. 107852.

51. Kabra, M., et al., *Nonviral base editing of KCNJ13 mutation preserves vision in a model of inherited retinal channelopathy.* The Journal of Clinical Investigation, 2023. **133**(19).

52. Khan, A.O., et al., *A distinct vitreo-retinal dystrophy with early-onset cataract from recessive KCNJ13 mutations.* Ophthalmic Genet, 2015. **36**(1): p. 79-84.

53. Elvis-Offiah, U.B., et al., *Our Clear-Cut Improvement to the Impact of Mouse and Rat Models in the Research Involving Female Reproduction*, in *Animal Models and Experimental Research in Medicine*. 2022, IntechOpen.

54. Lambert, L.J., et al., *Basic mouse methods for clinician researchers: harnessing the mouse for biomedical research*, in *Basic Science Methods for Clinical Researchers*. 2017, Elsevier. p. 291-312.

55. Jukic, A.M., et al., *Length of human pregnancy and contributors to its natural variation.* Human reproduction, 2013. **28**(10): p. 2848-2855.

56. Silk, J., et al., *Gestation length in rhesus macaques (Macaca mulatta).* International Journal of Primatology, 1993. **14**(1): p. 95-104.

57. Coe, C.L. and G.R. Lubach, *Maternal determinants of gestation length in the rhesus monkey.* Trends in developmental biology, 2021. **14**: p. 63.

58. Villanueva, S., et al., *Cleft Palate, Moderate Lung Developmental Retardation and Early Postnatal Lethality in Mice Deficient in the Kir7.1 Inwardly Rectifying K+ Channel.* PLoS One, 2015. **10**(9): p. e0139284.

59. Anderson, E.J.P., et al., *Late onset obesity in mice with targeted deletion of potassium inward rectifier Kir7.1 from cells expressing the melanocortin-4 receptor.* J Neuroendocrinol, 2019. **31**(1): p. e12670.

60. Zietara, A., et al., *K(ir)7.1 knockdown and inhibition alter renal electrolyte handling but not the development of hypertension in Dahl salt-sensitive rats.* Am J Physiol Renal Physiol, 2023. **325**(2): p. F177-F187.

61. Domingues, R.R., M.C. Wiltbank, and L.L. Hernandez, *Pregnancy Complications and Neonatal Mortality in a Serotonin Transporter Null Mouse Model: Insight Into the Use of Selective Serotonin Reuptake Inhibitor During Pregnancy.* Front Med (Lausanne), 2022. **9**: p. 848581.

62. Authier, F.J., *[Classification of muscle cells].* Rev Mal Respir, 2000. **17**(2 Pt 2): p. 525-30.

63. Ledingham, M., et al., *Cell adhesion molecule expression in the cervix and myometrium during pregnancy and parturition.* Obstetrics & Gynecology, 2001. **97**(2): p. 235-242.

64. Dalli, S. and A.L. Bernal, *Uterine Quiescence in Pregnancy and Labour.* EC Gynaecology, 2022. **11**: p. 34-55.

65. Shynlova, O., R. Kwong, and S.J. Lye, *Mechanical stretch regulates hypertrophic phenotype of the myometrium during pregnancy.* Reproduction, 2010. **139**(1): p. 247.

66. Weinbauer, G.F., et al., *Nonhuman primates as preclinical models for developmental and reproductive toxicity evaluation*, in *Developmental and Reproductive Toxicology*. 2016, CRC Press. p. 478-492.

67. Ye, X., *Uterine luminal epithelium as the transient gateway for embryo implantation.* Trends in Endocrinology & Metabolism, 2020. **31**(2): p. 165-180.

68. Demir, R., et al., *Structural differentiation of human uterine luminal and glandular epithelium during early pregnancy: an ultrastructural and immunohistochemical study.* Placenta, 2002. **23**(8-9): p. 672-684.

69. Salleh, N., et al., *The hormonal control of uterine luminal fluid secretion and absorption.* The Journal of membrane biology, 2005. **206**: p. 17-28.

70. Palygin, O., O. Pochynyuk, and A. Staruschenko, *Role and mechanisms of regulation of the basolateral Kir4. 1/Kir5. 1K+ channels in the distal tubules.* Acta Physiologica, 2017. **219**(1): p. 260-273.

71. Spencer, T.E. *Biological roles of uterine glands in pregnancy*. in *Seminars in reproductive medicine*. 2014. Thieme Medical Publishers.

72. Gray, C.A., et al., *Developmental biology of uterine glands.* Biology of reproduction, 2001. **65**(5): p. 1311-1323.

73. Thaler, I., et al., *Changes in uterine blood flow during human pregnancy.* American journal of obstetrics and gynecology, 1990. **162**(1): p. 121-125.

74. Fournier, S.B., J.N. D'Errico, and P.A. Stapleton, *Uterine Vascular Control Preconception and During Pregnancy.* Compr Physiol, 2021. **11**(3): p. 1871-1893.

75. Jackson, W.F., *Potassium channels in the peripheral microcirculation.* Microcirculation, 2005. **12**(1): p. 113-127.

76. Zaritsky, J.J., et al., *Targeted disruption of Kir2. 1 and Kir2. 2 genes reveals the essential role of the inwardly rectifying K+ current in K+-mediated vasodilation.* Circulation research, 2000. **87**(2): p. 160-166.

77. Ohno, Y., et al., *Inhibition of astroglial Kir4. 1 channels by selective serotonin reuptake inhibitors.* Brain research, 2007. **1178**: p. 44-51.

78. Kinboshi, M., et al., *Inhibition of inwardly rectifying potassium (Kir) 4.1 channels facilitates brain-derived neurotrophic factor (BDNF) expression in astrocytes.* Frontiers in molecular neuroscience, 2017. **10**: p. 408.

Chapter 7: Concluding remarks

Unknown causes of APOs are alarming due to the incidence of long-term health effects on mothers and offspring. Additionally, there is a need for better preventative and treatment options. Since the pathophysiology of APOs is poorly understood, ion channel dysfunction and genetic mutations could be causes of unknown cases. We are particularly interested in understanding the physiological connections between APOs and genetic mutations to *KNCJ13*. This gene encodes the ion channel, Kir7.1, which has been previously reported in the myometrium of the uterus. Additionally, we wanted to identify potential therapies that could target *KCNJ13* mutations.

This thesis work aimed to: A) compare the efficacy of gene therapy approaches in overcoming a PTC mutation to *KCNJ13* **(Chapter 2: genomic editing and ACE-tRNA therapy; Chapter 3; Chapter 4: HUB-101 gene augmentation)**, B) identify changes in pregnancy and labor due to the partial loss of Kir7.1 in a mouse model **(Chapter 5)**, and C) further characterize expression changes of Kir7.1 in the mouse and NHP uterus throughout pregnancy **(Chapter 6)**.

Since patients harboring *KCNJ13* mutations experience degenerative vision loss, we initially aimed to focus on developing therapies to overcome these mutations. Therapies that were cell-type specific were designed to target the RPE cells. However, successful therapies can be modified in the future to target cells in the uterus with Kir7.1 dysfunction. We first tested a gene correction approach. We attempted to create a R166X mutation harboring hiPSC-RPE cell line using genomic editing techniques **(Chapter 2)**. The successful creation of this line would allow for RPE-specific testing of genomic editing therapies to overcome the mutation. However, we were not able to create the mutation in these lines. We then made a cell line that stably expressed the R166X mutation to *KCNJ13* and tested three different genomic editing techniques (GE, BE, and PE). We observed one instance of BE that resulted in 10% editing; however, this result was not reproducible. GE and PE techniques did not edit the R166X mutation. Therefore, we determined that this mutant was challenging to edit, likely due to the presence of repeated bases near the mutation site. Previous research observed successful editing of another PTC to

KCNJ13 [1]. Therefore, this study demonstrates that the success of genomic editing techniques is mutation-specific. We then attempted to target the correction of the mutation at the transcriptional level using an ACE-tRNA therapy **(Chapter 3)**. This therapy demonstrated success by leading to Kir7.1 expression on the channel and partial recovery of channel function. We also observed that the R166X mutant protein was expressed on the membrane, leading us to hypothesize that R166X subunits could be co-assembling with WT subunits to create the tetrameric ion channel. Therefore, we wanted to further investigate if these subunits demonstrate co-localization on the membrane. We treated cells with GFP-tagged R166X and RFP-tagged WT plasmids in a 1:1 ratio and performed live-cell imaging. Cells were also treated with a GFP-tagged W53X and RFP-tagged WT plasmids as a negative control. Imaging and Pearson's coefficient revealed that R166X and WT membrane expression were highly correlated, compared to a low Pearson's coefficient for W53X and WT expression. Therefore, this study demonstrated that for ion channels with more than one subunit, mutations that are trafficked to the membrane can co-assemble with the WT protein translated following treatment. This was likely the reason that full recovery was not observed in ACE-tRNA-treated R166X cells. A study looking at a missense mutation to a potassium channel observed similar findings [2]. Future studies investigating increased doses of ACE-tRNA can further elicit this effect in membrane-trafficked mutants, like R166X.

Gene augmentation therapy delivers a healthy copy of the target gene to cells, thus demonstrating the ability to overcome multiple mutations to a single gene. This type of therapy could provide an alternative treatment option for patients with challenging mutations, like R166X. Our lab previously demonstrated that *KCNJ13* was successfully delivered to mutant patient-derived hiPSC-RPE cells using a Lentivirus [3]. However, Lentiviral vectors are not currently approved for ocular delivery of gene augmentation therapies. Therefore, we aimed to test a clinical-grade gene therapy, HUB-101, which utilized an AAV viral vector for h*KCNJ13* delivery to mRPE cells **(Chapter 4)**. Transducing mRPE cells allowed us to design primers that specifically differentiated between the endogenous m*Kcnj13* transcript and the exogenous h*KCNJ13* transcript delivered by HUB-101. We observed a dose-dependent increase in h*KCNJ13* transcript with no change in the endogenous m*Kcnj13* transcript. Therefore, HUB-101

successfully transduced RPE cells and delivered h*KCNJ13*. This study demonstrates that HUB-101 should be capable of transducing human RPE when it reaches the clinical trial stage. Pre-clinical animal studies are currently ongoing.

In conclusion, we demonstrated the promise of using ACE-tRNA and gene augmentation therapies to overcome mutations that are challenging to target with genomic editing techniques. Previous research in our lab demonstrated that genomic editing may be a therapeutic approach for some mutations, but not for all mutations. In the future, these therapies can be modified to treat *KCNJ13* mutations in the uterus.

To better understand the role of Kir7.1, we used a novel camera system to investigate the effects of partial loss of Kir7.1 on pregnancy and labor **(Chapter 5)**. Since HOMO mutations in *Kcnj13* lead to lethality in mice, WT C57BL/6J mice were compared to HET mutant mice. Previous research has demonstrated that HET mutations to *Kcnj13* lead to changes in renal physiology, but do not lead to disease phenotypes such as hypertension [4]. Therefore, we expected to see a similar effect on pregnancy and labor. The camera system was a successful approach to accurately monitor mouse pregnancy and labor. A detailed approach to camera setup and analysis was outlined in **Chapter 5**. We did not observe differences in the number of pups born or the length of time between pregnancy for WT versus HET mice. Pup survival demonstrated a significant difference in WT and HET mice. However, high variability in samples requires further investigation. When comparing labor times, HET had a trend towards longer labor times. This difference was not statistically significant, but it suggests that a partial loss of Kir7.1 may be leading to physiological changes in uterine myometrial function during labor. This finding further indicates that complete loss of Kir7.1 could lead to more significant changes in uterine myometrium physiology and emphasizes the importance of further investigation of this channel's role in labor. Additionally, the success of this camera system in our study demonstrates an improved model to study reproduction and should be utilized in future studies.

The trend towards altered labor physiology in HET mice prompted us to investigate changes in Kir7.1 expression throughout pregnancy and compare them with those in WT mice. A previous study on

Kir7.1 in the myometrium demonstrated that Kir7.1 expression in mouse myometrium was low at the start of pregnancy through day 13, increased from day 13 to day 15, and then decreased again from day 15 to day 18. [5]. We wanted to confirm this result in WT and compare it to our HET mice containing a partial loss of Kir7.1 due to a genetic mutation **(Chapter 6)**. We also investigated the expression of Kir7.1 in the other tissues in the uterus throughout pregnancy. Mouse findings were compared with NHP uterus samples to understand if our results were translatable to humans. We observed that Kir7.1 is not present in the myometrium in NP, D13, or D18 mouse and NHP uterus. Kir7.1 expression was observed in the mouse uterus on D15; however, no expression was observed in the NHP uterus during mid-pregnancy (GD90). Our mouse myometrial results confirm previous findings; however, our mid-gestation NHP results do not align with the current hypothesis that Kir7.1 is responsible for preventing contractions during mid-gestation. Demonstrating that there may be differences in Kir7.1 physiology between mice and humans. We obtained only one NHP GD90 sample to work with, so further investigation into the expression of Kir7.1 in mid-pregnancy is crucial to understanding the role of Kir7.1 in NHPs. No visual differences in Kir7.1 expression in the myometrium between WT and HET mice were observed. We also noted changes in myometrial histology throughout pregnancy. A novel finding was that Kir7.1 was expressed in the LE, GEp, and vasculature of NP samples, as well as throughout pregnancy. This result was observed in both mice and NHP, and no visual differences in expression were noted between WT and HET. Therefore, suggesting that the role of Kir7.1 in these tissues could be translatable between mouse and human physiology. Additionally, the presence of Kir7.1 in these tissues demonstrates that Kir7.1 could play a vital role in the maintenance of pregnancy in the uterus. This could implicate Kir7.1 dysfunction in causing unknown cases of APOs and infertility. Further investigation into the role of Kir7.1 in these tissues is necessary to understand if it plays a role in APOs. Total uterine expression changes in Kir7.1 were quantified between the WT and HET mouse uterus and the NHP uterus. In WT mice, there was a trend for Kir7.1 to increase from the NP uterus through D15, followed by a decrease between D15 and D18. For HET, this same trend was observed, but the changes were less pronounced. This difference between WT and HET Kir7.1 expression suggests that expression may not be as efficiently controlled in HET. For NHP, a significant increase in Kir7.1 expression was observed between NP and GD90 uterine samples.

This trend, where Kir7.1 increases from the NP state to mid-gestation, at D15 in mice and GD90 in NHP, suggests that mouse studies of Kir7.1 in the uterus may be translatable to humans. These findings support trends in Kir7.1 expression in the mouse uterine myometrium [5]. The previous study of Kir7.1 in the myometrium showed no increase in Kir7.1 within the myometrium until after D13. Our study revealed a slight increase in the NP and D13 whole uterus, which can be attributed to the presence of Kir7.1 in other tissues of the uterus. Additionally, the considerable decrease in Kir7.1 expression on D18 in mice supports that Kir7.1 expression must be decreased as the uterus moves towards labor, to allow for cell hyperpolarization and subsequent opening of voltage-gated Ca^{2+} channels. Therefore, supporting the current understanding of the role of Kir7.1 in uterine quiescence as outlined in McCloskey et al. (2014) [5]. Another interesting finding from this study was that HET mice weighed more on average than WT mice, and there was a trend towards HET mice gaining more weight during pregnancy. These findings support a previous study that demonstrated that a loss of Kir7.1 led to late-onset obesity in mice [6].

These findings prompted us to investigate the role of Kir7.1 in the myometrium in an *in vitro* model. We aimed to express Kir7.1 and the Ca2+ visualizer Geco1a in HUtSMC to observe changes in Ca2+ concentrations in cells resulting from alterations in Kir7.1 activity. Previous studies have demonstrated that OXT blocks Kir7.1 in the RPE cells of the eye and that P4 increases the activity of Kir7.1 in the choroid plexus of the brain [7, 8]. Therefore, we aimed to utilize OXT to block Kir7.1 and employ P4 to activate Kir7.1 in HUtSMC, subsequently recording the effect on Ca^{2+} concentrations. Before we could test this, we needed to deliver Kir7.1 and Geco1a to HUtSMC efficiently. We tested nucleofection, LNP, transfection, and transduction to deliver a GFP-tagged Kir7.1 and RFP-tagged Geco1a to the cells **(Appendix I)**. Efficient expression of Kir7.1 was only observed using transduction. However, no method was successful at getting Geco1a to express in HUtSMC. We determined that this was due to the serotype of virus used for Geco1a transduction. We demonstrated that two other types of viral capsids as potential candidates to deliver Geco1a in the future. Additionally, transfection of Kir7.1 and Geco1a in CHO-K1 and CHO-M1 cells demonstrated successful expression of both plasmids, confirming that the cell type was the limiting factor when attempting to deliver these plasmids to HUtSMC.

The use of a different viral delivery serotype to deliver Geco1a to HUtSMC can facilitate future investigations into the influence of OXT and P4 on Kir7.1 activity and subsequent Ca2+ concentrations.

Overall, we provided evidence for ACE-tRNA and gene augmentation therapy in treating mutations that are challenging to target using genomic editing techniques, such as the R166X mutation in *KCNJ13*. However, previous studies using the same genomic editing techniques on a different mutation to *KCNJ13* were successful, demonstrating the possibility of using genomic editing for some mutations. These therapies could be modified for future targeting of uterine tissues to treat APOs and infertility due to genetic mutations. To study the effect of partial loss of Kir7.1 in HET mice on labor, we demonstrated the success of a novel camera system. This setup allowed us to identify a trend in HET mice towards longer labor times. The use of this camera system in future reproductive studies could significantly improve the accuracy and knowledge within the reproductive field. Additionally, we identified the presence of Kir7.1 in the LE, GEp, and vasculature of the uterus throughout pregnancy and in a NP state. In addition to demonstrating that Kir7.1 expression increases as gestation progresses towards mid-gestation and decreases towards labor in the whole mouse uterus. These findings suggest that Kir7.1 dysfunction could be involved in causing other APOs and infertility; emphasizing the importance of further research into the function and dysfunction of Kir7.1 in these tissues. Our results suggest that patients harboring loss-of-function mutations to *KNCJ13* could suffer from APOs or infertility. Genetic therapies could prevent these adverse outcomes, therefore decreasing the likelihood of these patients and their offspring from suffering the long-term health effects resulting from APOs.

REFERENCES

1. Kabra, M., et al., *Nonviral base editing of KCNJ13 mutation preserves vision in a model of inherited retinal channelopathy.* The Journal of Clinical Investigation, 2023. **133**(19).
2. Ordog, B., et al., *Identification and functional characterisation of a novel KCNJ2 mutation, Val302del, causing Andersen-Tawil syndrome.* Can J Physiol Pharmacol, 2015. **93**(7): p. 569-75.
3. Shahi, P.K., et al., *Gene Augmentation and Readthrough Rescue Channelopathy in an iPSC-RPE Model of Congenital Blindness.* Am J Hum Genet, 2019. **104**(2): p. 310-318.
4. Zietara, A., et al., *K(ir)7.1 knockdown and inhibition alter renal electrolyte handling but not the development of hypertension in Dahl salt-sensitive rats.* Am J Physiol Renal Physiol, 2023. **325**(2): p. F177-F187.
5. McCloskey, C., et al., *The inwardly rectifying K+ channel KIR7.1 controls uterine excitability throughout pregnancy.* EMBO Mol Med, 2014. **6**(9): p. 1161-74.
6. Anderson, E.J.P., et al., *Late onset obesity in mice with targeted deletion of potassium inward rectifier Kir7.1 from cells expressing the melanocortin-4 receptor.* J Neuroendocrinol, 2019. **31**(1): p. e12670.
7. York, N., et al., *Oxytocin (OXT)-stimulated inhibition of Kir7.1 activity is through PIP2-dependent Ca(2+) response of the oxytocin receptor in the retinal pigment epithelium in vitro.* Cell Signal, 2017. **37**: p. 93-102.
8. Bjorkgren, I., et al., *The epithelial potassium channel Kir7.1 is stimulated by progesterone.* J Gen Physiol, 2021. **153**(10).

Appendix I: HUtSMC delivery of plasmids to evaluate the effects of common pregnancy hormones on Kir7.1 activity and subsequent Ca^{2+} concentration

Allison Spillane[1,2], Manya Mehra[1,2], Pawan K. Shahi[1,2], Bikash R. Pattnaik[1,2,3]

[1]University of Wisconsin-Madison, Department of Pediatrics, Wisconsin, USA.
[2]University of Wisconsin-Madison, McPherson Eye Research Institute, Wisconsin, USA.
[3]University of Wisconsin-Madison, Department of Ophthalmology and Visual Sciences, Wisconsin, USA

SUMMARY

Globally, APOs, including spontaneous preterm labor, lead to long-term health issues in mothers and offspring. While some pathophysiological causes of preterm labor are known, there are still unknown causes. Kir7.1 is an inwardly rectifying potassium channel that could lead to preterm labor if there is a loss of function. This channel helps maintain uterine myometrial quiescence by keeping the cell hyperpolarized, therefore, preventing the opening of Voltage-gated Ca^{2+} channels. Female patients who have not reached reproductive age have been identified as harboring mutations to *KCNJ13*, which encodes Kir7.1. Therefore, it is necessary to understand the role of Kir7.1 in uterine quiescence, and its potential impact on preterm labor due to the loss of Kir7.1. Additionally, pregnancy hormones OXT and P4 have been implicated in altering Kir7.1 activity in other tissues. Therefore, to further our understanding of Kir7.1's role in uterine quiescence, we tried to examine whether OXT and P4 would have the same impact on Kir7.1 and downstream internal Ca2+ concentrations in human uterine smooth muscle cells (HUtSMC). To visualize this, we wanted to deliver Kir7.1 and a Ca^{2+} visualizer (Geco1a) to HUtSMC. We attempted to deliver plasmids via nucleofection, lipid nanoparticle (LNP) transfection, and transduction. We observed that transduction was the only successful delivery method for delivering Kir7.1 to HUtSMC. Additionally, Geco1a was not delivered to the cells using any technique. We identified that this was due to the AAV serotype and identified two types of virus capsids that have the potential to successfully deliver Geco1a to these cells in future studies.

INTRODUCTION

APOs are a cause of long-term health issues in mothers and offspring globally [1-5]. One of these APOs is spontaneous preterm labor, which is characterized by spontaneous labor occurring before 37 weeks gestation [4-7]. Infants who are born prematurely are at a higher risk for long-term health effects, including retinopathy of prematurity, cerebral palsy, and intellectual disabilities [8-11]. Preterm labor is associated with pathophysiological causes such as P4 withdrawal, OXT activation, and premature activation of the decidua [12]. Several pathogen-associated causes have been implicated in causing premature activation of the decidua; however, the link between them is poorly understood [6, 11]. Additionally, some causes of preterm labor are unknown. The treatment options for spontaneous preterm labor are scarce; relying on bed rest and hydration for the prevention of preterm labor, and administration of pharmacological agents to delay contractions [11]. However, there is no substantial evidence supporting bed rest or hydration in the prevention of preterm labor, and pharmacological agents often only delay contractions by 24-48 hours. Therefore, it is vital that we better understand the pathophysiological causes of spontaneous preterm labor to prevent and treat preterm labor more effectively and reduce the incidence of long-term health effects that result.

Ion channels play a crucial role in maintaining a healthy pregnancy. Ca^{2+}, Na^{+}, K^{+}, and Cl^{-} channels are present in the uterine myometrium and play roles in contractility and quiescence [13-16]. Specifically, K+ channels play roles in maintaining uterine quiescence [16, 17]. Therefore, dysfunction of K+ channels could be a cause of unknown preterm labor. One of the K+ channels expressed in the uterine myometrium is Kir7.1, an inwardly rectifying potassium channel [16, 18]. In this study, Kir7.1 expression increased from gestational day 13 (D13) to D15 and decreased between D15 and D18 in mice [16]. In human uterine samples at term, Kir7.1 expression was higher in uteri not in labor. Expression decreased in uterine samples taken while in labor. The overexpression of Kir7.1 resulted in a decrease in myometrium contraction, and blocking or knocking out the channel led to an increase in contractility. Demonstrating that Kir7.1 has a significant influence over uterine quiescence and contractility. This study hypothesized that Kir7.1 prevents contractions by keeping the cell in a hyperpolarized state, therefore,

keeping voltage-gated Ca^{2+} channels closed. Decreased expression and blocking of Kir7.1 would then lead to cell depolarization, followed by subsequent opening of Ca2+ channels, allowing for contraction. Additionally, another study confirmed these findings in mice and demonstrated that P4, a known activator of Kir7.1, leads to further reduction in contractility through its action on Kir7.1 [19, 20]. However, no other studies have followed up on Kir7.1's role in contractility or its potential link with preterm labor.

Female patients who suffer from a complete loss of Kir7.1 function, due to recessive mutations in the *KCNJ13* gene, have been identified but have not reached reproductive maturity [21-24]. Therefore, the APOs associated with loss of Kir7.1 function in the uterine myometrium are not known and warrant further investigation.

To better understand the influence of pregnancy hormones on the role of Kir7.1 in the uterine myometrium during pregnancy. Our lab has previously demonstrated that OXTR activation via OXT inhibits Kir7.1 in the RPE cells of the eye [25]. Levels of OXT increase during labor to stimulate uterine myometrial contraction [26]. Therefore, OXT could be inhibiting any Kir7.1 expressed during partition. Additionally, P4 demonstrated the ability to activate Kir7.1 in the choroid plexus of the brain [20]. P4 concentrations are high at the onset of pregnancy and fluctuate until they drop at the end of pregnancy [27]. Therefore, P4 may increase the activity of Kir7.1 in early- and mid-gestation, resulting in the maintenance of uterine quiescence and the prevention of preterm labor. A study demonstrated that the addition of P4 in Kir7.1-expressing mouse myometrium led to a further decrease in contractility, compared to myometrium expressing Kir7.1 that was not treated with P4 [19]. This further supports that P4 may be helping to regulate Kir7.1's role on uterine quiescence during pregnancy.

We aimed to utilize OXT and P4 to modulate or activate Kir7.1 activity in primary human uterine smooth muscle cells (HUtSMC) and assess the response of free Ca2+ within the cell. We planned to use a Ca^{2+} visualizer (Geco1a) that would bind to free Ca^{2+} inside the cell and utilize live-cell imaging to quantify changes in free cellular Ca^{2+} marked by changes in Geco1a fluorescence. We hypothesize that Kir7.1 will be inhibited by OXT treatment and activated by P4 treatment. Downstream, we expect that free

Ca^{2+} inside the cell, and subsequent Geco1a fluorescence, will increase with OXT treatment and decrease with P4 treatment, due to Kir7.1's influence on cellular voltage.

Before we could investigate this, we needed to deliver Geco1a to HUtSMC. Additionally, since Kir7.1 has been shown not to express until mid-gestation, we needed to force the cells to express Kir7.1 [16]. We hypothesized that Kir7.1 and Geco1a plasmids would be successfully delivered and expressed in our cells via nucleofection, transfection, transduction, and lipid nanoparticle (LNP) delivery; and that the efficiency of expression would depend on the mode of delivery.

RESULTS

Nucleofection of HUtSMC results in low expression of the GFP^{WT} plasmid.

We investigated whether nucleofection would deliver Kir7.1 and Geco1a plasmids to HUtSMC. Cells were nucleofected in a 1:1 ratio with Kir7.1+Geco1a, Kir7.1+a dummy plasmid (dummy), Geco1a+dummy, or GFP^{WT}+dummy plasmid, according to company protocols. Additionally, a company's positive control from MaxCyte, TM2-GFP, was evaluated for MaxCyte nucleofection. The efficacy of two different nucleofection machines and three different programs was investigated, and fluorescence was visualized to calculate the percentage of cells expressing GFP-tagged Kir7.1 and RFP-tagged Geco1a after 24 hours. Low editing efficiency for the GFP^{WT} plasmid was demonstrated using two Lonza programs **(Fig. 1A and 1B)**. Additionally, only 1-2% of cells expressed the Kir7.1 plasmid, with no expression of Geco1a observed. For MaxCyte nucleofection, GFP^{WT} and TM2-GFP demonstrated successful delivery that was higher than Lonza **(Fig. 1C and D)**. However, for MaxCyte transduction, Kir7.1 delivery resulted in no more than 1% of cells expressing Geco1a. Therefore, nucleofection was not successful at delivering Kir7.1 or Geco1a to HUtSMC.

LNP delivery was unable to deliver plasmids to HUtSMC cells.

LNP delivery has been a novel and successful delivery method for DNA [28]. Therefore, we wanted to evaluate its ability to deliver plasmids to HUtSMC. Only 1% of cells demonstrated GFP^{WT} expression following LNP delivery **(Fig. 2A and B)**. Additionally, Kir7.1 and Geco1a were unable to be delivered to HUtSMC via LNP delivery. Therefore, LNP delivery was not successful in HUtSMC cells.

Geco1a and Kir7.1 are successfully transfected in CHO-K1 and CHO-M1, but not HUtSMC cells.

Delivery of Kir7.1 and Geco1a to HUtSMC via transfection was attempted at a 1:1 ratio, and the cells were visualized 24 hours after treatment. As a positive control, GFP^{WT} was delivered to cells at a low delivery efficiency **(Fig. 3A and B)**. However, only 4% of Kir7.1 was delivered to cells, and no delivery of Geco1a was achieved. Therefore, we wanted to investigate if delivery issues were due to issues with the Kir7.1 and Geco1a plasmids, or because HUtSMC are difficult to target with transfection. We transfected CHO-K1 and CHO-M1 with Kir7.1+Geco1a (1:1 ratio) and imaged for fluorescence. Kir7.1 and Geco1a were successfully delivered to both CHO-K1 and CHO-M1 cells, but not to HUtSMC **(Fig. 3C)**. This demonstrates that our plasmids were not the factor leading to low delivery efficiencies, but that HUtSMC cells were hard to target with transfection.

Lenti-Kir7.1 successfully transduced HUtSMC at a high delivery efficiency.

Transduction of HUtSMC with a Lenti-Kir7.1 and AAV-GC13-Geco1a was attempted. Our lab has previously demonstrated successful delivery of Kir7.1 to hiPSC-RPE cells using the Lenti-Kir7.1 that we chose for this study [29]. Expression of GFP-tagged Kir7.1 was imaged 6 and 12 days after transduction and demonstrated high delivery efficiency (100%) of Kir7.1 at both time points **(Fig. 4A and B)**. AAV-GC13-Geco1a was transduced 6 days after Kir7.1 expression and imaged 6 days later. No expression of Geco1a was observed. We aimed to determine whether the serotype of AAV contributed to the lack of

expression of AAV-GC13-Geco1a, so we investigated the delivery efficiency of AAV-GC13-GFP. Additionally, an AAV-GC03-GFP serotype was used for comparison. AAV-GC03 serotype successfully delivered GFP to cells at a high delivery efficiency 6 days after treatment **(Fig. 4C)**. In contrast, AAV-GC13 was not able to deliver GFP to HUtSMC cells, 6 days post-treatment. Confirming that the serotype of AAV was likely the cause of the unsuccessful delivery of Geco1a.

DISCUSSION

Inhibition and activation of Kir7.1 in mouse myometrium have been demonstrated as influencing uterine quiescence and contractility [16, 19]. However, no other studies have investigated the role of Kir7.1 in the uterus myometrium. OXT has been demonstrated in the inhibition of Kir7.1 of RPE cells, and P4 treatment has resulted in the activation of Kir7.1 in the choroid plexus and mouse uterine myometrium [19, 20, 25]. Demonstrating that these necessary pregnancy hormones could have the same effect on Kir7.1 in the uterus to maintain hormone control over uterine quiescence and contractility.

We wanted to investigate the effect of these hormones on Kir7.1 activity and subsequent Ca^{2+} channel activity in HUtSMC. Therefore, we needed to express Kir7.1 and Geco1a in the cells. We explored the efficacy of nucleofection, transfection, transduction, and LNP delivery of a GFP-tagged Kir7.1 and an RFP-tagged Geco1a to HUtSMC. Additionally, a GFP plasmid was used for comparison. Nucleofection, transfection, and LNP delivery were not able to deliver Kir7.1 to the cells, observing a maximum of 4% of cells expressing GFP-tagged Kir7.1 using transfection **(Fig. 1A and B, 2A and B, and 3A and B)**. Additionally, Geco1a was not delivered using any of these methods. To evaluate if the inability of these methods to deliver Geco1a was due to issues with the plasmid or the cell type, we transfected CHO-K1 and CHO-M1 cells with Kir7.1+Geco1a and imaged them under a live-cell imaging microscope. Transfected HUtSMC were imaged for comparison and demonstrated no efficient delivery of Kir7.1 or Gec1a **(Fig. 3C)**. However, CHO-K1 and CHO-M1 cells expressed Kir7.1 and Geco1a, demonstrating that our plasmid was not the issue. Rather, delivering plasmids to HUtSMC was

challenging, further confirmed by the low efficiency observed with GFP plasmid delivery **(Fig. 1A and B, 2A and B, and 3A and B)**. Additionally, these HUtSMC cells spontaneously contract in culture [30]. Demonstrating that a lack of free Ca^{2+} inside HUtSMC is not the cause of the lack of observed Geco1a expression.

Our lab has previously used Lentiviral transduction to deliver Kir7.1 to hiPSC-RPE cells efficiently [29]. Therefore, we used transduction to deliver Lenti-Kir7.1 and an AAV-GC13-Geco1a, that was available in our lab. 6 days after transduction, all cells expressed Kir7.1 **(Fig. 4A and B)**. In contrast, Geco1a was not expressed 6 days after transduction. To understand if the GC13-AAV serotype led to no Geco1a expression, we transduced cells with an AAV-GC13 containing GFP. An AAV-GC03 serotype containing GFP was also transduced for comparison. While AAV-GC03-GFP successfully delivered GFP to HUtSMC, the GC13 serotype did not **(Fig. 4C)**. Thus, demonstrating that the AAV serotype explains the lack of Geco1a delivery to HUtSMC.

These results demonstrate that HUtSMC are difficult to deliver plasmids to using nucleofection, LNPs, or transfection. Therefore, future studies should focus on transduction methods that utilize AAV-GC03 or Lentivirus delivery of Geco1a.

MATERIALS AND METHODS

Cell culture

Normal, HUtSMCs were ordered from ATCC (PCS-460-011) and maintained in vascular cell basal medium (ATCC, PCS-100-030) containing a vascular smooth muscle cell growth kit (ATCC, PCS-100-042) and 1% antibiotic-antimycotic (Anti-Anti, Gibco, 15240062) according to company recommendations. CHO-K1 and CHO-M1 cells were maintained in medium containing F12 (Gibco, 11765-054), with 10% fetal bovine serum (FBS, HyCloneTM Characterized Fetal Bovine Serum, Heat-inactivated, SH30396.03HI), 1% penicillin-streptomycin (Pen-Strep, GeminiBio, 400-109), and 1% anti-anti. Cells were maintained in a cell incubator at 37°C and 5% CO_2. The cells were split using Dulbecco's

Phosphate-buffered Saline (DPBS, GIBCO, 14190144) and gently dissociated using Accutase (Corning, 25-058-CI) once confluency reached around 80% and the media was changed every 2-3 days.

Nucleofection of HUtSMC

Cells were plated 24-hours before nucleofection. HUtSMC were nucleofected with a Lonza 4D Nucleofector with Kir7.1 plasmid (0.1ug) and Geco1a plasmid (0.1ug) in a 1:1 ratio, Kir7.1 plasmid (0.2ug), Geco1a plasmid (0.2ug), or GFP^{WT} plasmid (0.2ug). The following programs were tested: FF-130, FG-113, DS-137, CM-137, EH-106, and FP-113 using the SF cell line kit (Lonza, V4XC-2032). Additionally, nucleofection using a MaxCyte (info on machine) with the optimization 6 program was tested using the following plasmids: Kir7.1 plasmid (15ug) and Geco1a plasmid (15ug) in a 1:1 ratio, Kir7.1 plasmid (15ug), Geco1a plasmid (15ug), GFP^{WT} plasmid (15ug), or TM2 plasmid (5ug) provided by MaxCyte. Nucleofected cells were plated in 6-well plates and medium was changed 24 hours after treatment. The Kir7.1 plasmid was GFP tagged, and Geco1a was RFP tagged to allow for visualization of protein. Cells were imaged for fluorescence 24 hours after treatment. Imaging and analysis of percent of cells expressing fluorescence was performed on an EVOS M5000 microscope.

LNP delivery to HUtSMC

A C12-LNP particle was created and used for delivery of the following plasmids to HUtSMC: Kir7.1 (1ug) and Geco1a (1ug), Kir7.1 (1ug), Geco1a (1ug), or GFP^{WT} (1ug). Kir7.1 plasmid was tagged with GFP and the Geco1a plasmid was tagged with RFP to allow for fluorescent imaging. Cells were plated in a 6 well plate and imaged 24 hours after treatment. An EVOS M5000 microscope was used for fluorescent imaging and analysis.

Transfection of HUtSMC, CHO-K1, and CHO-M1 cells

Transfection of HUtSMC was performed using TransIT-LT1 (Mirus, MIR 2304), as suggested by Mirus, Opti-Mem (Gibco, 31985-070), and 2 µg in a 1:1 ratio of the following plasmids: Kir7.1 and Geco1a, Ca2+ and dummy, or GFP^{WT} and dummy. Additionally, CHO-K1 and CHO-M1 cells were transfected with TransIT-X2 (Mirus, MIR 6000), Opti-MEM, and Kir7.1 plasmid (1 µg) + Geco1a plasmid (1 µg) in a 1:1 ratio. This transfection reagent was selected due to its previous success in delivering Geco1a to CHO-M1 cells. Following transfection, cells were maintained in a 6-well plate, and the media was changed 24 hours after treatment. Cells were imaged using an EVOS M5000 microscope. Additionally, Kir7.1+Geco1a-treated cells were imaged 24 hours following treatment using a confocal microscope (Nikon Eclipse FN1) with a Hamamatsu ORCA-Flash4.0 digital camera (model: C11440-22CU) using NIS-Elements AR 5.41.02 software for capturing and analysis of images.

HUtSMC Transduction

Transduction of HUtSMC was performed using $7.8x10^9$ TU/ml GFP-tagged Lenti-Kir7.1 (Vector Builder, LVP-VB161020-1047mdf), $4.7x10^{10}$ TU/ml RFP-tagged AAV-GC13-Geco1 (OBiO, E10252), $2.4x10^{13}$ AAV-GC13-GFP (OBiO, GL3048-1), or $4.9x10^{12}$ AAV-GC03-GFP (OBiO, GL3048-2). 8ug of polybrene (Santa Cruz Biotechnology, sc-134220) was used to increase transduction efficiency. Cells were maintained in 35-mm dishes and imaged and analyzed 7 days after treatment using an EVOS M5000 microscope to detect fluorescence.

Statistical Analysis

A two-tailed Student's t-test was performed using Microsoft Excel for the statistical analysis. Differences were considered statistically significant at $p < 0.05$; the results are expressed as mean ±SEM.

FIGURES AND TABLES

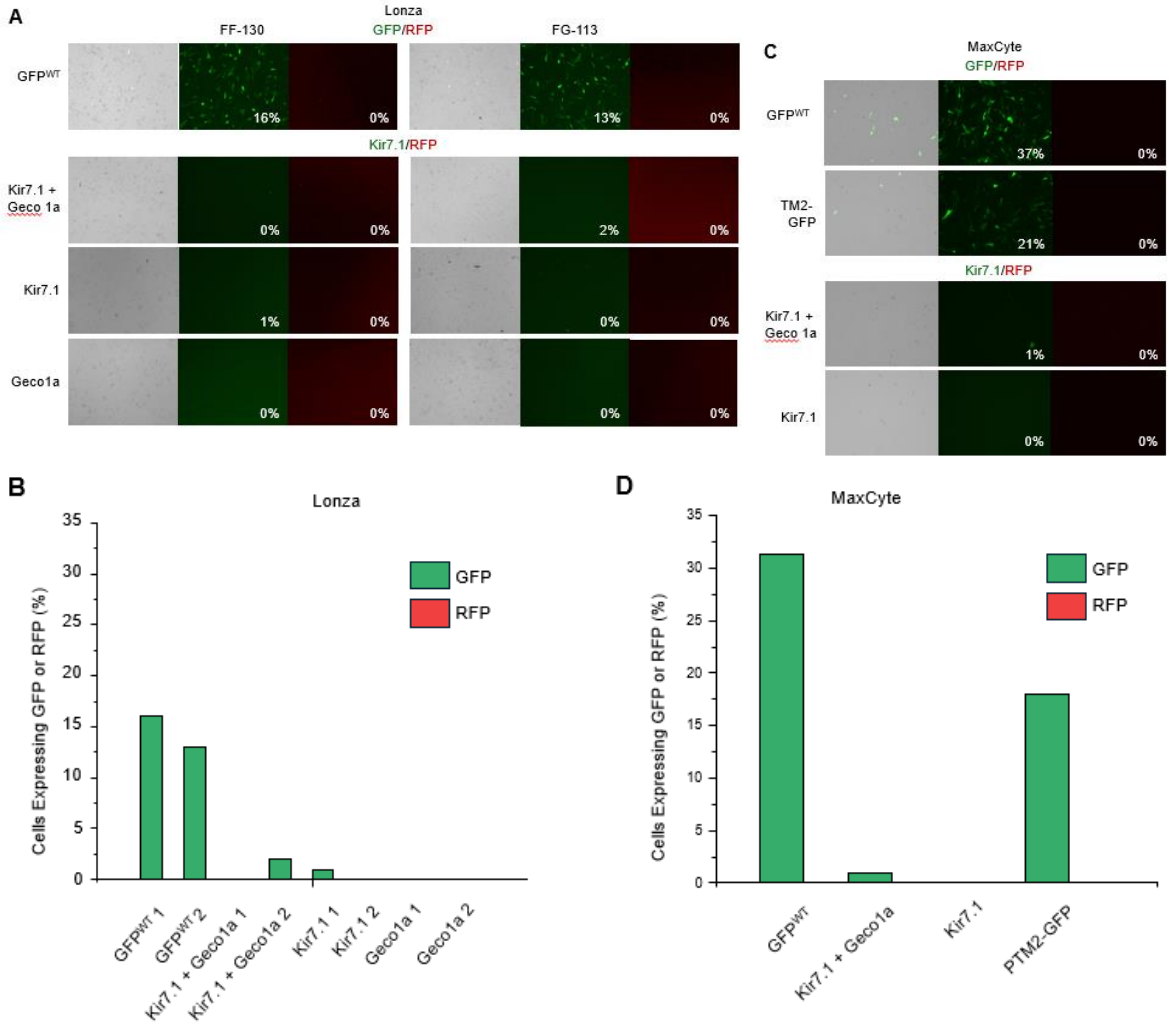

Figure 1: HUtSMC nucleofection demonstrates low expression when using GFP^{WT} plasmids. (A) Representative fluorescent images of nucleofection with Lonza programs FF-130 or FG-113, using plasmids containing either GFP, Kir7.1 + Geco1a (1:1 ratio), Kir7.1, or Geco1a. Percent of HUtSMC cells expressing either GFP or RFP 24 hours after treatment is demonstrated. GFP and GFP-tagged Kir7.1 expression is green, and RFP-tagged Geco1a is red. **(B)** Comparison of Lonza percentage treated cells using program FF-130 (1) or FG-113 (2). Two programs, FF-130 and FG-113, demonstrated low efficiency in the delivery of GFP^{WT} plasmid, at 16% and 13% respectively. 2% of cells expressed Kir7.1 following delivery of Kir7.1+Geco1a with the FG-113 program, but not with the FF-130 program. FF-130 delivered Kir7.1 to 1% of cells in the Kir7.1+dummy group, but no delivery was observed when using FG-113. No delivery of Geco1a was observed for Lonza nucleofection using either program. Percent GFP represented in green and percent RFP in red. **(C)** Nucleofection using a MaxCyte machine demonstrating the percentage of cells expressing a GFP- or RFP-tagged protein, 24 hours after treatment. A comparison was made between the GFP plasmid, Kir7.1+Geco1a (at a 1:1 ratio), Kir7.1, and TM2-GFP. GFP and GFP-tagged Kir7.1 expression is green, and RFP-tagged Geco1a is red. **(D)** Percentage of cells treated using the MaxCyte system. GFP^{WT} and TM2 demonstrated successful delivery at rates of 37% and 21%, respectively. Additionally, 1% of cells expressed Kir7.1 following Kir7.1+Geco1a nucleofection, but not in the Kir7.1+dummy group. There was no successful delivery of Geco1a. Percent GFP represented in green and percent RFP in red.

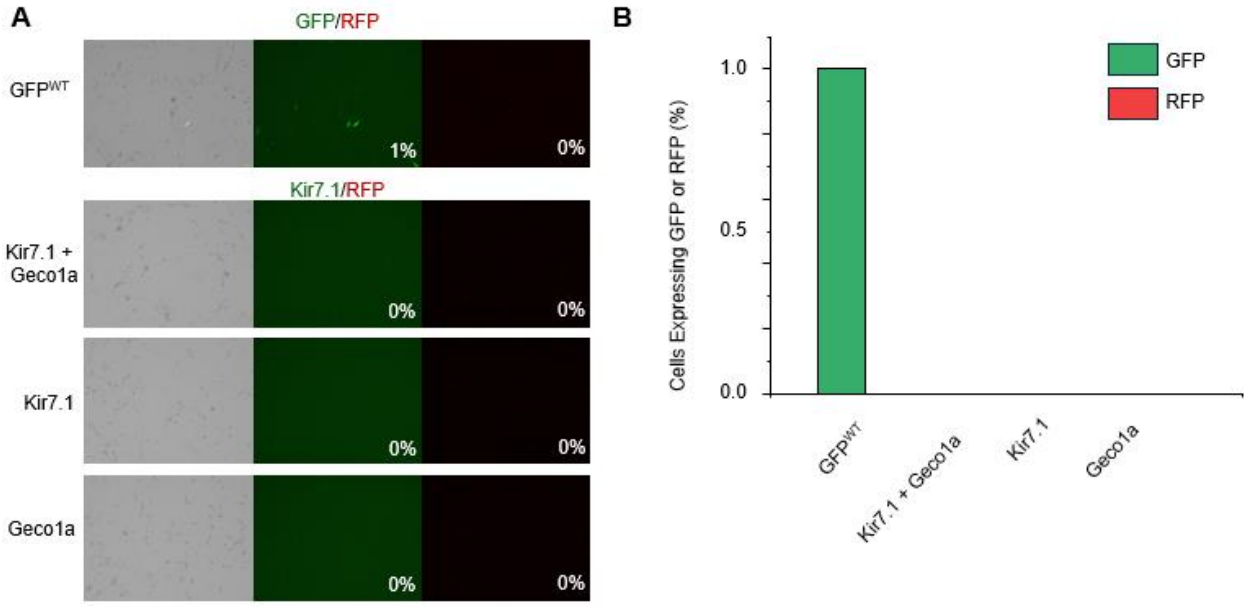

Figure 2: LNP delivery was unable to deliver plasmids to HUtSMC. (A) Fluorescent images demonstrating the percentage of cells expressing GFP (green), GFP-tagged Kir7.1 (green), or RFP-tagged Geco1a (red), 24 hours after LNP delivery. **(B)** Graph depicting the percentage of cells expressing GFP (green) or RFP (red), following LNP delivery. Only 1% of cells successfully expressed GFP^{WT} following treatment. No delivery of Kir7.1 or Geco1a was observed.

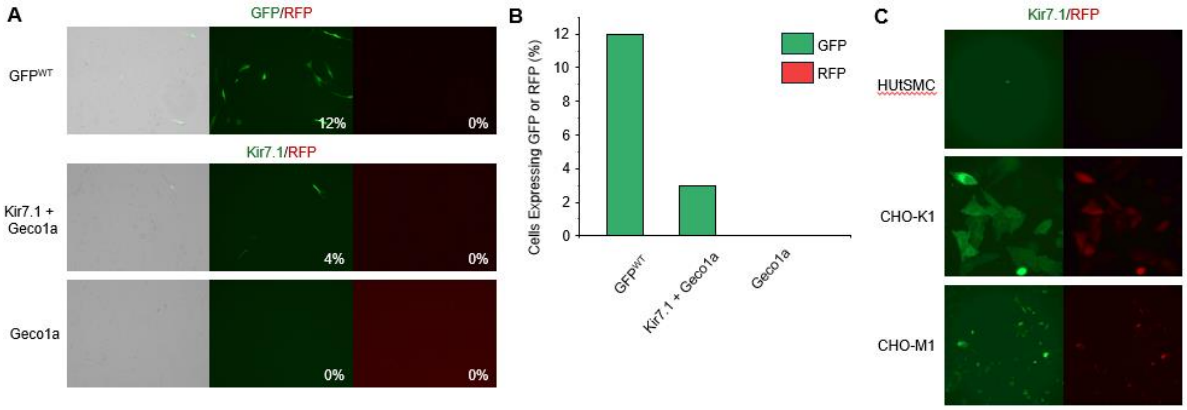

Figure 3: Transfection of Kir7.1 and Geco1a in CHO-K1 and CHO-M1 cells, but not HUtSMC. (A) Fluorescent images demonstrating transfection efficiency, 24 hours after treatment, of the following plasmids: GFP^{WT}+dummy, Kir7.1 + Geco1a, or Geco1a+dummy at a 1:1 ratio. Percentage of cells demonstrating either GFP (green, GFP-tagged Kir7.1 (green), or RFP-tagged Geco1a (red). **(B)** Percent of cells expressing either GFP (green), GFP-tagged Kir7.1 (green), or RFP-tagged Geco1a (red), 24 hours after transfection. Low delivery efficiency is observed with GFP^{WT} (12%) and Kir7.1 (4%). No delivery of Geco1a is observed. **(C)** Confocal images of HUtSMC, CHO-K1, or CHO-M1 cells 24 hours after transfection. GFP-tagged Kir7.1 is represented in green, and RFP-tagged Geco1a is represented in red.

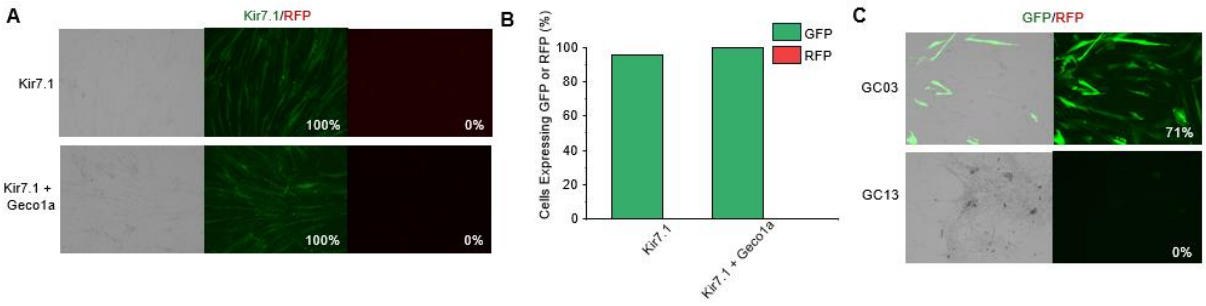

Figure 4: Transduction of HUtSMC demonstrated high efficiency for Lenti-Kir7.1 and AAV-GC03-GFP. (A) Fluorescent images taken 6 days after HUtSMC cells were transduced with either Lenti-Kir7.1 alone or Lenti-Kir7.1 and AAV-GC13-Geco1a. The percentage of cells expressing either GFP-tagged Kir7.1 (green) or RFP-tagged Geco1a (red) is shown. **(B)** Graph depicting percent GFP (green) and percent RFP (red) for Lenti-Kir7.1 and AAV-GC13-Geco1a transduction. All cells (100%) expressed Kir7.1 after 6 days (Kir7.1, top). Cells were then transduced with Geco1a and demonstrated no expression after 6 days. However, 100% of cells still expressed Kir7.1 12 days after transduction. (Kir7.1+Geco1a, bottom). **(C)** Images showing the percentage of GFP (green) from AAV-GC03-GFP- or AAV-GC13-GFP-transduced cells, 6 days post-treatment. 71% of cells expressed GFP from AAV-GC03 viral transduction, while AAV-GC13 delivery resulted in 0% GFP expression.

REFERENCES

1. Kramer, M.S., *The epidemiology of adverse pregnancy outcomes: an overview.* J Nutr, 2003. **133**(5 Suppl 2): p. 1592S-1596S.
2. *Adverse Birth Outcomes*, in *America's Children and the Environment*. 2013. p. 264-388.
3. Abadiga, M., et al., *Determinants of adverse birth outcomes among women delivered in public hospitals of Ethiopia, 2020.* Arch Public Health, 2022. **80**(1): p. 12.
4. Freaney, P.M., et al., *Temporal Trends in Adverse Pregnancy Outcomes in Birthing Individuals Aged 15 to 44 Years in the United States, 2007 to 2019.* J Am Heart Assoc, 2022. **11**(11): p. e025050.
5. Yee, L.M., E.C. Miller, and P. Greenland, *Mitigating the Long-term Health Risks of Adverse Pregnancy Outcomes.* JAMA, 2022. **327**(5): p. 421-422.
6. Romero, R., S.K. Dey, and S.J. Fisher, *Preterm labor: one syndrome, many causes.* Science, 2014. **345**(6198): p. 760-5.
7. Rundell, K. and B. Panchal, *Preterm Labor: Prevention and Management.* Am Fam Physician, 2017. **95**(6): p. 366-372.
8. Dong, Y. and J.L. Yu, *An overview of morbidity, mortality and long-term outcome of late preterm birth.* World J Pediatr, 2011. **7**(3): p. 199-204.
9. Khandre, V., J. Potdar, and A. Keerti, *Preterm Birth: An Overview.* Cureus, 2022. **14**(12): p. e33006.
10. Mwaniki, M.K., et al., *Long-term neurodevelopmental outcomes after intrauterine and neonatal insults: a systematic review.* Lancet, 2012. **379**(9814): p. 445-52.
11. Goldenberg, R.L., *The management of preterm labor.* Obstet Gynecol, 2002. **100**(5 Pt 1): p. 1020-37.
12. Ramachandran, A., et al., *Reframing spontaneous preterm birth as a preventable adverse outcome-A clinical audit of a preventative toolbox.* Acta Obstet Gynecol Scand, 2025. **104**(5): p. 906-912.

13. Wray, S., et al., *Calcium signaling and uterine contractility.* J Soc Gynecol Investig, 2003. **10**(5): p. 252-64.

14. Wray, S., C. Prendergast, and S. Arrowsmith, *Calcium-Activated Chloride Channels in Myometrial and Vascular Smooth Muscle.* Front Physiol, 2021. **12**: p. 751008.

15. Jones, K., et al., *Electrophysiological characterization and functional importance of calcium-activated chloride channel in rat uterine myocytes.* Pflugers Arch, 2004. **448**(1): p. 36-43.

16. McCloskey, C., et al., *The inwardly rectifying K+ channel KIR7.1 controls uterine excitability throughout pregnancy.* EMBO Mol Med, 2014. **6**(9): p. 1161-74.

17. Wray, S. and S. Arrowsmith, *Uterine Excitability and Ion Channels and Their Changes with Gestation and Hormonal Environment.* Annu Rev Physiol, 2021. **83**: p. 331-357.

18. Hibino, H., et al., *Inwardly rectifying potassium channels: their structure, function, and physiological roles.* Physiol Rev, 2010. **90**(1): p. 291-366.

19. Haoui, M., et al., *Kir7. 1 is the physiological target for hormones and steroids that regulate uteroplacental function.* Science Advances, 2025. **11**(10): p. eadr5086.

20. Bjorkgren, I., et al., *The epithelial potassium channel Kir7.1 is stimulated by progesterone.* J Gen Physiol, 2021. **153**(10).

21. Toms, M., *Investigating the pathophysiology of KCNJ13 and USH2A retinopathies using zebrafish models*. 2018, UCL (University College London).

22. Toms, M., et al., *Missense variants in the conserved transmembrane M2 protein domain of KCNJ13 associated with retinovascular changes in humans and zebrafish.* Exp Eye Res, 2019. **189**: p. 107852.

23. Kabra, M., et al., *Nonviral base editing of KCNJ13 mutation preserves vision in a model of inherited retinal channelopathy.* The Journal of Clinical Investigation, 2023. **133**(19).

24. Khan, A.O., et al., *A distinct vitreo-retinal dystrophy with early-onset cataract from recessive KCNJ13 mutations.* Ophthalmic Genet, 2015. **36**(1): p. 79-84.

25. York, N., et al., *Oxytocin (OXT)-stimulated inhibition of Kir7.1 activity is through PIP2-dependent Ca(2+) response of the oxytocin receptor in the retinal pigment epithelium in vitro.* Cell Signal, 2017. **37**: p. 93-102.

26. Blanks, A.M. and S. Thornton, *The role of oxytocin in parturition.* BJOG, 2003. **110 Suppl 20**: p. 46-51.

27. Johansson, E.D., *Plasma levels of progesterone in pregnancy measured by a rapid competitive protein binding technique.* Acta Endocrinol (Copenh), 1969. **61**(4): p. 607-17.

28. Alvarez-Benedicto, E., et al., *Optimization of phospholipid chemistry for improved lipid nanoparticle (LNP) delivery of messenger RNA (mRNA).* Biomater Sci, 2022. **10**(2): p. 549-559.

29. Shahi, P.K., et al., *Gene Augmentation and Readthrough Rescue Channelopathy in an iPSC-RPE Model of Congenital Blindness.* Am J Hum Genet, 2019. **104**(2): p. 310-318.

30. Chen, C., et al., *The Role of Formyl Peptide Receptor 1 in Uterine Contraction During Parturition.* Front Pharmacol, 2021. **12**: p. 696697.